2015

Asymptotic Fields for Cracks Terminating at Bi-Material Interface with Arbitrary Angles

Xiao Liu
Lehigh University

ASYMPTOTIC FIELDS FOR CRACKS TERMINATING AT BI-MATERIAL INTERFACE WITH ARBITRARY ANGLES

By

Xiao Liu

Presented to the Graduate and Research Committee
of Lehigh University
in Candidacy for the Degree of
Doctor of Philosophy

In
Mechanical Engineering

Lehigh University
January, 2015

Approved and recommended for acceptance as a dissertation in partial fulfillment of the requirements for the degree of Doctor of Philosophy.

_____
Date

_____
Prof. Herman F. Nied:
Committee Chairman and Dissertation Advisor
Dept. of Mechanical Engineering and Mechanics
Lehigh University

_____
Accepted Date

Committee Members

_____
Prof. Terry J. Delph
Dept. of Mechanical Engineering and Mechanics
Lehigh University

_____
Prof. Edmund Webb III
Dept. of Mechanical Engineering and Mechanics
Lehigh University

_____
Prof. Raymond A. Pearson
Dept. of Material Science and Engineering
Lehigh University

Acknowledgement

First, I would like to give my heartfelt appreciation to my academic advisor, Professor Herman F. Nied, for his continuous support and valuable guidance throughout my study and the accomplishment of this dissertation. I have had honor of knowing him, working with him, and learning from him in the past seven years. Every step in my progress is undoubtedly associated with his endless patience and untiring support.

I extend to special thanks to all my committee members, and my other friends who provided unreserved help to my research work.

The support of the Department of Mechanical Engineering and Mechanics at the P.C. Rossin College of Engineering, and the Semiconductor Research Corporation (SRC) is gratefully acknowledged.

I wish to give express gratitude and love to my parents Qiwen Liu and Guiying Li for their unconditional love, support, encouragement and advice over my entire life. Thank them for having me to be part of such a wonderful family. Finally, great thanks are dedicated to my wife, Xiaoru Gong, and my lovely daughter, Mina Yiran Liu, who have been caring, understanding me, helped me celebrate every accomplishment. They have always been believing in me and help me believe that I can achieve and fulfill my dream.

Table of Content

List of Figures

List of Tables

Abstract

The bi-material crack problem is an interesting and important topic in the field of fracture mechanics. The existing mainstream solutions, either analytical or computational, are commonly focused on some specific cases, e.g., a crack lying on exactly the bonded border of dissimilar materials, or a crack impinging upon a bi-material interface at a right angle. However, little attention is paid to the general cases, i.e., cracks approaching or attacking the material divided border arbitrarily, which is more likely to happen in the engineering products. With any possibility of the crack's incidence angle, the asymmetric nature of the geometry and the materials property induces more difficulties in the mathematical formulation of the crack-tip stress field. The conventional analytical methods may not be a convenient way for the derivation, especially of the fracture parameters. For this end, in this study, the Williams' expansion method is exploited to investigate the two-dimensional/three-dimensional fracture problem in which the crack terminates at a biomaterial interface with an arbitrary angle of incidence. The characteristic equation is obtained and solved to investigate the distribution of dominant roots. Mathematically, a matrix-based system is developed, which can be easily used to formulate the general asymptotic solution of the singular stress and displacement fields surrounding the crack-tip. The theory of singularities is introduced to represent the mixed-mode nature of the solution for the arbitrarily-oriented crack. This concept is further employed for the cases with complex singularities. After that, the relationship of the asymptotic field and the linear elastic fracture parameters is established directly through a linear system. In addition, taking advantage of the enriched element approach, the derived formulation in this study is programmed and implemented in a finite element analysis. This provides an efficient and effective method for simulating and solving different types of crack problems, especially with complicated geometries, loading patterns and material combinations. Then different mixed-mode fracture criteria for predicting the direction of crack growth are introduced. With the method discussed in this study, the maximum circumferential stress criterion is considered to be the most appropriate one, but needs to be

slightly modified for multiple material problems. Finally, some examples of numerical solution of the asymptotic fields are demonstrated using the computed stress intensity factors and the developed matrix system for the general crack cases with an arbitrary impinging angle with respect to an interface. The numerical results for specific cases are compared with the existing references.

Keywords

Crack, Arbitrary, Singularity, Asymptotic, Enriched, Propagation

1 Introduction

The reliability is an important issue in the assessment of an engineering product's quality. A perfectly safe service life for a material is undoubtedly desired to avoid any unexpected loss. Therefore, a comprehensive understanding of materials' mechanical behaviors is meaningful and vital for the stress analysis of solid.

In classical theory, the material firstly represents an elastic response to external loading, and then a plastic deformation follows until the ultimate failure. This process, which can be characterized by a stress-strain curve, defers for different types of materials and depends on the degree of plasticity, i.e., brittle or ductile. However, in practical engineering applications, it's pretty common for bulk materials to fail at applied stress levels much lower than the material's theoretical ultimate strength. This is mainly due to stress concentrations induced by holes, sharp corners or geometric discontinuities (Figure 1), and in the non-homogeneous case, the weakness of the dissimilar material boundary. As the worst case, a crack may leads to high local intensity in the near-tip field (Figure 2). The cracking failure of solids and structures always takes place as initial defects or flaws extend to a critical length under some extreme or cyclic loading. However, it's difficult to avoid the creation of material imperfections in the fabrication process and the service life. Thus, for scientists and engineers, the mechanism of cracking is a crucial subject whose object is to find the root cause of failure and to assess the maximum load-bearing capability for actual applications.

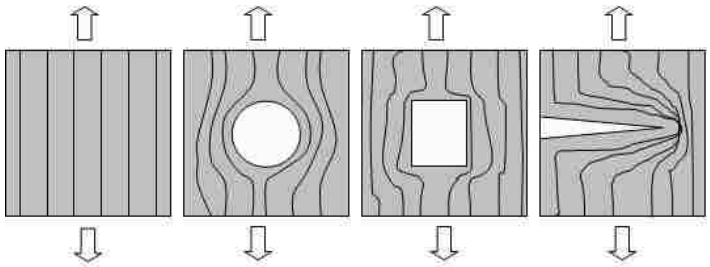

Figure 1: Different Types of Stress Concentration
(Image courtesy of Malinda Zarske, University of Colorado at Boulder, 2006)

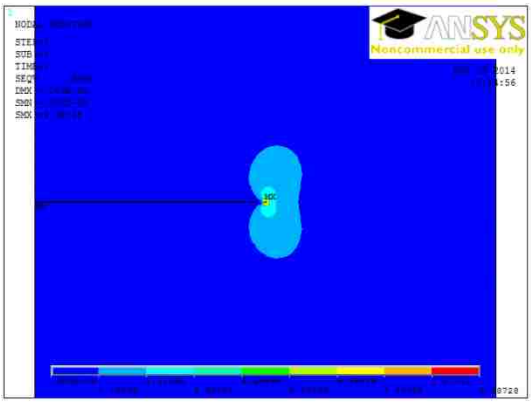

Figure 2: Stress Intensity in the Vicinity of Crack-Tip

1.1 Fracture Mechanics

Fracture mechanics is a specific field in solid mechanics to investigate and predict cracking behaviors in materials. The relevant problems are studied in analytical and experimental methods with energy-based criteria [1, 2] or stress-based criteria [3]. The application of fracture mechanics are characterized by certain mathematical concepts, which are essential for its proper practical analyses, and provide insight into the three-dimensional nature of homogeneous and interfacial crack propagation. Under the framework of Linear Elastic Fracture Mechanics (LEFM), the stress intensity factor and strain energy release rate are regarded as two significant parameters to characterize the singular behaviors around the crack tip. The former one gives the magnitude of stress in the vicinity of crack-tip from a stress-based perspective. The latter one is utilized to quantify the work required to advance a potential sub-crack using an energy-based perspective. Another significant characteristic quantity, the strength of the crack-tip singularity, cannot be ignored when one studies the asymptotic stress field. This is quantified in terms of a negative exponent of the radial distance from crack-tip and mathematically captures the extreme gradient of the stress field.

In practice, plastic behaviors can be observed in an area close to the crack-tip. For brittle and brittle-like materials, the plastic process zone is relatively small compared with the crack length, and the linear elastic fracture theory still dominates. However, for some other materials with nonlinear elastic or inelastic behavior under high-level loading, the magnitude of plastic process

zone is comparable to the crack size, and depends on the loading as well as the crack dimension. In this situation, LEFM cannot hold for accurate results any longer, and some other concepts are introduced such as crack tip opening displacement (CTOD), R-curve, J-integral, cohesive zone and etc. In fatigue crack growth specifically, the magnitude of cyclic loading is much lower than the fracture toughness. The plastic zone in the vicinity of the crack-tip is consequently small. Thus, the linear elastic fracture parameters are reasonable to apply as the driving force for crack propagation.Basically, the object of fracture mechanics research on homogeneous, non-homogeneous or layered materials is to improve the fracture resistance of structures and achieve some specialized requirements. For example, the ceramic materials have a very promising future in engineering products at high temperatures due to their high strength and low density. However ceramics have a relative low fracture toughness. Reinforcement in a ceramic matrix by adding transverse fibers has been verified to improve the toughness of the composite. This can be explained by the relative higher toughness of fibers which can impede the cracking movement (Figure 3). The fracture analyses of cracks in such fiber-reinforced matrices concentrated on the competition between sub-crack's debonding and advancing [4, 5, 6]. In some situations, it might be desired that any crack initialized in the matrix arrests on the interface, or deflects along the interface between fiber and matrix, rather than propagates into uncracked regions to result in functional damages

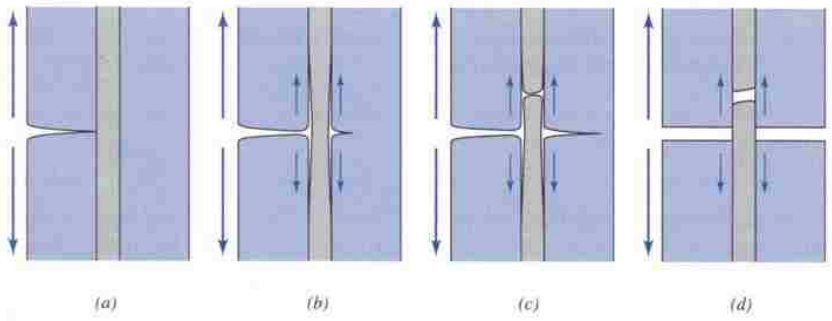

Figure 3: Cracking Behaviors in CMC Materials

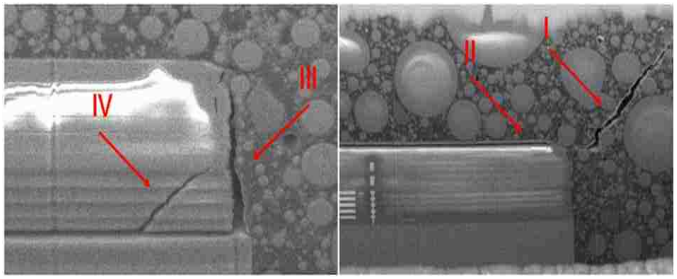

Figure 4: Various Cracks and Delaminations in TEPBGA-II Wire-bond Package.

Another application of fracture mechanics in design is in electronic packaging. From the perspective of structural mechanics, electronic devices can be considered as composite structures fabricated from very dissimilar materials [7]. Major mechanical failures of semiconductor packages are due to severe thermo-mechanical loading. Since a semiconductor package is composed of different material layers, thermal stresses are generated when the device experiences temperature changes. The material property mismatch, especially the coefficient of thermal expansion, produces high shearing and peeling stresses in the outer regions (free-edge). If the thermal conditions are severe enough, then the mechanical failure within single components or on the interface between layers can be observed (Figure 4). This kind of external conditions can be experienced by the package during the fabrication process and/or during the service life. Among these possible failure types, the debonding along the underfill/chip or underfill/substrate interfaces and mechanical failure of solder joints are the most common. When the semiconductor package experiences temperature changes, relative shearing displacements between the silicon-chip and the substrate are accommodated by the solder balls. Thus, the solder balls that are close to the free-end region of the package are subject to high shearing stresses, which may cause failure of these connections. Underfill material acts as a protective and supportive media within the package. So the debonding between the underfill and the chip or between the underfill and the substrate can also be observed. The analyses using fracture mechanics concepts can be used to predict the propagation of crack in a semiconductor packaging. The essential objective for manufacturing is to reduce the possibility of crack's initiation and prevent an existing crack from propagating to a critical region. For instance, it's desirable that cracks arising at the corner of the underfill/chip interface arrest before destroying

solder connections. As seen above, composite and laminated materials have been abundantly developed and applied in many engineering area. However, due to the bounding weakness and the material mismatch, cracking is more likely to arise in the vicinity of bonded interfaces. In the following, the analyses for different types of cracks with respect to the bi-material interface are introduced.

1.2 Bi-Material Cracks

In composite and laminated materials, both the robustness and the reliability of multi-material solids have received considerable attention. Interfaces are intrinsic to multi-material structures. This also causes discontinuities in thermal and elastic properties. The structural performance of such layered materials and systems generally depend on just these properties. The crack problems with respect to the interface have been studied under the framework of fracture mechanics since the middle of the 20th century [8-15]. Both analytical and numerical solutions have shown acceptable agreement with practical experimental results. A considerable amount of previous research work has focused mainly on particular cases, such as a crack along, perpendicular to, or parallel to the bonded interface. Because the mode III crack problem is relatively simple to be derived for any crack incidence of angle, most research work is regarding the crack of in-plane modes, i.e., Mode I and Mode II.

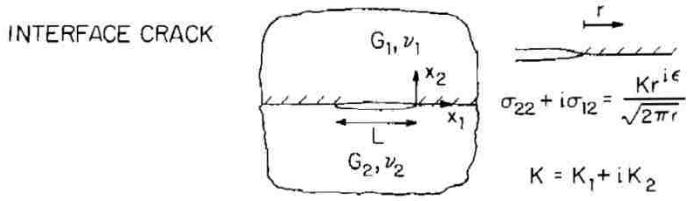

Figure 5: Interface Crack [21]

Interface Crack

The most famous case is the crack lying on the bonded line between two dissimilar materials [Figure 5]. It's well-known that, the displacement and stress fields present an oscillatory behavior in the vicinity of the crack tip for such kind of crack. In physics, this means two crack surfaces may overlap or interpenetrate near the tip field. One of the first analytical models concerning bi-

material interfacial fracture problems was presented by Williams in 1959 [8]. The most important contribution from this work was the analytically derived expressions of oscillatory displacement and stress field in the high singularity zone, which is near the crack tip for an interfacial crack model. The oscillatory behavior was characterized as

$$r^{\xi+i\rho} = r^{\xi}\{cos(\rho \log r) + isin(\rho \log r)\} \tag{1.1}$$

where $\xi = -\frac{1}{2}$, ρ is the imaginary part of the complex root and depends on the combination of materials, and r is the radial distance from crack tip. Erdogan [9] examined the case of two half-planes bonded to each other along a finite number of straight-line segments and evaluated the stress distributions near the ends of the cracks. Specific interface crack problems under different loading conditions were considered in his paper. The oscillatory behavior was interpreted by England [10] and Malyshev and Salganik [11] as the wrinkling of two surfaces of a crack and the overlapping of materials. Rice and Sih [12] formulated the problem through an approach of combining the eigenfunction expansion method with complex-variable theory of Muskhelishvili[13]. Two typical cases, a finite central crack and a semi-finite edge crack were considered lying on the bond of dissimilar elastic planes. The complex singularities given in their study will be introduced later.

In another end, the concept of contact zone in near-tip field was introduced to explain the oscillatory phenomenon, Comninou [14] believed that the oscillatory singularity of an interface crack originated from a hypothesis of direct transition between bonded and debonding segments, which were connected at the crack tip. Therefore, she introduced an analysis containing a frictionless contact zone which eliminated the oscillatory near-tip stresses. Actually, according to Comninou's study [15], the friction between crack surfaces cannot be ignored as it will affect the stress singularity. Rice [16] pointed out that the contact theory dominates if the small-scale contact conditions are satisfied. He suggested that the ratio of the contact zone size with respect to the crack length should be less than 0.01. In Sun and Qian's paper [17], they provided an equation representing the dimension of the contact zone for general interface cracks. According

to this equation, the contact length depends on the phase angle and the imaginary part of the strength of singularity.

Subinterface Crack

Another derivation from the interfacial crack is regarding a crack lying in one homogeneous side and parallel to the bonded line of dissimilar materials [Figure 6]. This is so-called subinterface crack. The depth of crack, or to say the distance to the interface, is relatively small rather than the crack's dimension. Due to the oscillatory nature by the interface, the strength of singularity for the subinterface crack is also arising as a complex number. Consequently, the complex stress intensity factor applies, but the crack depth needs to be considered in the formulation of the singular stress field [18].

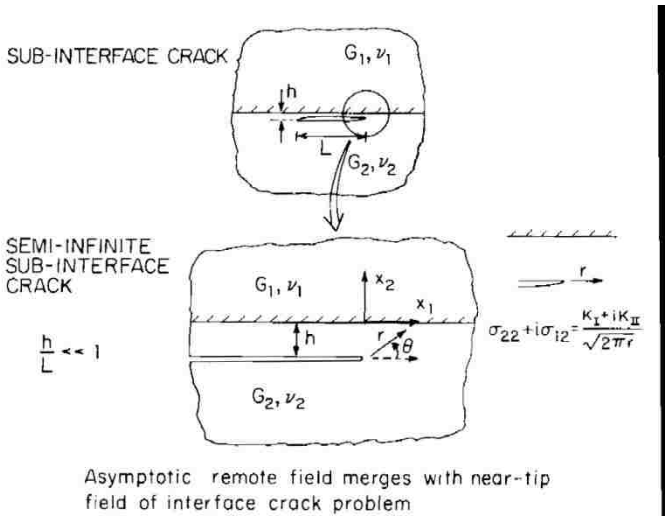

Figure 6: Subinterface cracks [18]

Crack Normal to the Interface

Another distinct bi-material crack problem is the crack normal to and terminating at a bi-material interface. In this situation, the local near-tip filed is symmetric in geometry and material properties. A general characteristic equation and discussion about such kind of was first given by Zak and Williams [19]. They used an eigenfunction expansion method to analyze the stress singularity at the crack tip. Their analysis revealed that the dominant singular behavior is of the order $r^{-\lambda}$, where λ is a real number dependent on the elastic moduli of the joined material. Cook and Erdogan [20] used the Mellin transform method to derive the governing equation of infinite and

finite cracks perpendicular to an interface, and obtained the stress intensity factors as a parameter to predict the initiation and propagation of a crack. Lin and Mar [21] presented a finite element analysis of the stress intensity factors for cracks perpendicular to the bi-material interface. The element is formulated based on the crack tip stress field and the hybrid formulation. Kaya [22] reviewed various two-dimensional and three-dimensional crack cases using the finite-part integral method, and the second dominant root of characteristic equation was taken into account to improve the convergence of calculated stress intensity factors. Sugimura [23] considered the effects of plasticity as a shielding or amplification for the propagation of the crack approaching perpendicularly to the interface. A basic equation for a finite crack normal to and terminating at a bi-material interface was developed by Wang [24, 25] using dislocation simulation approach. For the same kind of crack, Chang [26] proposed a pair of path-independent contour integrals which can be evaluated accurately to obtain the stress intensity factors. The SIFs and the distribution of stresses at the bi-material interface crack-tip were experimentally determined using the shadow optical method of caustics by Papadopoulos [27].

Crack with Inclined Angle to Interface

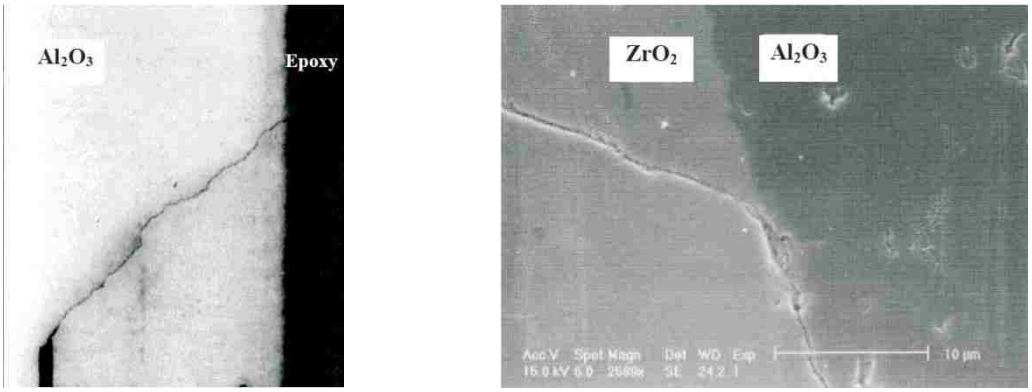

(a) Crack propagating to the interface[28] (b) Indentation crack deflecting into interface [29]

Figure 7: Cracks to Interface with Arbitrary Impinging Angles

However, in practical applications, a crack approaching an interface in a solid of dissimilar materials will not always hold a specific orientation relative to the bonded border as discussed above [Figure 7]. The existing analytical solutions may not be applied directly. So an investigation for arbitrarily oriented cracks with respect to the interface would be more meaningful for

determining the critical nature of such problems. In previous work, Bogy [30] examined the plane problem within the two-dimensional theory of elastostatics using Mellin transform method,. However, the applied boundary conditions of normal and shear stresses on bonded surfaces were not in accord with the nature of traction-free crack faces. Ashbaugh [31] also studied similar problems using particular mathematical techniques, but didn't demonstrate the general fields. In Fenner's paper [32], the eigenfunction expansion method, originally applied to the analysis of crack problems by Williams, was used to derive and compare the elastic stress singularities in the plane, bending and anti-plane strain problems respectively, for the general case of a crack meeting the interface at an arbitrary angle of incidence. Although the distribution phenomena of dominant roots versus angles for different combinations of materials were illustrated, the generalized solution was not given until the 1990's. A comprehensive analysis of the state of stress and stress intensity factors was also performed by Chen and Wang [33]. In this paper, the effects from various material combinations on the fracture behavior of an arbitrarily inclined crack terminating at a bi-material interface were investigated using the complex variable method. The general characteristic equation was represented in terms of elastic constants of bi-material properties and the crack incidence angle. In the study by Marsavina and Sadowski [34], the circumferential variation of the asymptotic stress field was illustrated. The stress intensity factors were computed by extrapolating the solution of finite element analysis. But they were only focused on those cases with real dominant roots.

In all these types of crack with respect to the interface, the conventional mode I and mode II stress fields are intrinsically coupled (except some particular cases), and cannot usually be characterized by the stress intensity factors respectively. For the complex singularity, Rice [16] brought in a new definition of the coupled stress intensity factor $K = k_I + ik_{II}$ associated with an elastic interface crack. The new quantities k_I and k_{II} are simply the real and imaginary parts of the complex stress intensity factor. For the real dominant roots, so-called split singularities, both strong and weak singularities are used simultaneously to derive the asymptotic solution. The second root is taken into account to improve the convergence of calculated stress intensity

factors [22]. Also, the weaker singularity has been shown to be able to readily affect whether the crack will penetrate or debond the interface [35].

The object of this study is to investigate an inclined crack at an interface, and to generate the general asymptotic field with respect to either complex or real strength of singularity.

It should be also noted that, the classic analytical methods are always limited to simple geometries, material combinations, external loads or their superposition. The use of numerical techniques, particularly the finite element method, has vastly broadened the range of problems that can be solved by computational approaches [21].

1.3 Finite Element Analysis of Cracks

Usually, the analytical solutions for stress intensity factors can be obtained in closed form only for very simple geometries, material combinations, external loads or their superposition. The use of numerical techniques has vastly broadened the range of problems that can be solved by computational approaches.

Among various numerical methods, the finite element method, accomplished by the extrapolation technique, is prevalently established as an engineering tool for solving crack problems. One of the earliest application associated with the finite element method for fracture mechanics was presented by Swedlow, Williams and Yang [36], Henshell and Shaw [37] and Barsoum [38] tried to get accurate stress solutions around crack tip by moving the mid node of a eight-node quadrilateral element to a quarter point position. However, it has been well recognized that in treating crack problems to compute stress singularities, the solutions converge very slowly if the finite elements include only the conventional polynomial displacement field without the “correct” singular terms. In order to obtain an accurate evaluation of the stress intensity factor, some investigators began to include the correct singular behavior in terms of r and θ as a parameter in the regular formulation.

The hybrid element theory [39] involving the effects of the crack tip singularity and the complex variable technique have been adopted to decrease the difference of stress intensity factors to 1%

compared with the theoretical solution or less using at least 20 to 50 degrees of freedom. The displacement compatibility is enforced in an integrated sense by minimizing a functional containing boundary displacements and additional unknown Lagrange multipliers. Following the hybrid approach, Lin and Mar [21] created a new type of bi-material element which encloses the crack tip and is embedded in a finite element representation of the plane surrounding the crack.

Recently, a similar finite element technique, named extended finite element method (XFEM), has been developed for modeling cracks and simulating crack growth with relatively coarse meshes [40-42], and it has been utilized for analyzing various cracking problems [43-45]. In XFEM, the standard displacement field is also integrated with the discontinuous field and the singular asymptotic crack tip field using the Healviside step function and the partition of unity method respectively. The elements don't need to explicitly conform to the crack's geometry. In addition, the mesh doesn't need to be refined very much around in the near-tip area. As a consequence, the facture parameters can be obtained accurately since the singular field is considered concurrently.

Another concept, often described as enriched finite elements, has much simplified the calculation of fracture parameters by incorporating the asymptotic solution, the partition of unity method and regular finite element analysis together. The specific element can be utilized in a regularly meshed model to numerically determine stress intensity factors and strain energy release rates directly. Compared with XFEM, the benefits of the latter approach would be the computation of fracture parameters without any post-processing, as well as the capability of obtaining the explicit crack opening displacement. In the enriched finite element, virtual nodes are added at the locations of crack tip nodes. The stress intensity factors are treated as extra degrees of freedom (DOFs) in the elemental displacement field, just like the regular nodal displacement DOF for real nodes. The assembled global stiffness matrix is regarded as an augmented matrix involving entries contributed from the asymptotic expression of singular displacement field in terms of stress intensity factors. The enriched element was first introduced by Benzley [46]. However, its accuracy could not be generally ascertained because neglecting the displacement compatibility between regular and enriched elements prevented rigorous convergence studies. This issue was

resolved by using the “transition” element. Initial applications of enriched elements were limited to two dimensional homogeneous problems. The explicit crack tip stress and displacement expressions including asymptotic terms were developed by Chen [47] to treat problems involving interface cracks between isotropic materials. This contribution extended Benzley’s work and also gave an inspiration for subsequent applications of 2D and 3D finite element analysis in fracture mechanics. Based on previous work, Ayan and Nied [48] implemented asymptotic terms into enriched elements of various types and developed a set of engineering programs, which provides fracture mechanics analysis for two-dimensional or three dimensional, isotropic or orthotropic fracture problems. One benefit of the enriched finite element method is that the fracture parameters of interest, K_I, K_{II}, K_{III}, are considered as additional unknowns in the formulation and computed simultaneously with other regular degrees of freedom. Another contribution in their work comes from the application of transition elements, through which the displacement compatibility is satisfied exactly on all element surfaces between the enriched crack tip elements and the regular elements. In 2006, the formulation for 3-D interfacial crack problems was implemented in the program by Ayan, Kaya and Nied [49].

The last method, the enriched finite element, is preferred in this study due to its straight and simplified process of computing stress intensity factors. The new formulation is developed and implemented for a crack with arbitrary impinging angle with respect to an interface.

1.4 Idealizations for 3D Cracks

The most common solutions of linear elastic fracture mechanics are specifically for two-dimensional crack models, and either the plane strain or the plane stress conditions are assumed. Different loading pattern are applied to create different crack modes, or the mixed-mode. Obviously, the practical fracture analysis actually involves three-dimensional crack surfaces that may be flat or uneven. These geometries may result in straight or curved crack fronts. However, it’s reasonable to have a 3D crack model to be simplified and modeled using some mathematical and geometrical idealizations. For example, a semi-infinite crack, with a non-straight crack front, is embodied in a 3D isotropic and elastic solid. A certain thin-sliced plate is assumed to be cut off

and perpendicular to the crack front at the intersection point, which is regarded as the tip of a 2D semi-infinite crack model within this plate. An appropriate local coordinates system can be created in which the crack front is always tangent to the anti-plane axis. If the curvature of the crack front at this point is not extremely sharp, the local singular field in the vicinity of the crack-tip can be treated respectively with two uncoupled loading patterns, i.e., in-plane and anti-plane [Figure 8]. Then the singular fields with respect to these two independent crack modes can be generated separately under the classic plane theory of elasticity.

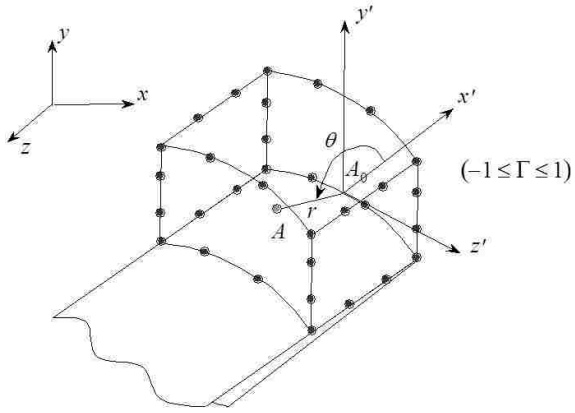

Figure 8: Local Field of 3D Crack-Tip

Basically, the leading edge of a 3D crack can be studied under the plane strain condition, and the 2D stress intensity factors agree very well with those in 3D models. It's already known that the free-edge effect prevails when a crack front intersects the free surfaces. However, the affected zone is generally quite small compared with the crack front size, so it can be ignored if some appropriate constraints are applied on the free surfaces [48].

Another concern for 3-D crack analysis comes from extreme stress gradients which may lead to significant errors. Sometimes this is caused by the large ratio between the model scale and the crack length. Theoretically, the introduction of stress singularity only characterizes the near-tip field, and doesn't satisfy the far-field very well. In finite element method, this might be controlled with a high density of mesh, but will also lead to a huge amount of elements and an unexpected computation overload. A reasonable strategy, so-called submodeling, has been widely used in computational analysis [Figure 9]. In this approach, a local model containing the crack is split out

from the global model and studied separately. Then the reasonable scale ratio with respect to the crack length can reduce the computational complexity and increase the accuracy. The global model still embodies the cut-out part but eliminate the crack. The boundary conditions for this sub-model can be derived or computed from the global analysis through boundary mapping.

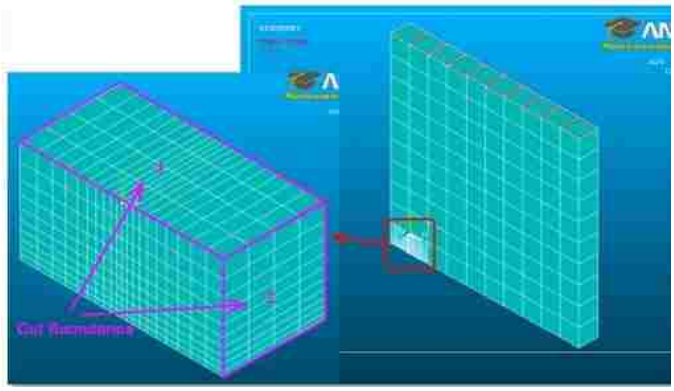

Figure 9: Sub-Model of the ¼-Symmetry Central Crack in a Plate

1.5 The Asymptotic Field with Split Singularities

Basically, the mathematical model of cracks can be formulated by using the fundamental method of the complex potential for plane elasticity and applying appropriate boundary conditions. To solve specific problems, some analytical approaches have been utilized such as the Westergarrd function method and the Williams' expansion method. Two common features have been found for various types of problem. The first observation is that the stress field can be represented by the sum of a series characterized by the negative exponents of radial distance. Since the location of interest is a finite region surrounding the crack-tip, the asymptotic terms in the sum with the singularity between (0, 1) have been verified as an adequate approximation for the exact result. Another common point is that, considering the asymptotic solution, the explicit functional form of the near-tip field is independent of the crack's large-scale geometry and the applied load. This means, for the cracks with the same shape, the asymptotic expressions of stress and displacement fields have only one variable to be determined from the applied loading. This uniqueness will be described later using the Williams' expansion method.

Mathematically, the singular field is dominated by the asymptotic terms with order of $r^{-\lambda}$, where λ is the radial distance from the crack-tip. The empirical solutions indicate $\lambda = 1/2$ for a crack

arising in a homogeneous medium, while $\lambda = \frac{1}{2} \pm i\rho$ is the resulting complex number for an interfacial crack. The stress intensity factor "*K*", a constant, is used to describe the stress concentration degree in the vicinity of a crack tip. But there are some prerequisites for the relevant mathematical model such as the materials are elastic and the interface between dissimilar sides is perfectly bonded. These assumptions are invalid within the fracture process zone and in the far-field. The materials in the process zone may deform plastically, and the near-tip geometry may have imperfections, i.e., nonlinear asperities or contacts between crack surfaces. In the far field, the stress distribution may be affected by the applied boundary conditions. However, in an annulus which surrounds the process zone and which is much smaller than the crack length, the singular stress field prevails and the elastic solutions in terms of *K* are recognized to represent the tip stress status accurately. Based on the "Small Scale Yielding Theory", the plastic behavior occurs within the process zone, but it can be thought of as being "controlled" by the singular stress field in this "*K*-annulus".

As mentioned above, in the interface crack problem, the dominant root λ arises as a pair of complex conjugates, of which the real part is 0.5 and the imaginary part depends on the difference in interficial material properties. This mismatch can be described using two non-dimensional parameters

$$\alpha = \frac{\kappa(\eta_1 + 1) - (\eta_2 + 1)}{\kappa(\eta_1 + 1) + (\eta_2 + 1)}$$
$$\beta = \frac{\kappa(\eta_1 - 1) - (\eta_2 - 1)}{\kappa(\eta_1 + 1) + (\eta_2 + 1)} \tag{1.2}$$

which are known as Dundur's elastic mismatch parameters. κ is the ratio of two shear modulus

$$\kappa = \frac{\mu_2}{\mu_1} = \frac{E_2}{E_1} * \frac{(1 + \nu_1)}{(1 + \nu_2)} \tag{1.3}$$

and η_i is defined as

$$\eta_i = \begin{cases} 3 - 4\nu_i & for\ Plane\ Strain \\ \dfrac{3-\nu_i}{1+\nu_i} & for\ Plane\ Stress \end{cases} \tag{1.4}$$

where ν_i is Poisson ratio for two different materials i=1,2.

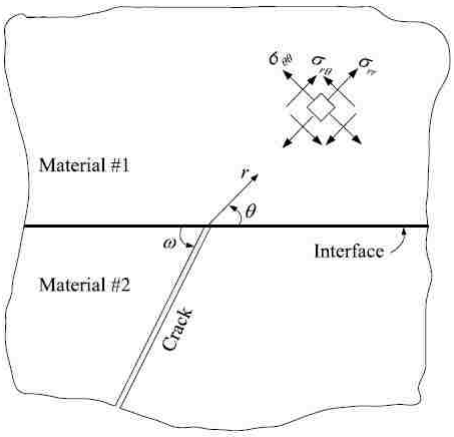

Figure 10: An Inclined Crack Terminating at the Interface [35]

Zhang and Suo [35] indicate that, as the impinging angle of the bi-material crack varies, λ switches between two unequal real numbers and a pair of complex conjugates, which are defined as the "split singularities". In the first case, two exponents, say, stronger and weaker, of the singular field coexist. The general asymptotic form of the in-plane singular stress fields is

$$\sigma_{ij}(r,\theta) = K_I(2\pi r)^{\lambda_1 - 1}\Sigma_{ij}^{I}(\theta) + K_{II}(2\pi r)^{\lambda_2 - 1}\Sigma_{ij}^{II}(\theta) \tag{1.5}$$

where K_I and K_{II} are Mode I and Mode II stress intensity factors and λ_1 , λ_2 are two dominant roots of the characteristic equation between (0,1). They are designated as the strength of singularity in the asymptotic field. The angular dependencies $\Sigma_{ij}^{I}(\theta)$ and $\Sigma_{ij}^{II}(\theta)$ can be determined from the derivation for the given material pair and the crack's incidence angle. A normalization is always adopted on the line ahead of the crack that

$$\Sigma_{\theta\theta}^{I}(\omega) = 1, \qquad \Sigma_{r\theta}^{II}(\omega) = 1 \tag{1.6}$$

where ω is the angle of the extension crack line [Figure 10]. Please note that $\Sigma_{\theta\theta}^{II}(\omega)$ and $\Sigma_{r\theta}^{I}(\omega)$ are not equal to zeros as the different singularities appear. For the complex singularities, the stress field has another form

$$\sigma_{ij}(r,\theta) = Re\left[K(2\pi r)^{\lambda_1-1}\right]\Sigma_{ij}^{1}(\theta,\rho) + Im\left[K(2\pi r)^{\lambda_1-1}\right]\Sigma_{ij}^{2}(\theta,\rho) \tag{1.7}$$

The interface crack is considered as a particular situation of this case. Different than the conventional definition, the complex stress intensity factor $K = k_1 + ik_2$, which characterizes the oscillatory behavior, is defined through

$$\sigma_{\theta\theta}(r,\omega) + i\tau_{r\theta}(r,\omega) = (k_1 + ik_2)(2\pi r)^{\lambda_1-1} \tag{1.8}$$

or

$$\sigma_{\theta\theta}(r,\omega) = Re\left[K(2\pi r)^{\lambda_1-1}\right] \ and \ \tau_{r\theta}(r,\omega) = Im\left[K(2\pi r)^{\lambda_1-1}\right] \tag{1.9}$$

In this study, the concept of the split singularity is extended to the complex field such that the angular functions $\Sigma_{\theta\theta}^{1}(\theta,\rho)$ and $\Sigma_{r\theta}^{2}(\theta,\rho)$ evaluated ahead of the crack-tip will not vanish for arbitrary incidence angles, but only for the special cases, i.e., the coplanar interfacial crack, or the crack normal to the interface. The details will be discussed later.

On the other hand, the asymptotic solution of the anti-plane mode problem is much simpler than the in-plane mode because the dominant root λ is always a single real number. The Mode III singularity can be defined as

[$$K_{III} = \lim_{r\to 0}\left[(2\pi r)^{1-\lambda}\tau_{\theta z}(r,\omega)\right] \tag{1.10}$$

Accordingly, the anti-plane singular stress fields are of the form

$$\begin{aligned} \tau_{\theta z}(r,\theta) &= (2\pi r)^{\lambda-1}K_{III}\Sigma_{\theta z}^{III}(\theta) \\ \tau_{rz}(r,\theta) &= (2\pi r)^{\lambda-1}K_{III}\Sigma_{rz}^{III}(\theta) \end{aligned} \tag{1.11}$$

The stress component $\tau_{zz}(r,\theta)$ is zero under the plane stress condition, and depends on K_I and K_{II} under plane strain conditions.

The concept of split singularities is the fundamental for generating the asymptotic solution of the crack-tip singular field. In this study, an unprecedented work is to extend this concept to the complex singularities.

1.6 Research Outline

In this study, a semi-infinite crack in the bonded dissimilar material plane will be derived using the Williams' series expansion technique. The crack terminates at the bi-material interface with an arbitrary orientation. The geometric model for such kind of problems is divided into three zones because of the asymmetric material distribution and displacement fields. As an improvement over previous solutions, the general characteristic equations for both in-plane problem and anti-plane problem are given explicitly in terms of the material property combination and the inclined angle θ between the crack and the bi-material interface. To test the validity of solutions, several specific cases, an interfacial crack, a crack perpendicular to the interface and a crack in a homogeneous medium, are investigated by setting up appropriate values for material and angle variables.

The general characteristic equations are solved by a self-adaptive numerical method revised on the basis of Newton-Raphson iteration. It can be concluded from this study that when the crack incidence angle has an arbitrary orientation, the strength of the stress singularity around the crack tip is dominated by a form of $r^{1-\lambda}$. λ is the closest root to the original point of the general characteristic equation, either complex, or real, and satisfies $0 < Real(\lambda) < 1$. The value of λ is associated with the material combination and the angle between crack and interface. The distribution of the dominant roots versus varying crack orientations for some specific combinations of materials are displayed graphically and discussed in detail in this study. In contrast to previous results available in the literature, the imaginary parts of complex eigenvalues will also be considered. Both real and imaginary parts provide a complete picture for studying the transition phenomenon between either a pair of conjugate complex roots, or two real roots within the dominant range of exponents between [0, 1]. This is the theoretical foundation for deriving the asymptotic displacement and strain field expressions, which are used in the succeeding finite element analysis.For in-plane loading modes, the overall asymptotic solution of the crack-tip field is developed through a simplified linear system. A matrix with a size of four-by-four is given to create the characteristic equation and generate the relationship between the stress field and the stress intensity factor. With another matrix with the same dimension, so-called linkage matrix, all the material zones are connected and represented in terms of stress intensity factors. The

concept of split singularities is used in the derivation due to the mixed-mode nature. Also, this concept is firstly employed for the complex singularities. It has been found that there is a slight difference in the general complex case rather than the interface crack, in which the opening mode and shear mode are orthogonally coupled. For a general situation with complex singularities, the normal stress and shear stress field are coupled with a complex factor. This new item works to redistribute the contribution from the complex stress intensity factor to the asymptotic field.

Furthermore, the enriched finite element method is extended to investigate 2D and 3D bi-material fracture problems, which involves cracks terminating at the bonded interfaces at an arbitrary incidence angle. The new formulation is programmed into an existing code, FRAC2D/FRAC3D, with the enriched element. Mixed-mode fracture problems are studied by calculating the stress intensity factors. The numerical solutions are given in some examples. With the computed fracture parameters and the formulated matrix system the asymptotic stress and displacement fields surrounding the crack-tip are shown in graphics. The energy-based and stress-based criteria are discussed and compared. The modified maximum hoop stress criterion is selected for predicting the crack propagation direction. An interesting model regarding a 3D crack with varing singularities is shown to explain some advantages of the new derived method. But more consideration will definitely be needed for this complicated case.

Finally, a brief introduction is given about the implement of a user-defined 3D element with enriched features in a commercial FEA code. This project was collaborated with Semiconductor Research Corporation, some other industrial companies. A more convenient way of using enriched finite element is provided to more users for carrying out fracture analyses.

2 General Characteristic Equation

2.1 Mathematical Model

As mentioned above, under the idealized conditions, the 3-D crack problems can be degenerated to the superposition of the in-plane mode and the anti-plane mode. A planar geometry (Figure 11) is widely used to model the bi-material problem in which a single semi-infinite crack impinging on the interface. Either in-plane or anti-plane remote loads can be applied on this universal geometry to simulate different modes of cracks. Two dissimilar elastic isotropic homogeneous materials are assumed to be perfectly bonded along the interface which is either a straight plain or has a radius of curvature sufficiently large so that the configuration can be approximated by that of two bonded half planes. The semi-infinite crack terminates at the interface with an angle of incidence ϕ, which could be restricted to an interval of $[0, \pi]$ for simplicity. The entire model is divided into three zones by the crack surfaces and the interface. The zones touching the crack surfaces are occupied by the first material and denoted by I and III, while the zone on the right side of the interface has different material properties and denoted by II. Numerical subscripts will be used to refer to field variables in these three zones. *r* is the radial distance from the crack tip and θ is the polar angle measured in a counterclockwise manner from the crack's extension line. As the angle ϕ is equal to π, the geometry will be reduced to represent a interface crack.

As discussed in the previous chapter, although this is a model containing a semi-infinite crack, it can be extended to any infinite or finite crack with straight or planer surfaces. If some controllable characteristic length, e.g., the global size of the sub-model or the local size of the crack-tip element, is set up as a reasonable scale, this configuration should be able to stand for the *K*-dominant zone appropriately. Then the numerical solution of the stress intensity factor would be meaningful for predicting the plastic behavior in the process zone. Considering the radius of the *K*-annulus is much smaller than the macroscopic scale, the remote boundary effect can be ignored and this model should be able to represent well the near-tip field very well.

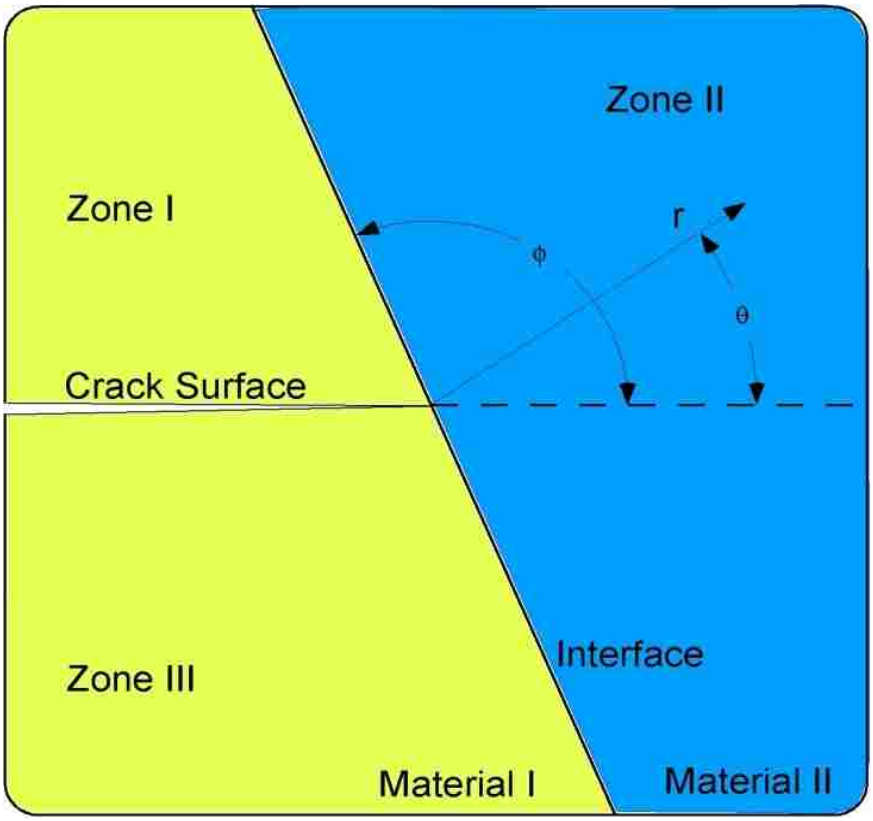

Figure 11: Geometry of A Semi-infinite Crack Terminating at the Interface

The in-plane boundary conditions are summarized as follows including the traction-free crack surfaces and the continuities of stresses and displacements across the interface.

$$\sigma_{1\theta\theta}(r,\pi) = \tau_{1r\theta}(r,\pi) = \sigma_{3\theta\theta}(r,-\pi) = \tau_{3r\theta}(r,-\pi) = 0 \tag{2.1}$$

$$\begin{aligned}
\sigma_{1\theta\theta}(r,\phi) &= \sigma_{2\theta\theta}(r,\phi) \\
\tau_{1r\theta}(r,\phi) &= \tau_{2r\theta}(r,\phi) \\
u_{1r}(r,\phi) &= u_{2r}(r,\phi) \\
u_{1\theta}(r,\phi) &= u_{2\theta}(r,\phi) \\
\sigma_{3\theta\theta}(r,\phi-\pi) &= \sigma_{2\theta\theta}(r,\phi-\pi) \\
\tau_{3r\theta}(r,\phi-\pi) &= \tau_{2r\theta}(r,\phi-\pi) \\
u_{3r}(r,\phi-\pi) &= u_{2r}(r,\phi-\pi) \\
u_{3\theta}(r,\phi-\pi) &= u_{2\theta}(r,\phi-\pi)
\end{aligned} \tag{2.2}$$

The anti-plane mode represents a state of deformation where there are only z-direction (out of plane) displacement components. The associated boundary conditions are obtained from the traction-free crack surfaces at $\theta = \pm\pi$, and the hypothesis of a perfect bonded interface.

$$\tau_{1\theta z}(r,\pi) = \tau_{3\theta z}(r,-\pi) = 0 \tag{2.3}$$

$$\begin{aligned} \tau_{1\theta z}(r,\phi) &= \tau_{2\theta z}(r,\phi) \\ u_{1z}(r,\phi) &= u_{2z}(r,\phi) \\ \tau_{2\theta z}(r,\phi-\pi) &= \tau_{3\theta z}(r,\phi-\pi) \\ u_{2z}(r,\phi-\pi) &= u_{3z}(r,\phi-\pi) \end{aligned} \tag{2.4}$$

2.2 In-Plane Mode

2.2.1 Fundamental Elastic Solutions

The geometry given above can be studied using the classic plane theory of elasticity for static body. It's already known to all that, if the body forces are absent, the equilibrium equations are expressed as

$$\begin{aligned} \frac{\partial \sigma_{xx}}{\partial x} + \frac{\partial \sigma_{xy}}{\partial y} &= 0 \\ \frac{\partial \sigma_{xy}}{\partial x} + \frac{\partial \sigma_{yy}}{\partial y} &= 0 \end{aligned} \tag{2.5}$$

where σ_{ij} are in-plane stress components. The strain components ε_{ij} can be defined by partial derivatives of displacements as

$$\varepsilon_{xx} = \frac{\partial u_x}{\partial x}, \qquad \varepsilon_{yy} = \frac{\partial u_y}{\partial y}, \qquad \varepsilon_{xy} = \frac{1}{2}\left(\frac{\partial u_x}{\partial y} + \frac{\partial u_y}{\partial y}\right) \tag{2.6}$$

where u_j are displacements in Cartesian coordinates. The relationship between stresses and strains in an isotropic solid are represented using the constants of Lame that

$$\begin{aligned} \sigma_{xx} &= \lambda\left(\varepsilon_{xx} + \varepsilon_{yy}\right) + 2\mu\varepsilon_{xx} \\ \sigma_{yy} &= \lambda\left(\varepsilon_{xx} + \varepsilon_{yy}\right) + 2\mu\varepsilon_{yy} \end{aligned} \tag{2.7}$$

$$\sigma_{xy} = 2\mu\varepsilon_{xy}$$

These equations can be also inverted as

$$\varepsilon_{xx} = \frac{1}{2\mu}\left\{\sigma_{xx} - \frac{\lambda}{2(\lambda+\mu)}\left(\sigma_{xx}+\sigma_{yy}\right)\right\}$$

$$\varepsilon_{yy} = \frac{1}{2\mu}\left\{\sigma_{yy} - \frac{\lambda}{2(\lambda+\mu)}\left(\sigma_{xx}+\sigma_{yy}\right)\right\} \tag{2.8}$$

$$\varepsilon_{xy} = \frac{1}{2\mu}\sigma_{xy}$$

where

$$\lambda = \begin{cases} \left(\frac{2\nu}{1-2\nu}\right)\mu & for\ plane\ strain \\ \left(\frac{2\nu}{1-\nu}\right)\mu & for\ plane\ stress \end{cases} \tag{2.9}$$

To ensure that the body remaining continuous under any loading conditions, the compatibility equation of strains is given to provide such restrictions

$$\frac{\partial^2\varepsilon_{xx}}{\partial y^2} + \frac{\partial^2\varepsilon_{yy}}{\partial x^2} = 2\frac{\partial^2\varepsilon_{xy}}{\partial x\partial y} \tag{2.10}$$

Combing equations (2.8) and (2.10) to have another form of the compatibility equation that

$$\nabla^2\left(\sigma_{xx}+\sigma_{yy}\right) = 0 \tag{2.11}$$

in which $\nabla^2 = \frac{\partial^2}{\partial x^2} + \frac{\partial^2}{\partial y^2}$ is the Laplace operator.

It's well known that, if a bi-harmonic stress function χ be given, the in-plane stresses can be expressed in the following manner

$$\sigma_{xx} = \frac{\partial^2\chi}{\partial y^2}, \qquad \sigma_{yy} = \frac{\partial^2\chi}{\partial x^2}, \qquad \sigma_{xy} = -\frac{\partial^2\chi}{\partial x\partial y} \tag{2.12}$$

Accordingly, the potential function χ, called Airy stress function, can be substituted into equation (2.11) to give a bihamonic equation that

$$\nabla^4\chi = 0 \tag{2.13}$$

where $\nabla^4 = \frac{\partial^4}{\partial x^4} + 2\frac{\partial^4}{\partial x^2 \partial y^2} + \frac{\partial^4}{\partial y^4}$ is the biharmonic operator.

To get the general solution, the complex representation of Muskhelishivili [13] is widely used for the plane problems of elasticity. The displacement and stress fields have a form that

$$\begin{aligned} 2\mu(u_x + iu_y) &= \eta\phi(z) - z\overline{\phi'(z)} - \overline{\psi(z)} \\ \sigma_x + \sigma_y &= 4Re\{\phi'(z)\} \\ \sigma_y - \sigma_x + 2i\varepsilon\tau_{xy} &= 2\{\bar{z}\phi''(z) + \psi'(z)\} \end{aligned} \tag{2.14}$$

where $z = x + iy$ is a complex number, μ the shear modulus, $\eta = 3 - 4\nu$ for plane strain and $\eta = \frac{3-\nu}{1+\nu}$ for plane stress. $\phi(z)$ and $\psi(z)$ are both analytic complex potentials and associated with χ as

$$\chi = Re\left[\bar{z}\phi(z) + \int^z \psi(z)\right] \tag{2.15}$$

2.2.2 Williams Expansion Approach

With appropriate boundary conditions, those equations for elastic field can be used to deduce the singular fields for the crack problem. Mathematical techniques, direct or indirect, are applied to solve these integral equations. One empirical approach was first introduced by Williams [50]. Using the semi-inverse method, Williams assumed an Airy stress function in polar coordinates of the form

$$\chi(r, \theta) = r^{\lambda+1} f(\theta) \tag{2.16}$$

where λ is the dominant root. Substituting the assumed Airy stress function into the bi-harmonic equation in polar form that

$$\left(\frac{\partial^2}{\partial r^2} + \frac{\partial}{r\partial r} + \frac{1}{r^2}\frac{\partial^2}{\partial \theta^2}\right) \cdot \left(\frac{\partial^2}{\partial r^2} + \frac{\partial}{r\partial r} + \frac{1}{r^2}\frac{\partial^2}{\partial \theta^2}\right) \chi = 0 \tag{2.17}$$

and requiring that $f(\theta)$ be defined for arbitrary values of the coordinate, *r*, results in an ordinary differential equation for $f(\theta)$ that can be written in compact form as

$$\left[\frac{d^2}{d\theta^2}+(\lambda-1)^2\right]\cdot\left[\frac{d^2}{d\theta^2}+(\lambda+1)^2\right]f(\theta)=0 \tag{2.18}$$

From this equation it follows that

$$f(\theta)=C_1\sin(\lambda+1)\theta+C_2\cos(\lambda+1)\theta+C_3\sin(\lambda-1)\theta+C_4\cos(\lambda-1)\theta \tag{2.19}$$

where the constants C_1, C_2, C_3, C_4 are to be determined from boundary conditions and loading. According, the expressions of stress and displacement fields in polar coordinates can be formed as

$$\sigma_{rr}=\frac{1}{r^2}\frac{\partial^2\chi}{\partial\theta^2}+\frac{1}{r}\frac{\partial\chi}{\partial r}=r^{\lambda-1}[f''(\theta)+(\lambda+1)f(\theta)] \tag{2.20}$$

$$\sigma_{\theta\theta}=\frac{\partial^2\chi}{\partial r^2}=r^{\lambda-1}[\lambda(\lambda+1)f(\theta)] \tag{2.21}$$

$$\tau_{r\theta}=-\frac{\partial}{\partial r}\left(\frac{1}{r}\frac{\partial\chi}{\partial\theta}\right)=r^{\lambda-1}[-\lambda f'(\theta)] \tag{2.22}$$

$$u_r=\frac{r^\lambda}{2\mu}\left[-(\lambda+1)f(\theta)+\left(\frac{1+\eta}{4}\right)g'(\theta)\right] \tag{2.23}$$

$$u_\theta=\frac{r^\lambda}{2\mu}\left[-f'(\theta)+\left(\frac{1+\eta}{4}\right)(\lambda-1)g(\theta)\right] \tag{2.24}$$

Where

$$g(\theta)=-\frac{4C_3}{\lambda-1}\sin(\lambda-1)\theta+\frac{4C_4}{\lambda-1}\cos(\lambda-1)\theta \tag{2.25}$$

For a two dimensional homogeneous problem [51], the boundary conditions will produce a linear algebraic system of four simultaneous equations for four unknown constants C_1, C_2, C_3, C_4. The nontrivial solution for these constants exists if the determinant of the four equations vanishes. After some algebraic simplifications, a characteristic equation, in terms of λ and the specific wedge angle α, can be obtained and used to solve for the eigenvalues. A limiting case of single-ended crack problem with $\alpha=\pi$, in which the wedge is fully closed upon itself, leads to a characteristic equation as

$$\sin 2\pi\lambda=0 \tag{2.26}$$

and the roots of which are

$$\lambda = \frac{n}{2} \; for\ all\ integer\ values\ of\ n\ (0, \pm 1, \pm 2, \dots)$$

Generally, roots for any $n \leq 0$ have to be rejected because they predict physically unbounded and unacceptable displacements. Then the Airy stress function yields

$$\chi(r,\theta) = \sum_{n=1,2,3,\dots} r^{\frac{n}{2}+1}\left[C_{1n}\sin\left(\frac{n}{2}+1\right)\theta + C_{2n}\cos\left(\frac{n}{2}+1\right)\theta + C_{3n}\sin\left(\frac{n}{2}-1\right)\theta + C_{4n}\cos\left(\frac{n}{2}-1\right)\theta\right] \tag{2.27}$$

A similar process was applied for the interfacial crack problem [8]. By contrast, this formulation results in a group of eight equations and eight unknown constants, $C_{11}, C_{12}, C_{13}, C_{14}, C_{21}, C_{22}, C_{23}, C_{24}$. These unknowns are derived from boundary conditions on the stress-free crack surfaces and the bonded interface between two separate isotropic homogeneous regions. The characteristic equation can be written in the form

$$\cot^2 \lambda\pi + \left[\frac{2\kappa(1-\sigma_2) - 2(1-\sigma_1) - (\kappa-1)}{2\kappa(1-\sigma_2) + 2(1-\sigma_1)}\right]^2 = 0 \tag{2.28}$$

where the subscripts indicate different regions, and κ is the shear modulus. If the material properties are not identical, it's not difficult to find that real solutions do not exist, as this equation is the sum of two positive terms equated to zero. Accordingly, the complex eigenvalues are admitted and depending on the combination of elastic materials from both sides. It should be noted that the complex roots arise as conjugates in pairs. From the physical perspective, the corresponding oscillating behavior takes place within the bi-material interfacial crack tip field.

From Equation (2.20-2.22), it is shown that the stress singularity around the crack tip is of the form $r^{\lambda-1}$. As previously discussed, the number of roots for the characteristic equation is infinite but those located in the range $0 < Real(\lambda) < 1$ will dominate the stress in the near-tip field. If all the roots are denoted as λ_j where $j = 1,2,..,n$, the solution of Airy stress function can be expressed as a sum of series

$$\chi(r,\theta) = \sum_{j=1,2,\dots,n} r^{\lambda_j+1}\big[C_{j1}\sin(\lambda_j+1)\theta + C_{j2}\cos(\lambda_j+1)\theta + C_{j3}\sin(\lambda_j-1)\theta + C_{j4}\cos(\lambda_j-1)\theta\big] \tag{2.29}$$

For a homogeneous crack, as an asymptotic solution, the terms associated with the dominant roots would be a sufficient approximation for $\chi(r,\theta)$, as well as for deriving the convergent solution of displacement and stress fields. Therefore, the summation notation is always removed and the expression above can be simplified as

$$\chi(r,\theta) = r^{\lambda_j+1}\big[C_{j1}\sin(\lambda_j+1)\theta + C_{j2}\cos(\lambda_j+1)\theta + C_{j3}\sin(\lambda_j-1)\theta + C_{j4}\cos(\lambda_j-1)\theta\big] \tag{2.30}$$

where the subscript *j* denotes the index of the dominant root. However, the recent research has uncovered that there are actually two roots in the dominant region for the characteristic equation. They exist either as two different numbers, real or complex, or as a repeated real number, such as the homogeneous case. It has also been pointed out that the second strength of singularity should be considered to improve the accuracy of stress and displacement results [22]. For the situation of complex singularities, the paired conjugates are involved into the asymptotic solution and it's equal to considering the real part and the imaginary part of the complex root as two parameters. In the real-number case, the stronger and the weaker roots play the role as the strength of singularity respectively for the opening mode and the in-plane shear mode. Then they are superposed to give the general solution for an in-plane mixed-mode crack.

2.2.3 In-plane Characteristic Equation

Substituting the field expressions (2.21-2.25) by the Williams' expansion series into the conditions defined in equations (2.1) and (2.2), a linear system is obtained including 12 linear equations with respect to 12 field unknowns $C_{n,i}$. Here the subscripts denote that this variable is correspondent with n^{th} geometric zone and i^{th} term in some equation. To make it simpler to operate, all the coefficients in equations are extracted to construct a 12×12 matrix for the in-plane mode. It can be noted that the numerical values of matrix entries depend on the strength of singularity λ, the

radial angle θ, the interface incidence angle ϕ, and the materials mismatch parameters, i.e., α, β and κ. To get non-trail solutions, the determinant of matrix needs to be equal to zero. Accordingly, the general characteristic equations are generated in terms of those parameters mentioned above. After a lot of tedious simplification work, the characteristic equation for in-plane mode is given that:

$$\begin{aligned}&\lambda^4\sin^4(\phi)\{(\beta-\alpha)^2(\beta-1)^2\}\\&\quad+\lambda^2\sin^2(\phi)\{(\beta-1)^2(\beta+1)(\beta-\alpha)[\cos(\lambda\pi)\cos(2\phi\lambda-\lambda\pi)]\\&\quad-(\beta^2+\alpha)(\beta-1)(\beta-\alpha)\}\\&\quad+\frac{1}{4}\{(\beta^2-1)\beta^2[\cos(-\lambda\pi+2\phi\lambda)-\cos(\lambda\pi)]^2\\&\quad-(\beta^2-1)[\alpha\cos(-\lambda\pi+2\phi\lambda)+\cos(\lambda\pi)]^2+(1+\alpha)^2\beta^2\}=0\end{aligned} \tag{2.31}$$

This equation agrees with preceding solutions very well. To confirm its validity and generality, specific conditions are introduced for the interface angle ϕ and material properties, then the corresponding forms are compared with the existing solutions by others [8, 20, 22]. Three particular cases, including the homogeneous problem, the crack perpendicular to interface and the interfacial crack problem, are given as follows

$$[\cos(\lambda\pi)]^2=0 \quad for\ homogeneous\ crack \tag{2.32}$$

$$\cos(\lambda\pi)=\frac{(\beta^2+\alpha)}{(\beta^2-1)}-2\lambda^2\frac{(\beta-\alpha)}{(\beta+1)}\ for\ the\ crack\ normal\ to\ interface \tag{2.33}$$

$$(1-\beta^2)[\cos(\lambda\pi)]^2+\beta^2=0 \quad for\ \ interface\ crack \tag{2.34}$$

2.3 Anti-Plane Mode

2.3.1 Anti-Plane Stress and Displacement Field

If the plane model is applied with anti-shear loading, there are no in-plane displacements produced and the only component is $u_z=w(x,y)$. The anti-plane shear strains are defined as

$$\varepsilon_{xz}=\frac{1}{2}\frac{\partial w}{\partial x},\qquad \varepsilon_{yz}=\frac{1}{2}\frac{\partial w}{\partial y} \tag{2.35}$$

The corresponding equilibrium equation is given as

$$\frac{\partial \sigma_{xz}}{\partial x} + \frac{\partial \sigma_{yz}}{\partial y} = 0 \tag{2.36}$$

Substituting the expressions of strains into equation (2.36) and using Hook's law gives the Laplace's equation for the anti-plane displacement *w* that

$$\nabla^2 w = 0 \tag{2.37}$$

The solution can be generated through the separable power series method. In polar coordinates, the trial solution has a form of summation that

$$w(r) = \sum_{n=0}^{\infty} r^{\lambda_n} f_n(\theta) \tag{2.38}$$

where $f_n(\theta) = C_{n,1} \sin(\lambda_n \theta) + C_{n,2} \cos(\lambda_n \theta)$. Under the plane strain condition, the shear stress components can be directly obtained from the elastic constitutive relationships that

$$\tau_{\theta z} = \mu \frac{1}{r} \frac{\partial w}{\partial \theta}, \qquad \tau_{rz} = \mu \frac{\partial w}{\partial r} \tag{2.39}$$

It's obvious that the stress component is proportional to $\boldsymbol{r^{\lambda_n - 1}}$. So similar to the in-plane situation, as the radial distance comes close to zero, the only meaningful term in equation (2.33) is related to the root $\boldsymbol{\lambda_n}$ situated in (0,1). It's has been verified that there is only a single real root in this range. However, Kaya [22] pointed out that if the dominant root is pretty close to the upper limit, another root in the range (1, 2) will also be not far from 1, and this second root should be factored in to improve the convergence to the exact solution.

2.3.2 Anti-plane Characteristic Equation

Again, substituting the field expressions (2.38) and (2.39) into the anti-plane conditions defined in equations (2.3) and (2.4), the corresponding linear system can be represented in a matrix form whose dimension is 6×6. The determinant of matrix is made to be zero, then the characteristic equation for the anti-plane mode is formed as:

$$\sin(\lambda\pi)\{(\kappa+1)\cos(\lambda\pi) + (\kappa-1)\cos[\lambda(\pi - 2\phi)]\} = 0 \tag{2.40}$$

which can be reduced to specific cases that

$$\sin(2\lambda\pi) = 0 \quad for\ homogeneous\ crack \tag{2.41}$$

$$\cos(\lambda\pi) = \frac{1-\kappa}{1+\kappa}\ for\ the\ crack\ normal\ to\ interface \tag{2.42}$$

$$\sin(2\lambda\pi) = 0 \quad for\ interface\ crack \tag{2.43}$$

These results have no difference compared with the referenced solutions given in [ ]. It can be observed that the characteristic equation for the homogenous crack has nothing different than the one for the interface crack. They all have 0.5 as the strength of singularity in the asymptotic field.

2.4 Dominant Roots

The left sides of equations (2.31) and (2.40) are all non-linear polynomials with respect to the dominant root. They involve not only λ of up to fourth order, but also trigonometric functions. Unfortunately, except the particular cases, i.e., the homogeneous crack or the interface crack, it's difficult to express the roots of these equations in a closed form. So the Newton-Raphson iteration technique is used to compute λ numerically. There would be more than one root for these characteristic equations, but not all of them can be accepted if considering the physical meaning. In addition, as explained previously, only the results in the range (0, 1) are of interest since the corresponding solutions derived from those roots are asymptotically dominating the stress field of near-tip area. Finally all the meaningful solutions can be superposed to give a better estimate.

2.4.1 Newton-Raphson Method

Newton's iterative method, also known as the Newton–Raphson method, is one of most widely used approaches for finding successively better approximations to the zeroes of a real-valued function. Actually it also can be applied to complex function directly. The essential idea of this method is as follows: one starts with an initial guess which is reasonably close to the true root, then the function is approximated by its tangent line, which can be computed using the algorithms of calculus, and one computes the x-intercept of this tangent line, which is easily done with

elementary algebra. This x-intercept will typically be a better approximation to the function's root than the original guess, and the method can be iterated as follows:

$$x_{n+1} = x_n - \frac{f(x_n)}{f'(x_n)} \tag{2.44}$$

Newton's method can often converge remarkably and quickly, especially if the iteration begins sufficiently near the desired root. Therefore, the initial estimated value, or called first guess, can be regarded as a limitation since it will be referred to decide the convergence speed. Sometimes, an improper starting estimated value will even lead to the convergence failure for solutions and the misunderstanding for users. Thus, a good implementation of this method always is required to both detect and overcome possible unfitted initial guesses and non-convergent solutions.

As stated above, only the roots dominating the singular behavior around the crack tip are emphasized and their real parts will fall into the range between 0 and 1, which is also the extent of first guess. Given that this range is relatively small and the acceptable error could be chosen as $O(10^{-6})$, the convergence speed will not depend too much on the choice of first guess, and the main issue is whether the first guess ensures the convergence to the final solution. Based on the considerations above, an improved Newton-Raphson method, i.e., a self-adaptive Newton-Raphson method, is introduced to compute roots of the general characteristic equation. The essential concept of this revised method is very simple and direct. Within an adjusted scope from 10^{-6} to $1 - 10^{-6}$, a certain number of equally spaced points are selected as possible initial estimated values. After that, every selected point will be used as a first guess for a regular complete Newton iteration program to calculate the roots. All the valid and meaningful solutions are stored and compared to avoid the repeats. This method traverses the entire range step by step to discover all the potential starting estimated values. In this scheme, the exceptional solutions from bad first guesses are neglected, while all the true solutions from valid first guesses are remained as a single copy. This procedure is completely automatic and makes the selection of initial estimates transparent and “free-of-controlled”. Although much more number of equally spaced points could result in more accurate first guesses, practical tests have certified that only

ten points are necessary to ensure the convergence and decrease the consumption of computing process. After all, the focus is not the starting estimate but the ending solution.

Another concern of this revised Newton method is properly obtaining the complex roots. As previously mentioned, the order of strength singularity is always inverse square root of the radial distance from crack tip for an isotropic homogeneous crack, which means the dominant root is real and $\lambda = 1/2$. When the crack is touching and perpendicular to a bi-material interface, equally to say $\phi = \pi/2$, the root is still a real number of which the numerical value is determined by the contribution from two bonded planes with dissimilar properties. In another hand, research on the interfacial crack problem, in which $\phi = 0$ or $\phi = \pi$, asserted that the singular stress field has an oscillatory behavior. This can be interpreted mathematically by a complex root $\lambda = \alpha + i\beta$, where $\alpha = 1/2$ is the real part and the imaginary part β depends on the combination of elastic materials. As the crack has an arbitrary orientation and the incidence angle ϕ varies between 0 and π, the existence of either real roots or complex roots cannot be assumed apriori. So the root-hunting method has to be used in a self-adaptive manner for both types of roots.

From the perspective of algebra, a complex number $\alpha + i\beta$ could be hypothetically regarded as a linear combination of two uncoupled real parts α and β, if the imaginary symbol "i" is assumed as a kind of coefficient. This hypothesis benefits the Newton-Raphson method to be applicable to not only a real-valued function but also the complex-valued. In the root-finding approach, a particular zero point involving both real and imaginary part is introduced to replace the conventional x-intercept of a real function curve. Accordingly, the fault-tolerance criterion needs to be considered in terms of a specific complex number.

Obviously, the initial estimate should take in the imaginary part, which has no effect on the evaluation of real solution. The testing results have verified three clues that 1) the convergence of the eigenvalue only depends on the real part of the first guess and has nothing to do with the imaginary part; 2) Although a different imaginary value of the first guess might result in a different imaginary part of the root, the absolute value of which is an invariant, and 3) the absolute value of the dominant root only depends on the material combination and crack angle. Actually this

phenomenon has been explained early in this chapter. One may remember that if a complex number is obtained as a root of some real function, its conjugate would appear as another solution. Both conjugates should be taken into account when deriving the final solution. But in the formulation, it's enough to consider only one of them due to the same real part and the same magnitude of imaginary part. For consistence with the existing solution, this picked complex root has to satisfy the regulation that its imaginary part is positive if the shear ratio $\kappa = \mu_2/\mu_1$ is less than zero and vise versa.

This self-adaptive Newton-Raphson iteration method has been implemented as a part of program for the subsequent finite element analysis.

2.4.2 Distribution of Roots For In-Plane Mode

Using the optimized Newton-Raphson method, the dominant roots for varying interface inclined angle and different material combinations are calculated. After each iterative calculation for a certain material case, roots are sorted in an ascending order of the real part if there is more than one result. Then they are treated as stronger and weaker singularities in the asymptotic solution. Eleven different shear ratios are specialized to study the relationship between the material mismatch and the strength of singularity. The distribution of roots with respect to inclined interface angle is represented graphically for real parts and imaginary parts separately. As discussed in previous studies, only the real part provides a contribution to the singularity strength in the vicinity of crack tip. In this study, the imaginary part is also involved to observe the transition phenomenon between complex eigenvalues and real eigenvalues. This analysis is repeated for the following cases that 1) from a perpendicular crack to an interfacial crack; 2) from a crack located within a stiffer material to a crack in a softer material. It should be mentioned that all the cases are treated under the plane stress condition.

Firstly, for varying crack incidence angles, the distribution of solutions for the dominant eigenvalue is shown in Figure 12 and Figure 13, real parts and imaginary parts respectively. Poisson's ratios of both material areas are assumed identical as $\nu_1 = \nu_2 = 0.3$, and the shear modulus ratio is specified with three values $\kappa = \frac{\mu_2}{\mu_1} = \frac{E_2(1+\nu_1)}{E_1(1+\nu_2)} = 0.2, 1, 5.$

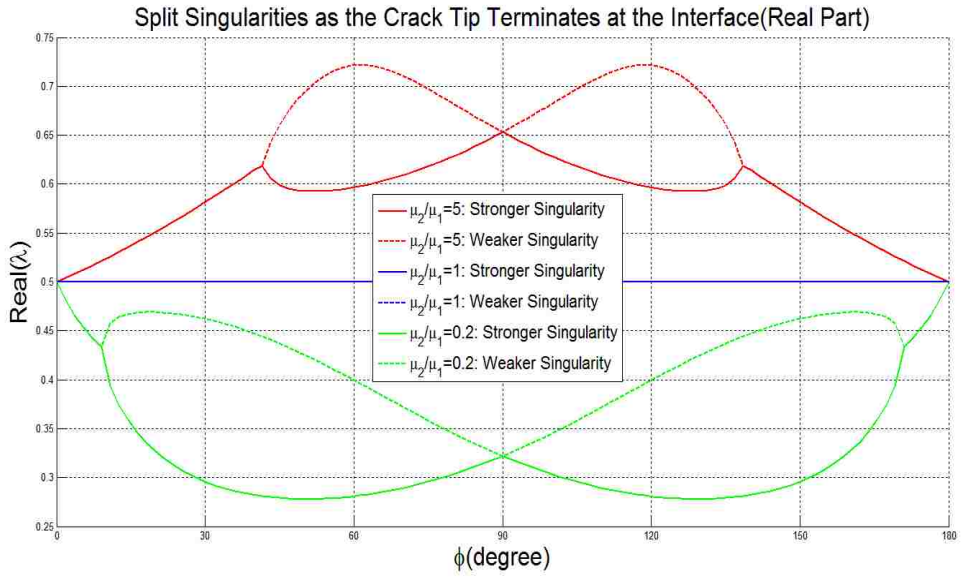

Figure 12: Distribution of Real Parts of Eigenvalues versus Crack Angle Incidence ϕ as $\kappa = \mu_2/\mu_1 = 0.2,1,5$ for In-plane Case.

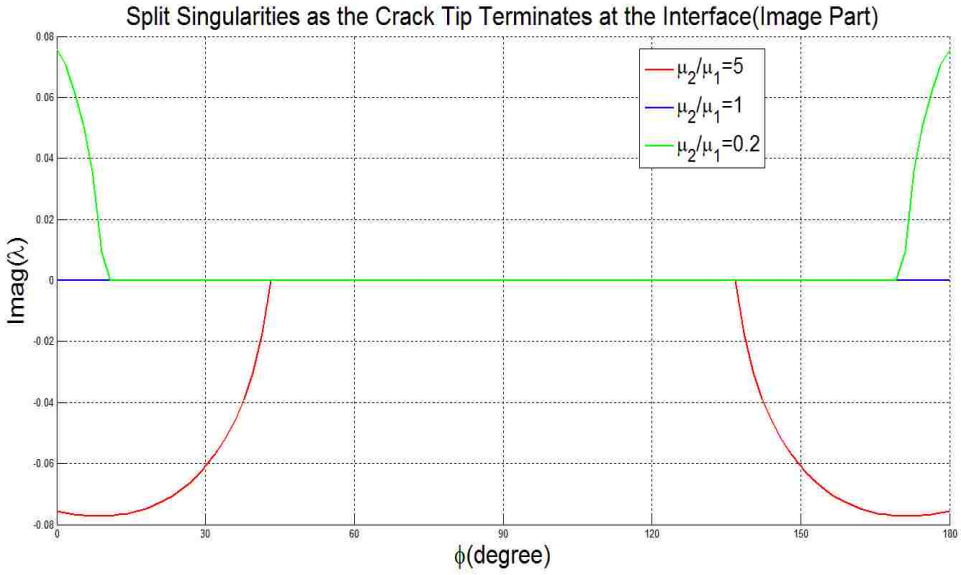

Figure 13: Distribution of Imaginary Parts of Eigenvalues versus Crack Angle Incidence ϕ as $\kappa = \mu_2/\mu_1 = 0.2,1,5$ for In-plane Case.

The curved shapes of split singularities in Figure 12 match perfectly with Fenner's results [32]. Observed together with Figure 15, some features of the root distribution can be concluded that

1) The distribution of roots is symmetric about $\phi = \pi/2$ for any material combination.

2) As $\kappa = 1$, which indicates a homogeneous problem, there is only one repeated root in this dominating region and $Real(\lambda) = 0.5$, $Imag(\lambda) = 0$. This agrees with the real solutions obtained by Williams.

3) As $\kappa \neq 1$, which means a bi-material crack problem, a second dominant root arises. It becomes closer and finally identical to the first root while the crack incidence ϕ approaches 90^o which is a right angle. On the other hand, as ϕ comes close to 0 or π, the eigenvalues change from two unequal real roots to a pair of conjugate complex numbers at a certain angle. It can be seen that the transition point in Figure 12 has the same value of ϕ where the imaginary part disappears in Figure 13 for both material combinations.

4) When $\kappa < 1$, the crack is embedded in the stiffer elastic material. The real part of root is less than an half that $Real(\lambda) < 0.5$ for all cases. The strongest singularity occurs at two certain angles, which are material-dependent and symmetric about $\phi = \frac{\pi}{2}$. As $\kappa > 1$, the material containing the crack becomes relatively softer. The real part of root is greater than a half that $Real(\lambda) > 0.5$, and the strongest singularity is located at $\phi = 0\ or\ \pi$. So the ratio of material properties determines the strength of singularity, which is stronger than 0.5 for $\kappa < 1$ and weaker for $\kappa > 1$.

5) As $\phi = 0\ or\ \pi$, the crack will overlap over the bonded line of two material zones, which becomes a typical interfacial crack. In accord with the solutions by Williams [19], the eigenvalue turns out as a pair of complex numbers, of which the real part is equal to 0.5 and the imaginary part, which introduces the oscillatory behavior, is controlled by the combination of material properties.

6) As $\phi = \pi/2$, the model is reduced to a special case of geometric symmetry with respect to the crack axis. The real eigenvalue comes to be a singular number, and coincide with the results given by Cook [20].

7) As ϕ becomes closer to $\pi/2$ from 0 or π, the diagram of real root is transformed from a single curve to two branches at a certain point. This indicates there might be two unequal dominant roots existing in some range of the crack incidence angle. Most of previous

research only considered the first root, which is the smaller value of λ within the interval of [0, 1]. However, Kaya's investigation [22] suggested that a second, or even more, root could provide contributions to the convergence and accuracy of the stress and displacement field around the crack tip. This idea will be examined further.

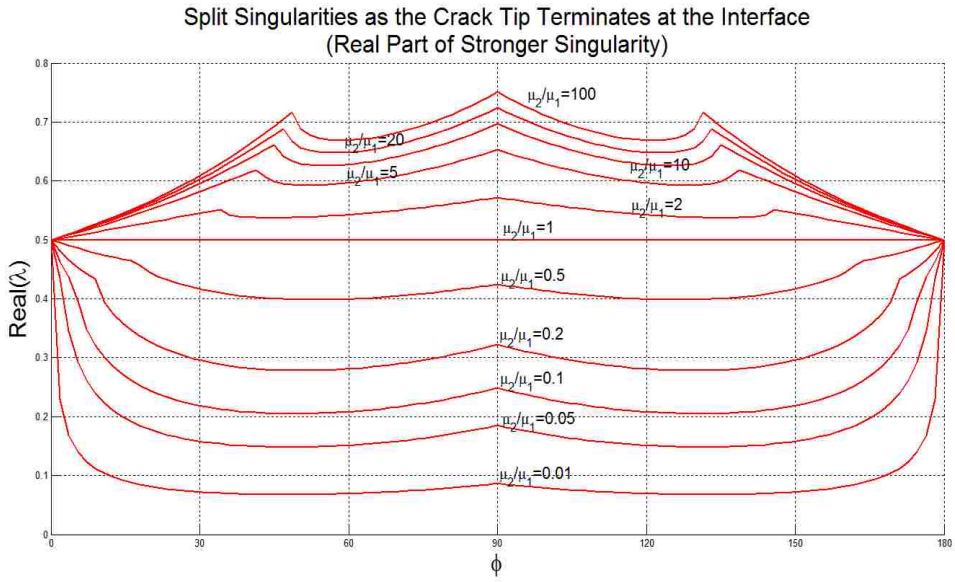

Figure 14: Distribution of first roots (real part) versus varying crack incidence angles for different material combinations under in-plane conditions.

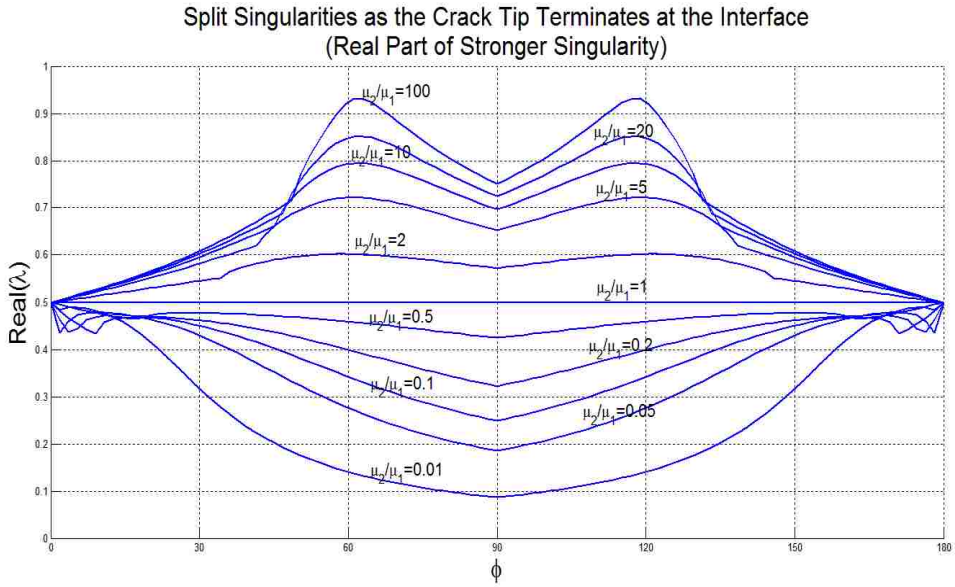

Figure 15: Distribution of second roots (real part) versus varying crack incidence angles for different material combinations under in-plane conditions.

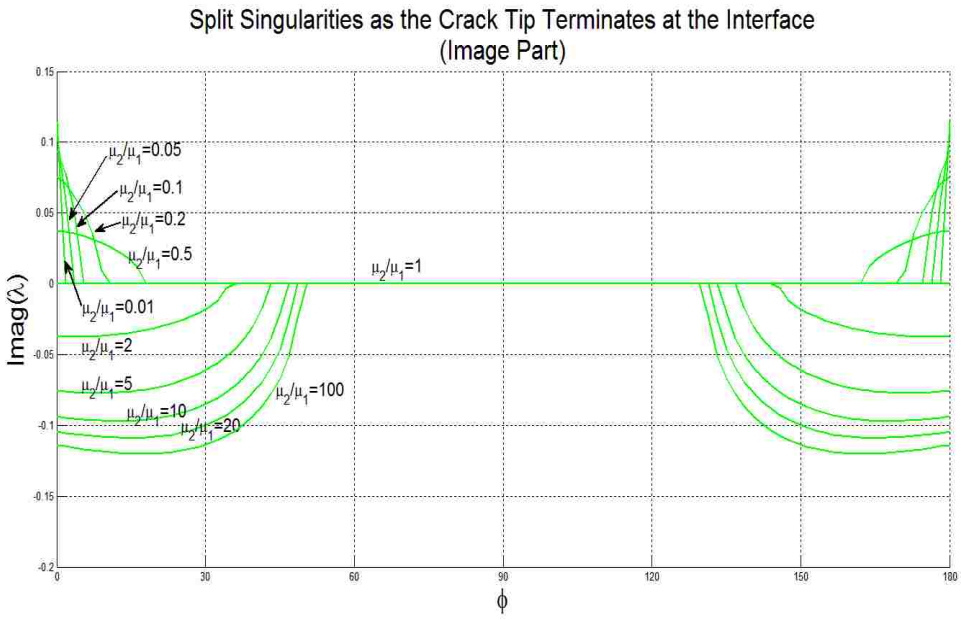

Figure 16: Distribution of roots (imaginary part) versus varying crack incidence angles for different material combinations under in-plane conditions.

Along with varying crack incidence angles from 0 to π, the first (stronger) real root, the second (weaker) real root and the corresponding imaginary part, if it's a complex number, are shown respectively in Figure 14-16. As mentioned above, eleven particular cases of bi-material plane stress problems are investigated with $\kappa = 0.01, 0.05, 0.1, 0.2, 0.5, 1, 2, 5, 10, 20, 100$. Some points worth paying attention to are listed as follows.

1) From the perspective of the real part of root, the strongest strength of singularity for each type of material combinations occurs as the interface rotates to a certain angle where λ hits the minimum (Figure 14). For the crack embedded in a stiffer elastic body, the strongest singularity is a real number. While the crack is located in the softer material, the strongest singularity results in an oscillatory behavior which happens as the crack is lying on the bonded interface (Figure 18).
2) The transition point of the incidence angle, at which a pair of conjugate complex is uncoupled and changed into two different real numbers, approaches zero as the side containing the crack becomes stiffer. Since the roots are distributed symmetrically with respect to the interface incline angle, only the range $[0^o, 90^o]$ is considered here for simplicity. On the other hand, if the crack's host material become softer to an extreme,

the transition angle comes closer to 50^o. This conclusion is also verified in Figure 17. However, if the side containing the crack is infinitely rigid, i.e., $\kappa = 0$, the model and the transition angle are physically meaningless and unacceptable.

3) It is also noted that, as the material surrounding crack becomes infinite rigid, the minimum dominant eigenvalue gets close to zero, which will result in an extremely strong singularity due to the stress field form $\sigma_{ij} \sim r^{\lambda-1}$.

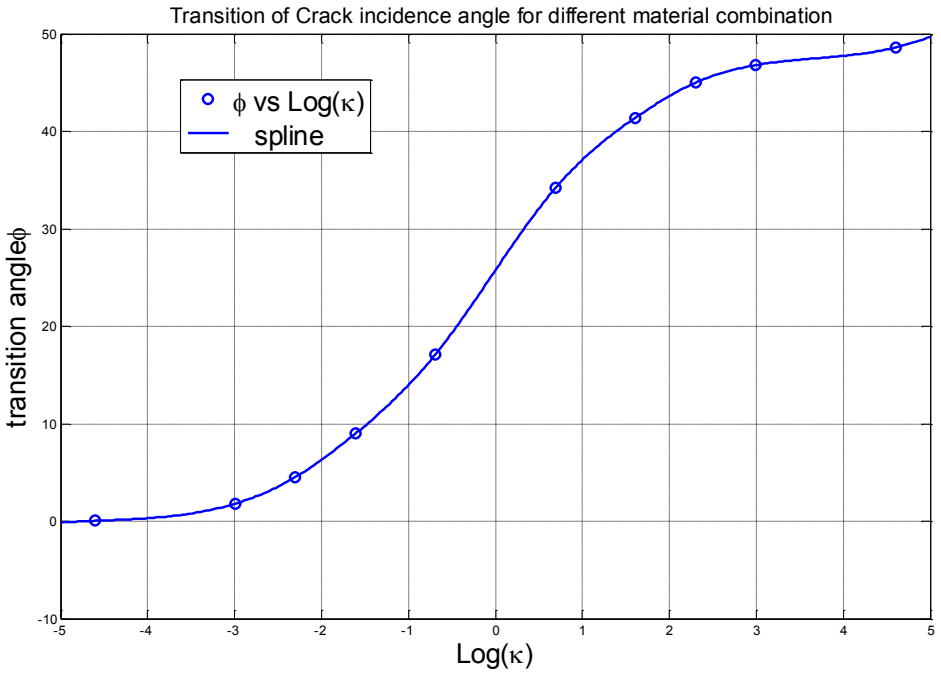

Figure 17: Distribution of transition angles (between complex roots and real roots) versus varying material combinations under in-plane conditions.

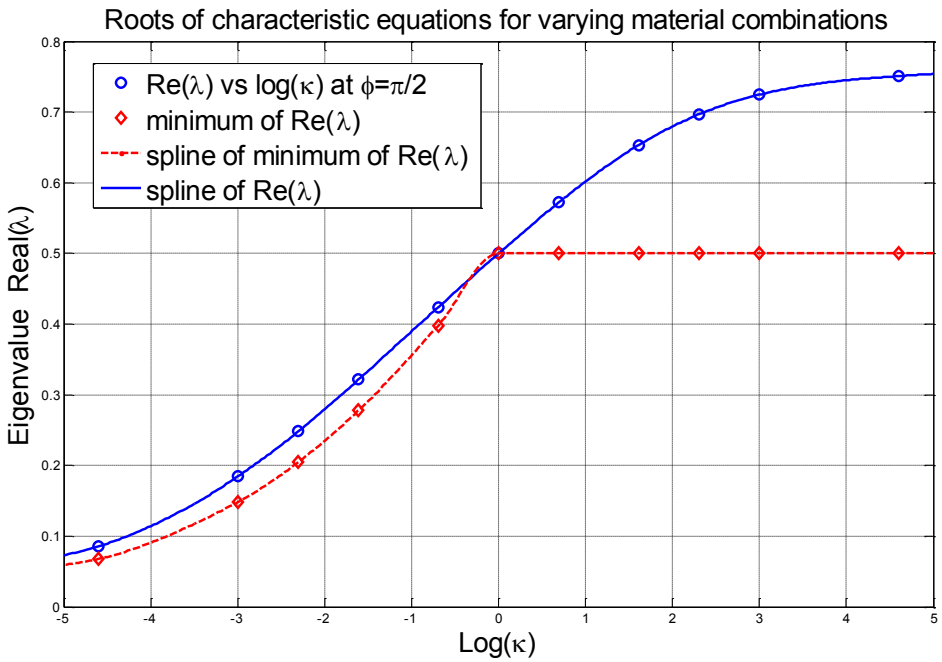

Figure 18: Distribution of real roots at right angle and minimum roots versus varying material combinations under in-plane conditions.

Once the dominant root is computed numerically, the singular field of stress and displacement in the vicinity of crack tip should be determined under the context of asymptotic analysis theory. In Williams' expansion form for the solution of the Airy stress function (Eqn. 2.30), there are four unknowns in the field expression. For the general case discussed here, the number of field constants is increased to twelve, i.e., $C_{n1}, C_{n2}, C_{n3}, C_{n4}$, where n=1,2,3 stands for three geometric zones. These unknowns can be determined by the strength of singularity and specific boundary conditions. However, the general characteristic equation is nonlinear so it is not easy to derive "closed form" expressions for the stresses, strains, and displacements. So an effective and convenient approach is needed to study the general case. In this study, it has been found out that these twelve field constants can be reduced to only two by using appropriate linear algebraic operations. If these two variables are treated as bases of a linear system, the asymptotic stress and displacement fields can be expressed in an algebraic form including some multiplied matrices.

2.4.3 Distribution of Roots For Anti-Plane Mode

The general characteristic equation (2.40) of the anti-plane problem can be also evaluated by the self-adaptive Newton-Raphson iteration technique to find the dominant roots. The distribution of roots is represented graphically for real part and imaginary part separately. The features can be summarized as below,

1) All the eigenvalues are real numbers.
2) For any kind of material combination, only one dominant root exists in the region of [0, 1].
3) There is no oscillating behavior around the crack tip if crack surfaces are not clamped.

Along with varying crack incidence angels, the distribution of solutions for the dominant eigenvalue in the anti-plane case is plotted in Figure 19. Poisson's ratios of both materials are assigned identically with $\nu_1 = \nu_2 = 0.3$, and the shear modulus ratio is specified as three values $\kappa = \frac{\mu_2}{\mu_1} = \frac{E_2(1+\nu_1)}{E_1(1+\nu_2)} = 0.2, 1, 5$. The curved shapes match perfectly with Fenner's results [32]. Some corresponding characteristics can be found that

1) As $\kappa = 1$, treated as a homogeneous case, the single root in dominating region is $\lambda = 0.5$, which is as same as the solution of in-plane problem.
2) For all $\kappa \neq 1$, there is only a single eigenvalue arising in the dominant area. As $\kappa < 1$, the crack is embedded in the stiffer elastic material. The real root is less than a half that is $\lambda < 0.5$, and the strongest singular behavior happens at $\phi = \pi/2$, the crack in normal to the interface; while as $\kappa > 1$, the material containing the crack becomes relatively softer. The root is larger than a half that $\lambda > 0.5$, and the strongest singular behavior occurs when the crack coincides with the interface.
3) As $\phi = 0 \; or \; \pi$, the problem becomes a typical interfacial crack case that the crack overlaps over the bonded line of two material zones. The simplified characteristic equation in this condition agrees with that of the homogeneous problem. So it might be thought of that the strength of singularity for a interfacial crack in anti-plane mode is independent of material combinations.

4) As ϕ rotates with any arbitrary degrees from 0 or π, only one eigenvalue exists within the interval of [0,1]. But Kaya's investigation [17] takes a second root, which is obtained in the region of [1, 2], into account, and gets more accurate results for stress intensity factors. For the consideration on the convergence and accuracy of stress and displacement fields around the crack tip, the contribution from the roots outside the dominant area [0, 1] cannot to be ignored and should be verified in fracture studies.

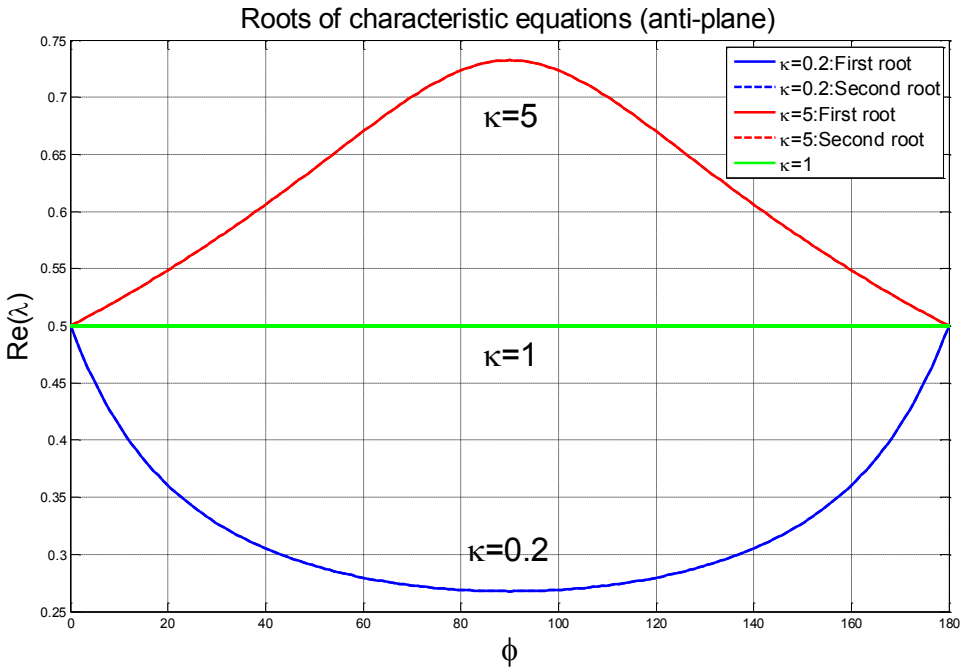

Figure 19: Distribution of eigenvalues versus crack incidence angle ϕ as $\kappa = \mu_2/\mu_1 = 0.2,1,5$ under anti-plane condition.

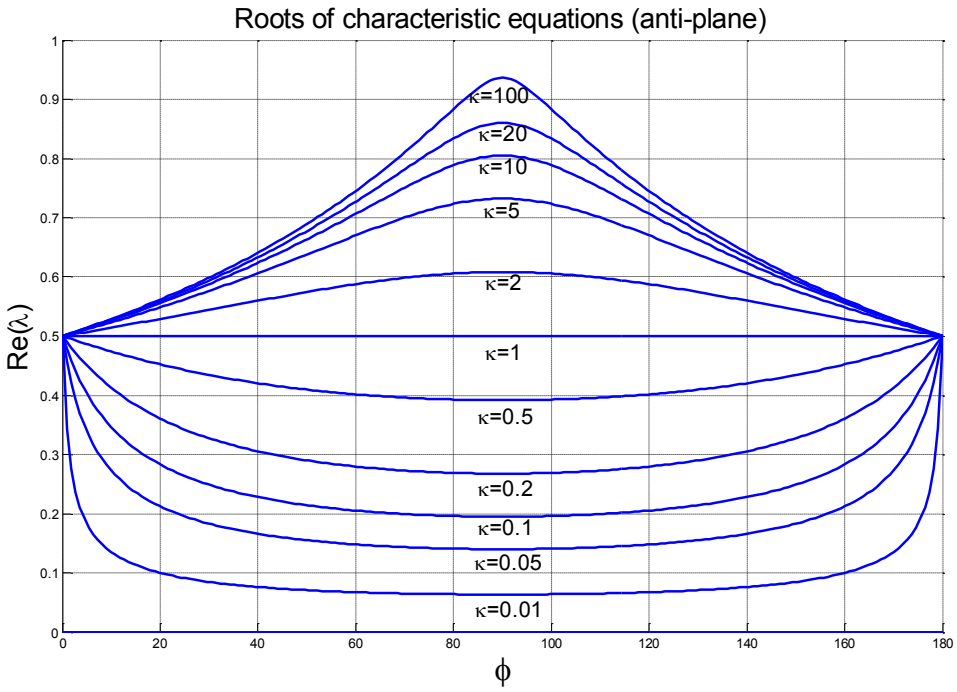

Figure 20: Distribution of roots versus varying crack incidence angles for different material combinations under anti-plane condition.

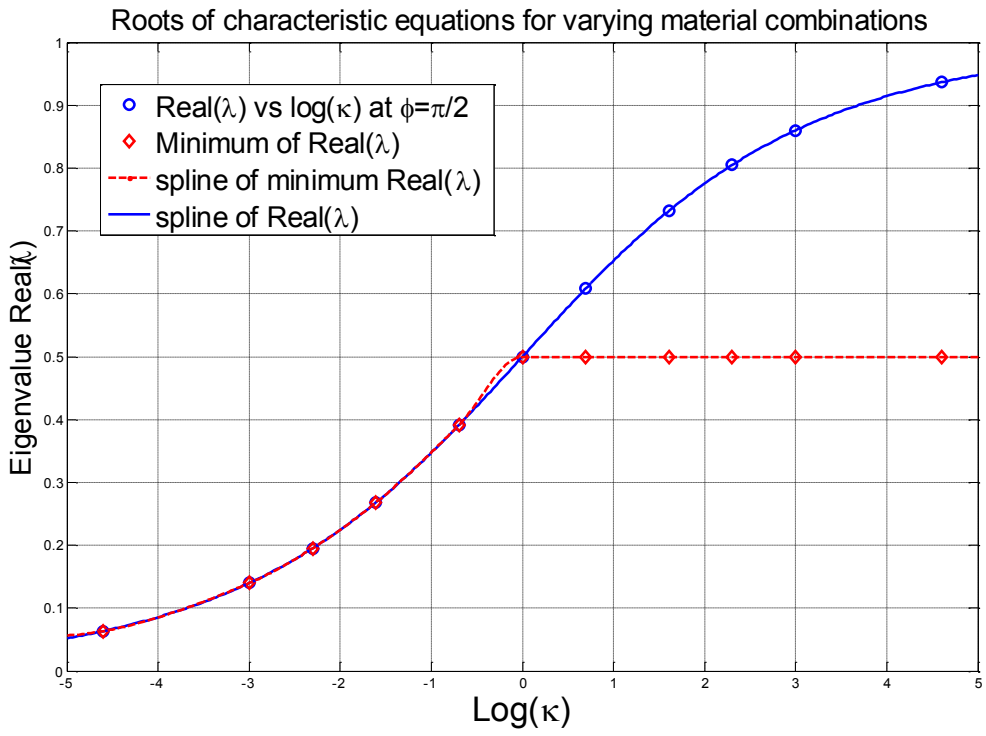

Figure 21: Distribution of roots at right angle and minimum roots versus varying material combinations under anti-plane conditions.

Figure 20 illustrates the distribution of eigenvalues with respect to varying crack incidence angles from 0 to π for eleven different cases with specific shear modulus ratio $\kappa = 0.01, 0.05, 0.1, 0.2, 0.5, 1, 2, 5, 10, 20, 100$. It's much simpler than the in-plane case but has some similar features that

1) If a crack is embedded in the stiffer elastic body, whatever the material mismatch is, the strongest singularity arises when the crack incidence angle is rotated to a right angle with respect to the bonded interface. While the crack is located in the softer side, the strongest singularity is constant as $\lambda = 0.5$ and the crack is lying on the interface. This point can be also observed in Figure 21.
2) As $k < 1$, the strength of singularity changes abruptly when the crack gets close to the interface and gently while it tends to a right angle. On the contrary, if $k > 1$, the varying rate of singularity doesn't have noticeable change from either $\phi = 0$ or $\phi = \pi$ to $\phi = \pi/2$. When the material mismatch is small, the distribution of λ with respect to ϕ is almost linear.
3) In accord with the in-plane problem, if the material surrounding the crack goes to infinitely rigid, the dominant root is closer to $\lambda = 0$, which will result in an extremely strong singularity due to the stress field form $\sigma_{ij} \sim r^{\lambda - 1}$.

The derivation of the general asymptotic solution for the singular stress and displacement fields of Mode-III will be given later. Since the dominant root always falls into the real-number field, it's not easy to find out the field expression in an explicit form. Similar with the in-plane problem, there are two field constants for each geometric zone. As a result, six unknowns constants C_{n1}, C_{n2}, where n=1,2,3 are to be determined. Fortunately, these six variables can be reduce to a single field constants through the boundary conditions using linear algebraic operations. The details will be given later.

3 The Enriched Finite Element Method

Usually, the analytical solutions for stress intensity factors can be obtained in closed form only for very simple geometries, material combinations, external loads or their superposition. The use of numerical techniques has vastly broadened the range of problems that can be solved by computational approaches.

Among various numerical approaches, the finite element method is prevalently established as an engineering tool with wide applications. The analysis of crack problems emphasizes the use of finite elements to describe mathematical singular behaviors that occur in elastic bodies. It has been well recognized that in treating crack problems to compute stress singularities, the solutions converge very slowly if the finite elements include only the conventional displacement field without singular terms. Some revised methods involve the singularities into the element's formulation, but require the post processing to get final solutions.

An improved finite element method incorporates the asymptotic analysis and the regular finite element method together. It is featured by enriched finite elements, which has been utilized to determine stress intensity factors and strain energy release rates directly without any post-processing work.

3.1 Crack-Tip Displacement Field

Next, an example is given to demonstrate the crack-tip displacement field for enriched finite element. Thinking about a 20-node hexahedron element, the displacement in local ξ direction for the crack-tip node is denoted as $u(\xi,\eta,\rho)$. It can considered as a superposition of the conventional isoparametric displacement u^d and the asymptotic field in terms of the stress intensity factors that

$$u(\xi,\eta,\rho) = u^d(\xi,\eta,\rho) + K_I f_1(\xi,\eta,\rho) + K_{II} g_1(\xi,\eta,\rho) + K_{III} h_1(\xi,\eta,\rho) \tag{3.1}$$

It's known that u^d can be represented as a polynomial up to third order

$$u^d = \sum_{m=1}^{20} a_m \xi^\alpha \eta^\beta \rho^\gamma, \qquad \alpha + \beta + \gamma \leq 3 \tag{3.2}$$

where a_m are unknown coefficients to be determined. If local nodal coordinates (ξ_j, η_j, ρ_j) for each node *j* are put into the equations above respectively, the conventional local displacement is obtained that

$$u_j^d = \sum_{m=1}^{20} a_m \xi_j^\alpha \eta_j^\beta \rho_j^\gamma = \sum_{m=1}^{20} [M^d]_{jm} a_m \tag{3.3}$$

where $M^d(\xi, \eta, \rho)$ is a 20×20 matrix containing all the polynomial terms evaluated at each node.

Following the same way, the asymptotic items in equation (3.1) can be represented in the form of matrix M^K. Then the complete nodal displacement in ξ direction are given as

$$\{u_j\}_{20\times1} = [M^d]_{20\times20}\{a_m\}_{20\times1} + [M^K]_{20\times3}\begin{Bmatrix} K_I \\ K_{II} \\ K_{III} \end{Bmatrix} \tag{3.4}$$

where

$$[M^K]_j = \{f_1(\xi_j, \eta_j, \rho_j) \quad g_1(\xi_j, \eta_j, \rho_j) \quad h_1(\xi_j, \eta_j, \rho_j)\} = \{f_{1j} \quad g_{1j} \quad h_{1j}\} \tag{3.5}$$

Using appropriate linear algebraic operations, the coefficient vector can be expressed in terms of u_j, M^d, M^K and K that

$$\{a_m\}_{20\times1} = [(M^d)^{-1}]_{20\times20}\{u_j\}_{20\times1} - [(M^d)^{-1}]_{20\times20}[M^K]_{20\times3}\begin{Bmatrix} K_I \\ K_{II} \\ K_{III} \end{Bmatrix} \tag{3.6}$$

in which

$$a_m = \sum_{j=1}^{20} [(M^d)^{-1}]_{mj}\, u_j - \sum_{j=1}^{20} [(M^d)^{-1}]_{mj}\, f_{1j} K_I - \sum_{j=1}^{20} [(M^d)^{-1}]_{mj}\, g_{1j} K_{II} - \sum_{j=1}^{20} [(M^d)^{-1}]_{mj}\, h_{1j} K_{III} \tag{3.7}$$

The notation "-1" means the inverse of matrix. The subscript of matrix indicates the row number and the column number.

Substituting $\{a_m\}_{20\times 1}$ back into equation (3.2) and (3.1) yields

$$\begin{aligned} u(\xi,\eta,\rho) = & \sum_{m=1}^{20}\sum_{j=1}^{20} \left(\xi^\alpha \eta^\beta \rho^\gamma\right)_m [(M^d)^{-1}]_{mj} u_j - \sum_{m=1}^{20}\sum_{j=1}^{20} \left(\xi^\alpha \eta^\beta \rho^\gamma\right)_m [(M^d)^{-1}]_{mj} f_{1j} K_I \\ & - \sum_{m=1}^{20}\sum_{j=1}^{20} \left(\xi^\alpha \eta^\beta \rho^\gamma\right)_m [(M^d)^{-1}]_{mj} g_{1j} K_{II} \\ & - \sum_{m=1}^{20}\sum_{j=1}^{20} \left(\xi^\alpha \eta^\beta \rho^\gamma\right)_m [(M^d)^{-1}]_{mj} h_{1j} K_{III} + K_I f_1(\xi,\eta,\rho) \\ & + K_{II} g_1(\xi,\eta,\rho) + K_{III} h_1(\xi,\eta,\rho) \end{aligned} \tag{3.8}$$

Obviously the summation over *m* can be represented in the following form

$$N_j(\xi,\eta,\rho) = \sum_{m=1}^{20} \left(\xi^\alpha \eta^\beta \rho^\gamma\right)_m \left[\left(M^d\right)^{-1}\right]_{mj} \tag{3.9}$$

which actually is the conventional interpolation function for node *j* in a 20-node hexahedron element. Accordingly, the displacement for crack-tip is represented by

$$\begin{aligned} u(\xi,\eta,\rho) = & \sum_{j=1}^{20} N_j(\xi,\eta,\rho) u_j + K_I \left(f_1(\xi,\eta,\rho) - \sum_{j=1}^{20} N_j(\xi,\eta,\rho) f_{1j} \right) \\ & + K_{II} \left(g_1(\xi,\eta,\rho) - \sum_{j=1}^{20} N_j(\xi,\eta,\rho) g_{1j} \right) \\ & + K_{III} \left(h_1(\xi,\eta,\rho) - \sum_{j=1}^{20} N_j(\xi,\eta,\rho) h_{1j} \right) \end{aligned} \tag{3.10}$$

The other displacement components can be obtained following the same process.

In this approach, virtual nodes are added at the same locations as crack tip nodes. The stress intensity factors of three modes, K_I, K_{II}, K_{III}, are treated as three extra degrees of freedom (DOFs) in the element displacement field, just like regular nodal displacements u_x, u_y, u_z, or *u, v, w* for the real nodes. The assembled global stiffness matrix is regarded as an augmented matrix involving terms contributed from the asymptotic expression of singular displacement fields in terms of stress intensity factors.

3.2 Enriched Finite Element Formulation

The enriched crack tip elements formulated by Benzley [46] for 2-D problems contain both the closed form asymptotic displacement field around the crack tip and the polynomial interpolation function. Chen [47] extended this approach to the interfacial crack problem. The enriched 3-D finite element method was developed and extended to isotropic and orthotropic, homogeneous and interfacial, two-dimensional and three dimensional crack problems by Ayan, Kaya and Nied [48, 49]. A program package consisting of FRAC2D and FRAC3D, based on the enriched finite element, has been developed especially for 2-D and 3-D fracture analyses at Lehigh University.

In the following section, the fundamental theory of 3-D enriched finite element is introduced briefly. The expressions of 2-D (in-plane) enriched element can be obtained by easily shutting off the anti-plane terms in the 3-D formulation.

In the 3-D enriched elements, displacement components *u*, *v*, and *w* take the form as follows,

$$\begin{aligned} u(\xi,\eta,\rho) = \sum_{j=1}^{r} N_j(\xi,\eta,\rho)\, u_j \\ + Z_0(\xi,\eta,\rho)\{K_I(\Gamma)F_1(\xi,\eta,\rho) + K_{II}(\Gamma)G_1(\xi,\eta,\rho) \\ + K_{III}(\Gamma)H_1(\xi,\eta,\rho)\} \end{aligned} \tag{3.11}$$

$$v(\xi,\eta,\rho) = \sum_{j=1}^{r} N_j(\xi,\eta,\rho)\, v_j + Z_0(\xi,\eta,\rho)\{K_I(\Gamma)F_2(\xi,\eta,\rho) + K_{II}(\Gamma)G_2(\xi,\eta,\rho) + K_{III}(\Gamma)H_2(\xi,\eta,\rho)\} \tag{3.12}$$

$$w(\xi,\eta,\rho) = \sum_{j=1}^{r} N_j(\xi,\eta,\rho)\, w_j + Z_0(\xi,\eta,\rho)\{K_I(\Gamma)F_3(\xi,\eta,\rho) + K_{II}(\Gamma)G_3(\xi,\eta,\rho) + K_{III}(\Gamma)H_3(\xi,\eta,\rho)\} \tag{3.13}$$

In equations (3.11-3.13), u_j, v_j, w_j represent the r unknown nodal displacements and $N_j(\xi,\eta,\rho)$ are the conventional element shape functions in terms of the element's local coordinates. $K_I(\Gamma), K_{II}(\Gamma), K_{III}(\Gamma)$ represent the mode I, II, and III stress intensity factors varying along the crack front defined by the interpolation functions $N_i(\Gamma)$.

$$K_I(\Gamma) = \sum_{i=1}^{s} N_i(\Gamma)\, K_I^i \tag{3.14}$$

$$K_{II}(\Gamma) = \sum_{i=1}^{s} N_i(\Gamma)\, K_{II}^i \tag{3.15}$$

$$K_{III}(\Gamma) = \sum_{i=1}^{s} N_i(\Gamma)\, K_{III}^i \tag{3.16}$$

where $K_I^i, K_{II}^i, K_{III}^i$ are the unknown stress intensity factors at the *i*th crack tip node in the enriched element. $N_i(\Gamma)$ is the element shape function along the element edge coinciding with the crack front. Written in terms of the crack tip nodal coordinates x_i, y_i, z_i, the crack front is defined by

$$x = \sum_{i=1}^{s} N_i(\Gamma)\, x_i, \qquad y = \sum_{i=1}^{s} N_i(\Gamma)\, y_i, \qquad z = \sum_{i=1}^{s} N_i(\Gamma)\, z_i \tag{3.17}$$

Thus, $\Gamma = \xi, \eta \; or \; \rho$, depending on which edge of the element touches the crack front. For example, for a 20-noded hexahedron element (Figure 22) that has a crack front located on the edge defined by the $\eta = -1, \rho = -1$, with $-1 \le \xi \le 1$,

$$K_I(\Gamma) = K_I(\xi) = \frac{1}{2}(-\xi + \xi^2)K_I^1 + (1 - \xi^2)K_I^2 + \frac{1}{2}(\xi + \xi^2)K_I^3 \tag{3.18}$$

In equation (3.18), K_I^1, K_I^2, K_I^3 are the mode I stress intensity factors at the nodes located at $\xi = -1, \xi = 0, \xi = 1$, respectively. The mode II and mode III stress intensity factors would be defined in a similar manner.

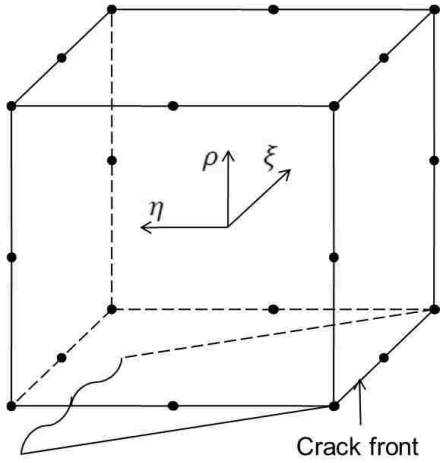

Figure 22: 20-Node Hexahedron Element Attached to Crack Front

3.2.1 Asymptotic Terms

The functions F_i, G_i, H_i in equation (3.11-3.13) are given by

$$F_i(\xi, \eta, \rho) = f_i(\xi, \eta, \rho) - \sum_{j=1}^{r} N_j(\xi, \eta, \rho) f_{ij} \tag{3.19}$$

$$G_i(\xi, \eta, \rho) = g_i(\xi, \eta, \rho) - \sum_{j=1}^{r} N_j(\xi, \eta, \rho) g_{ij} \tag{3.20}$$

$$H_i(\xi, \eta, \rho) = h_i(\xi, \eta, \rho) - \sum_{j=1}^{r} N_j(\xi, \eta, \rho) h_{ij} \tag{3.21}$$

In equations (3.19-3.21), f_i, g_i, h_i, where $i = 1, 2, 3$, contain the asymptotic displacement functions that are coefficients of the mode I, II, and III stress intensity factors transformed to the global coordinate system. The terms $f_{1j}, g_{1j}, h_{1j}, f_{2j}, g_{2j}, h_{2j}, f_{3j}, g_{3j}, h_{3j}$ in (3.19-3.21) are constants computed from the f_i, g_i, h_i functions evaluated at the *j*th node in the element.

Referring to equations (3.11-3.13), the asymptotic crack tip displacements in the local coordinate system can be defined in general forms that

$$\bar{u} = K_I \bar{f}_1 + K_{II} \bar{g}_1, \qquad \bar{v} = K_I \bar{f}_2 + K_{II} \bar{g}_2, \qquad \bar{w} = K_{III} \bar{h} \tag{3.22}$$

where $\bar{f}_1, \bar{g}_1, \bar{f}_2, \bar{g}_2, \bar{h}$ are local asymptotic terms. For a homogeneous, isotropic material problem, the expressions of these terms are

$$\bar{f}_1 = \frac{1}{2E}\sqrt{\frac{r}{2\pi}}\left((5 - 3\nu - 8\nu^2)\cos\left(\frac{\theta}{2}\right) - (1+\nu)\cos\left(\frac{3\theta}{2}\right)\right) \tag{3.23}$$

$$\bar{g}_1 = \frac{1}{2E}\sqrt{\frac{r}{2\pi}}\left((9 + \nu - 8\nu^2)\sin\left(\frac{\theta}{2}\right) + (1+\nu)\sin\left(\frac{3\theta}{2}\right)\right) \tag{3.24}$$

$$\bar{f}_2 = \frac{1}{2E}\sqrt{\frac{r}{2\pi}}\left((7 - \nu - 8\nu^2)\sin\left(\frac{\theta}{2}\right) - (1+\nu)\sin\left(\frac{3\theta}{2}\right)\right) \tag{3.25}$$

$$\bar{g}_2 = \frac{-1}{2E}\sqrt{\frac{r}{2\pi}}\left((3 - 5\nu - 8\nu^2)\cos\left(\frac{\theta}{2}\right) + (1+\nu)\cos\left(\frac{3\theta}{2}\right)\right) \tag{3.26}$$

$$\bar{h} = \frac{2}{E}\sqrt{\frac{2r}{\pi}}(1+\nu)\sin\left(\frac{\theta}{2}\right) \tag{3.27}$$

In equations (3.23-3.27), E and ν are Young's modulus and Poisson ratio. r and θ are measured locally from the crack front as shown in Figure 23. For an interfacial crack problem, the corresponding closed form expressions represented in the paper by Ayhan, Kaya and Nied [49] are derived using the complex function method. However this kind of derivation is not suitable for the bi-material problem with an arbitrary oriented crack in this study due to the complexity of its geometry and material. Thus, a simple method on the basis of linear algebra will be described later to show how to obtain the expressions of asymptotic terms.

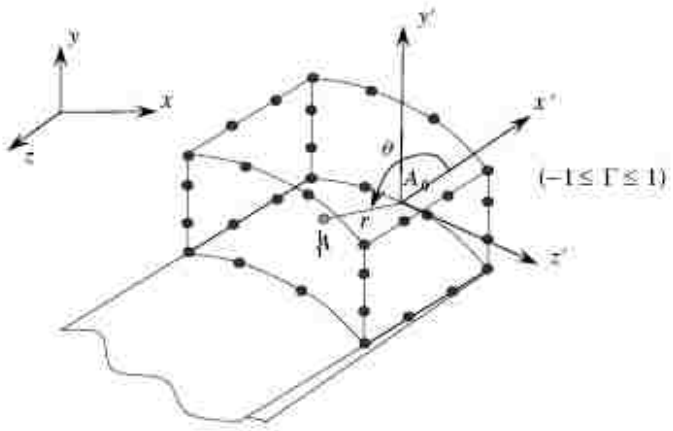

Figure 23: 32-noded hexahedron, showing orientation of local crack tip coordinate system with respect to global coordinates

The relationships between the local crack tip displacement components $\bar{u}_i$ (equations 3.22 – 3.27) and the global displacements u are created through the usual vector transformations. Using index notation

$$u_i = a_{ji}\bar{u}_j \tag{3.28}$$

where a_{ji} represents the direction cosines between the primed axes and the global axes in Figure 23, i.e., $a_{11} = \cos(x', x)$, $a_{12} = \cos(x', y)$, $a_{13} = \cos(x', z)$, etc. Transforming the asymptotic displacements in equation 3.22 to global coordinates yields the follow terms for f_i, g_i, h_i in Equations (3.9-3.11)

$$f_i = \bar{f}_1 a_{1i} + \bar{f}_2 a_{2i} \tag{3.29}$$

$$g_i = \bar{g}_1 a_{1i} + \bar{g}_2 a_{2i}$$

$$h_i = \bar{h} a_{3i}$$

It should be noted that the direction cosines used to perform the local-to-global transformations are in general different at every point in the enriched element. In addition, for element coordinate values of ξ, η, ρ located at the element nodes, the displacements are simply given by the leading terms in Equations (3.11-3.13), since F_i, G_i, H_i of equation (3.19-3.21) are identically zero at these points.

3.2.2 Enriched Element Stiffness Matrix

In this section, the local enriched element stiffness matrix is formulated for further analysis. The finite element equations are displacement based for an elastic continuum. Details concerning the finite element formulation, assembly of the global stiffness matrix, and solution of the system of equations are given in a number of references on this topic. Of particular importance in this study is the evaluation of the enriched element stiffness matrix, i.e.

$$[K] = \int_{-1}^{1}\int_{-1}^{1}\int_{-1}^{1} [B]^T [E][B] \det(J)\, d\xi d\eta d\rho \tag{3.30}$$

where *J* is the Jacobian matrix, [*B*] the strain shape function matrix, and [*E*] the material property matrix. Calculation of [*B*] requires evaluation of derivatives of Equations (3.11-3.13) that include derivatives of the analytic terms as well as the shape functions. The required derivatives of the displacement field with respect to *x*, *y*, and *z*, can be found by using the chain rule for differentiation or in matrix form, the inverse of the Jacobian, i.e.,

$$\begin{Bmatrix} \frac{\partial u}{\partial x} \\ \frac{\partial u}{\partial y} \\ \frac{\partial u}{\partial z} \end{Bmatrix} = [J]^{-1} \begin{Bmatrix} \frac{\partial u}{\partial \xi} \\ \frac{\partial u}{\partial \eta} \\ \frac{\partial u}{\partial \rho} \end{Bmatrix}, \quad \begin{Bmatrix} \frac{\partial v}{\partial x} \\ \frac{\partial v}{\partial y} \\ \frac{\partial v}{\partial z} \end{Bmatrix} = [J]^{-1} \begin{Bmatrix} \frac{\partial v}{\partial \xi} \\ \frac{\partial v}{\partial \eta} \\ \frac{\partial v}{\partial \rho} \end{Bmatrix}, \quad \begin{Bmatrix} \frac{\partial u}{\partial x} \\ \frac{\partial u}{\partial y} \\ \frac{\partial u}{\partial z} \end{Bmatrix} = [J]^{-1} \begin{Bmatrix} \frac{\partial u}{\partial \xi} \\ \frac{\partial u}{\partial \eta} \\ \frac{\partial u}{\partial \rho} \end{Bmatrix} \tag{3.31}$$

The explicit expressions for the derivatives of displacements with respect to (ξ, η, ρ) on the right hand side of (3.31) are obtained by directly differentiating (3.11-3.13), e.g.

$$\begin{aligned} \frac{\partial u(\xi,\eta,\rho)}{\partial \xi} = &\sum_{j=1}^{r} \frac{\partial N_j}{\partial \xi} u_j + \sum_{i=1}^{s} \left[\left\{ \frac{\partial Z_0}{\partial \xi} F_1 + Z_0 \frac{\partial F_1}{\partial \xi} \right\} N_i(\Gamma) + Z_0 F_1 \frac{\partial N_i(\Gamma)}{\partial \xi} \right] K_I^i \\ &+ \sum_{i=1}^{s} \left[\left\{ \frac{\partial Z_0}{\partial \xi} G_1 + Z_0 \frac{\partial G_1}{\partial \xi} \right\} N_i(\Gamma) + Z_0 G_1 \frac{\partial N_i(\Gamma)}{\partial \xi} \right] K_{II}^i \\ &+ \sum_{i=1}^{s} \left[\left\{ \frac{\partial Z_0}{\partial \xi} H_1 + Z_0 \frac{\partial H_1}{\partial \xi} \right\} N_i(\Gamma) + Z_0 H_1 \frac{\partial N_i(\Gamma)}{\partial \xi} \right] K_{III}^i \end{aligned} \tag{3.32}$$

$$\frac{\partial u(\xi,\eta,\rho)}{\partial \eta} = \sum_{j=1}^{r} \frac{\partial N_j}{\partial \eta} u_j + \sum_{i=1}^{s} \left[\left\{ \frac{\partial Z_0}{\partial \eta} F_1 + Z_0 \frac{\partial F_1}{\partial \eta} \right\} N_i(\Gamma) + Z_0 F_1 \frac{\partial N_i(\Gamma)}{\partial \eta} \right] K_I^i$$

$$+ \sum_{i=1}^{s} \left[\left\{ \frac{\partial Z_0}{\partial \eta} G_1 + Z_0 \frac{\partial G_1}{\partial \eta} \right\} N_i(\Gamma) + Z_0 G_1 \frac{\partial N_i(\Gamma)}{\partial \eta} \right] K_{II}^i \tag{3.33}$$

$$+ \sum_{i=1}^{s} \left[\left\{ \frac{\partial Z_0}{\partial \eta} H_1 + Z_0 \frac{\partial H_1}{\partial \eta} \right\} N_i(\Gamma) + Z_0 H_1 \frac{\partial N_i(\Gamma)}{\partial \eta} \right] K_{III}^i$$

$$\frac{\partial u(\xi,\eta,\rho)}{\partial \rho} = \sum_{j=1}^{r} \frac{\partial N_j}{\partial \rho} u_j + \sum_{i=1}^{s} \left[\left\{ \frac{\partial Z_0}{\partial \rho} F_1 + Z_0 \frac{\partial F_1}{\partial \rho} \right\} N_i(\Gamma) + Z_0 F_1 \frac{\partial N_i(\Gamma)}{\partial \rho} \right] K_I^i$$

$$+ \sum_{i=1}^{s} \left[\left\{ \frac{\partial Z_0}{\partial \rho} G_1 + Z_0 \frac{\partial G_1}{\partial \rho} \right\} N_i(\Gamma) + Z_0 G_1 \frac{\partial N_i(\Gamma)}{\partial \rho} \right] K_{II}^i \tag{3.34}$$

$$+ \sum_{i=1}^{s} \left[\left\{ \frac{\partial Z_0}{\partial \rho} H_1 + Z_0 \frac{\partial H_1}{\partial \rho} \right\} N_i(\Gamma) + Z_0 H_1 \frac{\partial N_i(\Gamma)}{\partial \rho} \right] K_{III}^i$$

Derivatives of displacements *v* and *w* with respect to (ξ, η, ρ) in Equation (3.31) are obtained in a similar manner. Derivatives of F_i, G_i, H_i in expressions (3.32-3.34) require differentiation of Equation (3.19-3.21) with respect to (ξ, η, ρ). This in turn means differentiation of Equations (3.19-3.21). These derivatives are determined through successive use of the chain rule. Derivatives of the primed co-ordinates with respect to the global co-ordinates, e.g. $\frac{\partial x'}{\partial x}, \frac{\partial y'}{\partial x}, \frac{\partial z'}{\partial x}, \ldots$, can be expressed in terms of the direction cosines, a_{ij}, i.e. using index notation $\frac{\partial x_i'}{\partial x_j} = a_{ij}$. Referring to Equation (3.29), the derivatives of f_1 with respect to the local co-ordinates x', y', z' are

$$\frac{\partial f_1}{\partial x'} = \frac{\partial \overline{f_1}}{\partial x'} a_{11} + \frac{\partial \overline{f_2}}{\partial x'} a_{21} \tag{3.35}$$

$$\frac{\partial f_1}{\partial y'} = \frac{\partial \overline{f_1}}{\partial y'} a_{11} + \frac{\partial \overline{f_2}}{\partial y'} a_{21} \tag{3.36}$$

$$\frac{\partial f_1}{\partial z'} = \frac{\partial \overline{f_1}}{\partial z'} a_{11} + \frac{\partial \overline{f_2}}{\partial z'} a_{21} \tag{3.37}$$

The closed form expressions of derivatives of local asymptotic terms in local crack front coordinates, e.g. $\frac{\partial \overline{f_1}}{\partial x'}, \frac{\partial \overline{f_2}}{\partial x'}, \frac{\partial \overline{f_1}}{\partial y'}, \frac{\partial \overline{f_2}}{\partial y'}, \frac{\partial \overline{f_1}}{\partial z'}, \frac{\partial \overline{f_2}}{\partial z'}$ in Equation (3.35-3.37), are given in the paper [48] for the homogenous crack and in the paper [49] for the interfacial crack respectively.

Since there are extra DOFs added with each virtual node in an enriched finite element, the dimension of elemental stiffness matrix would be enlarged to fit more entries from the asymptotic field. Taking the 20-noded hexahedron element as an example, the total number of regular displacement DOFs is $20 \times 3 = 60$. As preceding explained, only one of 12 edges coincides with the crack front. Three virtual nodes would be added at the same locations of those three crack-tip nodes, and every node has three SIFs K_I, K_{II}, K_{III} as extra DOFs. As a results, for each enriched element, they total number of DOFs would be $20 \times 3 + 3 \times 3 = 69$, and the matrix dimension should be 69×69. But in fact, the stiffness matrix of an enriched finite element always has larger size if considering the asymptotic contribution from its adjacent elements. This issue will be talked about later.

4 Arbitrary-Oriented Cracks

A bi-material solid, involving a semi-infinite crack terminating at the bonded interface with an arbitrary incidence angle, is formulated according to the Williams' expansion method, which is adopted due to its convenience in the linear solution space. For the purpose of implementation in enriched finite elements, the asymptotic crack tip displacement field in local (primed) coordinate system should be defined in terms of stress intensity factors K_I, K_{II}, K_{III} . Similar to the homogeneous and interfacial cases, the coefficients of K_I, K_{II}, K_{III} in Equation (3.22) and their derivatives, known as asymptotic terms, make contributions to both local and global stiffness matrices through transformations and the chain rule.

A new deriving approach is applied to the solutions in Williams' series type for getting explicit expressions of asymptotic crack tip displacement field. This approach is simply based on the linear algebraic transforms and the concept of split singularities.

4.1 Characteristic Matrices

First, the deriving process is discussed for the in-plane mode. The anti-plane mode can be formulated following the same strategy. Applying the boundary conditions (2.1) and (2.2) into the stress and the displacement functions (2.19-2.25), a 12×12 linear system, in the form of matrix $M_{12\times12}$ with respect to twelve unknown coefficients $C_{n,i}$, is generated.

$$\begin{bmatrix} * & * & * & * & * & * & * & * & 0 & 0 & 0 & 0 \\ * & * & * & * & * & * & * & * & 0 & 0 & 0 & 0 \\ * & * & * & * & * & * & * & * & 0 & 0 & 0 & 0 \\ * & * & * & * & * & * & * & * & 0 & 0 & 0 & 0 \\ 0 & 0 & 0 & 0 & * & * & * & * & * & * & * & * \\ 0 & 0 & 0 & 0 & * & * & * & * & * & * & * & * \\ 0 & 0 & 0 & 0 & * & * & * & * & * & * & * & * \\ 0 & 0 & 0 & 0 & * & * & * & * & * & * & * & * \\ * & * & * & * & 0 & 0 & 0 & 0 & 0 & 0 & 0 & 0 \\ * & * & * & * & 0 & 0 & 0 & 0 & 0 & 0 & 0 & 0 \\ 0 & 0 & 0 & 0 & 0 & 0 & 0 & 0 & * & * & * & * \\ 0 & 0 & 0 & 0 & 0 & 0 & 0 & 0 & * & * & * & * \end{bmatrix}_{12\times12} \begin{Bmatrix} C_{1,1} \\ C_{1,2} \\ C_{1,3} \\ C_{1,4} \\ C_{2,1} \\ C_{2,2} \\ C_{2,3} \\ C_{2,4} \\ C_{3,1} \\ C_{3,2} \\ C_{3,3} \\ C_{3,4} \end{Bmatrix}_{12\times1} = 0 \tag{4.1}$$

where $*$ indicates a non-zero entry.

All the matrix terms are determined if λ, ϕ, α and β have been specified. After that, this matrix can be treated, mathematically, as a linear relationship of these twelve unknowns. It can be regarded as the characteristic matrix of the general crack problem depicted in Figure 11. Based on this matrix, it becomes possible to represent the stress and displacement fields in terms of basis unknowns. From the perspective of elasticity, this characteristic matrix correlates all the three material zones through the continuity across the bonded interface.

After a series of row reductions, this 12×12 characteristic matrix can be simplified to a 4×4 matrix which is given in the equation below.

$$[M_{\mathrm{II}}(\lambda, \phi, \alpha, \beta)]_{4\times 4} \begin{Bmatrix} C_{2,1} \\ C_{2,2} \\ C_{2,3} \\ C_{2,4} \end{Bmatrix} = 0 \tag{4.2}$$

The matrix $[M_{\mathrm{II}}(\lambda, \phi, \alpha, \beta)]$ is of the form

$$\begin{bmatrix} 1 & 0 & \left(\frac{2\beta}{1+\beta}\right)\left(\frac{\lambda}{\lambda+1}\right)\cos[2\phi] + \left(\frac{1-\beta}{1+\beta}\right) & \left(\frac{2\beta}{1+\beta}\right)\left(\frac{\lambda}{\lambda+1}\right)\sin[2\phi] \\ 0 & 1 & -\left(\frac{2\beta}{1+\beta}\right)\left(\frac{\lambda}{\lambda+1}\right)\sin[2\phi] & \left(\frac{2\beta}{1+\beta}\right)\left(\frac{\lambda}{\lambda+1}\right)\cos[2\phi] + \left(\frac{\lambda-1}{\lambda+1}\right)\left(\frac{1-\beta}{1+\beta}\right) \\ 0 & 0 & Q_1 + Q_2 & Q_3 - Q_4 \\ 0 & 0 & Q_3 + Q_4 & Q_1 - Q_2 \end{bmatrix} \tag{4.3}$$

where

$$Q_1 = \sin[2\lambda\phi - \lambda\pi]\left\{\left(\frac{\beta-\alpha}{1+\alpha}\right)\lambda(1-\cos[2\phi])\right\} \tag{4.4}$$

$$Q_2 = \sin[2\lambda\phi - \lambda\pi]\left\{\left(\frac{\beta-\alpha}{1+\alpha}\right)\lambda^2(1-\cos[2\phi]) + \left(\frac{\beta}{1-\beta}\right)\right\} \tag{4.5}$$

$$\begin{aligned} Q_3 = \cos[2\lambda\phi - \lambda\pi]\left\{\left(\frac{\beta-\alpha}{1+\alpha}\right)(\lambda^2 - 1 - \lambda^2\cos[2\phi]) + \left(\frac{\beta}{1-\beta}\right)\right\} \\ + \cos[\lambda\pi]\left(\frac{1+\beta}{1+\alpha}\right) \end{aligned} \tag{4.6}$$

$$Q_{4=}\left(\frac{\beta-\alpha}{1+\alpha}\right)\lambda\sin[2\lambda\phi - \lambda\pi]\sin[2\phi] \tag{4.7}$$

The remaining four constants $C_{2,1}, C_{2,2}, C_{2,3}, C_{2,4}$ in equation (4.1) are used to characterize the geometric Zone II in the sketch (Figure 11). It has to be mentioned that, Zone II is the area where the crack extension line is situated in, and the conventional stress intensity factors are defined here.

For getting nontrivial solutions, the general form of the characteristic equation is obtained as the determinant of $M_{\mathrm{II}}(\lambda, \phi, \alpha, \beta)$ is equal to zero.

$$Q_1^2 - Q_2^2 - Q_3^3 + Q_4^2 = 0 \tag{4.8}$$

This is coincident with the one given in equation (2.31). Mathematically, it implies the matrix M_{II} is singular because $\mathrm{rank}[M_{\mathrm{II}}] < 4$ or $\mathrm{rank}[M_{12\times12}] < 12$. After tons of numerical tests, it has been found that there are two possibilities for the rank of the characteristic matrix,

a) As the dominant root λ arises as either a pair of complex conjugates or two unequal real numbers, where $\lambda_1 \neq \lambda_2$, the rank of matrix is equal to one less than the system dimension that $\mathrm{rank}[M_{\mathrm{II}}] = 3$, or $\mathrm{rank}[M_{12\times12}] = 11$. A typical example is the interface cracks.

b) As $\lambda_1 = \lambda_2$, which indicates a repeated real root, the rank is two less than the matrix size that $\mathrm{rank}[M_{\mathrm{II}}] = 2$, or $\mathrm{rank}[M_{12\times12}] = 10$. One may consider the homogenous crack or the crack normal to the interface for instance.

In the fundamental theory of linear algebra, if the dimension of a square matrix is $m \times m$ and its rank is equal to r and $r < m$, then the corresponding linear system has non-trial solutions. All the solutions can be represented by $n = m - r$ arbitrary constants as a basis. For the particular cases discussed above, the constants $C_{2,1}, C_{2,2}, C_{2,3}, C_{2,4}$ are able to be expressed in terms of one (for case a) or two (for case b) arbitrary unknowns for two cases respectively. The details will be given later.

Meanwhile, the other eight unknown field constants are linked to $C_{2,1}, C_{2,2}, C_{2,3}, C_{2,4}$ through the linear relationship matrix as below

$$\begin{Bmatrix} C_{1,1} \\ C_{1,2} \\ C_{1,3} \\ C_{1,4} \end{Bmatrix} = [M_{2\mathrm{II}}(\lambda, \phi, \alpha, \beta)]_{4\times 4} \begin{Bmatrix} C_{2,1} \\ C_{2,2} \\ C_{2,3} \\ C_{2,4} \end{Bmatrix} \tag{4.9}$$

$$\begin{Bmatrix} C_{3,1} \\ C_{3,2} \\ C_{3,3} \\ C_{3,4} \end{Bmatrix} = [M_{2\mathrm{II}}(\lambda, \phi - \pi, \alpha, \beta)]_{4\times 4} \begin{Bmatrix} C_{2,1} \\ C_{2,2} \\ C_{2,3} \\ C_{2,4} \end{Bmatrix} \tag{4.10}$$

and the relationship matrix $[M_{2II}(\lambda, \phi, \alpha, \beta)]$ has been formulated and given in a split form that

$$[M_{2II}]_{column(1,2)} = \begin{bmatrix} -\left(\frac{\beta-\alpha}{1+\alpha}\right)\lambda\cos[2L^+\phi] + \left(\frac{1+\beta}{1+\alpha}\right) & \left(\frac{\beta-\alpha}{1+\alpha}\right)\lambda\sin[2L^+\phi] \\ \left(\frac{\beta-\alpha}{1+\alpha}\right)\lambda\sin[2L^+\phi] & \left(\frac{\beta-\alpha}{1+\alpha}\right)\lambda\cos[2L^+\phi] + \left(\frac{1+\beta}{1+\alpha}\right) \\ \left(\frac{\beta-\alpha}{1+\alpha}\right)L^+\cos[2\lambda\phi] & -\left(\frac{\beta-\alpha}{1+\alpha}\right)L^+\sin[2\lambda\phi] \\ -\left(\frac{\beta-\alpha}{1+\alpha}\right)L^+\sin[2\lambda\phi] & -\left(\frac{\beta-\alpha}{1+\alpha}\right)L^+\cos[2\lambda\phi] \end{bmatrix} \tag{4.11}$$

$$[M_{2II}]_{column(3)} = \begin{bmatrix} -\left(\frac{\beta-\alpha}{1+\alpha}\right)L^-\cos[2\lambda\phi] - \left(\frac{2\beta}{1+\alpha}\right)\left(\frac{\cos[2\lambda\phi] - \lambda\cos[2\phi]}{L^+}\right) \\ \left(\frac{\beta-\alpha}{1+\alpha}\right)L^-\sin[2\lambda\phi] + \left(\frac{2\beta}{1+\alpha}\right)\frac{\sin[2\lambda\phi] - \lambda\sin[2\phi]}{L^+} \\ \left(\frac{\beta-\alpha}{1+\alpha}\right)\lambda\cos[2L^-\phi] + \left(\frac{1-\beta}{1+\alpha}\right) \\ -\left(\frac{\beta-\alpha}{1+\alpha}\right)\lambda\sin[2L^-\phi] \end{bmatrix} \tag{4.12}$$

$$[M_{2II}]_{column(4)} = \begin{bmatrix} \left(\frac{\beta-\alpha}{1+\alpha}\right)L^-\sin[2\lambda\phi] + \left(\frac{2\beta}{1+\alpha}\right)\frac{\sin[2\lambda\phi] + \lambda\sin[2\phi]}{L^+} \\ \left(\frac{\beta-\alpha}{1+\alpha}\right)L^-\cos[2\lambda\phi] + \left(\frac{2\beta}{1+\alpha}\right)\frac{\cos[2\lambda\phi] + \lambda\cos[2\phi]}{L^+} \\ -\left(\frac{\beta-\alpha}{1+\alpha}\right)\lambda\sin[2L^-\phi] \\ -\left(\frac{\beta-\alpha}{1+\alpha}\right)\lambda\cos[2L^-\phi] + \left(\frac{1-\beta}{1+\alpha}\right) \end{bmatrix} \tag{4.13}$$

where $L^+ = \lambda + 1$ and $L^- = \lambda - 1$. As a result, all three geometric fields are represented in linear combinations of those four unknown constants characterizing Zone II. In another word, all the fields around the crack-tip can be characterized by $C_{2,1}, C_{2,2}, C_{2,3}, C_{2,4}$. As mentioned above, these four arbitraries are reduced further to be only one or two field constants. Finally, the entire solution system can be constructed in terms of one or two "core" arbitrary unknowns. Next section will discuss how to relate the unknowns to the stress intensity factors.

4.2 Formulation of Asymptotic Fields

According to the classic linear algebra theory, the general solution of a linear equation system $[M_{n\times n}] = 0$ can be represented by a linear combination of the basis $\{V_1, V_2, \dots, V_j\}$ relative to the arbitrary constants $\{c_1, c_2, \dots, c_j\}$, which are treated as degrees of freedom (DOFs) in the perspective of engineering. $\{V_1, V_2, \dots, V_j\}$ are *n* linear independent vectors and the dimension j is determined by subtracting the rank of matrix from the dimension size that $j = n - rank[M_{n\times n}]$. However, the basis is not unique and varies with respect to the selection of the arbitrary constants. Inspired by this point, the scheme in this study is just to take the stress intensity factors into account as arbitraries in a linear system and formulate the asymptotic fields in terms of them. Next, three different cases are discussed in mathematics based on the rank of characteristic matrix and the nature of dominant roots.

4.2.1 Unequal Real Singularities

As the dominant roots arise as two real numbers, equal or unequal, the matrices $[M_{2\mathrm{II}}(\lambda, \phi, \alpha, \beta)]$, $[M_{\mathrm{II}}(\lambda, \phi, \alpha, \beta)]$ and $[M_{12\times12}]$ are all real valued. Considering the unequal situation firstly, substituting the stronger singularity λ_1 into the full form of the characteristic matrix yields $[M^1_{12\times12}]$. Its rank is equal to 11 as indicated previously. Without loss of the generality, the basis of the solution can be symbolized as $V^1_{12\times1} = \{v^1_1, v^1_2, \dots, v^1_{12}\}^T$ and the corresponding arbitrary constant is assumed as $c = C^1_{2,4}$. As a result, all the unknown constants in three geometric zones can be expressed as

$$C^1_{12\times1} = \left\{C^1_{1,1}, \dots, C^1_{1,4}, C^1_{2,1}, \dots, C^1_{2,4}, C^1_{3,1}, \dots, C^1_{3,4}\right\}^T = V^1_{12\times1}c = \{v^1_1, v^1_2, \dots, v^1_{12}\}^T C^1_{2,4} \tag{4.14}$$

Following the same manner, another set of solution can be found using the weaker singularity λ_2 and the corresponding matrix $[M^2_{12\times12}]$,

$$C^2_{12\times1} = \left\{C^2_{1,1}, \dots, C^2_{1,4}, C^2_{2,1}, \dots, C^2_{2,4}, C^2_{3,1}, \dots, C^2_{3,4}\right\}^T = V^2_{12\times1}c = \{v^2_1, v^2_2, \dots, v^2_{12}\}^T C^2_{2,4} \tag{4.15}$$

After appropriate linear transformations, the stress field and the displacement field in different zones can be treated in terms of $C^i_{2,4}$ corresponding to λ_i respectively. It has been known that the

general solution of the Airy function is actually a sum of series with respect to singularities. Therefore, these two groups of solutions can be superposed linearly to generate the overall asymptotic solutions that

$$\begin{aligned}\sigma_{ij}(n,r,\theta) &= \sigma_{ij}(n,r,\theta,\lambda_1) + \sigma_{ij}(n,r,\theta,\lambda_2) \\ &= r^{\lambda_1-1}\Gamma_{ij}^1(n,\theta)\, C_{2,4}^1 + r^{\lambda_2-1}\Gamma_{ij}^2(n,\theta)C_{2,4}^2\end{aligned} \tag{4.16}$$

$$u_j(n,r,\theta) = u_j(n,r,\theta,\lambda_1) + u_j(n,r,\theta,\lambda_2) = r^{\lambda_1}\Gamma_{uj}^1(n,\theta)\, C_{2,4}^1 + r^{\lambda_2}\Gamma_{uj}^2(n,\theta)C_{2,4}^2 \tag{4.17}$$

where $\Gamma_{ij}^m(n,\theta)$ and $\Gamma_{uj}^m(n,\theta)$ are the angular functions obtained through multiplication of the characteristic matrix $[M_{\mathrm{II}}(\lambda_m,\phi,\alpha,\beta)]$, the relationship matrix $[M_{2\mathrm{II}}(\lambda_m,\phi,\alpha,\beta)]$ and the basis vector $V_{12\times1}^m$. Please note these functions correspond to the arbitrary constants $C_{2,4}^1$ and $C_{2,4}^2$, not K_I and K_{II}. The parameter "*n*" indicates different geometric zones. To make it simple to be programmable, the stress and displacement fields are deduced to products of vectors and matrices which will be given later.

According to the definition of split singularities [35], the asymptotic stress field around the crack-tip is a linear superposition of Mode-I and Mode-II solutions. The equation (1.5) can be modified by adding some appropriate scripts that

$$\sigma_{ij}(n,r,\theta) = K_I(2\pi r)^{\lambda_1-1}\Sigma_{ij}^I(n,\theta) + K_{II}(2\pi r)^{\lambda_2-1}\Sigma_{ij}^{II}(n,\theta) \tag{4.18}$$

In the equation above, $\Sigma_{ij}^m(n,\theta)$ is also the angular function but defined with respect to the stress intensity factors. Following the conventional definition of stress intensity factors which is along the crack extension line and embedded in Zone II, equation (4.18) is assigned with specific notations, and the angular functions are normalized as

$$\Sigma_{\theta\theta}^I(2,0) = \Sigma_{r\theta}^{II}(2,0) = 1 \tag{4.19}$$

Taking advantage of (4.19), the same stress state represented by equations (4.16) and (4.18) should be identically equal that

$$r^{\lambda_1-1}\Gamma^1_{\theta\theta}(2,0)\,C^1_{2,4} + r^{\lambda_2-1}\Gamma^2_{\theta\theta}(2,0)C^2_{2,4} \equiv K_I(2\pi r)^{\lambda_1-1} + K_{II}(2\pi r)^{\lambda_2-1}\Sigma^{II}_{\theta\theta}(2,0)$$

$$r^{\lambda_1-1}\Gamma^1_{r\theta}(2,0)\,C^1_{2,4} + r^{\lambda_2-1}\Gamma^2_{r\theta}(2,0)C^2_{2,4} \equiv K_I(2\pi r)^{\lambda_1-1}\Sigma^{I}_{r\theta}(2,0) + K_{II}(2\pi r)^{\lambda_2-1} \tag{4.20}$$

where the specific angular functions $\Gamma^j_{\theta\theta}(2,0)$ and $\Gamma^j_{r\theta}(2,0)$ are formulated as

$$\Gamma^j_{\theta\theta}(2,0) = \left(\frac{4\beta\lambda_j^2}{1+\beta}\right)\left\{\sin^2[\phi] - \sin[\phi]\cos[\phi]\left(\frac{Q_3-Q_4}{Q_1+Q_2}\right)\right\} + \left(\frac{2\lambda_j}{1+\beta}\right) \tag{4.21}$$

$$\Gamma^j_{r\theta}(2,0) = \left(\frac{4\beta\lambda_j^2}{1+\beta}\right)\left\{\sin^2[\phi]\left(\frac{Q_3-Q_4}{Q_1+Q_2}\right) + \sin[\phi]\cos[\phi]\right\} - \left(\frac{\lambda_j}{1+\beta}\right)\left(\frac{Q_3-Q_4}{Q_1+Q_2}\right) \tag{4.22}$$

The constants Q_1, Q_2, Q_3, Q_4 are defined in equations (4.4-4.7).

As the radial distance is approaching to zero, comparing the coefficients of different magnitude orders leads to the equivalent relationship below

$$\begin{gathered}\Gamma^1_{\theta\theta}(2,0)C^1_{2,4} = K_I(2\pi)^{\lambda_1-1} \\ \Gamma^2_{\theta\theta}(2,0)C^2_{2,4} = K_{II}(2\pi)^{\lambda_2-1}\Sigma^{II}_{\theta\theta}(2,0) \\ \Gamma^1_{r\theta}(2,0)C^1_{2,4} = K_I(2\pi)^{\lambda_1-1}\Sigma^{I}_{r\theta}(2,0) \\ \Gamma^2_{r\theta}(2,0)C^2_{2,4} = K_{II}(2\pi)^{\lambda_2-1}\end{gathered} \tag{4.23}$$

Then the linear relationship between the stress intensity factors and the arbitrary constants is found that

$$K_I = (2\pi)^{1-\lambda_1}\Gamma^1_{\theta\theta}(2,0)C^1_{2,4} \;\; or \;\; C^1_{2,4} = \frac{K_I(2\pi)^{\lambda_1-1}}{\Gamma^1_{\theta\theta}(2,0)} \tag{4.24}$$

$$K_{II} = (2\pi)^{1-\lambda_2}\Gamma^2_{r\theta}(2,0)C^2_{2,4} \;\; or \;\; C^2_{2,4} = \frac{K_{II}(2\pi)^{\lambda_2-1}}{\Gamma^2_{r\theta}(2,0)} \tag{4.25}$$

Substituting equations (4.24) and (4.25) into the expression of (4.16) yields

$$\sigma_{\theta\theta}(n,r,\theta) = K_I(2\pi r)^{\lambda_1-1}\frac{\Gamma^1_{\theta\theta}(n,\theta)}{\Gamma^1_{\theta\theta}(2,0)} + K_{II}(2\pi r)^{\lambda_2-1}\frac{\Gamma^2_{\theta\theta}(n,\theta)}{\Gamma^2_{r\theta}(2,0)} \tag{4.26}$$

$$\tau_{r\theta}(n,r,\theta) = K_I(2\pi r)^{\lambda_1-1}\frac{\Gamma^1_{r\theta}(n,\theta)}{\Gamma^1_{\theta\theta}(2,0)} + K_{II}(2\pi r)^{\lambda_2-1}\frac{\Gamma^2_{r\theta}(n,\theta)}{\Gamma^2_{r\theta}(2,0)} \tag{4.27}$$

which gives the general forms of angular functions in equation (4.18)

$$\begin{aligned}
\Sigma^I_{\theta\theta}(n,\theta) &= \frac{\Gamma^1_{\theta\theta}(n,\theta)}{\Gamma^1_{\theta\theta}(2,0)} \\
\Sigma^{II}_{\theta\theta}(n,\theta) &= \frac{\Gamma^2_{\theta\theta}(n,\theta)}{\Gamma^2_{r\theta}(2,0)} \\
\Sigma^I_{r\theta}(n,\theta) &= \frac{\Gamma^1_{r\theta}(n,\theta)}{\Gamma^1_{\theta\theta}(2,0)} \\
\Sigma^{II}_{r\theta}(n,\theta) &= \frac{\Gamma^2_{r\theta}(n,\theta)}{\Gamma^2_{r\theta}(2,0)}
\end{aligned} \tag{4.28}$$

Eventually, K_I and K_{II} are treated as a set of arbitrary constants for the solution of entire system. Using the chain rule, all the asymptotic stress and displacement fields can be formulated in terms of two stress intensity factors. The corresponding basis can be expressed as

$$\begin{aligned}
V^{KI}_{12\times1} &= V^1_{12\times1} * \frac{(2\pi)^{\lambda_1-1}}{\Gamma^1_{\theta\theta}(2,0)} \\
V^{KII}_{12\times1} &= V^2_{12\times1} * \frac{(2\pi)^{\lambda_2-1}}{\Gamma^2_{r\theta}(2,0)}
\end{aligned} \tag{4.29}$$

Especially, the asymptotic crack-tip displacement fields are of the form

$$u_r(n,r,\theta) = (2\pi)^{\lambda_1-1}r^{\lambda_1}\frac{\Gamma^1_{ur}(n,\theta)}{\Gamma^1_{\theta\theta}(2,0)}K_I + (2\pi)^{\lambda_2-1}r^{\lambda_2}\frac{\Gamma^2_{ur}(n,\theta)}{\Gamma^2_{r\theta}(2,0)}K_{II} \tag{4.30}$$

$$u_\theta(n,r,\theta) = (2\pi)^{\lambda_1-1}r^{\lambda_1}\frac{\Gamma^1_{u\theta}(n,\theta)}{\Gamma^1_{\theta\theta}(2,0)}K_I + (2\pi)^{\lambda_2-1}r^{\lambda_2}\frac{\Gamma^2_{u\theta}(n,\theta)}{\Gamma^2_{r\theta}(2,0)}K_{II} \tag{4.31}$$

which can be implemented straight-forward in the formulation of enriched finite element.

4.2.2 Equal Real Singularities

As particular cases, the homogenous crack or the crack normal to the interface bears a repeated singularity that $\lambda_1 = \lambda_2$. However, both of them need to be taken into account, although

they lead to the same solution. These two identical dominant roots make the rank of $[M_{12\times12}]$ equal to 10, which means, mathematically, there are two basis vectors existing with respect to two arbitrary constants. Substituting λ_1 into the characteristic matrix and assuming the two constants are $C_{2,3}^1$ and $C_{2,4}^1$, the basis of solution should have the form that

$$\{C\}_{12\times1}^1 = \{C_{1,1}^1, \dots, C_{1,4}^1, C_{2,1}^1, \dots, C_{2,4}^1, C_{3,1}^1, \dots, C_{3,4}^1\} = [V_{12\times1}^1 \quad V_{12\times1}^2]_{12\times2} \begin{Bmatrix} C_{2,3}^1 \\ C_{2,4}^1 \end{Bmatrix}$$
$$= \begin{bmatrix} v_1^1 & v_1^2 \\ \vdots & \vdots \\ v_{12}^1 & v_{12}^2 \end{bmatrix}_{12\times2} \begin{Bmatrix} C_{2,3}^1 \\ C_{2,4}^1 \end{Bmatrix} \tag{4.32}$$

Taking advantage of the chain rule again, the stress and displacement fields in three geometric zones are expressed in terms of $C_{2,3}^1$ and $C_{2,4}^1$. Since two roots are identical, the deduced linear solution for λ_2 is as same as for λ_1. Then their superposition gives the asymptotic fields that

$$\sigma_{\theta\theta}(n,r,\theta) = 2r^{\lambda_1-1}[\Gamma_{\theta\theta}^1(n,\theta) \quad \Gamma_{\theta\theta}^2(n,\theta)] \begin{Bmatrix} C_{2,3}^1 \\ C_{2,4}^1 \end{Bmatrix} \tag{4.33}$$

$$\tau_{r\theta}(n,r,\theta) = 2r^{\lambda_1-1}[\Gamma_{r\theta}^1(n,\theta) \quad \Gamma_{r\theta}^2(n,\theta)] \begin{Bmatrix} C_{2,3}^1 \\ C_{2,4}^1 \end{Bmatrix} \tag{4.34}$$

$$u_r(n,r,\theta) = 2r^{\lambda_1}[\Gamma_{ur}^1(n,\theta) \quad \Gamma_{ur}^2(n,\theta)] \begin{Bmatrix} C_{2,3}^1 \\ C_{2,4}^1 \end{Bmatrix} \tag{4.35}$$

$$u_\theta(n,r,\theta) = 2r^{\lambda_1}[\Gamma_{u\theta}^1(n,\theta) \quad \Gamma_{u\theta}^2(n,\theta)] \begin{Bmatrix} C_{2,3}^1 \\ C_{2,4}^1 \end{Bmatrix} \tag{4.36}$$

where $\Gamma_{ij}^m(n,\theta)$ is similar to those angular functions for the unequal case, but m just indicates the indices of two arbitrary constants.

After that, the same process is carried out to get the local asymptotic fields in terms of K_I and K_{II}. It should be noted that non-dimensional angular functions $\Sigma_{ij}^I(n,\theta)$ and $\Sigma_{ij}^{II}(n,\theta)$ may have different restrictions rather than the previous case. For example, there are two more conditions to be satisfied:

$$\Sigma_{r\theta}^{I}(2,0) = \Sigma_{\theta\theta}^{II}(2,0) = 0 \tag{4.37}$$

For this case, equation (4.20) can be rewritten as

$$\begin{aligned} 2r^{\lambda_1-1}\Gamma_{\theta\theta}^{1}(2,0)\, C_{2,3}^{1} + 2r^{\lambda_1-1}\Gamma_{\theta\theta}^{2}(2,0)C_{2,4}^{1} &\equiv K_I(2\pi r)^{\lambda_1-1} \\ 2r^{\lambda_1-1}\Gamma_{r\theta}^{1}(2,0)\, C_{2,3}^{1} + 2r^{\lambda_1-1}\Gamma_{r\theta}^{2}(2,0)C_{2,4}^{2} &\equiv K_{II}(2\pi r)^{\lambda_1-1} \end{aligned} \tag{4.38}$$

or in the form of matrix that

$$\begin{bmatrix} \Gamma_{\theta\theta}^{1}(2,0) & \Gamma_{\theta\theta}^{2}(2,0) \\ \Gamma_{r\theta}^{1}(2,0) & \Gamma_{r\theta}^{2}(2,0) \end{bmatrix} \begin{Bmatrix} C_{2,3}^{1} \\ C_{2,4}^{1} \end{Bmatrix} = \frac{(2\pi)^{\lambda_1-1}}{2} \begin{Bmatrix} K_I \\ K_{II} \end{Bmatrix} \tag{4.39}$$

in which the specific angular functions are found as below

$$\begin{aligned} \Gamma_{\theta\theta}^{1}(2,0) &= \left(\frac{2\beta\lambda^2}{1+\beta}\right)\sin[2\phi] \\ \Gamma_{\theta\theta}^{2}(2,0) &= \left(\frac{2\beta\lambda^2}{1+\beta}\right)(1-\cos[2\phi]) + \left(\frac{2\lambda}{1+\beta}\right) \\ \Gamma_{r\theta}^{1}(2,0) &= -\left(\frac{2\beta\lambda^2}{1+\beta}\right)(1-\cos[2\phi]) + \left(\frac{2\lambda}{1+\beta}\right) \\ \Gamma_{r\theta}^{2}(2,0) &= \left(\frac{2\beta\lambda}{1+\beta}\right)\sin[2\phi] \end{aligned} \tag{4.40}$$

After appropriate matrix operations, $C_{2,3}^{1}$ and $C_{2,4}^{1}$ can be expressed in terms of K_I and K_{II}

$$\begin{Bmatrix} C_{2,3}^{1} \\ C_{2,4}^{1} \end{Bmatrix} = \frac{(2\pi)^{\lambda_1-1}}{2} \begin{bmatrix} \Gamma_{\theta\theta}^{1}(2,0) & \Gamma_{\theta\theta}^{2}(2,0) \\ \Gamma_{r\theta}^{1}(2,0) & \Gamma_{r\theta}^{2}(2,0) \end{bmatrix}^{-1} \begin{Bmatrix} K_I \\ K_{II} \end{Bmatrix} \tag{4.41}$$

Then the stress intensity factors are regarded as arbitraries for the solution system

$$\sigma_{\theta\theta}(n,r,\theta) = (2\pi r)^{\lambda_1-1}[\Gamma_{\theta\theta}^{1}(n,\theta) \quad \Gamma_{\theta\theta}^{2}(n,\theta)] \begin{bmatrix} \Gamma_{\theta\theta}^{1}(2,0) & \Gamma_{\theta\theta}^{2}(2,0) \\ \Gamma_{r\theta}^{1}(2,0) & \Gamma_{r\theta}^{2}(2,0) \end{bmatrix}^{-1} \begin{Bmatrix} K_I \\ K_{II} \end{Bmatrix} \tag{4.42}$$

$$\tau_{r\theta}(n,r,\theta) = (2\pi r)^{\lambda_1-1}[\Gamma_{r\theta}^{1}(n,\theta) \quad \Gamma_{r\theta}^{2}(n,\theta)] \begin{bmatrix} \Gamma_{\theta\theta}^{1}(2,0) & \Gamma_{\theta\theta}^{2}(2,0) \\ \Gamma_{r\theta}^{1}(2,0) & \Gamma_{r\theta}^{2}(2,0) \end{bmatrix}^{-1} \begin{Bmatrix} K_I \\ K_{II} \end{Bmatrix} \tag{4.43}$$

$$u_r(n,r,\theta) = (2\pi)^{\lambda_1-1} r^{\lambda_1}[\Gamma_{ur}^{1}(n,\theta) \quad \Gamma_{ur}^{2}(n,\theta)] \begin{bmatrix} \Gamma_{\theta\theta}^{1}(2,0) & \Gamma_{\theta\theta}^{2}(2,0) \\ \Gamma_{r\theta}^{1}(2,0) & \Gamma_{r\theta}^{2}(2,0) \end{bmatrix}^{-1} \begin{Bmatrix} K_I \\ K_{II} \end{Bmatrix} \tag{4.44}$$

$$u_\theta(n,r,\theta) = (2\pi)^{\lambda_1-1} r^{\lambda_1} [\Gamma^1_{u\theta}(n,\theta) \quad \Gamma^2_{u\theta}(n,\theta)] \begin{bmatrix} \Gamma^1_{\theta\theta}(2,0) & \Gamma^2_{\theta\theta}(2,0) \\ \Gamma^1_{r\theta}(2,0) & \Gamma^2_{r\theta}(2,0) \end{bmatrix}^{-1} \begin{Bmatrix} K_I \\ K_{II} \end{Bmatrix} \tag{4.45}$$

4.2.3 Complex Conjugated Singularities

For the complex singularities, the solution system of course needs to be developed in the field of complex number. Different than the real number case, the complex solution has its own features in the linear algebraic space. First of all, considering a null space for a system of linear equations in the complex field, the free variables and the associated bases arise necessarily in pairs and conjugated. A trick to find the general solution of the system is to treat the real part and the imaginary part as a linear combination through the imaginary unit. In this manner, the paired solution sets would be only related to two real arbitraries, and this kind of problem may be regard as an equivalent case in the real number field. This strategy benefits the derivation work in this research as the dominant root have a non-zero image part.

To be symbolized, first let the complex dominant roots be $\lambda_{1,2} = \xi \pm i\rho$. Then the corresponding matrices $[M_{2\mathrm{II}}(\lambda,\phi,\alpha,\beta)]$, $[M_{\mathrm{II}}(\lambda,\phi,\alpha,\beta)]$ and $[M_{12\times12}]$ are all complex valued. The rank of the characteristic matrix $[M_{12\times12}]$ is equal to 11 as explained previously. Using the similar linear transformations, all the unknown field constants of each solution system can be expressed in terms of a single complex variable, e.g., $C^1_{2,4}$ and $C^2_{2,4}$,. It should be emphasized that these two arbitraries should be defined in the complex field as well.

As is well-known, the functions of a pair of complex conjugates are also conjugated, i.e., $F(\bar{z}) = \overline{F(z)}$. Therefore, the solutions generated from $\lambda_{1,2} = \xi \pm i\rho$ can be correlated as

$$\begin{aligned} \sigma_{ij}(n,r,\theta,\lambda_1) &= \overline{\sigma_{ij}(n,r,\theta,\lambda_2)} \\ u_{ij}(n,r,\theta,\lambda_1) &= \overline{u_{ij}(n,r,\theta,\lambda_2)} \end{aligned} \tag{4.46}$$

Then the superposition of these two groups of solutions yields the asymptotic expression in a simplified form that

$$\sigma_{\theta\theta}(n,r,\theta)=\sigma_{\theta\theta}(n,r,\theta,\lambda_1)+\sigma_{\theta\theta}(n,r,\theta,\lambda_2)=Re\left[2r^{\lambda_1-1}\Gamma^1_{\theta\theta}(n,\theta)\,C^1_{2,4}\right] \tag{4.47}$$

$$\tau_{r\theta}(n,r,\theta)=\tau_{r\theta}(n,r,\theta,\lambda_1)+\tau_{r\theta}(n,r,\theta,\lambda_2)=Re\left[2r^{\lambda_1-1}\Gamma^1_{r\theta}(n,\theta)\,C^1_{2,4}\right] \tag{4.48}$$

$$u_r(n,r,\theta)=u_r(n,r,\theta,\lambda_1)+u_r(n,r,\theta,\lambda_2)=Re\left[2r^{\lambda_1}\Gamma^1_{ur}(n,\theta)\,C^1_{2,4}\right] \tag{4.49}$$

$$u_\theta(n,r,\theta)=u_\theta(n,r,\theta,\lambda_1)+u_\theta(n,r,\theta,\lambda_2)=Re\left[2r^{\lambda_1}\Gamma^1_{u\theta}(n,\theta)\,C^1_{2,4}\right] \tag{4.50}$$

where $\Gamma^m_{ij}(n,\theta)$ is the angular function in the complex field, which can be derived from the approach described in this study. The superscript "*m*" can be removed since only one root is needed in this formulation. So the asymptotic solution obtained this way is still meaningful physically.

To investigate the general case with complex singularities, the solution for the interfacial crack is reviewed firstly. The stress intensity factor is defined as a complex variable and can be expressed as

$$\begin{aligned}&\sigma_{\theta\theta}(2,r,0)+i\tau_{r\theta}(2,r,0)=K(2\pi r)^{\lambda_1-1}=(k_1+ik_2)(2\pi r)^{\lambda_1-1}\\ &\text{or}\quad \sigma_{\theta\theta}(2,r,0)=Re\left[K(2\pi r)^{\lambda_1-1}\right]\ and\ \tau_{r\theta}(2,r,0)=Im\left[K(2\pi r)^{\lambda_1-1}\right]\end{aligned} \tag{4.51}$$

. Accordingly, the stresses ahead of the crack-tip may be represented as

$$\begin{aligned}\sigma_{\theta\theta}(n,r,\theta)&=Re\left[K(2\pi r)^{\lambda_1-1}\right]\Sigma^R_{\theta\theta}(n,\theta)+Im\left[K(2\pi r)^{\lambda_1-1}\right]\Sigma^I_{\theta\theta}(n,\theta)\\ \tau_{r\theta}(n,r,\theta)&=Re\left[K(2\pi r)^{\lambda_1-1}\right]\Sigma^R_{r\theta}(n,\theta)+Im\left[K(2\pi r)^{\lambda_1-1}\right]\Sigma^I_{r\theta}(n,\theta)\end{aligned} \tag{4.52}$$

where $\Sigma^R_{ij}(r,\theta)$ and $\Sigma^I_{ij}(r,\theta)$ are real part and image part of the complex angular function $\bar{}$

$$\Sigma_{ij}(r,\theta)=\Sigma^R_{ij}(r,\theta)-i\Sigma^I_{ij}(r,\theta) \tag{4.53}$$

respectively. So the asymptotic stress and displacement fields in equation (4.52) can be represented in another form using the complex angular function as follows

$$\begin{aligned}\sigma_{\theta\theta}(n,r,\theta)&=Re\left[K(2\pi r)^{\lambda_1-1}\Sigma_{\theta\theta}(n,\theta)\right]\\ \tau_{r\theta}(n,r,\theta)&=Re\left[K(2\pi r)^{\lambda_1-1}\Sigma_{r\theta}(n,\theta)\right]\end{aligned} \tag{4.54}$$

To be consistent with the conventional definition by equation (4.51), the following conditions should be satisfied

$$\Sigma_{\theta\theta}^{R}(2,0) = \Sigma_{r\theta}^{I}(2,0) = 1 \tag{4.55}$$

But in this study, it has been found that $\Sigma_{\theta\theta}^{I}(2,0)$ and $\Sigma_{r\theta}^{R}(2,0)$ don't vanish except the case of interface crack.

Comparison of equations (4.47), (4.48) and (4.54) gives the sufficient condition for the equality between the different expressions of asymptotic solution ahead of the crack tip:.

$$\begin{aligned} K(2\pi)^{\lambda_1-1}\Sigma_{\theta\theta}(2,0) &= \Gamma_{\theta\theta}(2,0)C_{2,4} \\ K(2\pi)^{\lambda_1-1}\Sigma_{r\theta}(2,0) &= \Gamma_{r\theta}(2,0)C_{2,4} \end{aligned} \tag{4.56}$$

Accordingly, the following equivalent ratio must be satisfied:

$$\frac{\Sigma_{\theta\theta}(2,0)}{\Sigma_{r\theta}(2,0)} = \frac{\Gamma_{\theta\theta}(2,0)}{\Gamma_{r\theta}(2,0)} = p \tag{4.57}$$

The image part of angular function $\Sigma_{\theta\theta}(2,0)$ and the real part of $\Sigma_{r\theta}(2,0)$ are determined using the ratio "*p*". . In a particular case of the interface crack, the ratio is equal to a pure image constant that *p*=*i*. However, for any other cases with complex singularities, *p* is not a pure imaginary number in complex number field. Therefore, the equation (4.51) cannot be established directly, and the definition of the complex stress intensity factor is violated. According to the definition of complex stress intensity factors, $\Sigma_{\theta\theta}(2,0)$ and $\Sigma_{r\theta}(2,0)$ is supposed to be of the from as below

$$\begin{aligned} \Sigma_{\theta\theta}(2,0) &= 1 - i\chi \\ \Sigma_{r\theta}(2,0) &= \varsigma - i \end{aligned} \tag{4.58}$$

The ratio *p* is evaluated from $\Gamma_{\theta\theta}(2,0)$ and $\Gamma_{r\theta}(2,0)$. If *p* is not a pure imaginary number, the unknowns *x* and *y* can be obtained that

$$\chi = \frac{p\bar{p} - Im[p]}{Re[p]}$$
$$\varsigma = \frac{1 - Im[p]}{Re[p]} \tag{4.59}$$

where the notations $Im[\quad]$ and $Re[\quad]$ stand for the imaginary part and the real part of a complex number respectively.

Substituting $1 - i\chi$ into equation (4.56), the complex arbitrary constant $C_{2,4}$ can be represented in terms of *K*

$$C_{2,4} = K(2\pi)^{\lambda_1 - 1}\frac{(1 - i\chi)}{\Gamma_{\theta\theta}(2,0)} \tag{4.60}$$

The specific angular function in the complex field can be generated as

$$\Gamma_{\theta\theta}(2,0) = \left(\frac{4\beta\lambda^2\sin[\phi]}{1+\beta}\right)\left\{e^{i\left(\frac{\pi}{2}-\phi\right)} - e^{-i\phi}\left(\frac{Q_3 - Q_4}{Q_1 + Q_2}\right)\right\} + \left(\frac{2\lambda}{1+\beta}\right)\left\{1 - e^{i\frac{\pi}{2}}\left(\frac{Q_3 - Q_4}{Q_1 + Q_2}\right)\right\} \tag{4.61}$$

Then the asymptotic stress field and displacement field for complex singularities have the expression that

$$\sigma_{\theta\theta}(n,r,\theta) = Re\left[2(1 - i\chi)(2\pi r)^{\lambda - 1}\frac{\Gamma_{\theta\theta}(n,\theta)}{\Gamma_{\theta\theta}(2,0)}K\right] \tag{4.62}$$

$$\tau_{r\theta}(n,r,\theta) = Re\left[2(1 - i\chi)(2\pi r)^{\lambda - 1}\frac{\Gamma_{r\theta}(n,\theta)}{\Gamma_{\theta\theta}(2,0)}K\right] \tag{4.63}$$

$$u_r(n,r,\theta) = Re\left[2(1 - i\chi)(2\pi)^{\lambda - 1}r^{\lambda}\frac{\Gamma_{ur}(n,\theta)}{\Gamma_{\theta\theta}(2,0)}K\right] \tag{4.64}$$

$$u_\theta(n,r,\theta) = Re\left[2(1 - i\chi)(2\pi)^{\lambda - 1}r^{\lambda}\frac{\Gamma_{u\theta}(n,\theta)}{\Gamma_{\theta\theta}(2,0)}K\right] \tag{4.65}$$

Consequently, the relationship between the complex stress intensity factors and the complex free variables is formed linearly. Actually, the new item $(1 - i\chi)$ can be considered as a rotation factor, which works to redistribute the contribution from the complex stress intensity factor to the asymptotic field:

$$K(1-i\chi) = (k_1 + ik_2)(1-i\chi) = (k_1 + \chi k_2) + i(k_2 - \chi k_1) \tag{4.66}$$

The remaining work is just to have the asymptotic field represented by the complex singularities in the same way of developing the real singularities. The asymptotic terms should be obtained by separating the real part and complex part of the corresponding coefficients in the displacement field.

4.3 Field Expression in Matrix Form

In the formulation of singular field, the dominant roots represent the strength of singularity in the vicinity of crack-tip, and the corresponding angular functions describe the circumferential distribution of stress or displacement. Given the reference radial distance is fixed, the angle with the maximum angular value with respect to the stronger singularity (or superposed) always coincide with the most possible direction the crack will propagates along. But in the case of arbitrarily-oriented crack, these angular functions are difficult to be expressed in an explicit form due to the asymmetry nature of geometry. In this study, a convenient way for such kind of crack problem is demonstrated. The formulation of asymptotic field is constructed as a product of appropriate vectors and matrices as well as the strength of singularities and arbitrary unknowns. In terms of vectors or matrices, different field components have common multiplying factors named “common factor”, and also have their specific matrix named “field factor”. This approach is valid for both real and complex singularities. All the fields can be represented as below

$$\sigma_{\theta\theta}(n,r,\theta) = r^{\lambda-1}\{V_{TF}\}_{1\times4}[M_{ST}]_{4\times4}\{V_C\}_{4\times N}\{C_{2,j}\}_{N\times1} \tag{4.67}$$

$$\sigma_{rr}(n,r,\theta) = r^{\lambda-1}\{V_{TF}\}_{1\times4}[M_{SR}]_{4\times4}\{V_C\}_{4\times N}\{C_{2,j}\}_{N\times1} \tag{4.68}$$

$$\sigma_{r\theta}(n,r,\theta) = r^{\lambda-1}\{V_{TF}\}_{1\times4}[M_{SRT}]_{4\times4}\{V_C\}_{4\times N}\{C_{2,j}\}_{N\times1} \tag{4.69}$$

$$u_r(n,r,\theta) = r^{\lambda}\{V_{TF}\}_{1\times4}[M_{UR}]_{4\times4}\{V_C\}_{4\times N}\{C_{2,j}\}_{N\times1} \tag{4.70}$$

$$u_\theta(n,r,\theta) = r^{\lambda}\{V_{TF}\}_{1\times4}[M_{UT}]_{4\times4}\{V_C\}_{4\times N}\{C_{2,j}\}_{N\times1} \tag{4.71}$$

in which V_{TF} and V_C are common factors, and M_{SR}, M_{ST}, M_{SRT}, M_{UR} and M_{UT} are field factors. The subscript of the bracket denotes the dimension of matrix or vector. The vector $\{V_C\}_{4\times N}$ has to be

generated from equations (4.14, 4.15, 4.33-4.36, 4.47-4.50) for different geometric zones, and the dimension *N* depends on the number of arbitrary constants for different cases. It has to been mentioned that the matrix form shown above is specified for an individual or repeated singularity. If there are two different roots existing in the dominant zone, the final solution should be obtained by superposing the relevant solutions. The expressions of those vectors and matrices are given as below

$$V_{TF} = \{\sin[(\lambda+1)\theta] \quad \cos[(\lambda+1)\theta] \quad \sin[(\lambda-1)\theta] \quad \cos[(\lambda-1)\theta]\} \tag{4.72}$$

$$M_{SR} = \begin{bmatrix} -(\lambda^2+\lambda) & 0 & 0 & 0 \\ 0 & -(\lambda^2+\lambda) & 0 & 0 \\ 0 & 0 & -(\lambda^2-3\lambda) & 0 \\ 0 & 0 & 0 & -(\lambda^2-3\lambda) \end{bmatrix} \tag{4.73}$$

$$M_{ST} = \begin{bmatrix} (\lambda^2+\lambda) & 0 & 0 & 0 \\ 0 & (\lambda^2+\lambda) & 0 & 0 \\ 0 & 0 & (\lambda^2+\lambda) & 0 \\ 0 & 0 & 0 & (\lambda^2+\lambda) \end{bmatrix} \tag{4.74}$$

$$M_{SRT} = \begin{bmatrix} 0 & (\lambda^2+\lambda) & 0 & 0 \\ -(\lambda^2+\lambda) & 0 & 0 & 0 \\ 0 & 0 & 0 & (\lambda^2-\lambda) \\ 0 & 0 & -(\lambda^2-\lambda) & 0 \end{bmatrix} \tag{4.75}$$

$$M_{UR} = -\frac{1}{2\mu_n}\begin{bmatrix} (\lambda+1) & 0 & 0 & 0 \\ 0 & (\lambda+1) & 0 & 0 \\ 0 & 0 & (\lambda-\eta_n) & 0 \\ 0 & 0 & 0 & (\lambda-\eta_n) \end{bmatrix} \tag{4.76}$$

$$M_{UT} = -\frac{1}{2\mu_n}\begin{bmatrix} 0 & -(\lambda+1) & 0 & 0 \\ (\lambda+1) & 0 & 0 & 0 \\ 0 & 0 & 0 & -(\lambda+\eta_n) \\ 0 & 0 & (\lambda+\eta_n) & 0 \end{bmatrix} \tag{4.77}$$

In the case with repeated real singularities, the vector V_C has two columns with respect to two arbitrary constants. The vector for geometry zone II (n=2) has been given as below. The others for zone I and III (n=1 or 3) can be obtained by multiplying the relationship matrix

$$V_C^2|_{4\times 2}=\begin{bmatrix} -\left(\frac{2\beta}{1+\beta}\right)\left(\frac{\lambda}{\lambda+1}\right)\cos[2\phi]-\left(\frac{1-\beta}{1+\beta}\right) & -\left(\frac{2\beta}{1+\beta}\right)\left(\frac{\lambda}{\lambda+1}\right)\sin[2\phi] \\ \left(\frac{2\beta}{1+\beta}\right)\left(\frac{\lambda}{\lambda+1}\right)\sin[2\phi] & -\left(\frac{2\beta}{1+\beta}\right)\left(\frac{\lambda}{\lambda+1}\right)\cos[2\phi]-\left(\frac{\lambda-1}{\lambda+1}\right)\left(\frac{1-\beta}{1+\beta}\right) \\ 1 & 0 \\ 0 & 1 \end{bmatrix} \tag{4.78}$$

$$V_C^1=[M_{2\mathrm{II}}(\lambda,\phi,\alpha,\beta)]V_C^2 \tag{4.79}$$

$$V_C^3=[M_{2\mathrm{II}}(\lambda,\phi-\pi,\alpha,\beta)]V_C^2 \tag{4.80}$$

If the strength of singularity arises as two unequal real numbers, the vector V_C only has one column for each case. Please note that the relationship matrix would be different for two unequal dominant roots.

$$V_C^2\big|_{4\times 1}=\begin{Bmatrix} \left(\frac{2\beta}{1+\beta}\right)\left(\frac{\lambda}{\lambda+1}\right)\left\{\cos[2\phi]\left(\frac{Q_3-Q_4}{Q_1+Q_2}\right)-\sin(2\phi)\right\}+\left(\frac{1-\beta}{1+\beta}\right)\left(\frac{Q_3-Q_4}{Q_1+Q_2}\right) \\ -\left(\frac{2\beta}{1+\beta}\right)\left(\frac{\lambda}{\lambda+1}\right)\left\{\sin[2\phi]\left(\frac{Q_3-Q_4}{Q_1+Q_2}\right)+\cos[2\phi]\right\}-\left(\frac{1-\beta}{1+\beta}\right)\left(\frac{\lambda-1}{\lambda+1}\right) \\ -\frac{Q_3-Q_4}{Q_1+Q_2} \\ 1 \end{Bmatrix} C_{2,4} \tag{4.81}$$

$$V_C^1=[M_{2\mathrm{II}}(\lambda,\phi,\alpha,\beta)]V_C^2 \tag{4.82}$$

$$V_C^3=[M_{2\mathrm{II}}(\lambda,\phi-\pi,\alpha,\beta)]V_C^2 \tag{4.83}$$

The functional variables Q_1, Q_2, Q_3, Q_4 can be found in equations (4.4-4.7).

The corresponding vector in the solution system for the complex singularity has the same form as the previous case. The dimension of the vector V_C^j is 4×1 as well, but all the items are evaluated in the field of complex number.

4.4 Anti-Plane Asymptotic Field

It has been discussed that the asymptotic field under anti-plane loading can be derived using the similar stragtegy based on the linear matrix system. The singularity for Mode-III arises as a single real dominant root. So it's relatively simple to find the relationship between K_{III} and the field constants. The characteristic matrix is built in a form of 6-by-6 matrix.

$$\begin{bmatrix} \cos(\lambda\pi) & -\sin(\lambda\pi) & 0 & 0 & 0 & 0 \\ 0 & 0 & 0 & 0 & \cos(\lambda\pi) & \sin(\lambda\pi) \\ \cos(\lambda\phi) & -\sin(\lambda\phi) & -\kappa\cos(\lambda\phi) & \kappa\sin(\lambda\phi) & 0 & 0 \\ \sin(\lambda\phi) & \cos(\lambda\phi) & -\sin(\lambda\phi) & -\cos(\lambda\phi) & 0 & 0 \\ 0 & 0 & \kappa\cos[\lambda(\phi-\pi)] & -\kappa\sin[\lambda(\phi-\pi)] & -\cos[\lambda(\phi-\pi)] & \sin[\lambda(\phi-\pi)] \\ 0 & 0 & \sin[\lambda(\phi-\pi)] & \cos[\lambda(\phi-\pi)] & -\sin[\lambda(\phi-\pi)] & -\cos[\lambda(\phi-\pi)] \end{bmatrix} \tag{4.84}$$

where $\kappa = \mu_2/\mu_1$ is the ratio of shear moduli. After appropriate row reductions, the relationship between the to-be-determined field constants can be represented as

$$\begin{Bmatrix} C_{1,1} \\ C_{1,2} \end{Bmatrix} = \begin{bmatrix} (1-\kappa)\sin^2(\lambda\phi)+\kappa & (1-\kappa)\sin(\lambda\phi)\cos(\lambda\phi) \\ (1-\kappa)\sin(\lambda\phi)\cos(\lambda\phi) & (1-\kappa)\cos^2(\lambda\phi)+\kappa \end{bmatrix} \begin{Bmatrix} C_{2,1} \\ C_{2,2} \end{Bmatrix} \tag{4.85}$$

$$\begin{Bmatrix} C_{3,1} \\ C_{3,2} \end{Bmatrix} = \begin{bmatrix} (1-\kappa)\sin^2(\lambda\phi)+\kappa & (1-\kappa)\sin(\lambda\phi)\cos(\lambda\phi) \\ (1-\kappa)\sin(\lambda\phi)\cos(\lambda\phi) & (1-\kappa)\cos^2(\lambda\phi)+\kappa \end{bmatrix} \Big| \phi = \phi - \pi \begin{bmatrix} C_{2,1} \\ C_{2,2} \end{bmatrix} \tag{4.86}$$

Then the characteristic matrix is reduced to a 2-by-2 form

$$\begin{bmatrix} (1-\kappa)\sin(\lambda\phi)\sin(\lambda\phi-\lambda\pi)+\kappa\cos(\lambda\pi) & (1-\kappa)\cos(\lambda\phi)\sin(\lambda\phi-\lambda\pi)-\kappa\sin(\lambda\pi) \\ 0 & (1+\kappa)\sin(\lambda\pi) \end{bmatrix}$$

For the purpose of finding singular dominant roots, the following equation must to be satisfied

$$(1-\kappa)\sin(\lambda\phi)\sin(\lambda\phi-\lambda\pi)+\kappa\cos(\lambda\pi)=0 \tag{4.87}$$

which is just the characteristic equation for the anti-plane mode crack.

Obviously, the unknown constant $C_{2,1}$ has to be treated as the arbitrary of solution system. According to the definition of stress intensity factor in Mode-III, the expression of K_{III} in terms of $C_{2,1}$ is

$$K_{III} = \mu_2(2\pi)^{\frac{1}{2}}\lambda C_{2,1} \tag{4.88}$$

Using the chain rule, all the field constants can be represented in terms of K_{III} that

$$\begin{Bmatrix} C_{1,1} \\ C_{1,2} \\ C_{2,1} \\ C_{2,2} \\ C_{3,1} \\ C_{3,2} \end{Bmatrix} = \begin{bmatrix} (1-\mu_2/\mu_1)\sin^2(\lambda\phi)+\mu_2/\mu_1 \\ (1-\mu_2/\mu_1)\sin(\lambda\phi)\cos(\lambda\phi) \\ (1-\mu_2/\mu_2)\sin^2(\lambda\phi)+\mu_2/\mu_2 \\ (1-\mu_2/\mu_2)\sin(\lambda\phi)\cos(\lambda\phi) \\ (1-\mu_2/\mu_1)\sin^2(\lambda[\phi-\pi])+\mu_2/\mu_1 \\ (1-\mu_2/\mu_1)\sin(\lambda[\phi-\pi])\cos(\lambda[\phi-\pi]) \end{bmatrix} \mu_2^{-1}(2\pi)^{-\frac{1}{2}}\lambda^{-1}K_{III} \tag{4.89}$$

As a result, the out-of-plane displacement and the shear stresses can be represented by the following equations.

$$w = u_z(n,r,\theta) = \frac{r^{\lambda}(2\pi)^{\lambda-1}}{\lambda\mu_2}\{\sin(\lambda\theta) + (1-\mu_2/\mu_n)\cos(\lambda\phi^*)\sin(\lambda\phi^* - \lambda\theta)\}K_{III} \tag{4.90}$$

$$\tau_{rz}(n,r,\theta) = (\mu_n/\mu_2)(2\pi r)^{\lambda-1}\{\sin(\lambda\theta) + (1-\mu_2/\mu_n)\cos(\lambda\phi^*)\sin(\lambda\phi^* - \lambda\theta)\}K_{III} \tag{4.91}$$

$$\tau_{\theta z}(n,r,\theta) = (\mu_n/\mu_2)(2\pi r)^{\lambda-1}\{\cos(\lambda\theta) - (1-\mu_2/\mu_n)\cos(\lambda\phi^*)\cos(\lambda\phi^* - \lambda\theta)\}K_{III} \tag{4.92}$$

where the subscript "*n*" indicates geometrical zone in Figure 11. The phase angle ϕ^* in the trigonometric function is equal to the deflection angle of the interface ϕ as n = 1 or 2, and it should be replaced by $\phi - \pi$ for n =3.

The derivative of asymptotic displacements in Cartesian coordinates can be obtained using transformation operations.

$$\frac{\partial w}{\partial x} = \frac{\partial w}{\partial r}\frac{\partial r}{\partial x} + \frac{\partial w}{\partial \theta}\frac{\partial \theta}{\partial x} = \frac{\partial w}{\partial r}\cos(\theta) - \frac{1}{r}\frac{\partial w}{\partial \theta}\sin(\theta) \tag{4.93}$$

$$\frac{\partial w}{\partial y} = \frac{\partial w}{\partial r}\frac{\partial r}{\partial y} + \frac{\partial w}{\partial \theta}\frac{\partial \theta}{\partial y} = \frac{\partial w}{\partial r}\sin(\theta) + \frac{1}{r}\frac{\partial w}{\partial \theta}\cos(\theta) \tag{4.94}$$

$$\frac{\partial w}{\partial x} = \frac{r^{\lambda-1}}{\mu_2(2\pi)^{\frac{1}{2}}}\{(1-\mu_2/\mu_n)\cos(\lambda\phi)\sin(\lambda\phi - \lambda\theta + \theta) + \sin(\lambda\theta - \theta)\}K_{III} \tag{4.95}$$

$$\frac{\partial w}{\partial y} = \frac{r^{\lambda-1}}{\mu_2(2\pi)^{\frac{1}{2}}}\{-(1-\mu_2/\mu_n)\cos(\lambda\phi)\cos(\lambda\phi - \lambda\theta + \theta) + \cos(\lambda\theta - \theta)\}K_{III} \tag{4.96}$$

4.5 Particular Examples

Next, some particular cases are discussed to demonstrate the process of deriving the asymptotic field using the method provided in this study. The closed-forms are given for these simplified cases due to the symmetry nature.

4.5.1 Homogeneous Crack

For a homogeneous crack, the material mismatch vanishes and the Dundur's parameters are gone. As a result, the characteristic matrix (4.3) for the in-plane mode is simplified as

$$[M_{\mathrm{II}}(\lambda,\phi,0,0)]_{4\times4}=\begin{bmatrix}1 & 0 & 1 & 0\\ 0 & 1 & 0 & -\frac{1}{3}\\ 0 & 0 & 0 & \cos(\lambda\pi)\\ 0 & 0 & \cos(\lambda\pi) & 0\end{bmatrix} \tag{4.97}$$

Letting the determinant be zero gives the reduced form of the characteristic equation

$$[\cos(\lambda\pi)]^2=0 \tag{4.98}$$

And the strength of singularity is well-known as an half. Obviously the rank of the characteristic matrix is equal to two. Taking $C_{2,3}, C_{2,4}$ as arbitrary variables, after some proper linear operations, the field constants of Zone-II are represented as

$$\begin{Bmatrix}C_{2,1}\\ C_{2,2}\\ C_{2,3}\\ C_{2,4}\end{Bmatrix}=\{V_C\}_{4\times2}\{C_{2,j}\}_{2\times1}=\begin{Bmatrix}-1 & 0\\ 0 & \frac{1}{3}\\ 1 & 0\\ 0 & 1\end{Bmatrix}\begin{Bmatrix}C_{2,3}\\ C_{2,4}\end{Bmatrix} \tag{4.99}$$

The relationship matrix is expressed in a reduced form that

$$[M_{2II}(\lambda,\phi,0,0)]_{4\times4}=\begin{bmatrix}1 & 0 & 0 & 0\\ 0 & 1 & 0 & 0\\ 0 & 0 & 1 & 0\\ 0 & 0 & 0 & 1\end{bmatrix} \tag{4.100}$$

This unit matrix denotes that all those three geometric zones have equivalent stress and displacement fields. Then all the twelve field constants can be expressed in terms of $C_{2,3}, C_{2,4}$ that

$$\begin{Bmatrix}C_{1,1}\\ C_{1,2}\\ C_{1,3}\\ C_{1,4}\end{Bmatrix}=\begin{Bmatrix}C_{2,1}\\ C_{2,2}\\ C_{2,3}\\ C_{2,4}\end{Bmatrix}=\begin{Bmatrix}C_{3,1}\\ C_{3,2}\\ C_{3,3}\\ C_{3,4}\end{Bmatrix}=\begin{Bmatrix}-1 & 0\\ 0 & \frac{1}{3}\\ 1 & 0\\ 0 & 1\end{Bmatrix}\begin{Bmatrix}C_{2,3}\\ C_{2,4}\end{Bmatrix} \tag{4.101}$$

The corresponding field matrices and vectors are also obtained using the specific values

$$V_{TF} = \left\{\sin\left(\frac{3}{2}\theta\right) \quad \cos\left(\frac{3}{2}\theta\right) \quad \sin\left(-\frac{1}{2}\theta\right) \quad \cos\left(-\frac{1}{2}\theta\right)\right\} \tag{4.102}$$

$$M_{SR} = \begin{bmatrix} -3/4 & 0 & 0 & 0 \\ 0 & -3/4 & 0 & 0 \\ 0 & 0 & 5/4 & 0 \\ 0 & 0 & 0 & 5/4 \end{bmatrix} \tag{4.103}$$

$$M_{ST} = \begin{bmatrix} 3/4 & 0 & 0 & 0 \\ 0 & 3/4 & 0 & 0 \\ 0 & 0 & 3/4 & 0 \\ 0 & 0 & 0 & 3/4 \end{bmatrix} \tag{4.104}$$

$$M_{SRT} = \begin{bmatrix} 0 & 3/4 & 0 & 0 \\ -3/4 & 0 & 0 & 0 \\ 0 & 0 & 0 & -1/4 \\ 0 & 0 & 1/4 & 0 \end{bmatrix} \tag{4.105}$$

$$M_{UR} = -\frac{1}{2\mu_n}\begin{bmatrix} 3/2 & 0 & 0 & 0 \\ 0 & 3/2 & 0 & 0 \\ 0 & 0 & (1/2-\eta_n) & 0 \\ 0 & 0 & 0 & (1/2-\eta_n) \end{bmatrix} \tag{4.106}$$

$$M_{UT} = -\frac{1}{2\mu_n}\begin{bmatrix} 0 & -3/2 & 0 & 0 \\ 3/2 & 0 & 0 & 0 \\ 0 & 0 & 0 & -(1/2+\eta_n) \\ 0 & 0 & (1/2+\eta_n) & 0 \end{bmatrix} \tag{4.107}$$

Next, according to the definition of split singularities, K_I and K_{II} can be expressed as

$$K_I = V_{TF}|_{\theta=0} * M_{ST} * \begin{pmatrix} -1 & 0 \\ 0 & \frac{1}{3} \\ 1 & 0 \\ 0 & 1 \end{pmatrix} \begin{Bmatrix} C_{2,3} \\ C_{2,4} \end{Bmatrix} = \{0 \quad 1\} \begin{Bmatrix} C_{2,3} \\ C_{2,4} \end{Bmatrix} \tag{4.108}$$

$$K_{II} = V_{TF}|_{\theta=0} * M_{SRT} * \begin{pmatrix} -1 & 0 \\ 0 & \frac{1}{3} \\ 1 & 0 \\ 0 & 1 \end{pmatrix} \begin{Bmatrix} C_{2,3} \\ C_{2,4} \end{Bmatrix} = \{1 \quad 0\} \begin{Bmatrix} C_{2,3} \\ C_{2,4} \end{Bmatrix} \tag{4.109}$$

Using the inverse matrix and substituting into equation (4.101) gives the expression of field constants in terms of K_I and K_{II}

$$\begin{Bmatrix} C_{2,3} \\ C_{2,4} \end{Bmatrix} = \begin{bmatrix} 0 & 1 \\ 1 & 0 \end{bmatrix} \begin{Bmatrix} K_I \\ K_{II} \end{Bmatrix} \tag{4.110}$$

$$\begin{Bmatrix} C_{1,1} \\ C_{1,2} \\ C_{1,3} \\ C_{1,4} \end{Bmatrix} = \begin{Bmatrix} C_{2,1} \\ C_{2,2} \\ C_{2,3} \\ C_{2,4} \end{Bmatrix} = \begin{Bmatrix} C_{3,1} \\ C_{3,2} \\ C_{3,3} \\ C_{3,4} \end{Bmatrix} = \begin{bmatrix} 0 & -1 \\ \frac{1}{3} & 0 \\ 0 & 1 \\ 1 & 0 \end{bmatrix} \begin{Bmatrix} K_I \\ K_{II} \end{Bmatrix} \tag{4.111}$$

Next, the angular functions in the field expression with respect to the real split singularities are found by combining equation (4.102-4.107, 4.111) into (4.67-4.71)

$$\Sigma_{\sigma r}^{I}(\theta) = -\frac{1}{4}\cos\left(\frac{3}{2}\theta\right) + \frac{5}{4}\cos\left(\frac{1}{2}\theta\right) \tag{4.112}$$

$$\Sigma_{\sigma r}^{II}(\theta) = \frac{3}{4}\sin\left(\frac{3}{2}\theta\right) - \frac{5}{4}\sin\left(\frac{1}{2}\theta\right) \tag{4.113}$$

$$\Sigma_{\sigma\theta}^{I}(\theta) = \frac{1}{4}\cos\left(\frac{3}{2}\theta\right) + \frac{3}{4}\cos\left(\frac{1}{2}\theta\right) \tag{4.114}$$

$$\Sigma_{\sigma\theta}^{II}(\theta) = -\frac{3}{4}\sin\left(\frac{3}{2}\theta\right) - \frac{3}{4}\sin\left(\frac{1}{2}\theta\right) \tag{4.115}$$

$$\Sigma_{\sigma r\theta}^{I}(\theta) = \frac{1}{4}\sin\left(\frac{3}{2}\theta\right) - \frac{1}{4}\sin\left(\frac{1}{2}\theta\right) \tag{4.116}$$

$$\Sigma_{\sigma r\theta}^{II}(\theta) = \frac{3}{4}\cos\left(\frac{3}{2}\theta\right) + \frac{1}{4}\cos\left(\frac{1}{2}\theta\right) \tag{4.117}$$

$$\Sigma_{ur}^{I}(\theta) = -\frac{1}{2\mu_n}\left\{\frac{1}{2}\cos\left(\frac{3}{2}\theta\right) + \left(\frac{1}{2} - \eta_n\right)\cos\left(\frac{1}{2}\theta\right)\right\} \tag{4.118}$$

$$\Sigma_{ur}^{II}(\theta) = -\frac{1}{2\mu_n}\left\{-\frac{3}{2}\sin\left(\frac{3}{2}\theta\right) + \left(\frac{1}{2} - \eta_n\right)\sin\left(-\frac{1}{2}\theta\right)\right\} \tag{4.119}$$

$$\Sigma_{u\theta}^{I}(\theta) = -\frac{1}{2\mu_n}\left\{-\frac{1}{2}\sin\left(\frac{3}{2}\theta\right) + \left(\frac{1}{2} + \eta_n\right)\sin\left(\frac{1}{2}\theta\right)\right\} \tag{4.120}$$

$$\Sigma_{u\theta}^{II}(\theta) = -\frac{1}{2\mu_n}\left\{-\frac{3}{2}\cos\left(\frac{3}{2}\theta\right) + \left(\frac{1}{2} + \eta_n\right)\cos\left(\frac{1}{2}\theta\right)\right\} \tag{4.121}$$

These functions coincide with the solution given by Sun [52].

To get the asymptotic terms in the Cartesian coordinates, the polar displacement fields need to be transformed using the rotation direction cosines. Then we get that

$$\bar{f}_1 = \left(\frac{r}{2\pi}\right)^{\frac{1}{2}} \{\cos(\theta)\, \Sigma^I_{ur}(\theta) - \sin(\theta)\, \Sigma^I_{u\theta}(\theta)\} \tag{4.122}$$

$$= \frac{1}{2\mu_n}\left(\frac{r}{2\pi}\right)^{\frac{1}{2}} \left\{-\frac{1}{2}\cos\left(\frac{3}{2}\theta\right) + \left(\eta_n - \frac{1}{2}\right)\cos\left(\frac{1}{2}\theta\right)\right\}$$

$$\bar{g}_1 = \left(\frac{r}{2\pi}\right)^{\frac{1}{2}} \{\cos(\theta)\, \Sigma^{II}_{ur}(\theta) - \sin(\theta)\, \Sigma^{II}_{u\theta}(\theta)\} \tag{4.123}$$

$$= \frac{1}{2\mu_n}\left(\frac{r}{2\pi}\right)^{\frac{1}{2}} \left\{\frac{1}{2}\sin\left(\frac{3}{2}\theta\right) + \left(\eta_n + \frac{3}{2}\right)\cos\left(\frac{1}{2}\theta\right)\right\}$$

$$\bar{f}_2 = \left(\frac{r}{2\pi}\right)^{\frac{1}{2}} \{\sin(\theta)\, \Sigma^I_{ur}(\theta) + \cos(\theta)\, \Sigma^I_{u\theta}(\theta)\} \tag{4.124}$$

$$= \frac{1}{2\mu_n}\left(\frac{r}{2\pi}\right)^{\frac{1}{2}} \left\{-\frac{1}{2}\sin\left(\frac{3}{2}\theta\right) + \left(\eta_n + \frac{1}{2}\right)\sin\left(\frac{1}{2}\theta\right)\right\}$$

$$\bar{g}_2 = \left(\frac{r}{2\pi}\right)^{\frac{1}{2}} \{\sin(\theta)\, \Sigma^{II}_{ur}(\theta) + \cos(\theta)\, \Sigma^{II}_{u\theta}(\theta)\} \tag{4.125}$$

$$= \frac{1}{2\mu_n}\left(\frac{r}{2\pi}\right)^{\frac{1}{2}} \left\{-\frac{1}{2}\cos\left(\frac{3}{2}\theta\right) + \left(\frac{3}{2} - \eta_n\right)\cos\left(\frac{1}{2}\theta\right)\right\}$$

The strength of singularity for anti-plane mode is nothing but 1/2. Then the corresponding enriched terms is obtained directly by simplifying equation (4.90)

$$\bar{h} = \left(\frac{r}{2\pi}\right)^{\frac{1}{2}} \frac{2}{\mu}\sin\left(\frac{\theta}{2}\right) \tag{4.126}$$

These results agree with the solution by Ayhan and Nied[48].

4.5.2 Interface Crack

As the inclination angle of interface ϕ is equal to π, the geometry in Figure 11 represents an interfacial crack between dissimilar media. The characteristic equation is reduced to

$$\begin{bmatrix} 1 & 0 & \left(\frac{\lambda}{1+\lambda}\right)+\left(\frac{1-\beta}{1+\beta}\right)\left(\frac{1}{1+\lambda}\right) & 0 \\ 0 & 1 & 0 & \frac{\lambda}{1+\lambda}-\frac{1}{1+\lambda}\left(\frac{1-\beta}{1+\beta}\right) \\ 0 & 0 & \sin(\lambda\pi)\left(\frac{\beta}{1-\beta}\right) & \cos(\lambda\pi)\left(\frac{1}{1-\beta}\right) \\ 0 & 0 & \cos(\lambda\pi)\left(\frac{1}{1-\beta}\right) & -\sin(\lambda\pi)\left(\frac{\beta}{1-\beta}\right) \end{bmatrix} \tag{4.127}$$

Then the characteristic equation is obtained from the determinant of this matrix which should be equal to zero

$$\sin^2(\lambda\pi)\left(\frac{\beta}{1-\beta}\right)^2+\cos^2(\lambda\pi)\left(\frac{1}{1-\beta}\right)^2=0 \tag{4.128}$$

Or

$$(1-\beta^2)\cos^2(\lambda\pi)+\beta^2=0 \tag{4.129}$$

which leads to the dominant roots of the characteristic equation represented in a closed form

$$\lambda_{1,2}=\frac{1}{2}\pm\frac{i}{2\pi}\ln\left(\frac{1-\beta}{1+\beta}\right) \tag{4.130}$$

If imaginary part is symbolized as ε, then the following equation is not hard to be derived

$$\frac{1-\beta}{1+\beta}=e^{2\pi\varepsilon} \tag{4.131}$$

In this situation, the rank of matrix is equal to 3, and the asymptotic field should be formed in terms of only one arbitrary constant, e.g., $C_{2,4}$. Since these two complex singularities are conjugated to each other, only the case of $\lambda=\lambda_1$ is considered in the following discussion. Substituting equation (4.131) into the characteristic matrix and applying appropriate row deductions gives the expressions for the four field variables of material zone II

$$\begin{Bmatrix} C_{2,1} \\ C_{2,2} \\ C_{2,3} \\ C_{2,4} \end{Bmatrix}=\begin{Bmatrix} \left(\frac{e^{2\pi\varepsilon}+\lambda}{1+\lambda}\right)i \\ \left(\frac{e^{2\pi\varepsilon}-\lambda}{1+\lambda}\right) \\ -i \\ 1 \end{Bmatrix} C_{2,4} \tag{4.132}$$

As the inclined angle of interface stops at $\phi = \pi$, the geometric zone I in the sketch vanishes. The bonded border is only extended along the direction of $\phi - \pi = 0$. Then the relationship matrix is reduced to

$$\begin{bmatrix} -\left(\frac{\beta-\alpha}{1+\alpha}\right)\lambda + \left(\frac{1+\beta}{1+\alpha}\right) & 0 & \left(\frac{\beta-\alpha}{1+\alpha}\right)(1-\lambda) - \left(\frac{2\beta}{1+\alpha}\right)\left(\frac{1-\lambda}{1+\lambda}\right) & 0 \\ 0 & \left(\frac{\beta-\alpha}{1+\alpha}\right)\lambda + \left(\frac{1+\beta}{1+\alpha}\right) & 0 & -\left(\frac{\beta-\alpha}{1+\alpha}\right)(1-\lambda) + \left(\frac{2\beta}{1+\alpha}\right) \\ \left(\frac{\beta-\alpha}{1+\alpha}\right)(1+\lambda) & 0 & \left(\frac{\beta-\alpha}{1+\alpha}\right)\lambda + \left(\frac{1-\beta}{1+\alpha}\right) & 0 \\ 0 & -\left(\frac{\beta-\alpha}{1+\alpha}\right)(1+\lambda) & 0 & -\left(\frac{\beta-\alpha}{1+\alpha}\right)\lambda + \left(\frac{1-\beta}{1+\alpha}\right) \end{bmatrix} \tag{4.133}$$

After appropriate matrix operations, the fields constants of the other material zones are generated in terms of $C_{2,4}$ that

$$\begin{Bmatrix} C_{3,1} \\ C_{3,2} \\ C_{3,3} \\ C_{3,4} \end{Bmatrix} = \begin{Bmatrix} i\left(\frac{1+\lambda e^{2\pi\varepsilon}}{1+\lambda}\right) \\ \left(\frac{1-\lambda e^{2\pi\varepsilon}}{1+\lambda}\right) \\ -ie^{2\pi\varepsilon} \\ e^{2\pi\varepsilon} \end{Bmatrix} C_{2,4} \tag{4.134}$$

The corresponding field matrices and vectors for the interface crack are given as below

$$V_{TF} = \left\{\sin\left[\left(\frac{3}{2}+i\varepsilon\right)\theta\right] \quad \cos\left[\left(\frac{3}{2}+i\varepsilon\right)\theta\right] \quad \sin\left[\left(-\frac{1}{2}+i\varepsilon\right)\theta\right] \quad \cos\left[\left(-\frac{1}{2}+i\varepsilon\right)\theta\right]\right\} \tag{4.135}$$

$$M_{SR} = \begin{bmatrix} -\left(\frac{3}{4}-\varepsilon^2+2i\varepsilon\right) & 0 & 0 & 0 \\ 0 & -\left(\frac{3}{4}-\varepsilon^2+2i\varepsilon\right) & 0 & 0 \\ 0 & 0 & \left(\frac{5}{4}+\varepsilon^2+2i\varepsilon\right) & 0 \\ 0 & 0 & 0 & \left(\frac{5}{4}+\varepsilon^2+2i\varepsilon\right) \end{bmatrix} \tag{4.136}$$

$$M_{ST} = \begin{bmatrix} \left(\frac{3}{4}-\varepsilon^2+2i\varepsilon\right) & 0 & 0 & 0 \\ 0 & \left(\frac{3}{4}-\varepsilon^2+2i\varepsilon\right) & 0 & 0 \\ 0 & 0 & \left(\frac{3}{4}-\varepsilon^2+2i\varepsilon\right) & 0 \\ 0 & 0 & 0 & \left(\frac{3}{4}-\varepsilon^2+2i\varepsilon\right) \end{bmatrix} \tag{4.137}$$

$$M_{SRT} = \begin{bmatrix} 0 & \left(\frac{3}{4} - \varepsilon^2 + 2i\varepsilon\right) & 0 & 0 \\ -\left(\frac{3}{4} - \varepsilon^2 + 2i\varepsilon\right) & 0 & 0 & 0 \\ 0 & 0 & 0 & -\left(\frac{1}{4} + \varepsilon^2\right) \\ 0 & 0 & \left(\frac{1}{4} + \varepsilon^2\right) & 0 \end{bmatrix} \tag{4.138}$$

$$M_{UR} = -\frac{1}{2\mu_n}\begin{bmatrix} \left(\frac{3}{4} - \varepsilon^2 + 2i\varepsilon\right) & 0 & 0 & 0 \\ 0 & \left(\frac{3}{4} - \varepsilon^2 + 2i\varepsilon\right) & 0 & 0 \\ 0 & 0 & \left(\frac{1}{2} - \varepsilon^2 + i\varepsilon - \eta_n\right) & 0 \\ 0 & 0 & 0 & \left(\frac{1}{2} - \varepsilon^2 + i\varepsilon - \eta_n\right) \end{bmatrix} \tag{4.139}$$

$$M_{UT} = \frac{-1}{2\mu_n}\begin{bmatrix} 0 & -\left(\frac{3}{4} - \varepsilon^2 + 2i\varepsilon\right) & 0 & 0 \\ \left(\frac{3}{4} - \varepsilon^2 + 2i\varepsilon\right) & 0 & 0 & 0 \\ 0 & 0 & 0 & \left(\varepsilon^2 - i\varepsilon - \eta_n - \frac{1}{2}\right) \\ 0 & 0 & \left(\frac{1}{2} - \varepsilon^2 + i\varepsilon + \eta_n\right) & 0 \end{bmatrix} \tag{4.140}$$

The definition of complex stress intensity factor $K = K_1 + iK_2$ is related to the complex-valued opening tensile stress and in-plane shear stress ahead of the crack-tip with respect to $\lambda = \lambda_1$. Their matriculated forms are given as

$$\begin{aligned} \sigma_{\theta\theta}(2, r, 0) &= r^{\lambda-1}\{V_{TF}\}_{1\times4}[M_{ST}]_{4\times4}\{V_C\}_{4\times1}\{C_{2,j}\}_{1\times1} = r^{\lambda-1}\lambda\left(\frac{2}{1+\beta}\right)C_{2,4} \\ \tau_{r\theta}(2, r, 0) &= r^{\lambda-1}\{V_{TF}\}_{1\times4}[M_{SRT}]_{4\times4}\{V_C\}_{4\times1}\{C_{2,j}\}_{1\times1} = -ir^{\lambda-1}\lambda\left(\frac{2}{1+\beta}\right)C_{2,4} \end{aligned} \tag{4.141}$$

Then complex *K* is expressed in terms of $C_{2,4}$

$$Kr^{\lambda-1} = \sigma_{\theta\theta}(2, r, 0) + i\tau_{r\theta}(2, r, 0) = 2r^{\lambda-1}\lambda\left(\frac{2}{1+\beta}\right)C_{2,4} \tag{4.142}$$

Or

$$K = \lambda\left(\frac{4}{1+\beta}\right)C_{2,4} = \lambda\left[\frac{4\cosh(\pi\varepsilon)}{e^{-\pi\varepsilon}}\right]C_{2,4} \tag{4.143}$$

As a result, the complex-defined SIF is converted as the arbitrary unknown for the asymptotic field. All the other field constants have the form that

$$\begin{Bmatrix} C_{2,1} \\ C_{2,2} \\ C_{2,3} \\ C_{2,4} \end{Bmatrix} = \begin{Bmatrix} \left(\frac{e^{2\pi\varepsilon}+\lambda}{1+\lambda}\right)i \\ \left(\frac{e^{2\pi\varepsilon}-\lambda}{1+\lambda}\right) \\ -i \\ 1 \end{Bmatrix} \left[\frac{e^{-\pi\varepsilon}}{4\lambda\cosh(\pi\varepsilon)}\right] K \tag{4.144}$$

$$\begin{Bmatrix} C_{3,1} \\ C_{3,2} \\ C_{3,3} \\ C_{3,4} \end{Bmatrix} = \begin{Bmatrix} \left(\frac{1+\lambda e^{2\pi\varepsilon}}{1+\lambda}\right)i \\ \left(\frac{1-\lambda e^{2\pi\varepsilon}}{1+\lambda}\right) \\ -ie^{2\pi\varepsilon} \\ e^{2\pi\varepsilon} \end{Bmatrix} \left[\frac{e^{-\pi\varepsilon}}{4\lambda\cosh(\pi\varepsilon)}\right] K \tag{4.145}$$

After algebraic operations, the angular functions in the field expression with respect to the complex singularities are given as below (eqn. 4.146-4.155).

$$\Sigma^R_{\sigma r}(n,\theta) = -\frac{e^{-\varepsilon\theta^*}}{4\cosh(\pi\varepsilon)}\left[\cos\left(\frac{3\theta}{2}\right)\right] + \frac{e^{\varepsilon\theta^*}}{4\cosh(\pi\varepsilon)}\left[\frac{1}{2}\cos\left(\frac{3\theta}{2}\right) + \varepsilon\sin\left(\frac{3\theta}{2}\right) + \frac{5}{2}\cos\left(\frac{\theta}{2}\right) + \varepsilon\sin\left(\frac{\theta}{2}\right)\right]$$

$$\Sigma^I_{\sigma r}(n,\theta) = -\frac{e^{-\varepsilon\theta^*}}{4\cosh(\pi\varepsilon)}\left[\sin\left(\frac{3\theta}{2}\right)\right] + \frac{e^{\varepsilon\theta^*}}{4\cosh(\pi\varepsilon)}\left[-\frac{1}{2}\sin\left(\frac{3\theta}{2}\right) + \varepsilon\cos\left(\frac{3\theta}{2}\right) + \frac{5}{2}\sin\left(\frac{\theta}{2}\right) - \varepsilon\cos\left(\frac{\theta}{2}\right)\right]$$

$$\Sigma^R_{\sigma\theta}(n,\theta) = \frac{e^{-\varepsilon\theta^*}}{4\cosh(\pi\varepsilon)}\left[\cos\left(\frac{3\theta}{2}\right)\right] + \frac{e^{\varepsilon\theta^*}}{4\cosh(\pi\varepsilon)}\left[-\frac{1}{2}\cos\left(\frac{3\theta}{2}\right) - \varepsilon\sin\left(\frac{3\theta}{2}\right) + \frac{3}{2}\cos\left(\frac{\theta}{2}\right) - \varepsilon\sin\left(\frac{\theta}{2}\right)\right]$$

$$\Sigma^I_{\sigma\theta}(n,\theta) = \frac{e^{-\varepsilon\theta^*}}{4\cosh(\pi\varepsilon)}\left[\sin\left(\frac{3\theta}{2}\right)\right] + \frac{e^{\varepsilon\theta^*}}{4\cosh(\pi\varepsilon)}\left[\frac{1}{2}\sin\left(\frac{3\theta}{2}\right) - \varepsilon\cos\left(\frac{3\theta}{2}\right) + \frac{3}{2}\sin\left(\frac{\theta}{2}\right) + \varepsilon\cos\left(\frac{\theta}{2}\right)\right]$$

$$\Sigma^R_{\sigma r\theta}(n,\theta) = \frac{e^{-\varepsilon\theta^*}}{4\cosh(\pi\varepsilon)}\left[\sin\left(\frac{3\theta}{2}\right)\right] + \frac{e^{\varepsilon\theta^*}}{4\cosh(\pi\varepsilon)}\left[-\frac{1}{2}\sin\left(\frac{3\theta}{2}\right) + \varepsilon\cos\left(\frac{3\theta}{2}\right) + \frac{1}{2}\sin\left(\frac{\theta}{2}\right) - \varepsilon\cos\left(\frac{\theta}{2}\right)\right]$$

$$\Sigma^I_{\sigma r\theta}(n,\theta) = \frac{e^{-\varepsilon\theta^*}}{4\cosh(\pi\varepsilon)}\left[-\cos\left(\frac{3\theta}{2}\right)\right] + \frac{e^{\varepsilon\theta^*}}{4\cosh(\pi\varepsilon)}\left[-\frac{1}{2}\cos\left(\frac{3\theta}{2}\right) - \varepsilon\sin\left(\frac{3\theta}{2}\right) - \frac{1}{2}\cos\left(\frac{\theta}{2}\right) - \varepsilon\sin\left(\frac{\theta}{2}\right)\right]$$

$$\Sigma^R_{ur}(n,\theta) = -\frac{e^{-\varepsilon\theta^*}}{8\mu_n\left(\frac{1}{4}+\varepsilon^2\right)\cosh(\pi\varepsilon)}\left[\frac{1}{2}\cos\left(\frac{3\theta}{2}\right) + \varepsilon\sin\left(\frac{3\theta}{2}\right)\right] - \frac{e^{\varepsilon\theta^*}}{8\mu_n\cosh(\pi\varepsilon)}\left[-\cos\left(\frac{3\theta}{2}\right) + \cos\left(\frac{\theta}{2}\right)\right]$$

$$+\frac{\eta_n e^{\varepsilon\theta^*}}{8\mu_n\left(\frac{1}{4}+\varepsilon^2\right)\cosh(\pi\varepsilon)}\left[\frac{1}{2}\cos\left(\frac{\theta}{2}\right) + \varepsilon\sin\left(\frac{\theta}{2}\right)\right]$$

$$\Sigma_{ur}^{I}(n,\theta) = -\frac{e^{-\varepsilon\theta^*}}{8\mu_n\left(\frac{1}{4}+\varepsilon^2\right)\cosh(\pi\varepsilon)}\left[\frac{1}{2}\sin\left(\frac{3\theta}{2}\right)-\varepsilon\cos\left(\frac{3\theta}{2}\right)\right]-\frac{e^{\varepsilon\theta^*}}{8\mu_n\cosh(\pi\varepsilon)}\left[\sin\left(\frac{3\theta}{2}\right)+\sin\left(\frac{\theta}{2}\right)\right]$$

$$+\frac{\eta_n e^{\varepsilon\theta^*}}{8\mu_n\left(\frac{1}{4}+\varepsilon^2\right)\cosh(\pi\varepsilon)}\left[\frac{1}{2}\sin\left(\frac{\theta}{2}\right)-\varepsilon\cos\left(\frac{\theta}{2}\right)\right]$$

$$\Sigma_{u\theta}^{R}(n,\theta) = -\frac{e^{-\varepsilon\theta^*}}{8\mu_n\left(\frac{1}{4}+\varepsilon^2\right)\cosh(\pi\varepsilon)}\left[-\frac{1}{2}\sin\left(\frac{3\theta}{2}\right)+\varepsilon\cos\left(\frac{3\theta}{2}\right)\right]-\frac{e^{\varepsilon\theta^*}}{8\mu_n\cosh(\pi\varepsilon)}\left[\sin\left(\frac{3\theta}{2}\right)+\sin\left(\frac{\theta}{2}\right)\right]$$

$$+\frac{\eta_n e^{\varepsilon\theta^*}}{8\mu_n\left(\frac{1}{4}+\varepsilon^2\right)\cosh(\pi\varepsilon)}\left[-\frac{1}{2}\sin\left(\frac{\theta}{2}\right)+\varepsilon\cos\left(\frac{\theta}{2}\right)\right]$$

$$\Sigma_{u\theta}^{I}(n,\theta) = -\frac{e^{-\varepsilon\theta^*}}{8\mu_n\left(\frac{1}{4}+\varepsilon^2\right)\cosh(\pi\varepsilon)}\left[\frac{1}{2}\cos\left(\frac{3\theta}{2}\right)+\varepsilon\sin\left(\frac{3\theta}{2}\right)\right]-\frac{e^{\varepsilon\theta^*}}{8\mu_n\cosh(\pi\varepsilon)}\left[\cos\left(\frac{3\theta}{2}\right)-\cos\left(\frac{\theta}{2}\right)\right]$$

$$+\frac{\eta_n e^{\varepsilon\theta^*}}{8\mu_n\left(\frac{1}{4}+\varepsilon^2\right)\cosh(\pi\varepsilon)}\left[\frac{1}{2}\cos\left(\frac{\theta}{2}\right)+\varepsilon\sin\left(\frac{\theta}{2}\right)\right]$$

In these equations,

$$\theta^* = \begin{cases}\theta-\pi & for\ \ n=2\\ \theta+\pi & for\ \ n=3\end{cases} \tag{4.153}$$

It can be noted that as ε vanishes, these angular functions are deduced to be as same as equations (4.112-4.121) which are specified for the homogeneous crack.

Similar with the prior case discussed for deriving the enriched terms, the coordinates transformation is applied to find the coefficients of *K* in the expression of asymptotic displacement fields.

$$\frac{\bar{f}_1}{2} = (2\pi)^{-\frac{1}{2}}\cos(\theta)\,Real\left[r^{\lambda}\Sigma_{ur}(n,\theta)\right]-(2\pi)^{-\frac{1}{2}}\sin(\theta)\,Real\left[r^{\lambda}\Sigma_{u\theta}(n,\theta)\right] \tag{4.153}$$

$$\frac{\bar{g}_1}{2} = (2\pi)^{-\frac{1}{2}}\cos(\theta)\,Imag\left[r^{\lambda}\Sigma_{ur}(n,\theta)\right]-(2\pi)^{-\frac{1}{2}}\sin(\theta)\,Imag\left[r^{\lambda}\Sigma_{u\theta}(n,\theta)\right] \tag{4.154}$$

$$\frac{\bar{f}_2}{2} = (2\pi)^{-\frac{1}{2}}\sin(\theta)\,Real\left[r^{\lambda}\Sigma_{ur}(n,\theta)\right]+(2\pi)^{-\frac{1}{2}}\cos(\theta)\,Real\left[r^{\lambda}\Sigma_{u\theta}(n,\theta)\right] \tag{4.155}$$

$$\frac{\bar{g}_2}{2} = (2\pi)^{-\frac{1}{2}}\sin(\theta)\,Imag\left[r^{\lambda}\Sigma_{ur}(n,\theta)\right]+(2\pi)^{-\frac{1}{2}}\cos(\theta)\,Imag\left[r^{\lambda}\Sigma_{u\theta}(n,\theta)\right] \tag{4.156}$$

Then the final solution for these enriched terms are found as below (eqn. 4.157-4.160)

$$\bar{f}_1(n) = -\frac{r^{\frac{1}{2}}(2\pi)^{-\frac{1}{2}}}{4\mu_n \cosh(\pi\varepsilon)}\left\{\frac{e^{-\varepsilon\theta^*}}{\frac{1}{4}+\varepsilon^2}\left[\frac{1}{2}\cos\left(\frac{\theta}{2}+\varepsilon\ln r\right)+\varepsilon\sin\left(\frac{\theta}{2}+\varepsilon\ln r\right)\right]+e^{\varepsilon\theta^*}\left[\cos\left(\frac{3\theta}{2}+\varepsilon\ln r\right)-\cos\left(\frac{\theta}{2}-\varepsilon\ln r\right)\right]\right.$$
$$\left.+\frac{e^{\varepsilon\theta^*}\eta_n}{\frac{1}{4}+\varepsilon^2}\left[-\frac{1}{2}\cos\left(\frac{\theta}{2}-\varepsilon\ln r\right)+\varepsilon\sin\left(\frac{\theta}{2}-\varepsilon\ln r\right)\right]\right\}$$

$$\bar{g}_1(n) = -\frac{r^{\frac{1}{2}}(2\pi)^{-\frac{1}{2}}}{4\mu_n \cosh(\pi\varepsilon)}\left\{\frac{e^{-\varepsilon\theta^*}}{\frac{1}{4}+\varepsilon^2}\left[\frac{1}{2}\sin\left(\frac{\theta}{2}+\varepsilon\ln r\right)-\varepsilon\cos\left(\frac{\theta}{2}+\varepsilon\ln r\right)\right]+e^{\varepsilon\theta^*}\left[\sin\left(\frac{3\theta}{2}+\varepsilon\ln r\right)+\sin\left(\frac{\theta}{2}-\varepsilon\ln r\right)\right]\right.$$
$$\left.+\frac{e^{\varepsilon\theta^*}\eta_n}{\frac{1}{4}+\varepsilon^2}\left[-\frac{1}{2}\sin\left(\frac{\theta}{2}-\varepsilon\ln r\right)+\varepsilon\cos\left(\frac{\theta}{2}-\varepsilon\ln r\right)\right]\right\}$$

$$\bar{f}_2(n) = -\frac{r^{\frac{1}{2}}(2\pi)^{-\frac{1}{2}}}{4\mu_n \cosh(\pi\varepsilon)}\left\{\frac{e^{-\varepsilon\theta^*}}{\frac{1}{4}+\varepsilon^2}\left[-\frac{1}{2}\sin\left(\frac{\theta}{2}+\varepsilon\ln r\right)+\varepsilon\cos\left(\frac{\theta}{2}+\varepsilon\ln r\right)\right]+e^{\varepsilon\theta^*}\left[\sin\left(\frac{\theta}{2}-\varepsilon\ln r\right)+\sin\left(\frac{3\theta}{2}+\varepsilon\ln r\right)\right]\right.$$
$$\left.+\frac{e^{\varepsilon\theta^*}\eta_n}{\frac{1}{4}+\varepsilon^2}\left[-\frac{1}{2}\sin\left(\frac{\theta}{2}-\varepsilon\ln r\right)-\varepsilon\cos\left(\frac{\theta}{2}-\varepsilon\ln r\right)\right]\right\}$$

$$\bar{g}_2(n) = -\frac{r^{\frac{1}{2}}(2\pi)^{-\frac{1}{2}}}{4\mu_n \cosh(\pi\varepsilon)}\left\{\frac{e^{-\varepsilon\theta^*}}{\frac{1}{4}+\varepsilon^2}\left[\frac{1}{2}\cos\left(\frac{\theta}{2}+\varepsilon\ln r\right)+\varepsilon\sin\left(\frac{\theta}{2}+\varepsilon\ln r\right)\right]+e^{\varepsilon\theta^*}\left[\cos\left(\frac{\theta}{2}-\varepsilon\ln r\right)-\cos\left(\frac{3\theta}{2}+\varepsilon\ln r\right)\right]\right.$$
$$\left.+\frac{e^{\varepsilon\theta^*}\eta_n}{\frac{1}{4}+\varepsilon^2}\left[\frac{1}{2}\cos\left(\frac{\theta}{2}-\varepsilon\ln r\right)+\varepsilon\sin\left(\frac{\theta}{2}-\varepsilon\ln r\right)\right]\right\}$$

The corresponding strength of singularity in Mode-III is equal to 1/2 again. Accordingly, the asymptotic terms are formulated by specifying and extracting from equation (4.90)

$$\bar{h}(n) = \left(\frac{r}{2\pi}\right)^{\frac{1}{2}}\frac{2}{\mu_n}\sin\left(\frac{\theta}{2}\right) \tag{4.161}$$

These formulas coincide with the equations given by Ayhan and Nied [48] for the interfacial crack.

5 Numerical Solutions

The formulations derived above are implemented into a specific finite element program. Then the enriched crack-tip element has the new features of solving the problem with an arbitrarily-oriented crack terminating at the interface. One representative example, a finite crack in the center area of a 2-D dissimilar media (Figure 24), is examined for various material combinations and different load patterns. The edges of this rectangular plate are applied with normal tensile stresses. The straight crack is terminating at a bonded interface. As the incidence angle varies, some specific cases are formed with distinct natures of dominant roots as discussed above. In this paper, different situations, perpendicular to the interface, lying along the interface or hitting the interface with an oblique angle are studied respectively. The stress intensity factors are computed simultaneously with other regular DOFs. Then they are normalized to be compared the existing solutions.

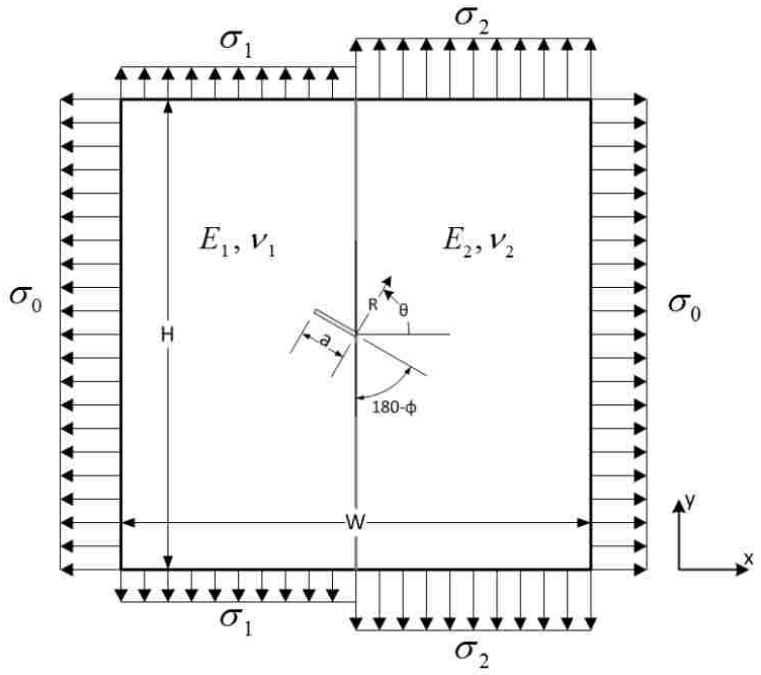

Figure 24: The geometry of a center crack terminating at the interface with an arbitrary incidence angle

To satisfy the continuity of the displacements across the interface, the remote loads have to meet particular requirements, which depend on the specific material combination. For the geometry

sketch of Figure 24 in the Cartesian coordinates, the normal strain components in y direction should be continuous across the bonded line that

$$\varepsilon_{yy}^{1} = \varepsilon_{yy}^{2}$$

As a result, the relationship between the remote normal stresses in y-direction can be generated for the plane stress and the plane strain conditions respectively that

$$\sigma_{yy}^{2} = \sigma_{yy}^{1}\frac{E_2}{E_1} + \sigma_x\left(\nu_2 - \frac{E_2}{E_1}\nu_1\right) \quad for\ plane\ stress \tag{5.1}$$

$$\sigma_{yy}^{2} = \frac{E_2(1-\nu_1^2)}{E_1(1-\nu_2^2)}\sigma_{yy}^{1} + \sigma_x\left(\frac{\nu_2}{1-\nu_2} - \frac{E_2(\nu_1+\nu_1^2)}{E_1(1-\nu_2^2)}\right) for\ plane\ strain \tag{5.2}$$

So in the finite element model, the applied stresses are specified differently for the material areas on either side of the interface.

5.1 Interface Crack

As $\phi = 0\ or\ \pi$, the general problem turns to a popular case with the crack coinciding with the interface (Figure 25). It should be noted that, for comparison, the dimensions of the finite plate and the crack are specified exactly as same as those adopted by other authors. The ratio of the crack length with the plate width is fixed as 1/10. The other specific properties can be found in Table 1. The plane stress condition is taken into account. The finite element model created in ANSYS can be checked in Figure 26.

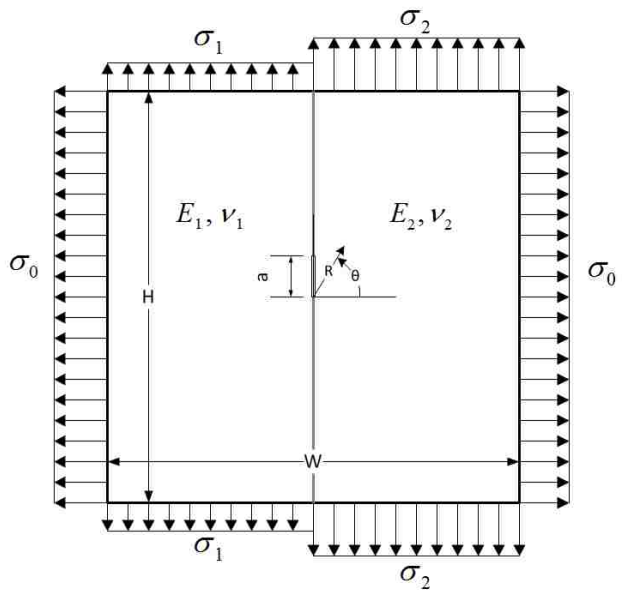

Figure 25: The geometry of a center crack lying on the interface

Definition of K	$K = K_I + iK_{II} = \lim_{r\to 0,\theta=0}\{(\sigma_{\theta\theta} + i\tau_{r\theta})(2\pi r)^{1-\lambda}\}$
Full/Half	Full
Wide	20in
Height	20in
Crack Length	2in
P.Strain/Stress	Plane Stress
Crack Mode	Mode I/II
Load	Varing loads (psi)

Table 1: The properties used for the finite element model of the interface crack

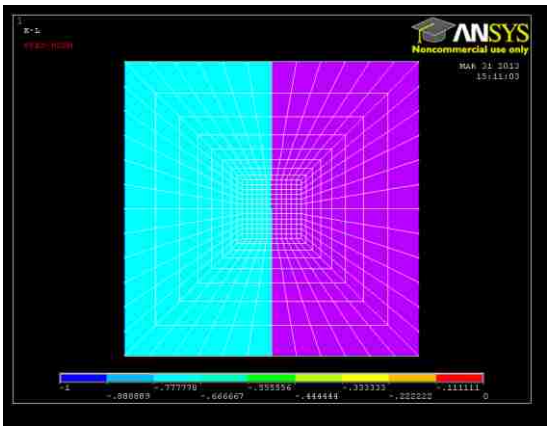

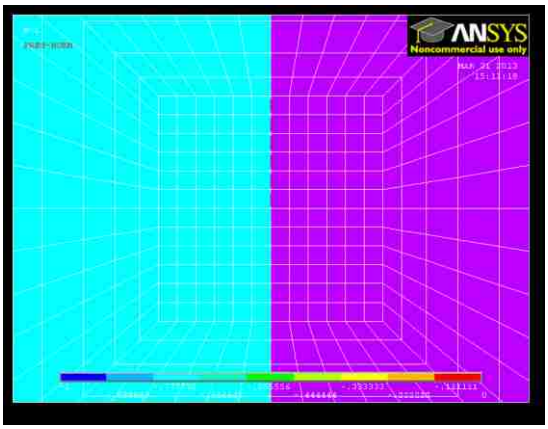

(a) Fit View (b) Close-up View

Figure 26: Finite element model of the interface crack in ANSYS

For the interface crack, since the singular fields in the vicinity of the crack tip are coupled, the coventional stress intensity factor was redefined with a complex by Rice and Sih [12] that

$$K^{RS} = K_I^{RS} + iK_{II}^{RS} = \lim_{r\to 0,\theta=0}\{(\sigma_{\theta\theta} + i\tau_{r\theta})2\sqrt{2}e^{\pi\varepsilon}\} \tag{5.3}$$

Hutchinson [18] introduced another representation of the complex stress intensity factor as

$$K^{H} = K_I^{H} + iK_{II}^{H} = \lim_{r\to 0,\theta=0}\{(\sigma_{\theta\theta} + i\tau_{r\theta})\sqrt{2\pi r}r^{i\varepsilon}\} \tag{5.4}$$

In this paper, all the results are converted to the latter form and the dimensions are unified to be compared. These different definitions can be related through a contant coefficient which reflects the distinction of the dimensions of K. Seven groups of material combinations are investigated for the interface crack, including a degenerated homogeneous case. For simplicity, the Young's modulus for the material zone 1 remains unchanged. The ratio of shear moduli is ranged from 1 to 1000 (Table 2). The remote loads are specified as desired to keep the continuous strains across the interface.

Case No.	$\frac{\mu_2}{\mu_1}$	E_1	E_2	ν_1	ν_2	σ_0	σ_1	σ_2
1	1.0	1.0	1.0	0.3	0.3	1.0	0.0	0.0
2	3.0	1.0	0.3333	0.3	0.3	1.0	1.0	0.53
3	10.0	1.0	0.1	0.3	0.3	1.0	1.0	0.37
4	23.1	1.0	0.045	0.3	0.35	1.0	1.0	0.38
5	100.0	1.0	0.01	0.3	0.3	1.0	1.0	0.31
6	144.2	1.0	0.0072	0.3	0.35	1.0	1.0	0.36
7	1000.0	1.0	0.001	0.3	0.3	1.0	1.0	0.3

Table 2: Material properties used for the interface crack model

The stress intensity factors of both crack-tips are tabulated as below (Tables 3 & 4). It can be observed that the results by the enriched finite element method are pretty close to the reference solutions [12, 21, 47]. The maximum error, around 5%, arises as the ratio of material properties becomes notable. It's not hard to be explained by the mismatch of the orders of magnitudes in

mathematical operations that originates from the large discrepancy of the material properties. The minor difference of SIF between the left and the right tips is thought of to come from the asymmetric geometry, of which only one end of the crack is located on the centroid of the plane.

	K_I^H				
$\frac{\mu_2}{\mu_1}$	EFM		Rice/Sih (EXACT)	Lin/Mar(FE)	Chen(FE)
	Left	Right			
1.0	1.78185	1.78267	1.772	1.790	1.809
3.0	1.79180	1.79234	1.778	1.795	1.822
10.0	1.80936	1.80924	1.791	1.804	1.847
23.1	1.81162	1.81145	1.792	1.804	1.851
100.0	1.82200	1.82121	1.798	1.810	1.864
144.2	1.81868	1.81769	1.797	1.805	1.860
1000.0	1.82194	1.82161	1.800	1.810	1.866

Table 3: Numerical results of the Mode-I stress intensity factors for the interface cracks

	K_{II}^H				
$\frac{\mu_2}{\mu_1}$	EFM		Rice/Sih (EXACT)	Lin/Mar(FE)	Chen(FE)
	Left	Right			
1.0	0.00200	0	0.0	0.0	0.0
3.0	0.12902	0.13205	0.130	0.131	0.129
10.0	0.22035	0.22393	0.217	0.217	0.224
23.1	0.23065	0.23250	0.224	0.225	0.236
100.0	0.27112	0.27570	0.263	0.263	0.281
144.2	0.25096	0.25669	0.244	0.244	0.261
1000.0	0.27832	0.27964	0.268	0.268	0.287

Table 4: Numerical results of the Mode-II stress intensity factors for the interface cracks

The stress intensity factor for the interface crack is a coupled complex number. So it doesn't make sense to correlate K_I and K_{II} to some phycial interpretation separately. A better way is to take the stress intensity factor amplitude $|K|$ to describe the concentrated degree of the singular field, and it's also associated with the energy release rate of the dissimilar crack. It can be noted in Table 5 that, the resulted $|K|$ by enriched finite element method is very reasonable compared the exsiting solutions.

$\frac{\mu_2}{\mu_1}$	$\lvert K\rvert = \sqrt{K_I^2 + K_{II}^2}$				
	EFM		Rice/Sih (EXACT)	Lin/Mar(FE)	Chen(FE)
	Left	Right			
1.0	1.782	1.783	1.772	1.790	1.809
3.0	1.796	1.797	1.784	1.800	1.826
10.0	1.823	1.823	1.805	1.816	1.861
23.1	1.826	1.826	1.806	1.817	1.866
100.0	1.842	1.842	1.817	1.829	1.885
144.2	1.836	1.836	1.813	1.822	1.878
1000.0	1.843	1.843	1.821	1.829	1.888

Table 5: The absolute value of the stress intensity factors for the interface cracks

5.2 Crack Normal to Interface

The crack perpendicular to and terminating at the interface is also a classic topic in fracture mechanics analysis. The enriched finite element method makes it easier to solve this kind of problem with a direct way of calculating the SIFs. In the geometry (Figure 27), the incidence angle becomes a right angle. One crack-tip is located on the bonded line, and another one is fully embedded in the homogenous media. Letting the remote loading along the x-direction be nothing, a pure Mode I crack was widely investigated analytically and numerically in previous studies. It should be noted that most analytical solutions were derived for a finite crack in an infinite or half-infinite plane. In finite element analysis, the model size is specified and the scale of the crack length should be befittingly small to satisfy the analytical conditions. In this paper, an example with the ratio $\frac{crack\ length}{Plate\ dimension} = 0.05$ is computed firstly using the newly-derived enriched finite element formulation (Figure 28).

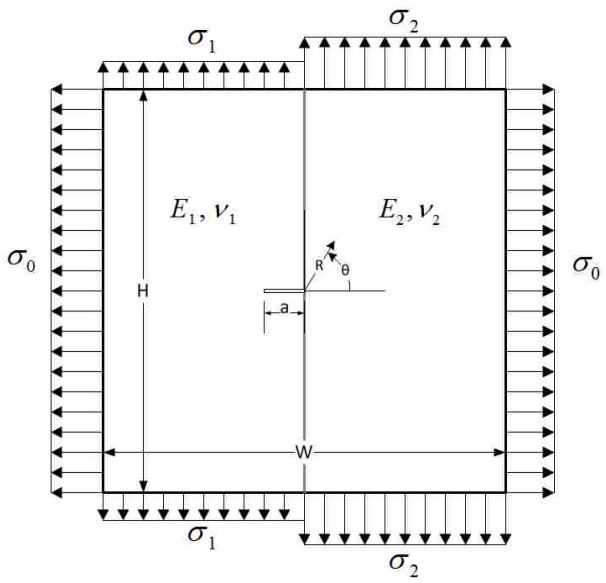

Figure 27: The geometry of a center crack terminating at and perpendicular to the interface

Definition of K	$K = K_I + iK_{II} = \lim_{r\to 0,\theta=0}\{(\sigma_{\theta\theta} + i\tau_{r\theta})(2\pi r)^{1-\lambda}\}$
Full/Half	Full
Width	40in
Height	40in
Crack Length	2in
P.Strain/Stress	Plane Stress
Crack Mode	Mode I
Load	Varing loads on remote $\sigma_0 = 0\ psi,\ \sigma_1 = 1\ psi,\ \sigma_2 = \frac{E_2}{E_1}\ psi$

Table 6: The properties used for the finite element model of the crack perpendicular to the interface

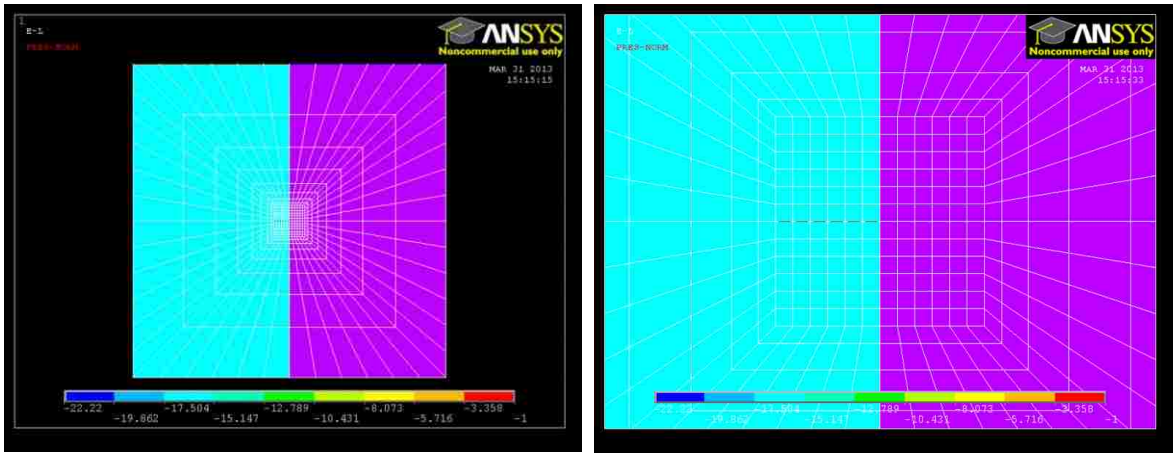

(a) Fit View (b) Close-up View

Figure 28: Finite element model of the crack perpendicular to the interface in ANSYS

In this case, five groups of material pairs are adopted in correspondence with the exiting solutions. The corresponding dominant root is given for each case. The stress intensity factor is normalized to be comparable. The results (Tables 7 & 8) exhibit good agreement with the previous pioneers and the differences range from 0.3% to 6.8%. The exception occurs as the shear ratio becomes pretty small and the error turns out to be about 20%. In this situation, the material medium containing the crack is extremely compliant. Then the entire model may be treated as an "edge crack", which would have different singular field than the case we refer to. Another possible reason for the error is, just as stated in the interface case, the big mismatch of material properties which results in the ill-conditioned matrix system and rounding error.

Two tips: (biomaterial crack tip)							
		$\sqrt{2}K_I/\sigma_1(2\pi a_0)^{1-\lambda}$	Normalized K_I				
μ_2/μ_1	Root	EFM	Lin	Cook	Chen	Kaya	Wang
138.46	0.73345	5.04825	4.978	4.922	5.001		5.002
23.07	0.71102	4.26272	4.241	4.176	4.231	4.232	4.232
1	0.50000	0.99807	0.995	1.00			
0.043	0.17577	0.10583	0.095	0.074	0.095	0.0955	0.0955
0.00722	0.074921	0.02327	0.0196	0.0079	0.0192		0.0192

Table 7: Normalized results of the Mode-I stress intensity factors for the crack normal to the interface

Two tips: (homogenous crack tip)							
		$\sqrt{2}K_I/\sigma_1(2\pi a_0)^{1-\lambda}$	Normalized K_I				
μ_2/μ_1	Root	EFM	Lin	Cook	Chen	Kaya	Wang
138.46	0.5	0.86413	0.833	0.871	0.870		0.870
23.07	0.5	0.87273	0.855	0.879	0.879	0.8787	0.879
1	0.5	0.99763	0.995	1.00			
0.043	0.5	1.38823	1.371	1.353	1.340	1.3398	1.340
0.00722	0.5	1.57755	1.529	1.509	1.474		1.474

Table 8: Normalized results of the Mode-I stress intensity factors for the homogenous crack

In the study of the stress state for a finite solid, the effect from remote applied edges has to be taken into account. This is why the FEM is more suitable to solve practical engineering problems. To verify it, more examples with different scales of crack size are investigated using the enriched

finite element method. The crack length is fixed as 2 inches and the model size is specified as 10, 20, 40, 80, 160 inches respectively. The results are demonstrated in the form of logarithm values (Figures 29 & 30) for convenience. Obviously, as the crack length scale increases and the crack-tips get more adjacent to the free edges, the error becomes more noticeable. The results of the bi-material crack-tip are convergent when the dimension ratio is below 1/20. Thus, it can be concluded that, as the crack's length ratio is no more 0.05 with respect to the model size, the finite element model is able to represent the problem with a finite center crack in an infinite solid.

Another study is carried out for the same model with different mesh densities. In this test, the edge size of the enriched finite element touching the crack-tip is regarded as the characteristic length Δ, and it's changed every time as the model is remeshed. The ratio Δ/a varies from 1/4 to 1/12 as desired, where a is the crack length. The results for the crack with a fixed scale $\frac{a}{W} = 0.1$ don't fluctuate too much as checked for different shear ratios μ_2/μ_1 (Figure 31). This observation consolidates the previous statement that the SIF's errors don't come from the mesh density but the edge effect.

Compared with the crack-tip lying on the bonded border, the other end of the crack in the homogeneous medium holds the results with more deviations. It can be explained by the free-edge effect due to its closer distance to the nearest edge.

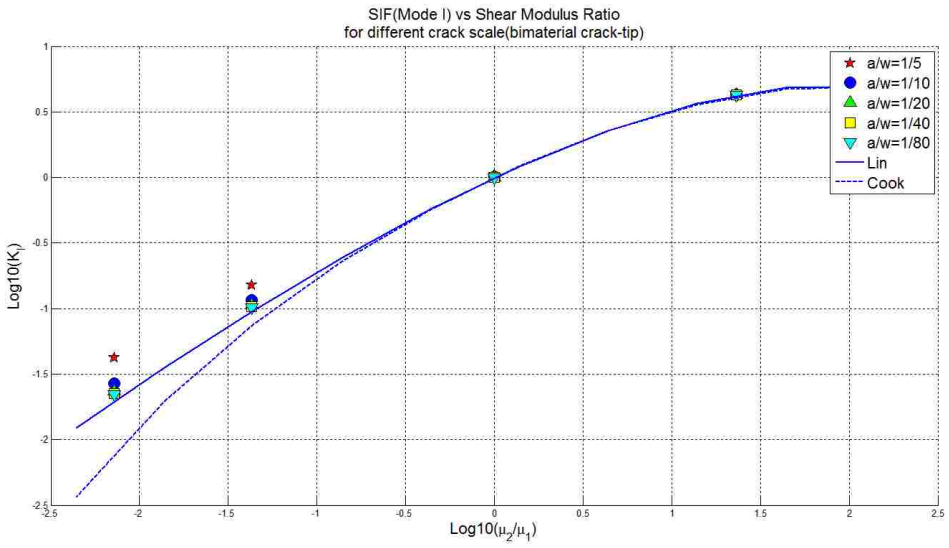

Figure 29: The stress intensity factors (algorithm value) of biomaterial crack-tip for different scales of the crack

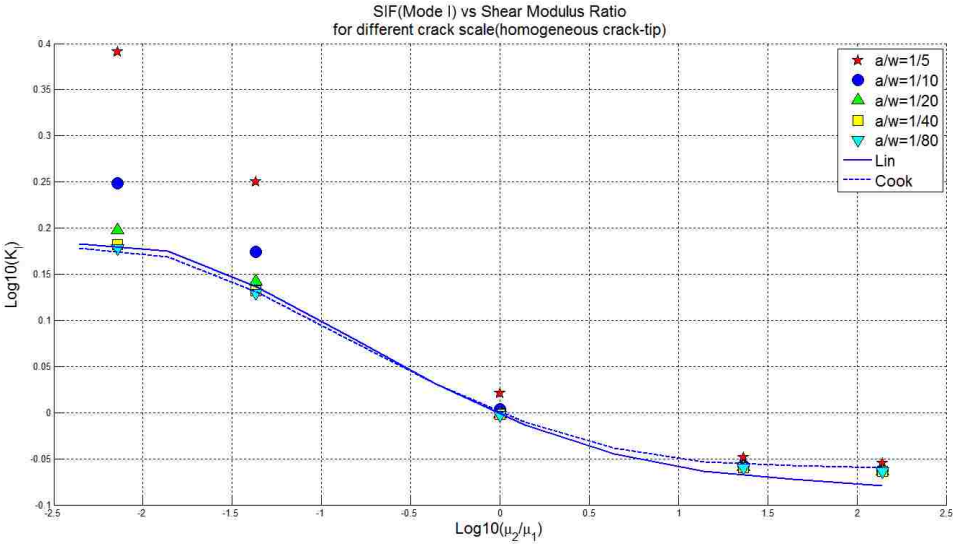

Figure 30: The stress intensity factors (algorithm value) of homogeneous crack-tip for different scales of the crack

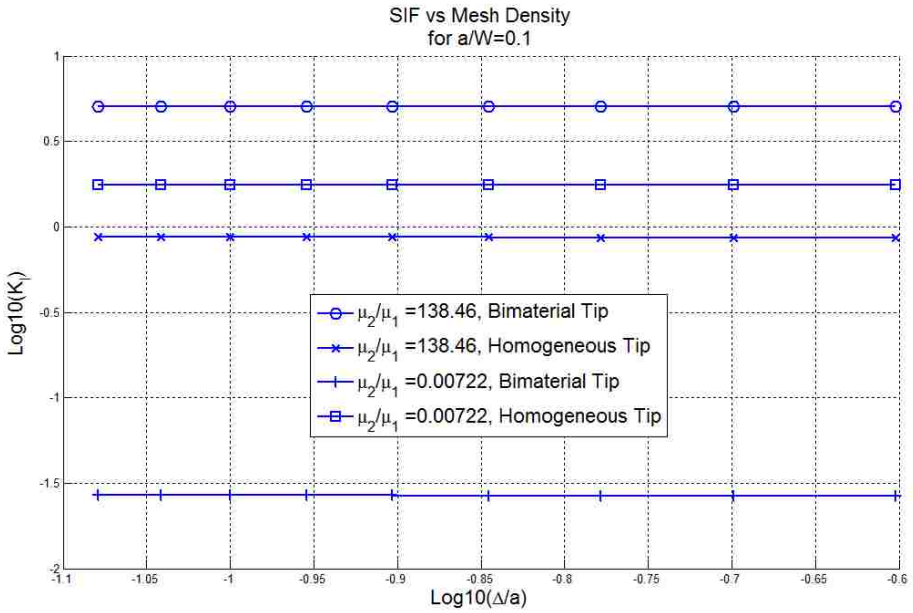

Figure 31: The stress intensity factors (algorithm value) of homogeneous crack-tip for different mesh densities

The check of the stress intensity factors has preliminarily verified the new derived formulation in this study. Another contribution is that the overall asymptotic field can be established for a bi-material crack. Thereafter, in another example, a semi-infinite crack which is touching and perpendicular to the interface was investigated for different material combinations. The asymptotic solution was normalized and the angular functions were adjusted into a comparable dimension with the existing solution [20]. The good coincidence can be observed (Figure 32).

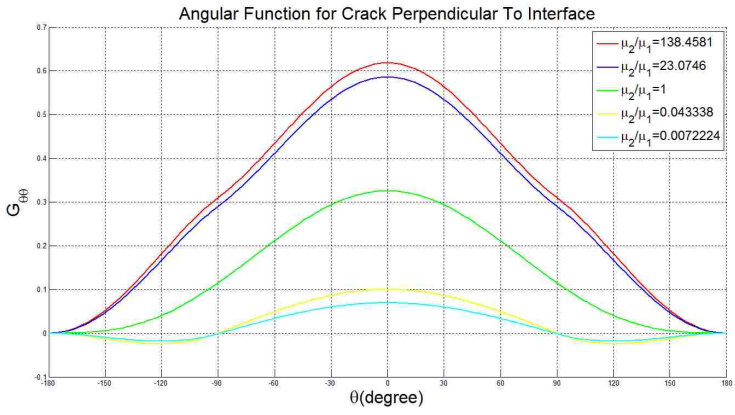

(a) Normalized angular function $G_{\theta\theta}$ for a crack normal to interface with point loads on crack surfaces

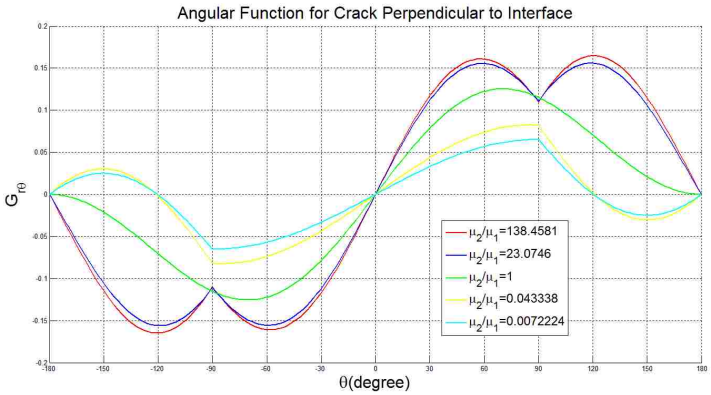

(b) Normalized angular function $G_{r\theta}$ for a crack normal to interface with point loads on crack surfaces

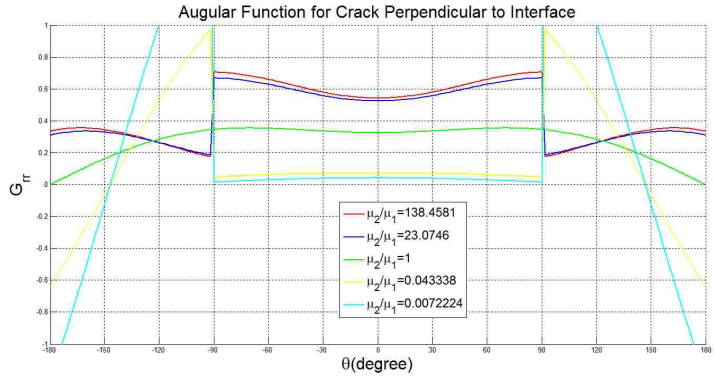

(c) Normalized angular function G_{rr} for a crack normal to interface with point loads on crack surfaces

Figure 32: Normalized angular functions for a crack normal to interface with point loads on crack surfaces

5.3 Crack with Arbitrary Impinging Angle to the Interface

Next, the general case of a crack with an oblique angle to the interface arises as ϕ varies between 0 and π. In the literature search, it's been found that the analytical solutions are limited and the existing solutions mainly focused on very simple geometries and some experimental methods. Due to the asymmetric nature, this kind of problem is believed to involve a lot of tedious mathematical deriving work and not easy to generate the explicit solution in closed form. For this situation, the numerical methods should be a good alternative to get the estimated solution. With the help of the enriched finite element method, the fracture parameters as well as the singular field can be obtained for some sophisticated geometries. The stress and displacement

components for the crack-tip area are given in a matriculated form which has simplified very much the post-analysis. Since the uncertainty of the singularities, either real or complex, a suitable definition of the stress intensity factors should be applied as the local asymptotic field is formulated.

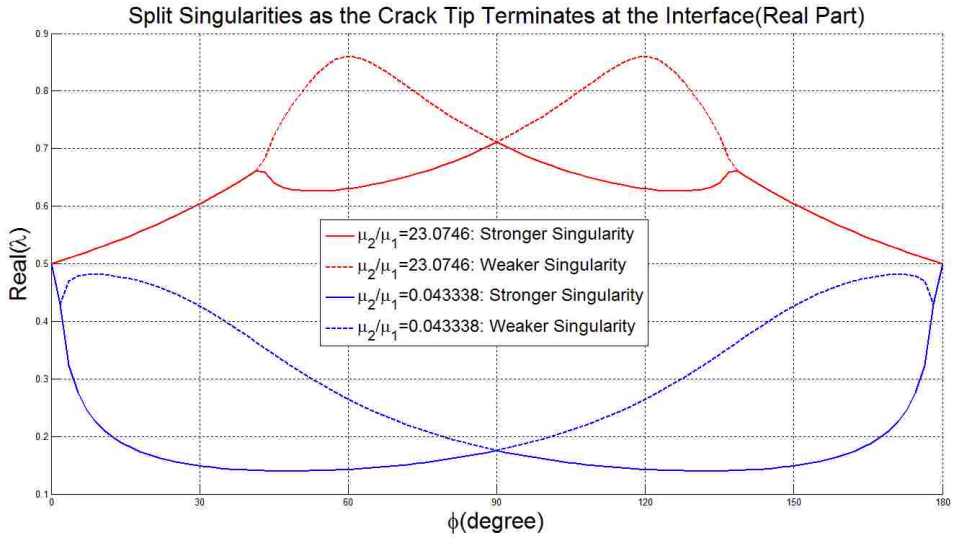

(a) Real part

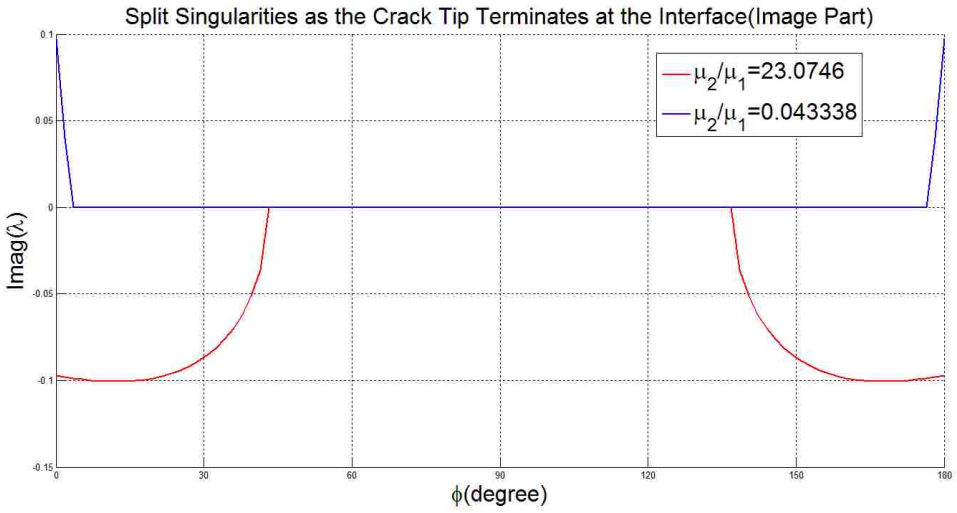

(b) Image part

Figure 33: Distribution of split singularities versus varying crack incidence angles as $\frac{\mu_2}{\mu_1} = 23.07\ and\ 0.043$ for in-plane mode

To investigate this kind of problem, two material combinations are taken into account specifically. The shear ratios are 23.07 and 0.043 respectively and being inverse of each other. The split singularities can be observed in Figure 33 above. It may be noted that, as the crack pass through from the softer side to the stiffer side, the transition from complex dominant roots to real roots occurs as the incidence angle reaches around 45 degrees and 135 degrees. If the crack advances towards the softer solid, the complex singularities only occur when the crack is close to being parallel to the interface.

Next, the finite element model of a finite crack in a thin plate is employed again to study the stress intensity factors for a series of arbitrarily-oriented crack cases with specific angles. The geometry is as same as that used for the previous case of a perpendicular crack. The ratio of the crack length to the plate's edge length is kept as 0.05. One end of the crack is fixed at the centroid of the plate and the crack-tip on the interface. Another end-tip rotates from 90 degrees (normal to the interface) to 180 degrees (along the interface) clockwise with a step of 7.5 degrees. So only obtuse impinging angles are considered (Figure 34).

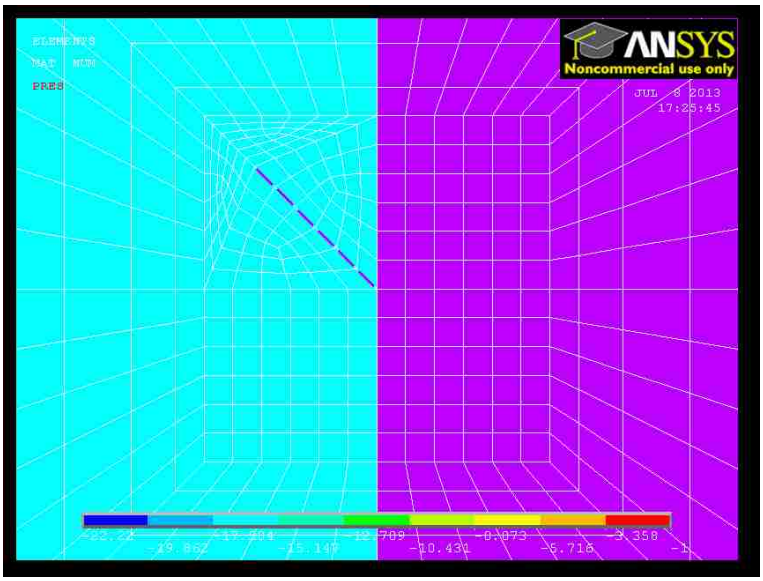

Figure 34: Finite element model of the crack attacking the interface with arbitrary angles in ANSYS

In the first test, a uniaxial tensile stress is applied on the top and bottom edges of the model. The numerical solutions of the split singularities as well as K_I and K_{II} are listed in Table 9 and Table 10. The corresponding phase angles are also given to characterize the mixity of the stress field

ahead of the crack-tip. It may be concluded from the phase angle that, as penetrating into the stiffer side, the crack is forced to stay away from deflecting into or paralleling the interface. This trend is not affected by the impinging angle which only leads to the changes of the crack's deflection angle. In contrast, it is not easy for the crack-tip to go forward in the softer material. Since the shear stress overwhelms the opening stress, the crack will probably deviate from the original direction and approach the bonded border. However, it has to be mentioned that, in this general case, the ratio of two mode stress intensity factors is not identical to the ratio of the shear stress and the normal stress ahead of the crack-tip. The phase angle may be inadequate to predict the crack's propagation. A more reasonable method just based on the stress state in the *K*-dominant field will be discussed later.

Furthermore, it should be also noted that, while the singularity is complex, the units of the stress intensity factors implies they cannot be attached with a physical explanation. So the complex *K* is suggested to be transformed by "$L^{i\varepsilon}$", and the phase angle should be rotated by "$\varepsilon \ln(L)$", where *L* is a reference length. The choice of the reference length can be arbitrary within a range of length scale, either based on the geometrical dimensions of the crack body or a material length scale [12, 16, 53]. However, the numerical results differ little, even negligible, if the small values of ε are considered [16]. For simplicity, the unity length is employed here for the cases featured with complex singularities. So the phase angles don't change after rotation.

$\frac{\mu_2}{\mu_1} = 23.04$	$\sigma_0 = 0\ psi, \quad \sigma_1 = 1\ psi, \quad \sigma_2 = \sigma_1 \frac{E_2}{E_1}\ psi$					
	Stronger Singularity	Weaker Singularity	K_I	K_II	K_II/K_I	Phase angle (Deg.)
90	0.71102	0.71102	5.12660	0	0	0
97.5	0.68204	0.74670	2.06212	-0.17351	-0.84142	-40.07804
105	0.65917	0.78910	1.69974	-2.60806	-1.53439	-56.90665
112.5	0.64196	0.83439	1.42237	-4.43639	-3.11902	-72.22343
120	0.63049	0.86023	1.25141	-7.07588	-5.65432	-79.97061
127.5	0.62633	0.81842	1.24701	-6.06124	-4.86061	-78.37444
135	0.63967	0.72263	1.62186	-5.62056	-3.46550	-73.90404

142.5	0.64044-0.06320I	-0.36719	-1.25316	3.41286	-106.33109
150	0.60425-0.08672I	-0.35462	-0.90080	2.54019	-111.48814
157.5	0.57269-0.09685I	-0.26527	-0.68417	2.57916	-111.19248
165	0.54520-0.10039I	-0.16383	-0.46547	2.84124	-109.38999
172.5	0.52116-0.10001I	-0.07590	-0.23086	3.04154	-108.19985
180	0.50000-0.097101I	-0.64082E-3	0.18397E-3	-0.28709	163.98183

Table 9: Non-normalized results of stress intensity factors for the crack attacking the interface with arbitrary angles as the shear ratio is 23.04 under uniaxial loading

	$\sigma_0 = 0\ psi, \quad \sigma_1 = 1\ psi, \quad \sigma_2 = \sigma_1 \frac{E_2}{E_1}\ psi$					
$\frac{\mu_2}{\mu_1} = 0.043$	Stronger Singularity	Weaker Singularity	K_I	K_II	K_II/K_I	Phase angle
90	0.17577	0.17577	0.340389	0	0	0
97.5	0.16360	0.19125	0.15405	0.17408	1.12999	48.49246
105	0.15423	0.21070	0.13838	0.15659	1.13160	48.53280
112.5	0.14730	0.23495	0.12055	0.13595	1.12774	48.43564
120	0.14261	0.26486	0.10102	0.11406	1.12911	48.47022
127.5	0.14013	0.30095	0.80817E-1	0.91676E-1	1.13437	48.60243
135	0.13999	0.34253	0.60737E-1	0.69438E-1	1.14326	48.82405
142.5	0.14265	0.38640	0.41549E-1	0.48160E-1	1.15912	49.21499
150	0.14906	0.42659	0.23944E-1	0.29405E-1	1.22809	50.84505
157.5	0.16143	0.45718	0.84932E-2	0.15676E-1	1.84565	61.55058
165	0.18541	0.47577	-0.43520E-2	0.81177E-02	-1.86530	118.19605
172.5	0.24224	0.48143	-0.15189E-1	0.57304E-02	-0.37727	159.32984
180	0.50000E+ 0.09710I		-0.28829E-	-0.83025E-	0.28799	-163.93407

		4	5		

Table 10: Non-normalized results of stress intensity factors for the crack attacking the interface with arbitrary angles as the shear ratio is 0.043 under uniaxial loading

As the crack lies on the interface, the results' order of magnitude is pretty low and may be unacceptable. This is because the remote tensile stress is parallel to the crack surface. So the asymptotic shearing and opening stresses in the vicinity of the crack-tip are relatively small. To avoid the possible round-off error, in the second test, a biaxial loading is applied for the same model. The corresponding results are shown as below (Tables 11 & 12). It can be observed the mixity of the singular stress field is not as severe as that under the biaxial condition. But its effect on the crack's selection of the advancing direction doesn't change in nature.

$\frac{\mu_2}{\mu_1} = 23.04$	$\sigma_0 = 1\ psi, \quad \sigma_1 = 1\ psi, \quad \sigma_2 = \sigma_1 \frac{E_2}{E_1} + \sigma_0 \left(\nu_2 - \nu_1 \frac{E_2}{E_1}\right)\ psi$					
ϕ	Stronger Singularity	Weaker Singularity	K_I	K_II	K_II/K_I	Phase angle (Deg.)
90	0.71102	0.71102	5.12525	0	0	0
97.5	0.68204	0.74670	2.30923	-1.55998	-0.67554	-34.04063
105	0.65917	0.78910	2.15582	-2.13535	-0.99051	-44.72675
112.5	0.64196	0.83439	2.04997	-3.38864	-1.65301	-58.82793
120	0.63049	0.86023	2.00336	-5.40873	-2.69982	-69.67563
127.5	0.62633	0.81842	2.07937	-5.20117	-2.50132	-68.20900
135	0.63967	0.72263	2.58326	-6.28196	-2.43180	-67.64663
142.5	0.64044-0.06320I		0.11981	-2.01745	-16.83931	-86.60149
150	0.60425-0.08672I		0.40647	-1.77982	-4.37872	-77.13558
157.5	0.57269-0.09685I		0.82353	-1.61855	-1.96537	-63.03251
165	0.54520-0.10039I		1.23224	-1.34399	-1.09069	-47.48379
172.5	0.52116-0.10001I		1.53049	-0.96495	-0.63048	-32.23081
180	0.50000-0.09710I		1.79852	-0.22844	-0.12701	-7.23860

Table 11: Non-normalized results of stress intensity factors for the crack attacking the interface with arbitrary angles as the shear ratio is 23.04 under biaxial loading

$\frac{\mu_2}{\mu_1} = 0.043$	$\sigma_0 = 1\ psi, \quad \sigma_1 = 1\ psi, \quad \sigma_2 = \sigma_1 \frac{E_2}{E_1} + \sigma_0 \left(\nu_2 - \nu_1 \frac{E_2}{E_1}\right)\ psi$					
ϕ	Stronger Singularit	Weaker Singularit	K_I	K_II	K_II/K_I	Phase angle

	y	y				
90	0.17577	0.17577	0.33912	0	0	0
97.5	0.16360	0.19125	0.13687	0.20254	1.47975	55.94961
105	0.15423	0.21070	0.11248	0.21977	1.95378	62.89529
112.5	0.14730	0.23495	0.9214E-1	0.23987	2.60323	68.98634
120	0.14261	0.26486	0.7464E-1	0.26517	3.55278	74.27969
127.5	0.14013	0.30095	0.5954E-1	0.29601	4.97280	78.62982
135	0.13999	0.34253	0.4613E-1	0.33176	7.19217	82.08433
142.5	0.14265	0.38640	0.3393E-1	0.36642	10.79991	84.70987
150	0.14906	0.42659	0.2226E-1	0.38553	17.31922	86.69545
157.5	0.16143	0.45718	0.9847E-2	0.37374	37.95365	88.49072
165	0.18541	0.47577	-0.742E-2	0.33797	-45.51976	91.25850
172.5	0.24224	0.48143	-0.581E-1	0.36343	-6.25770	99.07927
180	0.50000E+ 0.09710I		1.79891	0.22855	0.12705	7.24051

Table 12: Non-normalized results of stress intensity factors for the crack attacking the interface with arbitrary angles as the shear ratio is 0.043 under biaxial loading

There is another important thing to be aware of. According to the theory of split singularity (Equations 1.6 & 1.7), if the crack is not normal to or coincident with the interface, the circumferential stress and the shear stress ahead of the crack-tip are contributed from both K_I and K_{II}. As a result, the phase angle cannot be regarded as the ratio of those two stress components. The corresponding angular functions, a reference radial distance and the singularities should be taken into account as the following equations

$$\frac{\tau_{r\theta}(2,r,0)}{\sigma_{\theta\theta}(2,r,0)} = \frac{\Sigma^{I}_{r\theta}(2,0) + \frac{K_{II}}{K_I}(2\pi r)^{\lambda_2-\lambda_1}}{1 + \frac{K_{II}}{K_I}(2\pi r)^{\lambda_2-\lambda_1}\Sigma^{II}_{\theta\theta}(2,0)} \quad (for\ real\ singularities) \tag{5.5}$$

$$\frac{\tau_{r\theta}(2,r,0)}{\sigma_{\theta\theta}(2,r,0)} = \frac{\Sigma^{R}_{r\theta}(2,0) + \frac{Im\left[K(2\pi r)^{\lambda_1-1}\right]}{Re\left[K(2\pi r)^{\lambda_1-1}\right]}}{1 + \frac{Im\left[K(2\pi r)^{\lambda_1-1}\right]}{Re\left[K(2\pi r)^{\lambda_1-1}\right]}\Sigma^{I}_{\theta\theta}(2,0)} \quad (for\ complex\ singularities) \tag{5.6}$$

5.4 Criteria for Crack Propagation

The points of interest for cracking prediction is when the crack start to grow and in which direction it goes. In fracture mechanics research, it's necessary to apply a quantitative criterion to decide

the crack's movement. The most common way is nothing but the comparison of a characteristic strength parameter of the material, such as the fracture toughness, with a critical load factor, for example, the stress intensity factor. For mixed-loaded cracks, a single facture parameter is obviously inadequate since the crack's advancement is influenced by not only the opening driving load but also the shearing impact load. Their resultant force and their ratio is coincident with the weakest direction in which the crack is most possible to break through.

Basically, the existing strategy of predicting crack's propagation may be categorized into two approaches. The first one is to pay attention to the stress state around the original crack-tip before it advances. For a pure Mode-I homogeneous crack, the stress intensity factor is compared with the material toughness to decide if the crack will go straight. In pure Mode-II, the crack's angle of inflection is constant and the crack starts to grow if the shearing toughness is achieved. The situation of mixed-mode cracks is a little bit complicated. The criterion in terms of the combined action of stress intensity factors for homogeneous media should be considered as

$$\left(\frac{K_I}{K_{Ic}}\right)^2 + \left(\frac{K_{II}}{K_{IIc}}\right)^2 \geq 1 \tag{5.7}$$

where K_{Ic} and K_{IIc} are Mode-I toughness and Mode-II toughness respectively. This is equivalent to the standard based on the stain energy release rate that

$$G \geq G_c \tag{5.8}$$

Another scheme is to assume the crack has already had a small extension in some direction. Thus the point of interest moves to the crack-tip area of the sub-crack. The stress state is compared with the critical value to check if the hypothetic extended part really exists. The preferred propagation direction should have the maximum principle stress or maximum strain energy release rate. This approach is also used for the crack in dissimilar media by considering two subcracks. One is located along the interface and another completely stays in the homogenous solid. The ratios of their stress states at tips respectively with the weakness along the bonded border and the strength of the homogenous solid are referred to decide if the crack

will dedond the interface, penetrate the interface or deflect back. The corresponding criterion using strain energy release rates is represented as below

$$\frac{G_p}{G_{Ic}} \; ? \; \frac{G_d}{G_c} \tag{5.9}$$

where G_p and G_d are the strain energy release rates in two possible directions, while G_{Ic} and G_c are the toughness of the interface and the Mode-I toughness in the homogenous solid.

In practical research, there are some popular fracture criteria for mixed-mode cracks which will be introduced here.

Maximum Tensile Stress Criterion

A criterion which is featured with the maximum tensile stress was proposed by Erdogan and Sih [54] to study the mixed-mode fracture. They assumed that the crack's propagation takes places in the direction with the maximum circumferential stress $\sigma_{\theta\theta}$ near the crack-tip, and the crack starts to grow as $\sigma_{\theta\theta}^{max}$ is equal to or larger than the critical stress leading to the opening mode fracture.

For a homogeneous crack, the stress components $\sigma_{\theta\theta}$ and $\sigma_{r\theta}$ in polar coordinates can be presented as

$$\sigma_{\theta\theta} = (2\pi r)^{-\frac{1}{2}} \cos\left(\frac{\theta}{2}\right)\left\{K_I \cos^2\left(\frac{\theta}{2}\right) - \frac{3}{2}K_{II}\sin(\theta)\right\} \tag{5.10}$$

$$\sigma_{r\theta} = (2\pi r)^{-\frac{1}{2}} \cos\left(\frac{\theta}{2}\right)\left\{\frac{1}{2}K_I \sin(\theta) + \frac{1}{2}K_{II}[3\cos(\theta) - 1]\right\} \tag{5.11}$$

It can be noted that the hoop stress $\sigma_{\theta\theta}$ reaches its maximum limit as the shear stress $\sigma_{r\theta}$ vanishes. Under this situation, if the direction is assumed with a radial angle $\theta = \theta_0$, the following condition is valid

$$\cos\left(\frac{\theta_0}{2}\right)\left\{\frac{1}{2}K_I \sin(\theta_0) + \frac{1}{2}K_{II}[3\cos(\theta_0) - 1]\right\} = 0 \tag{5.12}$$

Ignoring the portion which indicates crack surfaces, the cracking angle is determined by the expression in the brackets. According to the maximum tensile stress criterion, the critical hoop stress can be obtained in terms of the Mode-I toughness as

$$\sigma_{\theta\theta}^{c} = \frac{K_{Ic}}{\sqrt{2\pi r}} \tag{5.13}$$

Substituting $\sigma_{\theta\theta}^{c}$ into equation (5.12) gives the mixed-mode condition of the maximum tensile stress criterion

$$\cos\left(\frac{\theta_0}{2}\right)\left\{K_I \cos^2\left(\frac{\theta_0}{2}\right) - \frac{3}{2}K_{II}\sin(\theta_0)\right\} = K_{Ic} \tag{5.14}$$

For a pure Mode-I crack that $K_{II} = 0$, the equation (5.14) is deduced to imply that the propagation will go along the original direction. As the crack-tip are is completely under Mode-II loading, in which $K_I = 0$, the angle of deflection is well-known as

$$\theta_0 = \text{acos}(1/3) = -70.5\ degrees$$

Strain Energy Density Criterion

Another criterion based on the strain energy density was introduced and asserted by Sih [55]. Taking a two-dimensional homogeneous crack solid as an example, the strain energy stored in a differential body with a unit thickness can be expressed as

$$dU = \left\{\frac{1}{2\mu}\left[\frac{1+\eta}{8}(\sigma_{rr}^2 + \sigma_{\theta\theta}^2) - \frac{3-\eta}{4}\sigma_{rr}\sigma_{\theta\theta} + \tau_{r\theta}^2\right]\right\}dV \tag{5.15}$$

where η is the constant defined in equation (1.4) for plane stress and plane strain conditions respectively. If the stress components are replaced by the stress intensity factors, the equation above can be rewritten to give the expression for the density of strain energy that

$$W = \frac{dU}{dV} = r^{-1}\{a_1 K_I^2 + a_2 K_I K_{II} + a_3 K_{II}^2\} \tag{5.16}$$

in which the coefficients a_j are given as below

$$a_1 = \frac{1}{16\mu\pi}[1+\cos(\theta)][\eta - \cos(\theta)]$$

$$a_2 = \frac{1}{16\mu\pi}\sin(\theta)\,[1-\eta+2\cos(\theta)]$$

$$a_3 = \frac{1}{16\mu\pi}\{[3\cos(\theta_0)-1][1+\cos(\theta)] + (1+\eta)[1-\cos(\theta)]\}$$

It should be mentioned that the strain energy density *W* has a singularity with the order of r^{-1}. This singular behavior was removed by Sih and the remaining finite part known as "strain energy density factor" is just a function with respect to the radial angle

$$S = a_1 K_I^2 + a_2 K_I K_{II} + a_3 K_{II}^2 \tag{5.17}$$

The criterion using this factor can be described as that the crack starts to extend in the direction with the minimum strain energy density factor, and it would happen when the minimum value reaches the critical value.

For a homogenous crack with pure Mode-I stress state, the extension direction will still be straight-forward, and the critical value of the factor can be represented in terms of the toughness of K_I that

$$S_{Ic} = K_{Ic}^2 \left(\frac{\eta - 1}{8\mu\pi}\right) \tag{5.18}$$

In the Mode-II homogenous crack, the deflection angle id determined by η that

$$\theta_0 = -\operatorname{acos}\left(\frac{\eta - 1}{6}\right) \tag{5.19}$$

The initialization strain energy density factor can be expressed as

$$S_{IIc} = K_{IIc}^2 \left(\frac{14\eta - \eta^2 - 1}{384\mu}\right) \tag{5.20}$$

Maximum Energy Release Rate Criterion

The strain energy release rate is the energy dissipated during fracture per unit of newly created fracture surface area. Griffith declared that the crack's extension prefers the direction in which the maximum potential energy is released. Thus, to use this energy-based criterion for a 2-D in-plane crack, a kinked sub-crack needs to considered and the energy release rate at the new-tip is represented as

$$G_{kink} = \frac{1 + \eta}{8\mu}(K_I^2 + K_{II}^2) \tag{5.21}$$

where K_I and K_{II} are the stress intensity factors of the extended crack-tip. If the dimension of the sub-crack is small enough compared with the K dominant zone surrounding the original crack-tip, K_I and K_{II} can be thought of to be related linearly with the stress intensity factors k_I and k_{II} of the main crack-tip that

$$\begin{Bmatrix} K_I \\ K_{II} \end{Bmatrix} = \begin{bmatrix} c_{11}(\omega,\phi) & c_{12}(\omega,\phi) \\ c_{21}(\omega,\phi) & c_{22}(\omega,\phi) \end{bmatrix} \begin{Bmatrix} k_I \\ k_{II} \end{Bmatrix} \tag{5.22}$$

The dimensionless relationship function $c_{ij}(\phi)$ depends on the incidence angle and the deflection angle if an interface is involved. For the homogeneous crack, only the angle ϕ takes control, and the constants were given by Nuismer [56] and Cotterell and Rice [57] as below

$$\begin{aligned} c_{11} &= \frac{1}{2}\cos\left(\frac{\phi}{2}\right)\{1+\cos(\phi)\} \\ c_{12} &= -\frac{3}{2}\cos\left(\frac{\phi}{2}\right)\sin(\phi) \\ c_{21} &= \frac{1}{2}\cos\left(\frac{\phi}{2}\right)\sin(\phi) \\ c_{22} &= \frac{1}{2}\cos\left(\frac{\phi}{2}\right)\{3\cos(\phi)-1\} \end{aligned} \tag{5.23}$$

The corresponding functions for the crack touching the interface have been by He and Hutchinson [58], as well as Zhang and Suo [35] respectively.

Then substituting equation (5.23) in equation (5.22) yields

$$\begin{aligned} G_{kink}(\omega,\phi) = \frac{1+\eta}{8\mu}\{&(c_{11}^2+c_{21}^2)k_I^2 + (c_{12}^2+c_{22}^2)k_{II}^2 \\ &+ 2(c_{11}c_{12}+c_{21}c_{22})k_I k_{II}\} \end{aligned} \tag{5.24}$$

Then the crack is predicted to grow along the direction $\phi = \phi_0$ with maximum of G_{kink}. Also in such a direction, the pure Mode-I holds at the kinked crack-tip. Thus the toughness of the opening mode G_{Ic} is regarded as the critical value to decide if the crack will extend.

If the crack front is embedded in a homogeneous medium or grows along the bonded interface, the stress state around the crack-tip would remain self-similar as the crack propagates. For these

cases, an energy-based parameter, the strain energy release rate, is the most appropriate criterion to study the fracture propagation, especially for the crack bearing stresses in multi-directions. It's already been shown that the local field in the vicinity of the singular point is of mixed-mode for crack with an arbitrary angle of incidence. So the local fracture process may not be controlled by using a single parameter fracture criterion. Unfortunately, such kind of crack-tip doesn't remain a self-similar behavior due to a change of the singular state as it advances. The energy-based methods may not be applicable since the strain energy release rate would go unbounded or vanish as the crack-tip touches the interface. This depends on the material mismatch on the path of the crack's propagation.

In such situations, one criterion, probably more practical and reasonable to predict the crack's growth, would be the "maximum hoop stress criterion" [53]. According to this standard, the crack propagation occurs at the location where the hoop stress $\sigma_{\theta\theta}$ in a homogeneous medium hits the maximum in a specific radial distance and when it exceeds the critical stress as

$$\sigma_{\theta\theta}(\delta_p, \theta_c) \geq \sigma_c \tag{5.25}$$

where σ_c is a material constant representing the strength of a certain material, and θ_c describes the direction with the highest circumferential stress. δ_p is the characteristic size of the fracture process zone. Basically, it may be determined for a specific material by experiment. In another hand, the possibility of deflecting into the interface cannot be ignored due to the weakness of the bonding. The stress state for the interfacial crack-tip is treated in a similar way and equation (80) can be modified as

$$\left.\begin{matrix}(\sigma_{\theta\theta}^2 + \sigma_{r\theta}^2)^{0.5} & (\sigma_{\theta\theta} > 0) \\ \sigma_{r\theta} + f\sigma_{\theta\theta} & (\sigma_{\theta\theta} < 0)\end{matrix}\right\} \geq \sigma_c^I \ @ \ r = \delta_p^I \tag{5.26}$$

where σ_c^I represents the bonding adhesive strength, δ_p^I is the critical size of the fracture process zone and *f* is the coefficient of friction. For the specific cases in this study, because the crack-tip area is composed of multiple materials and different singularities, the critical equation (5.25) may be modified to

$$\sigma_{\theta\theta}^{i}\left(\delta_p, \theta_c^{i}\right) \geq \sigma_c^{i} \tag{5.27}$$

The superscript indicates different material zones. Obviously, there would be four possible directions of crack's progress. One may find the most preferred path by comparing the ratio of the numerical result to the critical value that

$$Max\left\{\frac{\sigma_{\theta\theta}^{1}}{\sigma_c^{1}}, \frac{\sigma_{\theta\theta}^{2}}{\sigma_c^{2}}, \frac{((\sigma_{\theta\theta}^{I})^2 + (\sigma_{r\theta}^{I})^2)_{branch1}^{0.5}}{\sigma_c^{I}}, \frac{((\sigma_{\theta\theta}^{I})^2 + (\sigma_{r\theta}^{I})^2)_{branch2}^{0.5}}{\sigma_c^{I}}\right\} \tag{5.28}$$

In practical applications, all these material-based critical properties should be obtained by experiment firstly. After that, once the singular strength, appropriate stress intensity factors and corresponding angular functions are generated, the stress state around the singular point is determined. Then it would not be hard to predict the crack's growth path by using suitable fracture criteria.

For the general case of a crack-tip touching the interface with an oblique angle, a prevailing approach is to assume the crack had advanced with a small propagation length in different directions, either advancing in homogenous or deflecting into the bonded border. Then the focus for this kind of problem is changed to comparing the stress state of the new sub-cracks with appropriate criteria. The stress singularities are already known for these new crack-tips. With the help of numerical methods, the corresponding fracture parameters can be found with a linear relationship with the stress intensity factors of the main crack [35, 58]. This method can be implemented using the finite element method. But it requires a lot of remodeling and remeshing work to determine the strain engery release rate of the sub crack-tip in different directions. As comparison, the approach introduced in this study would much simplify the whole analysis without repeating the modeling process.

5.5 In-Plane Asymptotic Fields

Although more mechanical or geometrical parameters have been involved to formulate the singular behavior surrounding a crack-tip, the asymptotic solution is considered as a good estimate of the stress field if the characteristic length is chosen properly.

In this study, the objective is to provide a more convenient way of studying the overall stress state in the vicinity of the singular point. The enriched element method has been able to get the numerical solution of the stress intensity factors. The calculation of the dominant roots of singularity is an additional benefit. The angular functions can be also generated through a universal linear system. One may substitute the characteristic length in a specific scale into the functions to establish an accurate stress distribution. For a general purpose, in this investigation, one fiftieth of the crack size is used as a reference length. Lack of material-based data for practical applications, this test just gives a tentative trial showing how to treat this kind of problem.

In the first case, the material mismatch is removed and crack is completely in a homogenous medium. The top and bottom edges of model are applied with normal tension stresses, tangential displacements and biaxial normal stresses respectively. The distribution of the hoop stress, the shear stress and the radial stress surrounding the crack-tip are shown in Figure 35 respectively. The impinging angle of the crack to the interface steps from 90 degrees to 180 degrees with an increment of 15 degrees. From these figures, it's easy to observe the location with the maximum stress value. With an appropriate criterion, the most possible orientation of the crack propagation may be determined which will be talked about later.

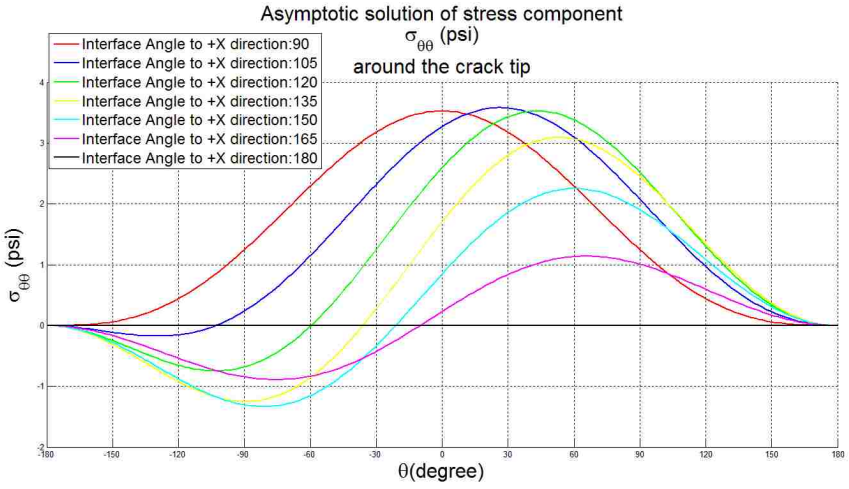

(a-1) Circumferential stress under uniaxial loading

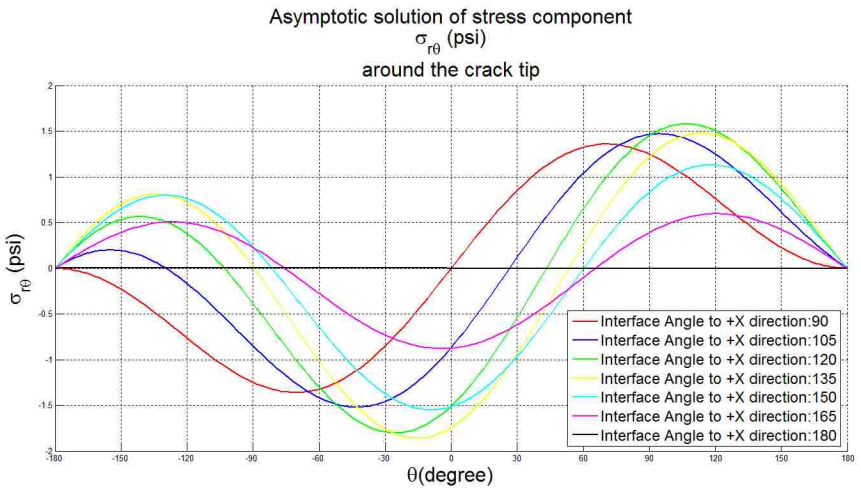

(a-2) Shear stress under uniaxial loading

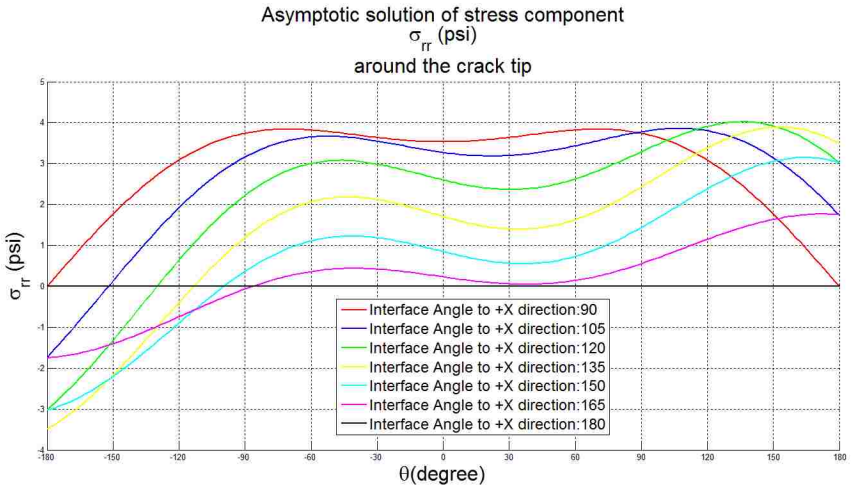

(a-3) Radial stress under uniaxial loading

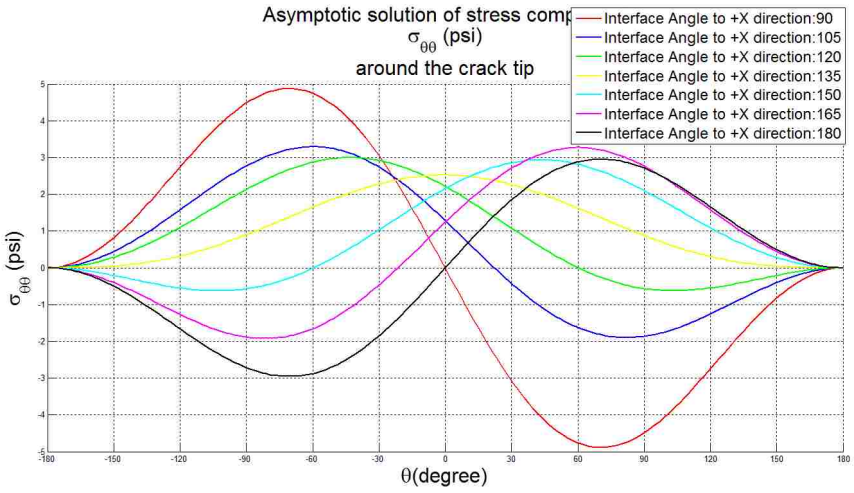

(b-1) Circumferential stress under applied tangential displacements

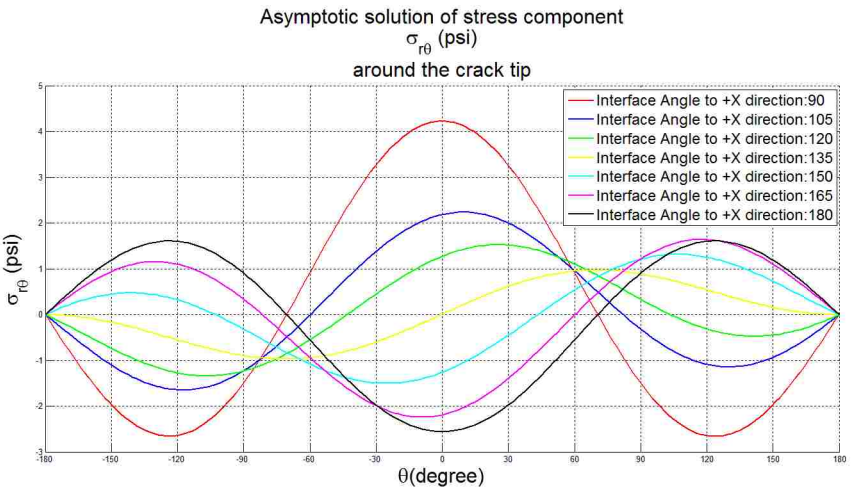

(b-2) Shear stress under applied tangential displacements

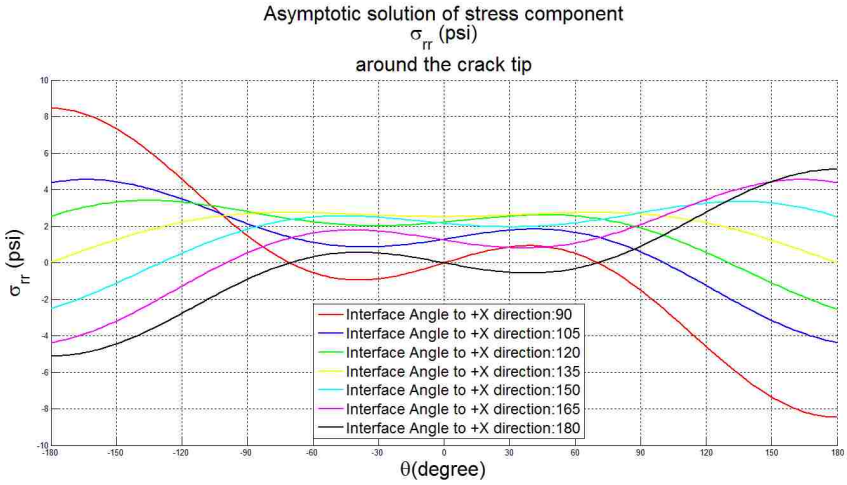

(b-3) Radial stress under applied tangential displacements

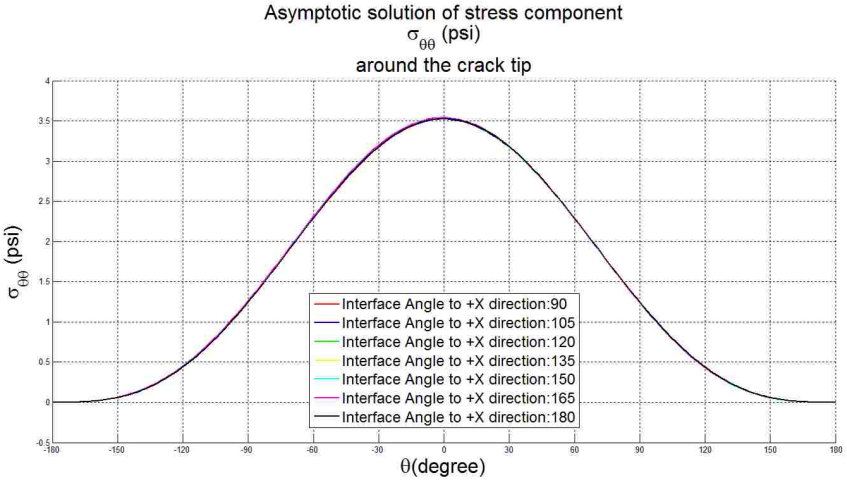

(c-1) Circumferential stress under biaxial loading

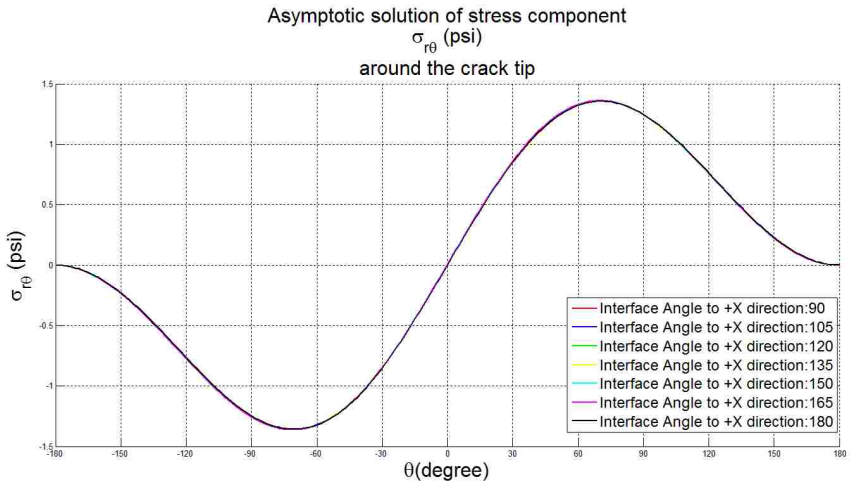

(c-2) Shear stress under biaxial loading

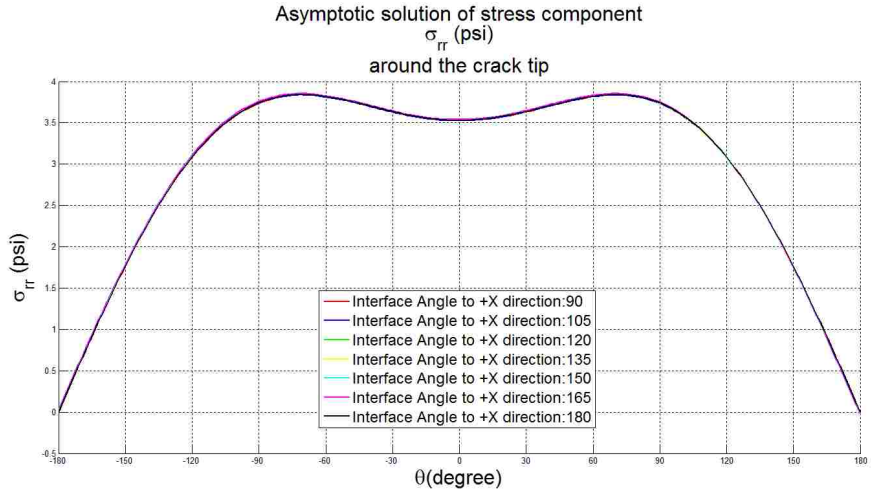

(c-3) Radial stress under biaxial loading

Figure 35: Distributions of asymptotic stress components under different loading pattens for the homogenous crack

In the second case, again, two specific material combinations are chosen to make the shear modulus ratio equal to 23.04 and 0.043. The uniaxial normal loading and biaxial normal loading, which are corresponding to tables 9-12, are applied for two separate tests. Please note the rotation angle θ, in degree, is measured from the crack extension line.

Basically, if crack comes from the softer side (Figure 36), the highest stresses take place as the crack's impinging angle is around 120 degrees for both uniaxial and biaxial loading. The horizontal load obviously alters and amplifies the stress state as the crack is rotated close to the interface. For other orientations, the additional loading condition doesn't affect the phase too

much but shrink the amplitude of stress. The situation is very different when the crack breaks into the softer side (Figure 37). Firstly, under the uniaxial loading, the maximum stress happens as the crack is normal to the interface. Then the horizontal loading appears as a big effect on the crack-tip field. The stresses are enlarged drastically and the locations with maximum values also shift accordingly.

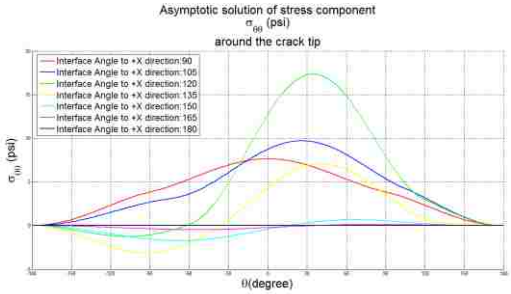

(a-1) Circumferential stress under uniaxial loading

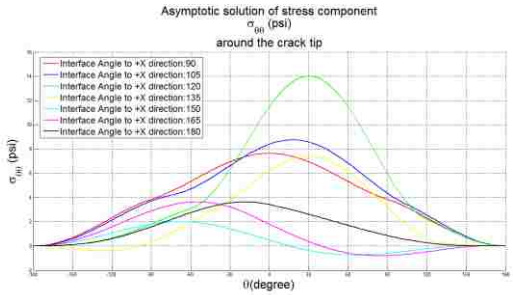

(b-1) Circumferential stress under biaxial loading

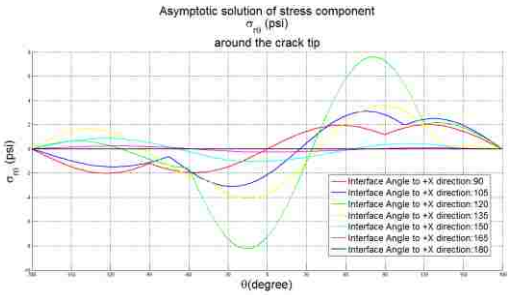

(a-2) Shear stress under uniaxial loading

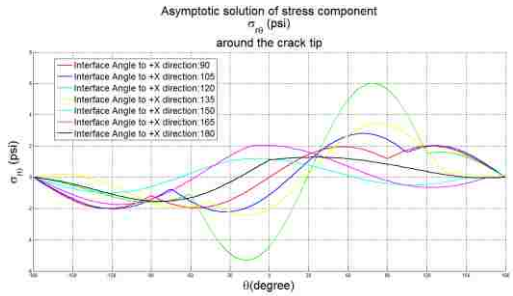

(b-2) Shear stress under biaxial loading

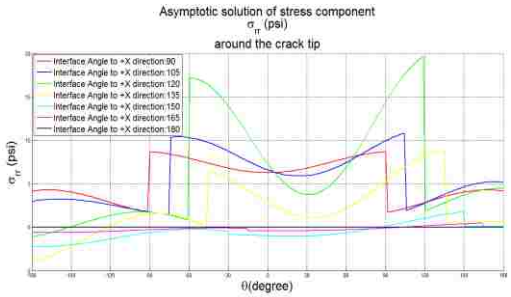

(a-3) Radial stress under uniaxial loading

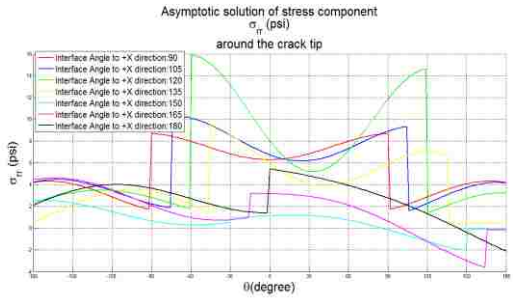

(b-3) Radial stress under biaxial loading

Figure 36: Distributions of asymptotic stress components under different loading pattens for the crack terminating at the interface with varying anlges as the shear modulus ratio is 23.04

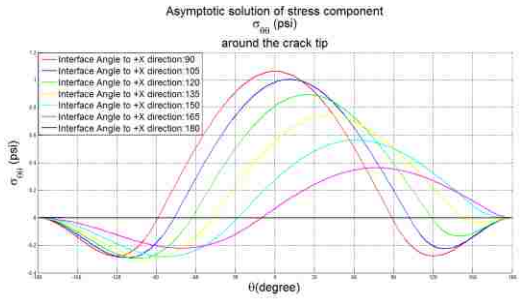

(a-1) Circumferential stress under uniaxial loading

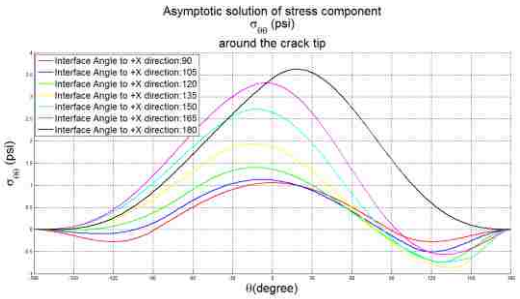

(b-1) Circumferential stress under biaxial loading

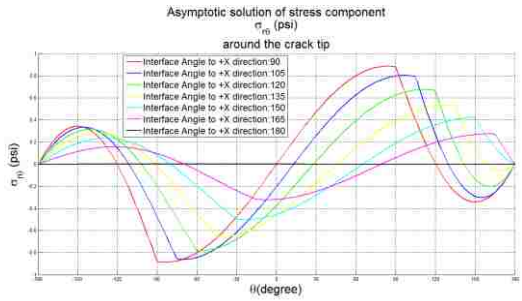

(a-2) Shear stress under uniaxial loading

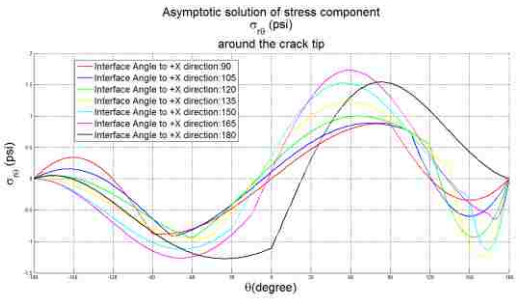

(b-2) Shear stress under biaxial loading

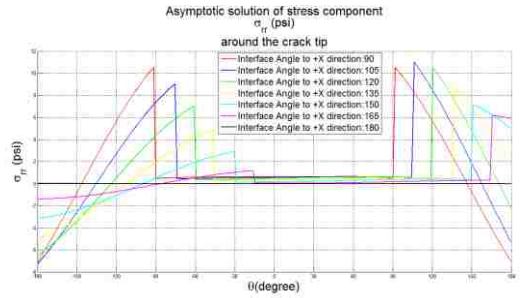

(a-3) Radial stress under uniaxial loading

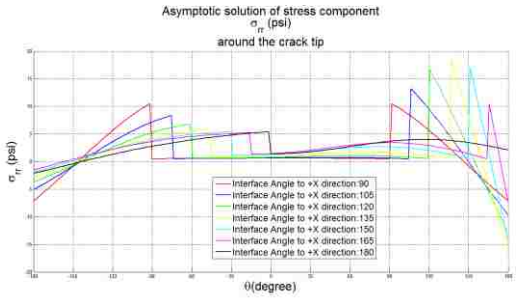

(b-3) Radial stress under biaxial loading

Figure 37: Distributions of asymptotic stress components under different loading pattens for the crack terminating at the interface with varying anlges as the shear modulus ratio is 0.043

Although there is no exact referenced solution to compare with, some interesting phenomena may need to be emphasized in the graphs of the asymptotic solutions. In Figure 36, the yellow curve represents the case with an impinging angle 135^o and double real singularities, and the light blue curve is associated with the case of 150^o with a pair of conjugated complex singularities. So the transition of singularities occurs as these two situations switch. It's not difficult to observe that, the asymptotic solution has a big change between these two cases. However, this only happens as the crack is located in the softer side. On the other end, if the crack is in the stiffer side, the transition of singularities arises between two cases represented by the purple curve and

the black curve respectively. In this situation, the impinging angle rotates from 165^o to 180^o, and the change of the asymptotic field is very smooth. So it might be included that, in some situation, the transition of the singularity may result in dramatic change for the asymptotic field with respect to the crack impinging on the interface with a rotating angle.

It can be seen that although the stress field ahead of the crack-tip is of mixed-mode, the maximum circumferential stress still occurs at some location where the shear stress vanishes, and obviously this specific location is decided by the angular functions with split singularities. This coincides with the principle stress theory and the maximum tension criterion for the homogenous. So the same criterion is still valid to use. In this study, although the critical value is not provided and the applied loads are not for real, the maximum $\sigma_{\theta\theta}$ is still an indication of predicting the propagation's direction.

For simplicity, the bonding is assumed to be perfect along the interface. So the last two items in equation (5.28) can be ignored. In addition, the ratio of critical circumferential stresses for the stiffer and softer materials is considered as 3.91 according to a reference. Using the modified maximum hoop stress criterion, the most possible direction of the advancing crack is determined for each case described above (Figure 38). To make it clear, the figures depicting the incidence angles and the predicted propagation angles are given as below.

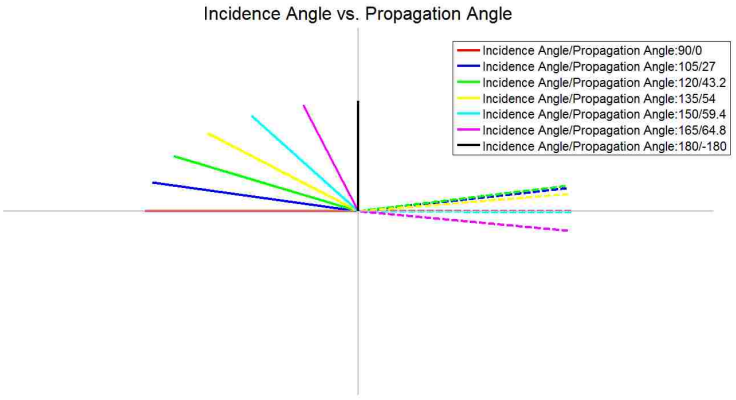

(a) Crack propagation under uniaxial loading

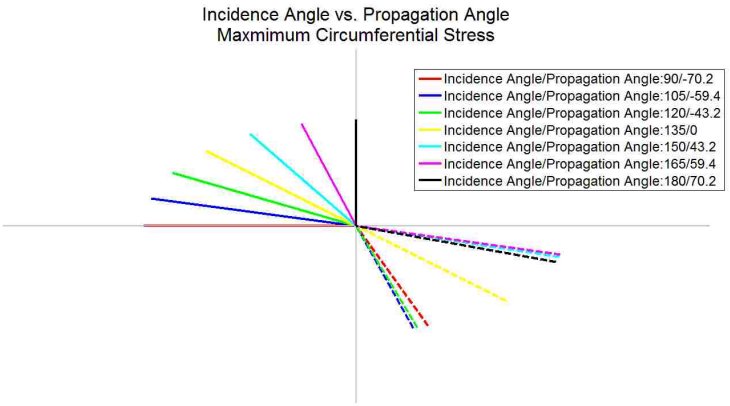

(b) Crack propagation under tangential displacement

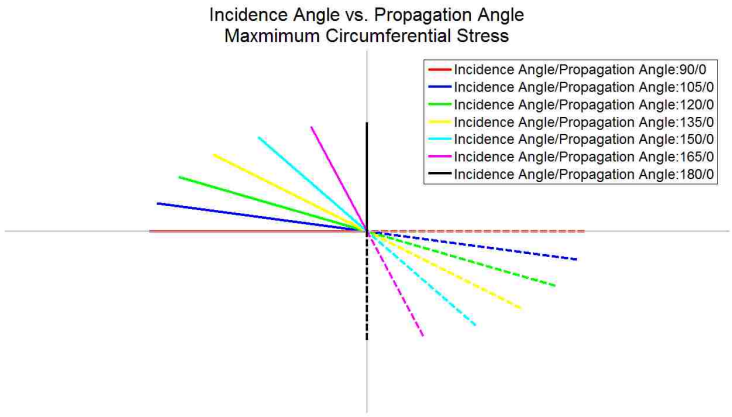

(c) Crack propagation under biaxial loading

Figure 38: Prediction of crack propagation (homogeneous) under different loading patterns using modified maximum circumferential criterion

In Figure 39, the material mismatch is ignored and the crack is completely embedded in a homogeneous media. Under applied uniaxial tensile stresses, the crack extension directions agrees very well with the theoretical solution by Erdogan and Sih [54], only except the situation when the crack is parallel to the loading (Figure 39). In such a condition, the magnitude of crack-tip stress is relatively small and can be ignored.

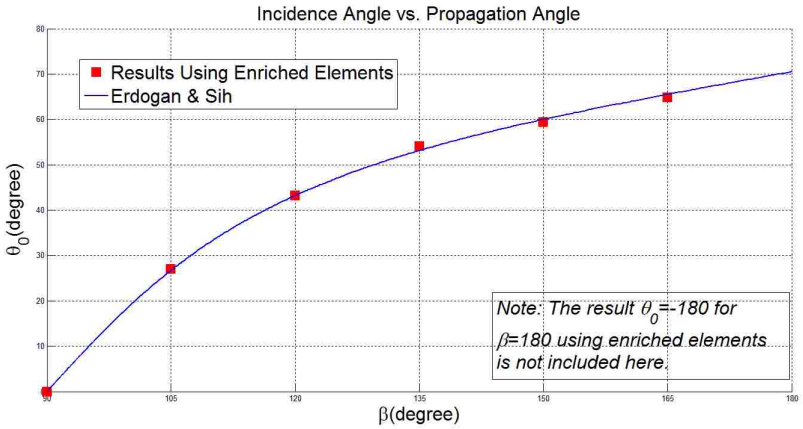

Figure 39: Prediction of crack propagation (homogeneous) under uniaxial loading

As the tangential displacements are applied uniformly (Figure 38-b), the stress state in the *K*-dominant area is of pure mode-II for the crack perpendicular to the bonding line. The corresponding propagation direction, where $\theta_0 = -70.2^o$, is coincident to the well-known homogenous solution -70.5^o. When the crack rotated to the position with an angle of 135^o to the negative vertical direction, the crack-tip area is of pure opening-mode and the crack advances straightforward.

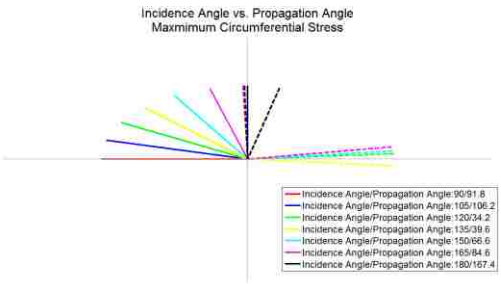

(a) Crack propagation under uniaxial loading as the shear modulus ratio is 23.04

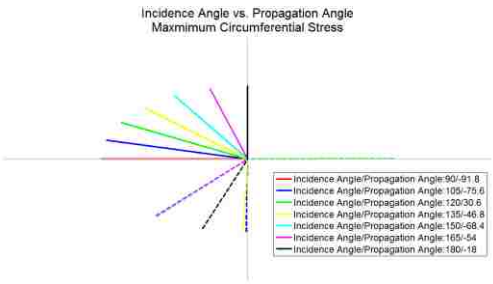

(b) Crack propagation under biaxial loading as the shear modulus ratio is 23.04

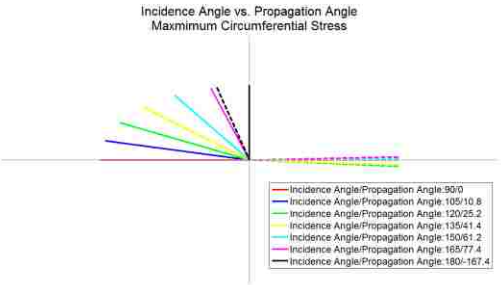

(c) Crack propagation under uniaxial loading as

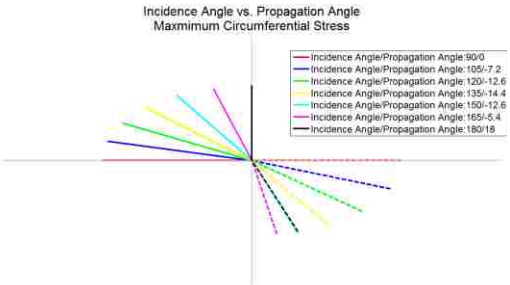

(d) Crack propagation under uniaxial loading as

Figure 40: Prediction of crack propagation (dissimilar) under different loading patterns using modified maximum circumferential criterion

Under biaxial loading, the homogenous crack is kept on a pure mode-I stress state for all impinging angles (Figure 38-c).

When the crack is embedded in dissimilar media, the crack extension prefers the direction not only with the maximum circumferential stress, but also the less stiff side (Figure 40). Under uniaxial loading, it seems the perpendicular main crack, coming from the softer side, is impeded to move forward, and more likely to reflect back to its home side and go along a path close to the interface. The same situation happens to the crack with a rotation angle of 15^o. It also implies they might be deflecting into the interface if the bonding is weak. As the crack continues to enlarge its impinging angle, the propagation breaks up the bonding and shifts near the region normal to the interface. Although decreasing the stress's magnitude, the additional horizontal loading obviously changes the pattern of the crack's extension. Under biaxial loading, the cracks tend to pull back rather than penetrate into the away side. The only exceptional case occurs when crack moves to the position with an angle of 30^o. It should be noted the interface crack is likely to kink into the softer side if the remote loading is severe enough and the bonding is not bad.

In the other side, it seems easier for the crack coming from the stiffer side to move forward into the softer medium. If the uniaxial stresses are loaded, the propagation doesn't have too many choices and is confined to a general direction nearly normal to the interface. With adding horizontal remote stresses, the singularity dominant field is altered to be overwhelmed by the opening mode. All the rotated cracks tend to advance almost straightforward with small deflected angles.

5.6 Anti-Plane Crack

Next, a particular case is demonstrated to verify the new formulation of asymptotic field for the anti-plane mode. A finite central crack terminating at and perpendicular to the bonded interface is studied in a 3-D thin plate with the same geometry as the previous in-plane problem. The

theoretical solutions about the pure anti-shear mode are scarce and very restricted on the boundary conditions. Actually, for an actual 3-D crack, it's difficult to separate the in-plane shear and the out-of-plane shear for consideration since they always concur in the singularity dominant zone. In this study, the finite element model is severely constrained and the in-plane displacements are assigned to be zero only the anti-plane component w is free. So all the nodes

Full/Half	Full
Width	40in
Height	40in
Thickness	2in
Crack Length	2in
P.Strain/Stress	Plane Strain
Crack Mode	Mode III
Loading	Anti-plane displacement w=1in on the bottom and w=-1in on the top
Materials	Shear ratio=23.04 and 0.043

Table 13: Dimension and Material Properties for Anti-Plane Crack Model

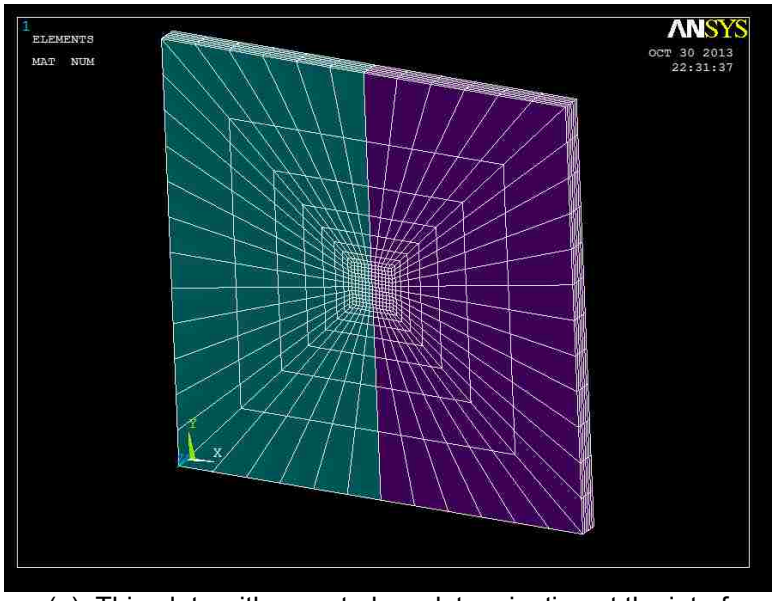

(a) Thin plate with a central crack terminating at the interface

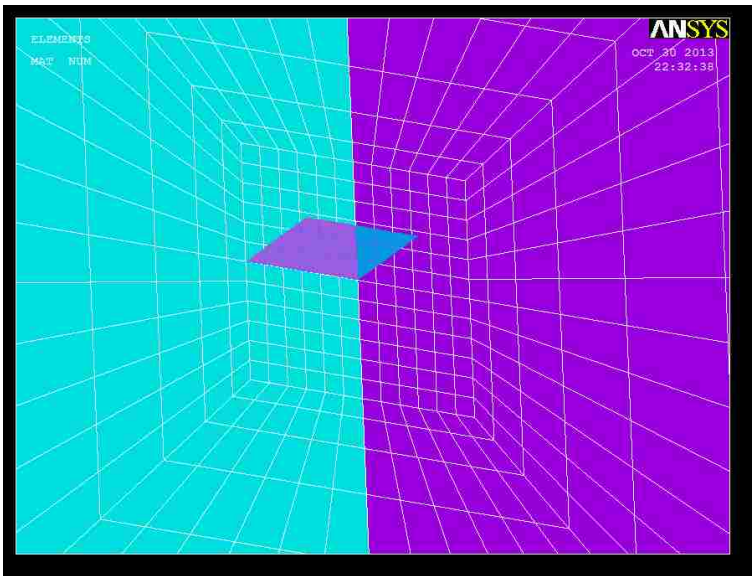

(b) Close-up view of the crack surfaces and front

Figure 41: Anti-Plane Crack Model in ANSYS

are able to move only along the direction parallel to the crack front. Under this kind of condition, it can be observed that the crack-tip's opening field almost vanishes. Also, except on the free surfaces, the magnitude of in-plane shear field is relatively small and can be ignored compared with that of the Mode-III. Since ANSYS and FRAC3D don't accept shear stress as a boundary condition for regular types of element, a uniform anti-plane displacement loading is applied on the top and bottom surfaces of the plate. In this study, two tests are demonstrated and the results are compared with existing solutions.

Results of Test 1

In the first model, y-displacement is constrained for the entire model. The finite element model is allowed to move in x-direction as well as out-of-plane direction. The numerical results are normalized firstly by dividing by the nominal stress on the plane coinciding with crack-surfaces. The nominal stress can be obtained from the shear strain that

$$\frac{\partial w_1}{\partial y} = \frac{\partial w_2}{\partial y} = \epsilon_0, \qquad y \to \pm\infty \tag{5.29}$$

Then the nominal stress on either side the interface is given as

$$\tau_{10} = \mu_1 \epsilon_0 \sin\phi \tag{5.30}$$

$$\tau_{20} = \mu_2 \epsilon_0 \sin\phi$$

where μ_i is the shear modulus and ϕ is the inclined angle of interface as shown in the first chapter. The normalized stress intensity factor for the crack-tip residing on the interface is defined by

$$\overline{K}_{III} = \frac{K_{III}}{\tau_{10} a_0^{1-\lambda_{III}} (2\pi)^{0.5}} \tag{5.31}$$

In the equation above, a_0 is half length of the finite crack. λ_{III} is the strength of singularity for Mode-III. The last term $(2\pi)^{0.5}$ of the denominator is used to unify the definition of K_{III} between in Frac3D and in theoretical solutions.

It can be noticed in Figure 42 and 43 that K_{III} along the crack front is not consistent but comparable with theoretical solutions. The result is fluctuating when the shear modulus ratio is 23.04, and it's confined in the zones close to two ends of the crack front. This behavior may not be explained only by the effect from free surfaces, since this kind of influence is more noticeable as the crack is embedded in the softer material. To get the exact details, the layer of mesh close to the free surfaces should be refined.

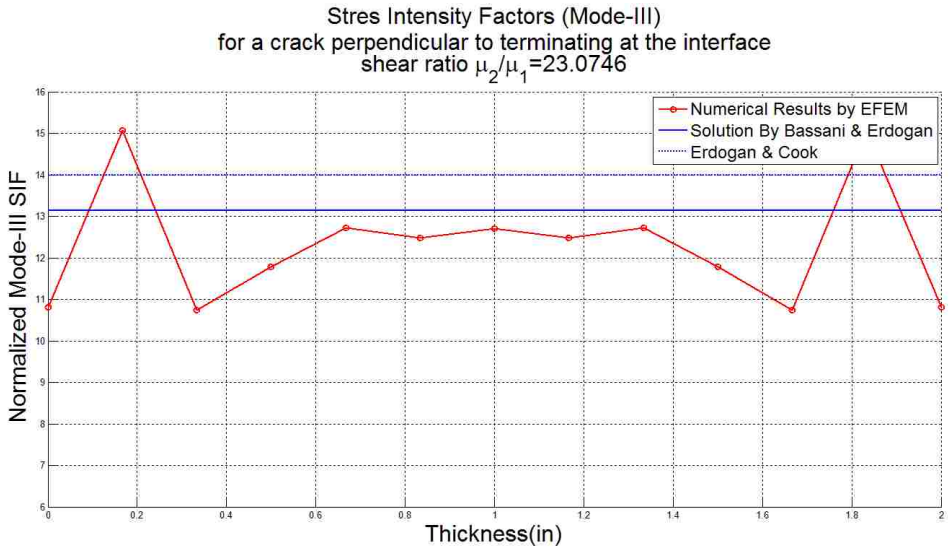

Figure 42: $\frac{\mu_2}{\mu_1} = 23.04$, Mode-III crack penetrates into the stiffer side

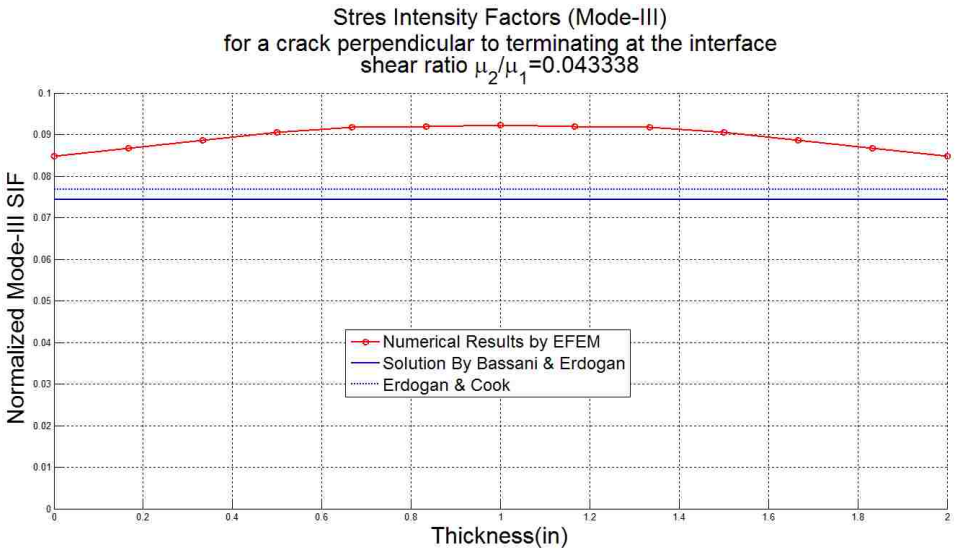

Figure 43: $\frac{\mu_2}{\mu_1} = 0.043$, Mode-III Crack penetrates into the softer side

Actually what is focused on in this test is the pure Mode-III field. However, as mentioned earlier, the required boundary conditions are so hard to be satisfied in a multi-layer finite element model. As the loading is anti-symmetric with respect to the crack surface, the crack-tip on the mid-plane with thickness z=1 inch is the only one where K_I and K_{II} vanish. Therefore, the stress intensity factor of Mode-III at this location is believed to represent a pure anti-plane shear behavior.

Results of Test 2

In the second case, both in-plane displacements are assigned to be zero for the entire model. Then all the nodes are allowed to move only in the direction parallel to the crack front. The numerical values of K_{III} are much more even. However, the fluctuating behavior still exists in the small area near the free surfaces for the crack advancing towards the softer side.

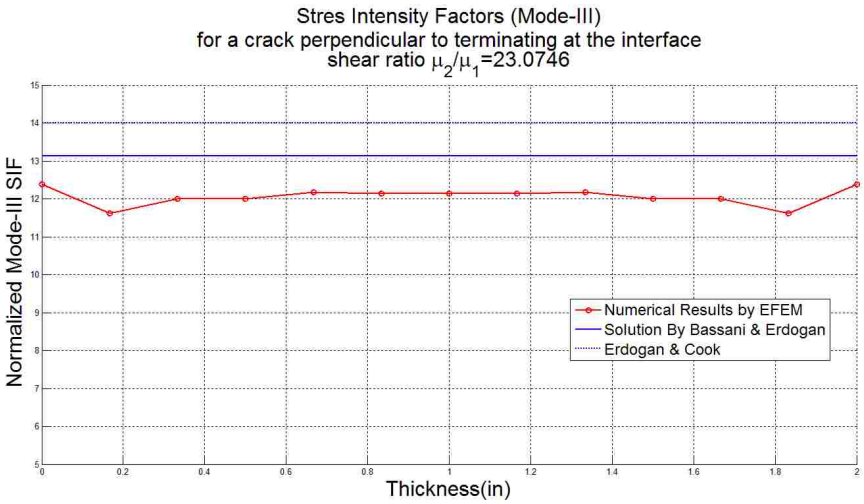

Figure 44: $\frac{\mu_2}{\mu_1} = 23.04$, Mode-III Crack penetrates into the stiffer side

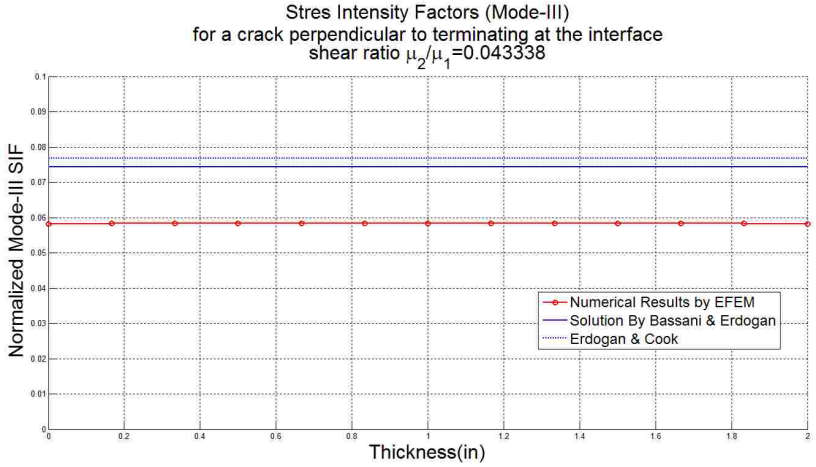

Figure 45: $\frac{\mu_2}{\mu_1} = 0.043$, Crack penetrates to the softer side

5.7 Conclusion and Discussion

Overall, with the help of the enriched elements, the crack problem with an arbitrary angle of incidence can be solved using the finite element analysis. The most benefit is obviously that the stress intensity factors are computed directly with other degrees of freedom. This has greatly simplified and improved the research process on the crack problems, particularly for those with complicated geometries, loading configurations. Also, this method has been suitable for different

types of cracks related to the interface after the new formulation is embedded in the program. The normalized numerical results of the fracture parameters for some specific problems, such as the homogeneous crack, the interfacial crack and the crack normal to the interface, have shown an excellent agreement with the existing theoretical solutions. But due to the sophisticated mathematical work, previous investigations and referenced solutions are very limited for the arbitrarily-oriented crack. Then the discussion is furthered to the approach of using the numerical results to predict the crack's propagation. Since the crack touching the interface is not self-similar progressed, the energy-based parameter cannot be used to characterize the singular behavior. In addition, lack of critical data for such kind of cracks, the stress intensity factors cannot be used as a criterion directly for predicting the crack's extension. In this study, the matrix-based linear system provides a simple way of generating the asymptotic stress and displacement fields around the crack-tip. So the maximum circumferential stress would be a better choice. It is modified to take into account of the multiple material areas. The examples with dummy properties give a good start describing how to determine the advancing crack's location using the results by the enriched element method. Although the results for the homogenous crack are coincident perfectly with those well-known solutions, it has to be emphasized that some idealizations are assumed and the material properties are not real in those examples. So, to be more practical, the experiment-based critical data need to be obtained before the numerical analysis. Moreover, the weakness of the interface should not be ignored. The complete criterion should consider both the crack's extension in the homogenous and the possible debonding between two media.

6 Three-Dimensional Cracks

In practical engineering applications, the fracture actually occurs in the form of three-dimensional cracks, which consists of planar crack surfaces and transverse crack fronts. Basically, two-dimensional analytical solutions based on the theory of elasticity still serve prominently as the foundation for solving 3-D crack problems because of its relative simplicity and efficiency in development and computation.

The classic assumption is that the spacial region surrounding the crack front is controlled by the plane strain state through most the thickness of the solid. But as the crack front gets closer to the free-edge, the plane stress condition dominates. There are also some special opinions from different researchers. Kwon and Sun found that the distribution of stress intensity factors for the 3-D crack vary against different plate thicknesses [59]. In their research, a technique was introduced to compute the fracture parameters without 3-D calculation. This was accomplished by establishing the relationship between the SIF for 3-D crack and the SIF for 2-D crack on the mid-plane.

$$\frac{K_{3\mathrm{D}}}{K_{2\mathrm{D}}} = \sqrt{\frac{1}{1-\nu^2}} \tag{6.1}$$

They also believed there is a transition zone between the plane strain region and the plane stress region. This transition can be characterized by using a parameter called “degree of plane strain” that

$$D_{p\epsilon} = \frac{\sigma_{zz}}{\nu\left(\sigma_{xx}+\sigma_{yy}\right)} \tag{6.2}$$

On the other hand, it cannot be ignored that free edge effects result in rapid changes in the stress intensity factors near the end intersection of the crack front and the exterior surface. Theoretically, the singularity is a function of the angle of intersection and Poisson’s ratio [60, 61]. If the crack front is perpendicular to the free surface and $\nu = 0.3$, for example, the strength of singularity is weaker than 0.5 for the opening mode, but stronger than 0.5 for the in-plane and anti-plane

shearing modes. Thus, as the homogenous crack front touches the free edge, the Mode-I stress intensity factor vanishes, while K_{II} and K_{III} are going to be infinity. Benthem introduced a new concept, named "vertex singularity", to characterize the strength of singular stress state of the crack-tip near the free-loaded surface [62]. His idea can be expressed in the form that

$$\sigma_{\theta\theta} = \frac{V}{\sqrt{2\pi\theta}}\rho^{-\lambda} \tag{6.3}$$

where ρ is the radial distance from the intersection point, θ is the intersection angle measured between the crack front and the normal vector of the free surface. For a specific Poisson's ratio $\nu = 0.3$, the value of vertex singularity is around 0.45. However, this formula is only valid when θ is very small.

Basically, the conventional finite element methods are unable to capture the free-edge effect since the special singularity at the vertex of the crack front is not taken into account. In the analyses using the enriched finite element, the abrupt variation of the stress intensity factors can be observed if adequate layers of elements are created at the region close to the free-surface [48]. Another better way is also provided in the program that the constraints can be specialized for the stress intensity factors since they are considered as extra degrees of freedom. Thus, for desirable purposes, the well-known solution, e.g., $K_I = 0, K_{\mathrm{II}} = K_{III} \to \infty$, can be imposed as boundary conditions at the crack-tip node on the intersection corner node. Ayhan and Nied refined the mesh with 15 layers near the end the crack-front to studied a semicircular crack in a solid. They found that the severe changing behavior of the SIFs is confined in a small region which is at the last 1^{o} along the crack front.

Just as explained previously, in this study, the 3-D crack is regarded as a superposition of the in-plane coupled mode and the anti-plane mode. The asymptotic field is created at each node by cutting a 2-D plane going through this node and perpendicular to the crack front. The idealization is to correlate the 2-D crack singular fields and the 3-D crack behavior. In the enriched finite element method, this strategy is assured by the inside connectivity of the element and the inter-element compatibility.

6.1 Crack Front with Varying singularities

Next, the focus is turned onto the 3-D singularities. For a three-dimensional crack in a homogeneous solid, the stress gradient of the asymptotic field is uniform along the crack front only except the small portion close to the external surfaces. Thus, the strength of singularity arises as a constant 0.5 which is as same as the 2-D homogenous crack. For the cracks in dissimilar media, if the relative angle between the crack surface and the interface is invariant, the strength of singularity is considered equal to the corresponding 2-D value for the entire crack front. For examples as shown in Figure 46, there is a planar crack terminating at the interface with different orientations. The inclined angles of the interfacial surface and the crack surface are equal to 90^o, 116.6^o, 180^o respectively. The corresponding strength of singularity can be computed using the 2-D approach described previously.

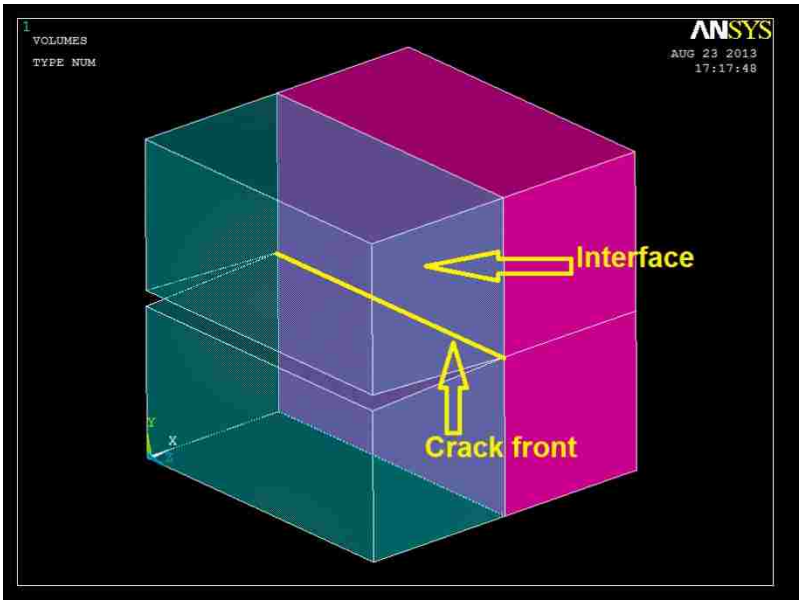

(a) $\phi = 90^o$

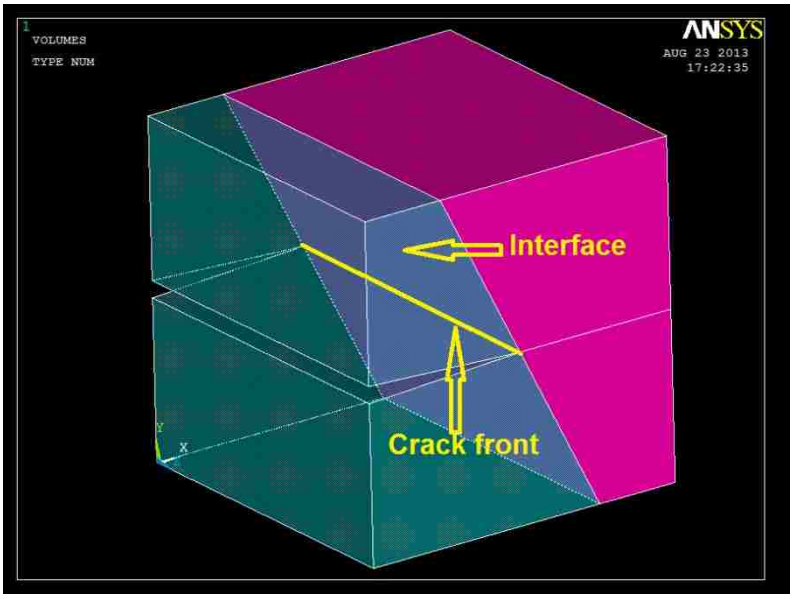

(b) $\phi = 116.6^o$

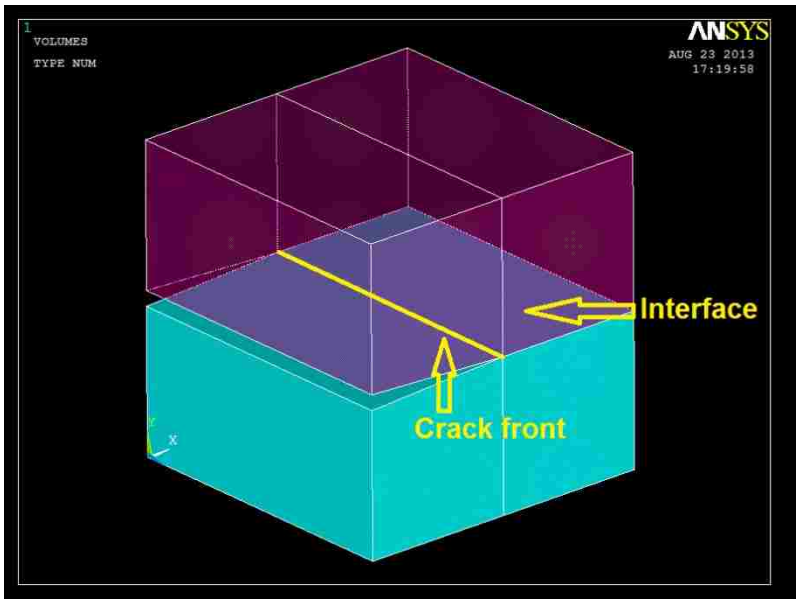

(c) $\phi = 180^o$

Figure 46: Example of 3D Arbitrarily-Oriented Cracks

If this cube is regarded as a sub-part of a global model, the exterior surfaces except the side with the crack opening are cut-boundaries. Thus, the free-edge effects are ignored and all the stress gradients in the direction normal to the crack front can be considered identical along the crack.

But in some completed cases, the crack front might be an irregular curve. As a result, the asymptotic field perpendicular to the crack front at different locations is no longer unchanged.

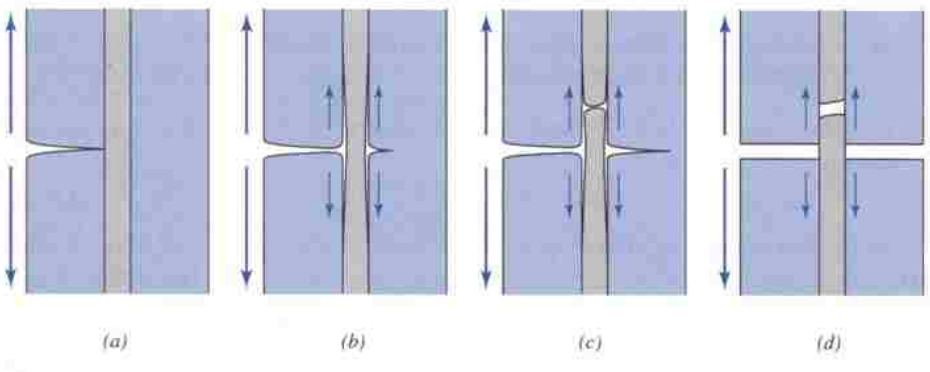

(a) Cracking in fiber-reinforced material

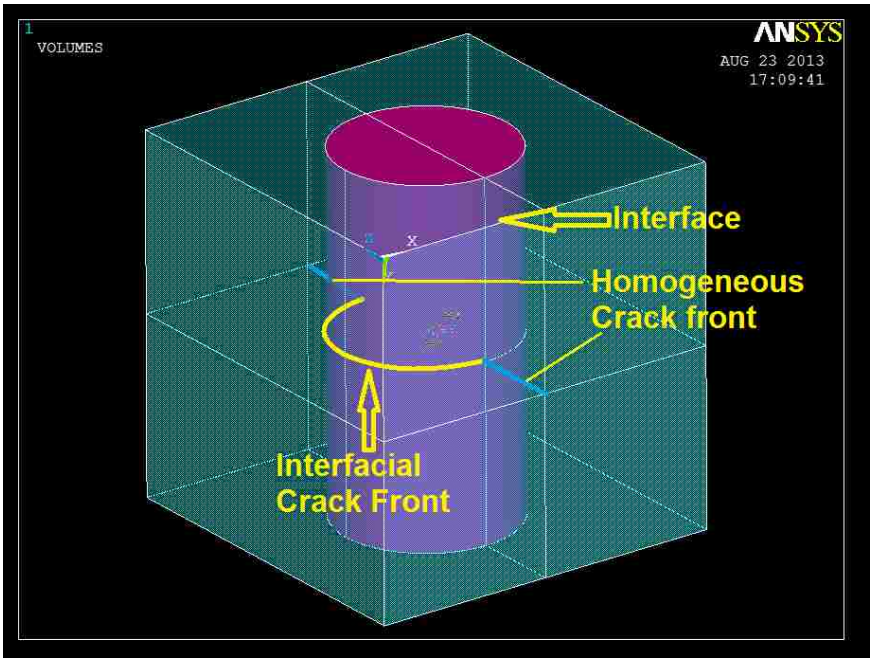

(b) $\phi = 90^o$ along the semi-circular crack front

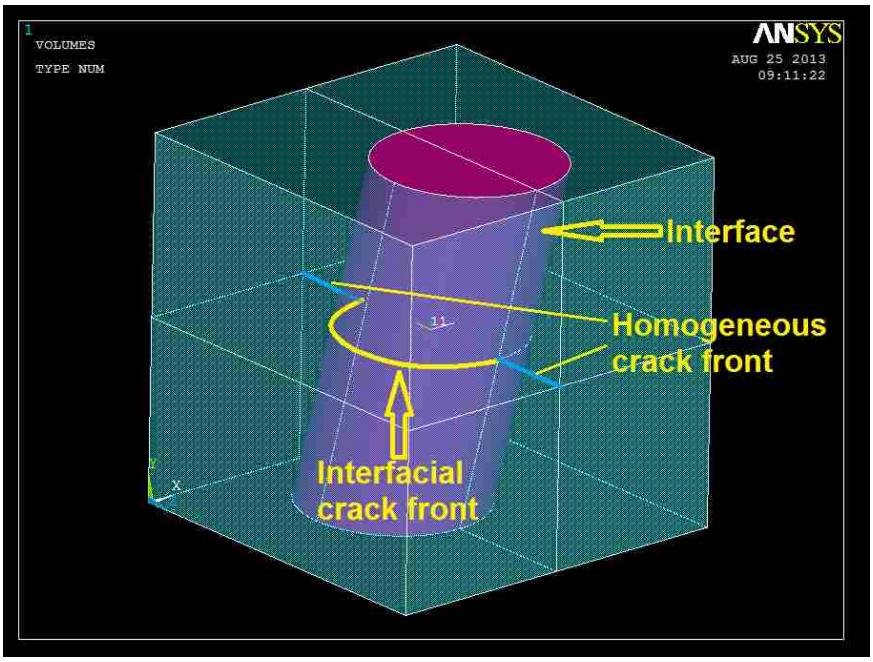

(c) ϕ varies from 73.3^o to 106.7^o along the irregular curved crack front

Figure 47: Crack Front with Varying Impinging Angles in CMC

The example in Figure 47 is an element of the fiber-reinforced crystal. A homogeneous planar crack initiates in the matrix and propagates under cyclic loading. As the crack front arrives at the fiber cylinder, an interfacial crack arises on the bonded border between the fiber and the matrix. It should be noted that since the interfacial plane is curved, at the very first stage, the crack font just touches the fiber at a single point. After that, the original crack may bypass the fiber and continue to break the matrix material, debond the interface with the fiber, or migrate into the fiber and tear apart the cylinder. Obviously the second situation is as desired because it will avoid the deep cracking of the main structure. However, under some severe conditions, it's possible that the homogeneous crack prefers the path into the interior of fiber and make the reinforced part disabled. Thus, it's meaningful to investigate the stress state on the interface as the homogenous crack meets the fibers. In the first case, the original crack is assumed to extend halfway and surround the cylinder, so the intersection boundary between two material surfaces is shaped as a semicircle. Since the axial direction of the fiber is perpendicular to the crack surface, the inclined angle of the interface area on each cut-off 2-D plane of the asymptotic field is 90^o at everywhere along the front arc. The second case is rather complicated as the crack's propagation is not

normal to the fiber's axial direction. The crack front intersecting the exterior of the fiber cylinder would be a semi-elliptical curve, if the same strategy is applied to define the asymptotic crack-tip field, the different inclined angles of the bonded border will lead to varying strengths of singularity throughout the entire front. Firstly, if the local coordinate system is creates as shown in Figure 48, the semicircular crack front can be represented as the function below

$$\frac{x^2}{a^2}+\frac{y^2}{b^2}=1, \qquad b>a>0, \qquad x\le 0$$

where *a* is the radius of the cylinder and one-half of the minor axis of the ellipse, while $b = a/\sin(\phi)$ is the one-half of the major axis.

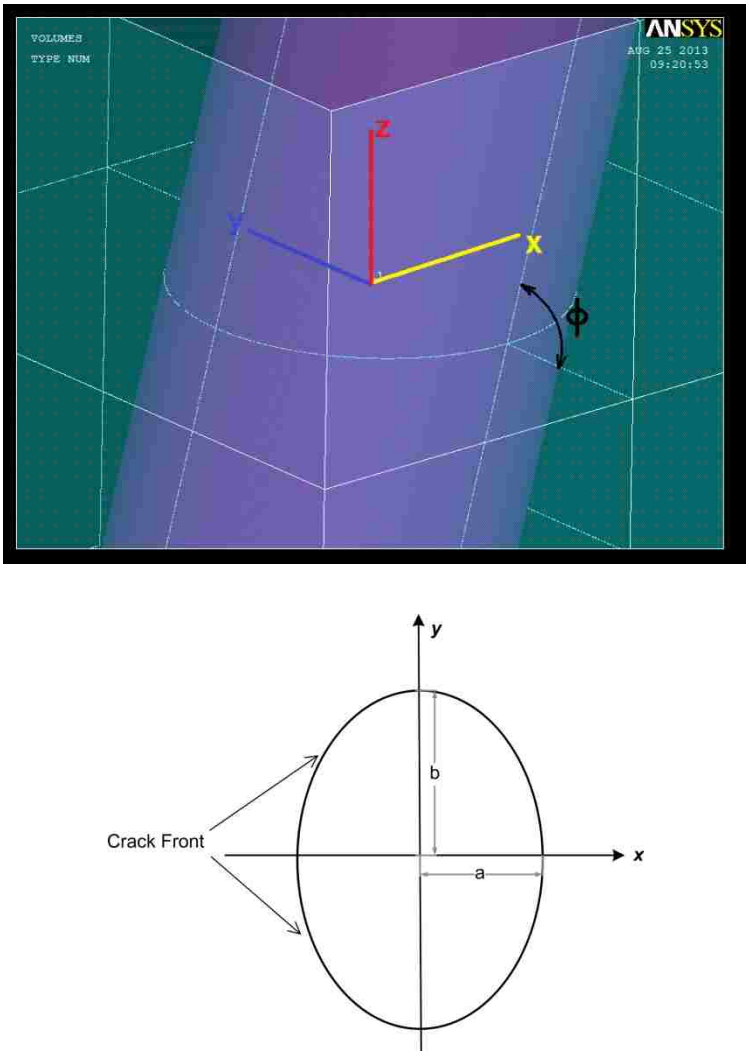

Figure 48: Local Coordinates in semicircular crack front

To get the inclined angle of the interface at a certain crack-tip, a flat plane is specified at this point and required to perpendicular to the crack front. For example, such five planes are created at five different points which are located at 0/4, 1/4, 1/2, 3/4 and 4/4 of the length on the crack front (Figure 49). It can be noted that, if the angle of inclination between the fiber and the crack surface is not far away from 90^o, the interface border in the asymptotic region at any point along the front can be treated as a straight line. Thus, the sketch in Figure 11 can be used to characterize the singular field in such kind of 3-D crack. As the inclination ratio of the fiber becomes larger, even extremely being parallel to the crack surface, the shape of interface is closely like a semicircle surface, which is beyond the research in this study.

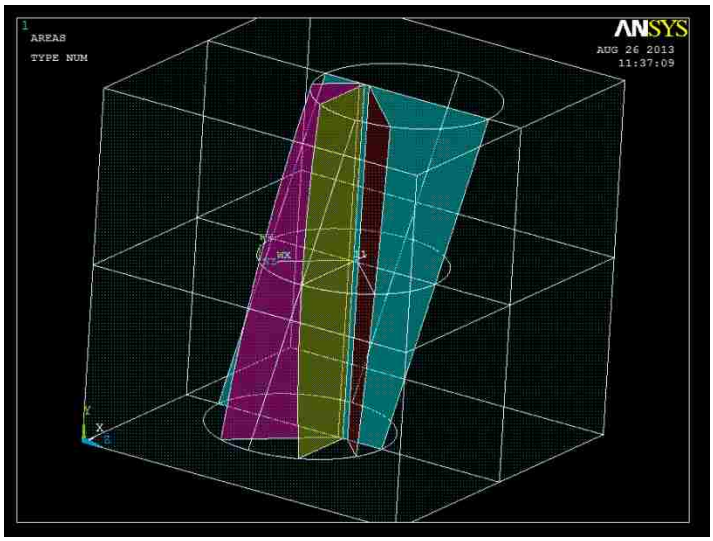

(a)

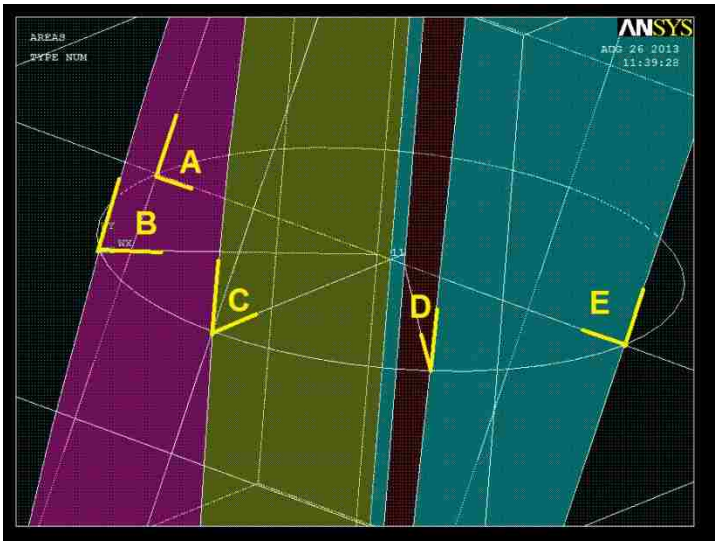

(b)

Figure 49: Cut-Off Planes Perpendicular to Crack Front

In the figure above, the inclined angle of the interface at five locations are symbolized as "*A*", "*B*", "*C*", "*D*" and "*E*" respectively. At location A and E, the specific values can be obtained directly by the slop ratio of the fiber axis. At location C, the crack surface is perpendicular to the interface. The angle values of the other locations need to be computed using the local crack-tip coordinates.

For the fiber with a slop ratio $\frac{dy}{dz} = 0.3$, the distribution of interface angles along the entire crack front is demonstrated in Figure 58. The corresponding strengths of singularity are also plotted in Figure 59.

6.2 Finite Element Model and Numerical Results

To check the new formulation of asymptotic field, a relatively complicated mode is investigated. A cube matrix with a fiber going through it is created. An edge crack starting from the matrix meets the fiber's surface. The homogeneous crack continues to advance surrounding the fiber and finally generate a curved crack terminating at the interface. The dimension of the solid model is given in Table 14. A cube matrix is traversed by a cylindrical fiber. This can be regarded as a sub-model of a global fiber-reinforced solid. Three cases are tested with different material combinations or different geometries. In the first one, the crack surface is normal to the fiber's

axial direction (Figure 50), so the interface intersects the crack surface with 90 degrees as a constant at any location. In the second test, the material mismatch is removed and a homogeneous crack is given. In the last one, the fiber has an inclined angle around 16.69 degrees (Figure 51). Therefore the interface impinging angle varies along the crack front. Four upper-corner nodes are applied with equivalent point forces in the vertical direction.

Full/Half	Full
Width	2in
Height	2in
Thickness	2in
Radius of Fiber	0.5in
P.Strain/Stress	Plane Strain
Crack Mode	Mixed Mode
Loading	Point force at four top corners $F_y = 1\ lbf$
Materials	Shear ratio=23.04 and 0.043

Table 14: Dimension and Material Properties for 3D Inclined Crack Model in CMC

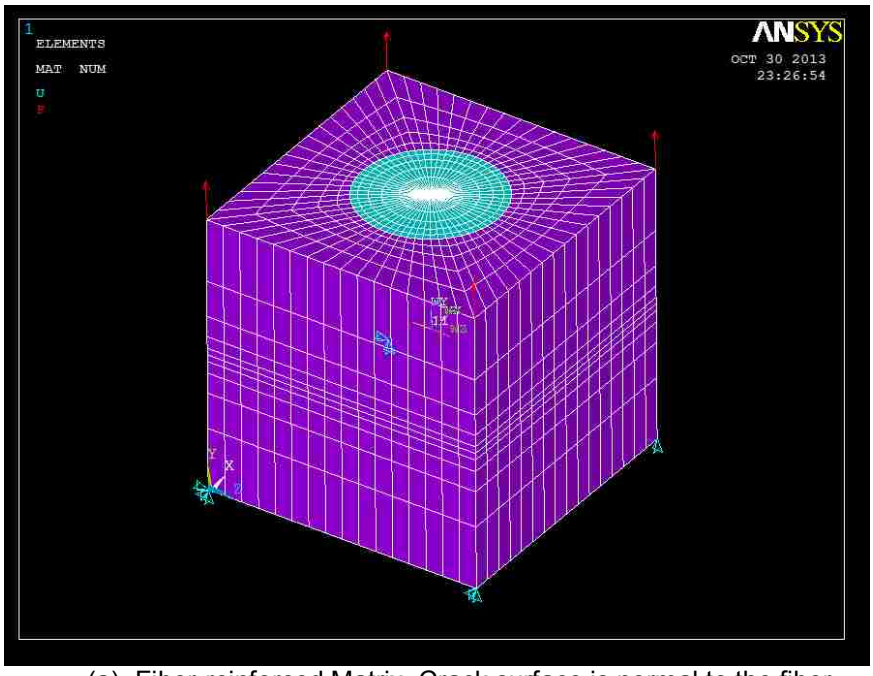

(a) Fiber-reinforced Matrix, Crack surface is normal to the fiber

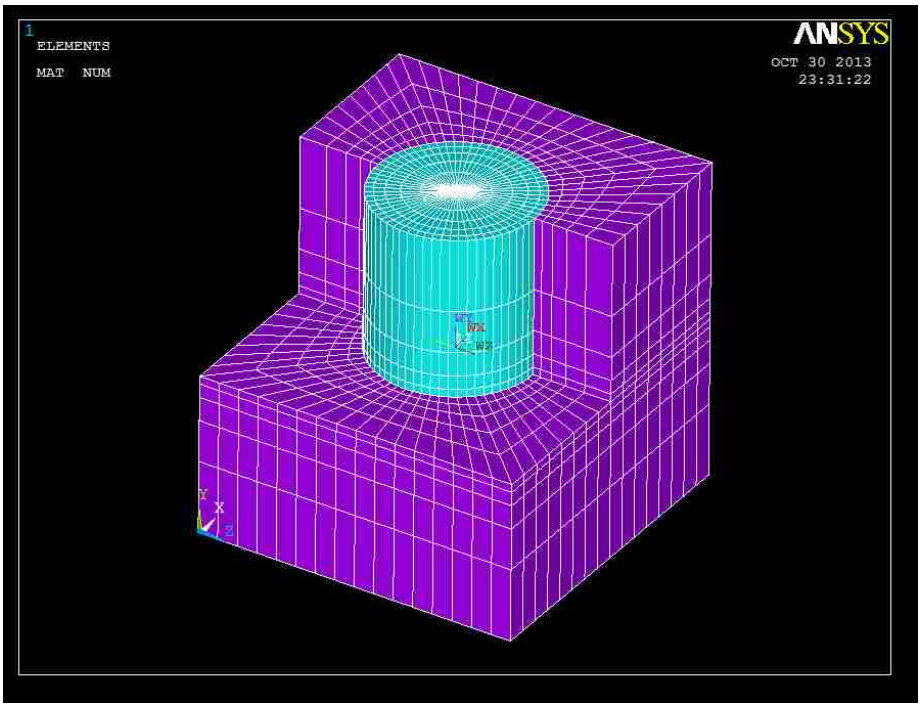

(b) Semi-perspective view of the fiber:

Figure 50: Crack Normal to Interface In CMC

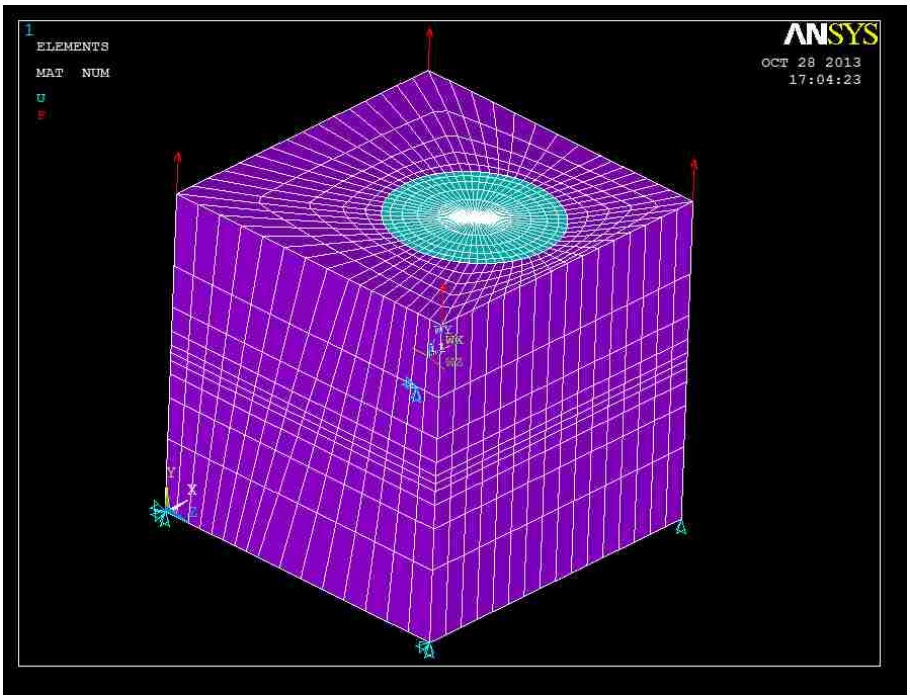

(a) Fiber-reinforced Matrix, Crack surface is not normal to the fiber

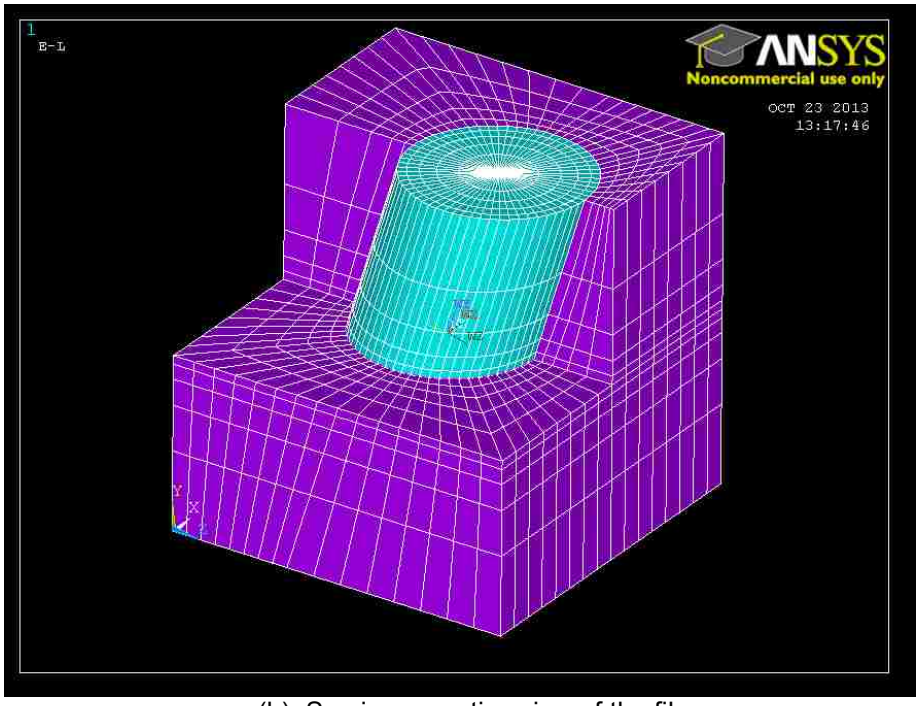

(b) Semi-perspective view of the fiber

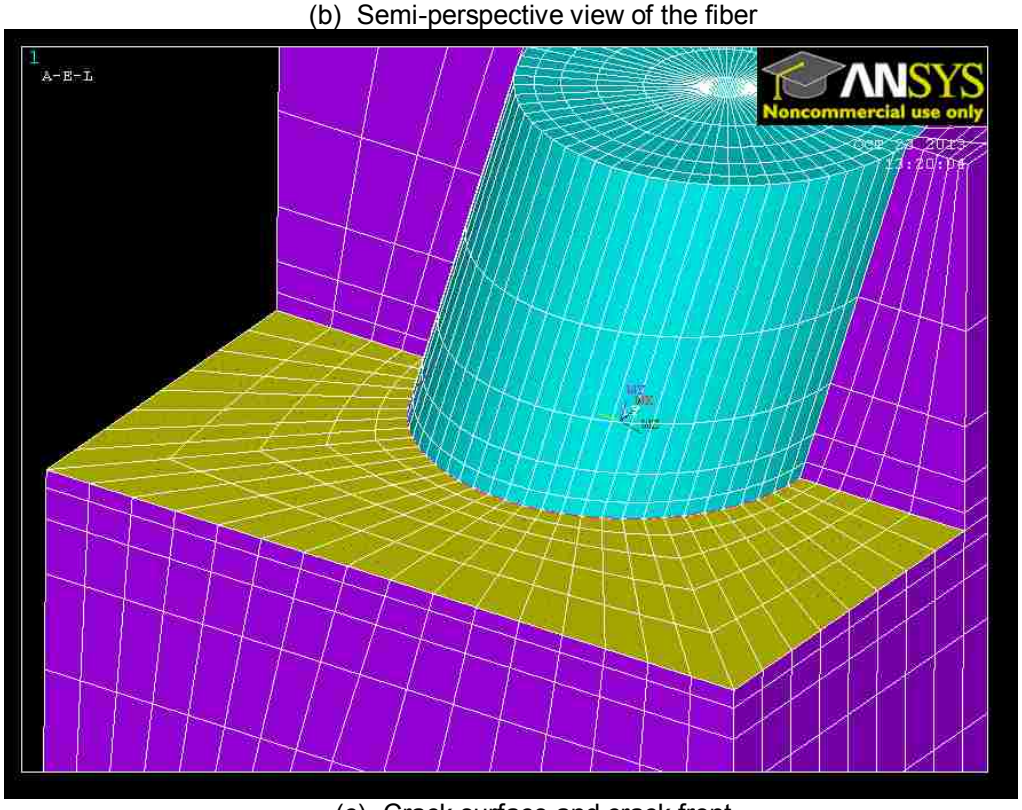

(c) Crack surface and crack front

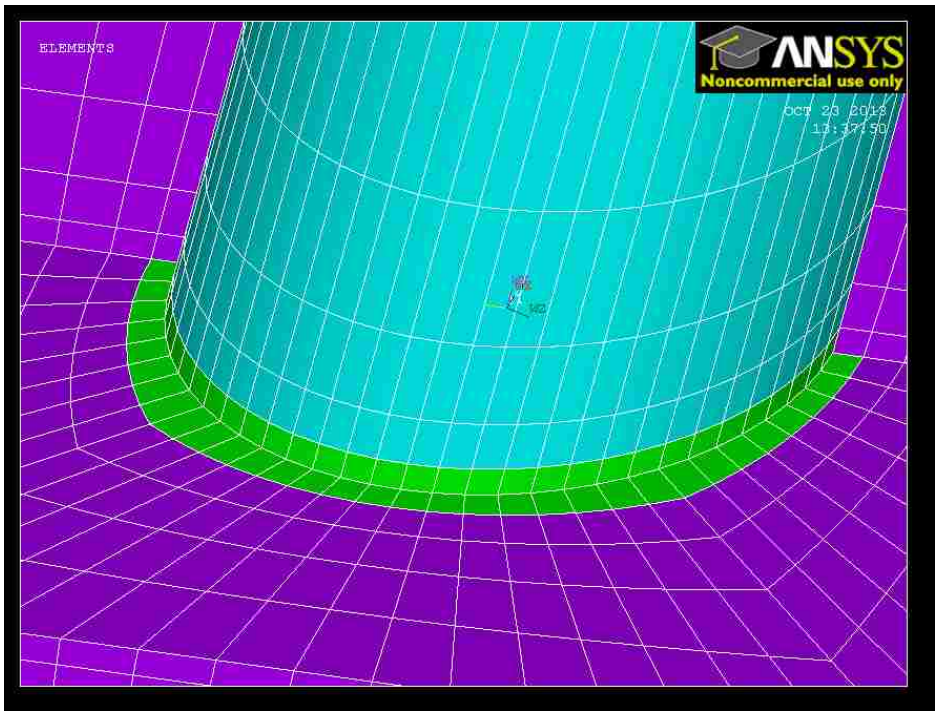

(d) Close-up view of the crack-tip elements

(e) Only the crack-tip elements are selected

Figure 51: Crack Inclined to Interface In CMC

Actually, the whole crack front in this model consists of three sections, a semi-circular crack front and two straight crack fronts. The former one touches the interface between the fiber and the matrix and can be treated as a bi-material crack front. The latter parts are embedded within the homogeneous solid so they are still considered as the front of a homogeneous crack. From Figure 51, it can be observed that at the concave corners where the semi-circle front connects the straight sections, there should be a transition area between two different asymptotic fields. A strategy in FRAC3D is to regard them as two cracks and compute the results simultaneously. In this study, for simplicity, only the bi-material crack is taken into account.

Results of Test 1

The crack front is a semi-circle. Since the crack's impinging angle is constant as 90 degrees along the whole crack front, the split singularities are identical. The specific values of λ have been given in Figure 52 & Figure 53. Compared with λ_1 and λ_2, the singularity of Mode III is stronger as $\frac{\mu_2}{\mu_1} = 23.04$, and weaker as $\frac{\mu_2}{\mu_1} = 0.043$.

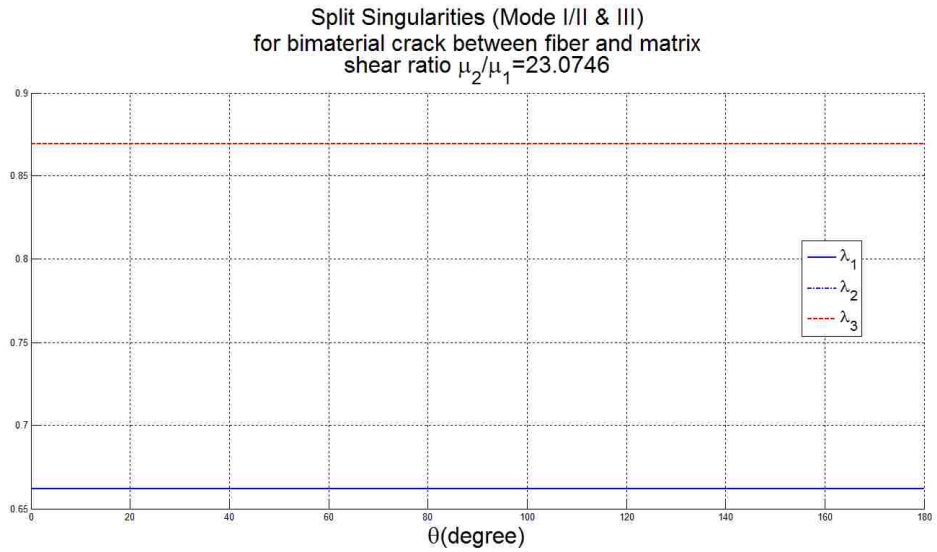

Figure 52: Stress Singularities for Crack Normal to Interface in CMC as $\frac{\mu_2}{\mu_1} = 23.07$

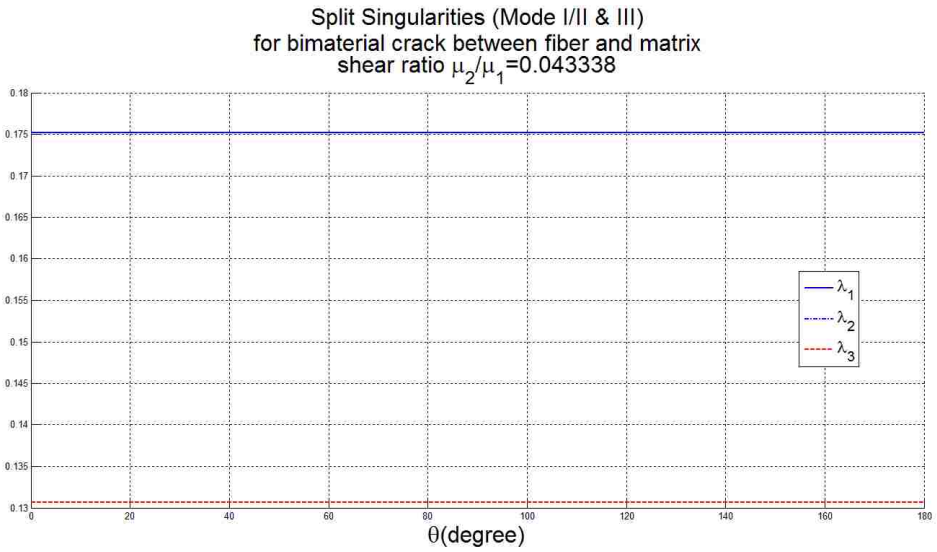

Figure 53: Stress Singularities for Crack Normal to Interface in CMC as $\frac{\mu_2}{\mu_1} = 0.043$

However, the stress intensity factors exhibit different magnitudes for three modes (Figure 54, 55). To make it clear, they are normalized with their maximum absolute value respectively. It's obvious that the magnitude of K_{II} and K_{III} are relatively small and might be ignored for both material combinations. Due to the difference between the in-plane and anti-plane stress gradients, a more reasonable way of determining the stress status in such a 3-D crack tip would be either the method based on energy theory or using the principle stress concept. However, according to the

previous discussion of 2-D cracks, the energy release rate cannot be used when the crack-tip stops at the interface. Furthermore, it's well known that the opening mode within the SDZ predominates the crack's propagation if the crack bears tensile stresses, and the direction is preferred to minimize the shear stresses. This agrees very well with the principle stress theory.

In actual product of ceramic matrix reinforced by fibers, it's very common that the original cracking extends widespread across a bundle of fibers. For an initially bonded fiber, debonding process occurs by the imposed tensile stress on the interface as the matrix crack passes through it [4]. For a frictionally restrained fiber, the sliding may occur when the interfacial shear stress exceeds the friction. For the first case, the existing solutions are almost obtained based on the assumption that the crack had propagated in the matrix and resulted in the detachment along the interface. Accordingly, the critical strain energy release rates in the matrix and the critical debonding energy release rate are compared to determine the crack's advancing trend, and calculate the length of sub-crack. In this study, a theoretical solution is derived for the instant moment particularly as the crack-tip touches the interface without any further action. The interface is assumed to be perfectly bonded, and no sliding, debonding or spalling is taken into account. The specific stress intensity factors just characterize the stress status in the vicinity of crack tip. But the complete asymptotic stress and displacement fields can be formulated in matrix form for the whole crack front. The approach described for the 2-D crack may be extended and applied to a 3-D situation. After appropriate stress transformations, the maximum principle stress may be utilized as a criterion to find the point with highest possibility to advance. It should be mentioned that since this is a multi-material system, the difference of homogenous critical stresses as well as the critical interfacial stress should not be neglected when looking for the potential sub-cracking start.

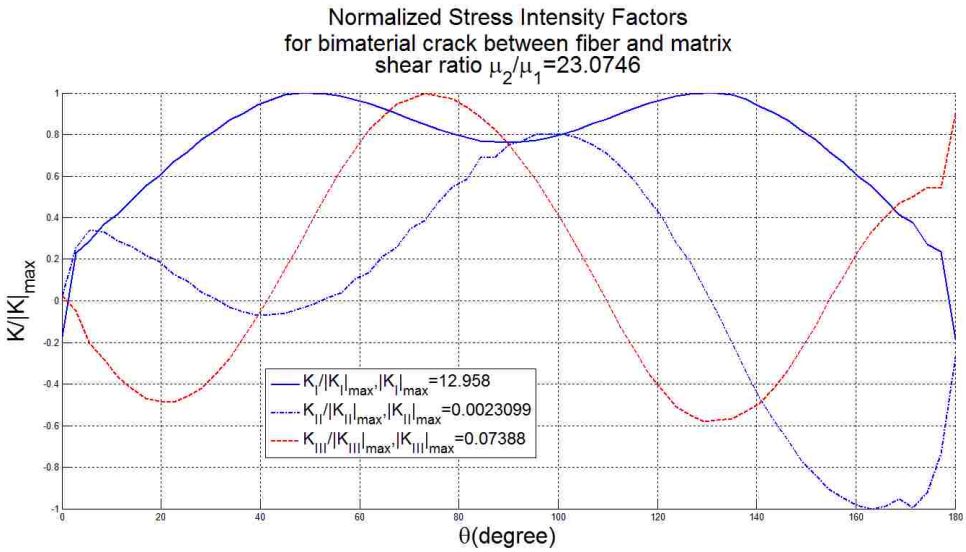

Figure 54: SIFs for Crack Normal to Interface in CMC as $\frac{\mu_2}{\mu_1} = 23.07$

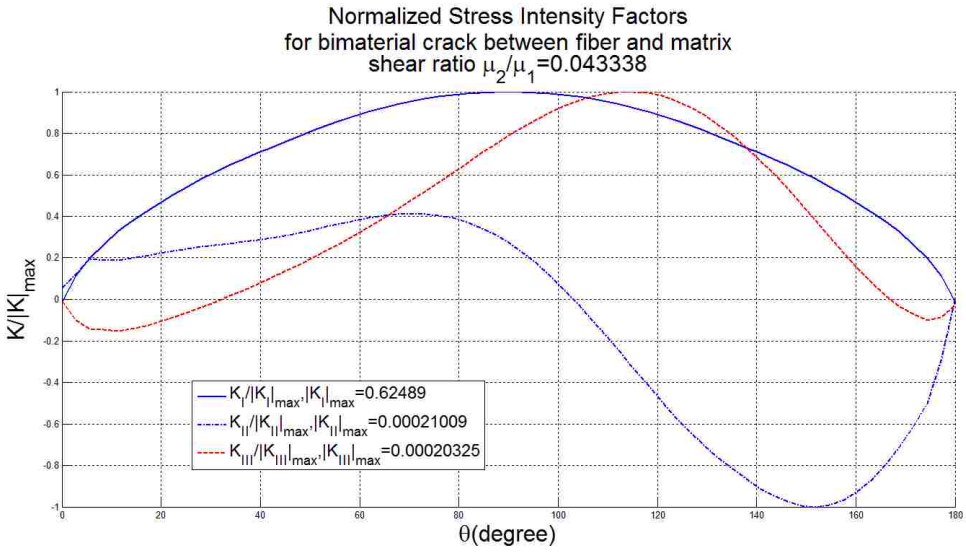

Figure 55: Stress Singularities for Crack Normal to Interface in CMC as $\frac{\mu_2}{\mu_1} = 0.043$

In Figure 54, the crack is in the softer material, and it's not hard to find that the maximum opening stress occurs at two symmetrical locations, 50 degrees and 130 degrees rotating from the straight section of the crack front. Actually this "bi-maximum" phenomenon is caused particularly by the applied loading and boundary conditions. Furthermore, it implies there might be possible that the crack propagates concurrently from two locations. The asymmetry of K_{II} and K_{III} may come from numerical errors by the discrepancy of singularities for different modes. It should be mentioned

that the difference $|\lambda_1 - \lambda_3| \approx 0.207$ is relatively larger than 0.045 of the other case that the shear modulus ratio is reciprocal.

If the crack is launching from the stiffer side (Figure 55), the results are distributed more smoothly. But the opening tensile stress still dominates the asymptotic field. The maximum value occurs at the mid-point of the crack front.

Results of Test 2

In this test, the material mismatch disappears and the crack is simplified to a homogeneous crack. For this case, the singularities for three modes are the same and equal to 0.5 (Figure 56). The maximum stress happens not at the mid-point of the crack front. This may be explained by those four corner point forces that cannot distribute the loading evenly along the whole crack front.

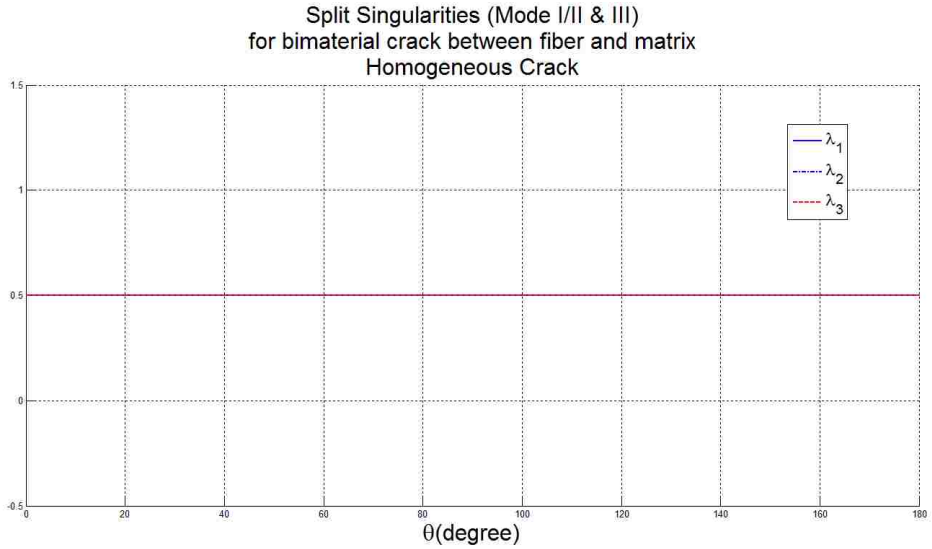

Figure 56: Stress Singularities for Homogeneous Crack in CMC

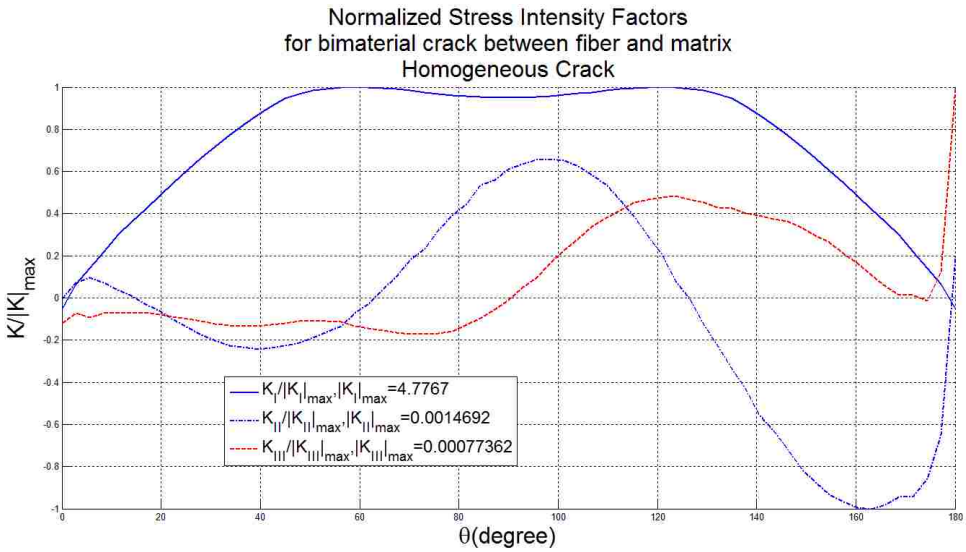

Figure 57: SIFs for Homogeneous Crack in CMC

Results of Test 3

In this case, the matrix's geometry, the boundary constraints and the loading conditions stay unchanged. The fiber's diameter is also kept the same but it is leaned to form a specific angle between the fiber's axial direction and the global axis normal the crack surface. As a result, the crack front turns into a semi-elliptical circle with the axis ratio 1.044. The varying crack's impinging angle is shown in Figure 58. As predicted previously, the distribution of angle is symmetric about $\theta = \frac{\pi}{2}$, where the crack surface is perpendicular to the interface.

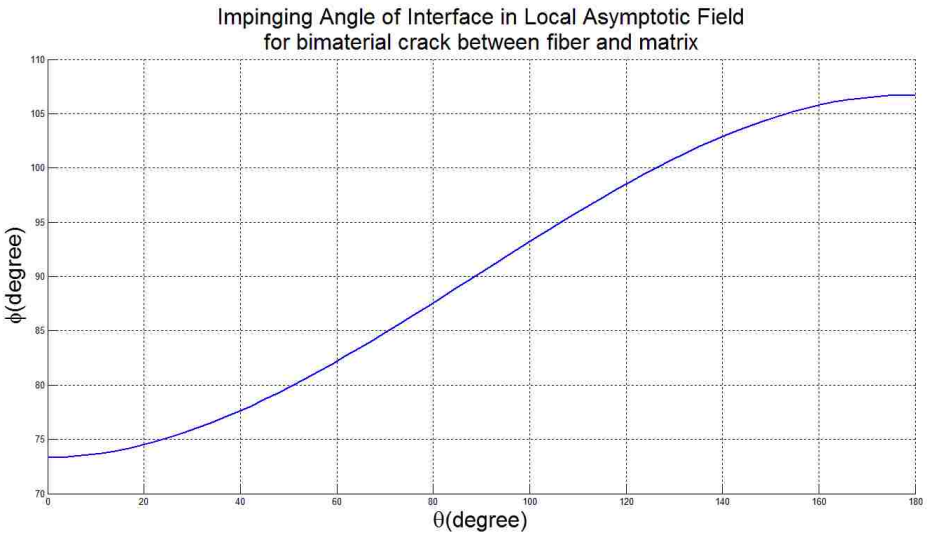

Figure 58: Varying Impinging Angle of Crack Front to Interface in CMC

The split singularities of in-plane mode arise as two different real numbers (Figure 59 & 60), and convert to a repeat root at the symmetric point. The singularity for Mode-III also changes along the crack front and has its extremum at the mid-point.

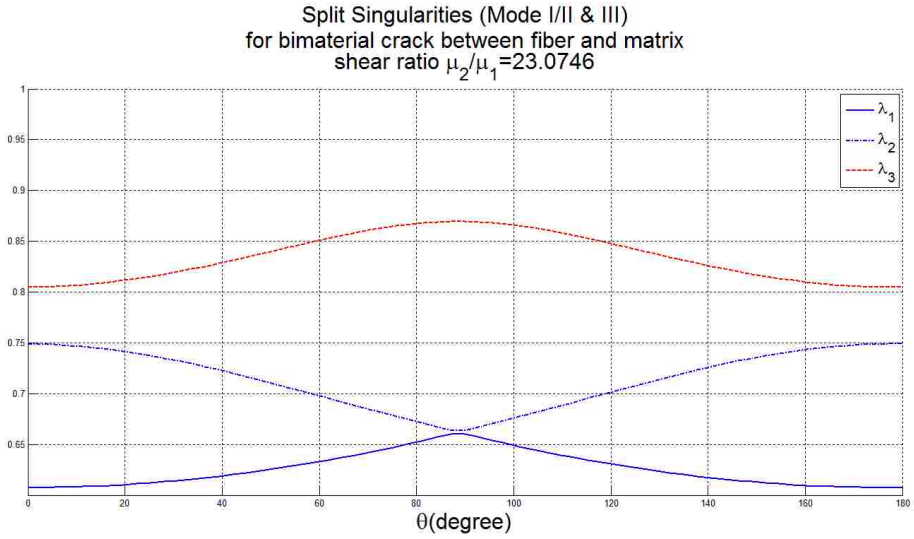

Figure 59: Split Singularities along Crack Front with Varying Impinging Angle in CMC as $\frac{\mu_2}{\mu_1} = 23.07$

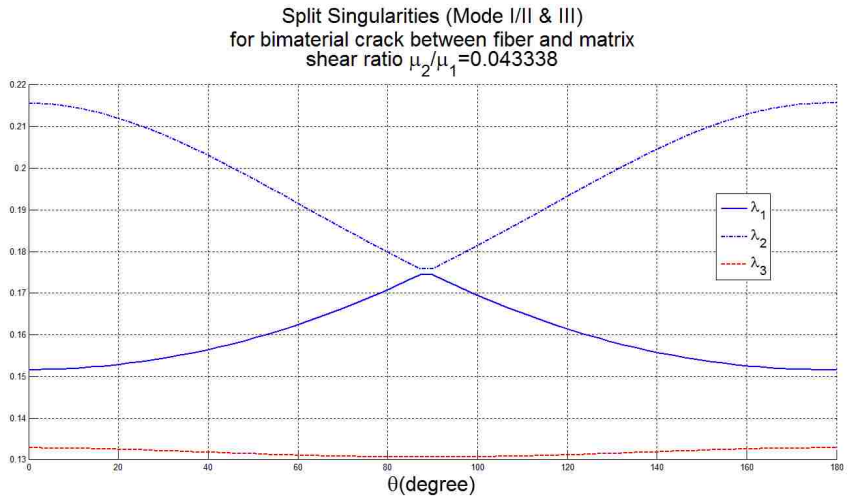

Figure 60: Split Singularities along Crack Front with Varying Impinging Angle in CMC as $\frac{\mu_2}{\mu_1} = 0.043$

The normalized SIFs display the fluctuating behavior again, especially as the interface angle is approaching to 90 degrees (Figure 61 & 62). However, since the singularities are not uniform, K and λ should be taken into account together to determine the stress status.

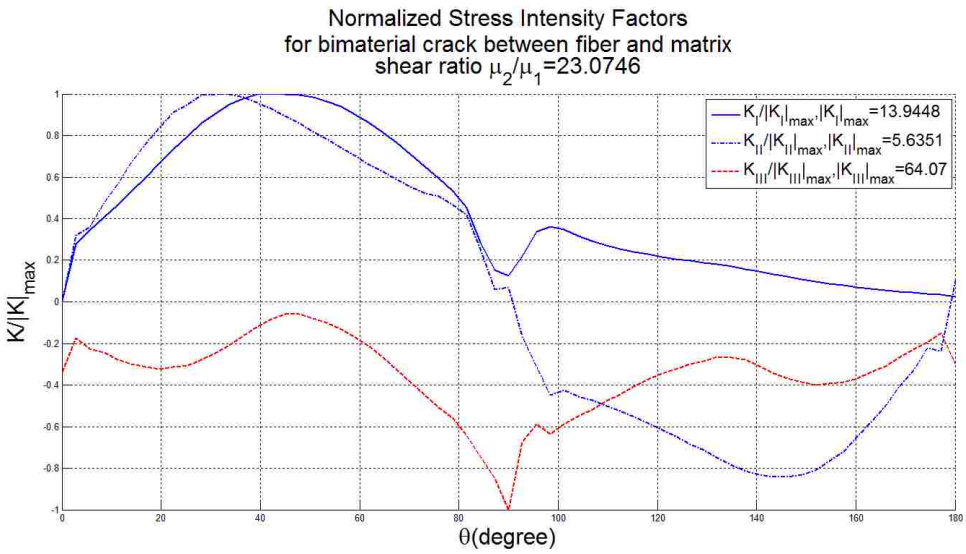

Figure 61: SIFs along Crack Front with Varying Impinging Angle in CMC as $\frac{\mu_2}{\mu_1} = 23.07$

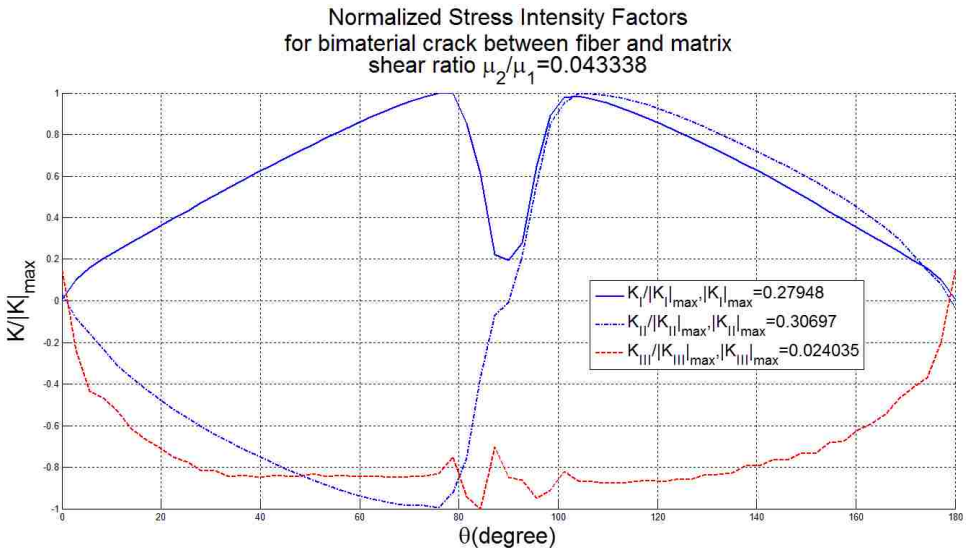

Figure 62: SIFs along Crack Front with Varying Impinging Angle in CMC as $\frac{\mu_2}{\mu_1} = 0.043$

6.3 Some Issues for 3-D Crack tip element

In numerical analysis, to get an approximation of the definite integral in the enriched element formulation, the Gauss quadrature rule is applied to give the weighted sum of function values at specified points within the domain of integration. This technique works fine with 2-D crack problems, but brings in a special case for 3-D enriched crack tip elements which is worth emphasizing on it.

As discussed previously, the asymptotic field is built surrounding a crack-tip by cutting off a plane perpendicular to the crack-front at the tip point. In finite element analysis, the integration rule requires to create such as plane going through not the structural node in the element but the integration point for the element.

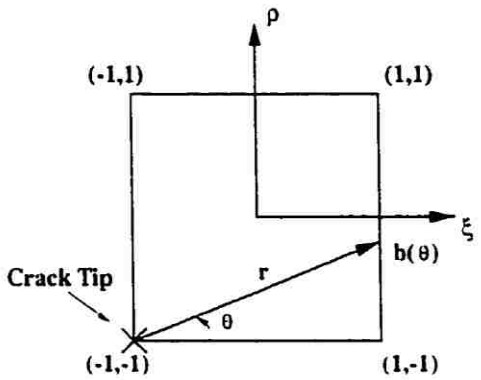

Figure 63: 2D Local Coordinates at Crack-tip

For 2-D cracks, the crack-tip and the integration points are embraced in the same plane which is normal to the anti-plane normal vector (Figure 63). Thus, the asymptotic field of every integration point can be represented by the formulation derived for the crack-tip.

In 3-D crack problems, the integration points are located in 3-D coordinates. Their asymptotic field is defined by the corresponding plane and the crack-tip coincides with the perpendicular intersecting point on the crack-front. As seen in Figure 51-e, if irregular-shaped or skewed elements are used to fit the front curve, it's possible that the normal plane going though some integration point will intersect the crack front but on the edge of the other element. Under this kind of situation, the asymptotic fields of adjacent elements may contribute reciprocally to each other. The element stiffness matrix will depend on unknown stress intensity factors associated with a different enriched element.

This problem was firstly addressed by Ayhan and Nied [48]. They deal with it in a consistent manner using the same expressions derived previously, but with additional unknown out-of-element stress intensity factors embedded into the element formulation. In a typical calculation, when a plane's normal intersection on the crack front is detected outside the self-element, new unknown stress intensity factors are involved to formulate the enriched element stiffness matrix, from elements immediately adjacent to the current element. For example as shown in Figure 64, if the element attaching to the crack front and embracing the intersection point A_0 is a cubic element, nine additional unknown DOFs (K_I, K_{II}, K_{III} at 3 neighbouring nodes except the shared node) should be included in the stiffness matrix of the element containing point *A*. In the existing

code of enriched finite element, at most four successive neighbouring element (2 to the left and 2 to the right) is taken into account to generate the elemental stiffness matrix. Accordingly, the dimension of the augmented matrix would be $3 \times (S + 5 \times N - 4)$, in which S is the number of nodes in one element, and N indicates the element's dimension order ($N = 2$ for linear elements; $N = 3$ for quadratic elements; $N = 4$ for cubic elements).

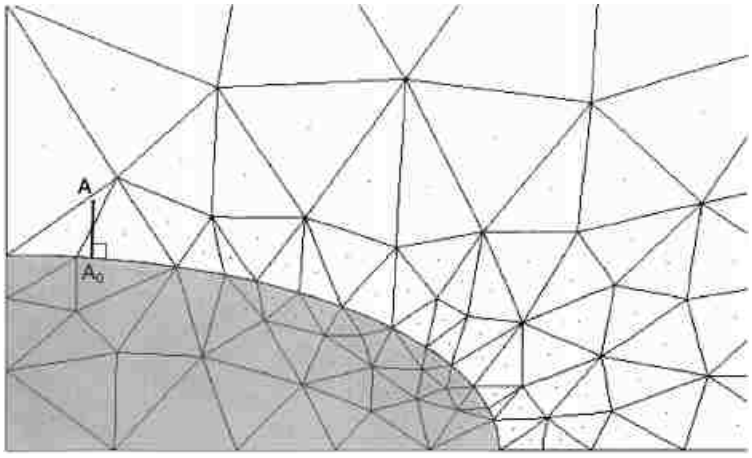

Figure 64: Planform view of a semi-elliptic crack showing vector from one enriched element crossing through to another enriched element on the crack front [48]

Determination of the singularity at the integration point

It's already shown that, in finite element analysis, the plane of asymptotic field is defined at integration points rather than at crack-tip nodes. Thus, as the singularity varies along the crack-front, the specific value for the normal plane traversing the integration point also needs to be determined.

First of all, the singularity at each element node touching the crack front is to be computed. Since the interface plane is not a flat or regular surface, some nodes out of the crack front are required to define the curvature of interface. In enriched finite element method, a strategy is applied to automatically adjust the crack-tip element's orientation. Then the local nodal numbers coinciding to the front is always consistent. Meanwhile, for those enriched elements attaching to the interface plane also have the same nodes on the bi-material border. These nodes can be connected element by element to generate a "reference line" that is linear, quadratic or cubic piece wisely. The intersection point of the normal plane and this reference line must be located on

a segment between two neighboring nodes. If the mesh density along the crack front is refined appropriately, the line segment between every two consecutive nodes can be treated as a straight line. Then the intersection point is obtained using the approach as below.

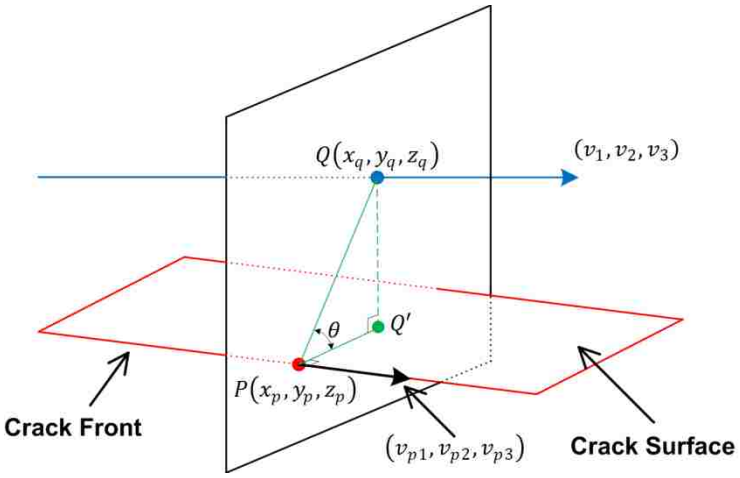

Figure 65: Creation of Local Coordinates at Crack-tip for Varying Impinging Angle to Interface

As seen in Figure 65, if a straight line or an arc with negligible curvature is not parallel to a flat plane in space, these must be an intersection point between them. This plane is created perpendicular to the crack front at the crack-tip node *P*. The line is assumed to pass through a point $Q(x_q, y_q, z_q)$ and along the direction defined by vector (v_1, v_2, v_3). In another hand, a point $P(x_p, y_p, z_p)$ is considered on a flat plane with the normal vector (v_{p1}, v_{p2}, v_{p3}). The line can be written as an equation in the parametric form

$$x = x_q + v_1 t, \qquad y = y_q + v_2 t, \qquad z = z_q + v_3 t \tag{6.4}$$

The plane is represented using an equation in the point-normal equation

$$v_{p1}(x - x_p) + v_{p2}(y - y_p) + v_{p3}(z - z_p) = 0 \tag{6.5}$$

Substituting Equation (6.4) into Equation (6.5) gives the expression of independent variable *t* that

$$t = \frac{(x_p - x_q)v_{p1} + (y_p - y_q)v_{p2} + (z_p - z_q)v_{p3}}{v_{p1}v_1 + v_{p2}v_2 + v_{p3}v_3} \tag{6.6}$$

If the denominator part is equal to zero, it indicates the line is parallel to the plane. If it is not, putting back *t* into equation (6.5) gives the coordinates of the intersection point *Q*. Next, finding

the projective point *Q'* on the crack surface plane, the angle $\angle QPQ'$ is just the inclination of the interface with respect to the crack plane. The strength of singularity is then calculated for this nodal location, and the same process is carried out for all the nodes on the crack front.

To get the singularity for the asymptotic field plane passing through a Gauss integration point, the same strategy as for the stress intensity factors is applied using the interpolation functions $N_i(\Gamma)$. $\lambda_I(\Gamma), \lambda_{II}(\Gamma)$ represent the split singularities of mixed-mode in-plane field varying along the crack front, and $\lambda_{III}(\Gamma)$ is another one for anti-plane field. They are defined by the interpolation functions as

$$\lambda_I(\Gamma) = \sum_{i=1}^{s} N_i(\Gamma)\, \lambda_I^i \tag{6.7}$$

$$\lambda_{II}(\Gamma) = \sum_{i=1}^{s} N_i(\Gamma)\, \lambda_{II}^i \tag{6.8}$$

$$\lambda_{III}(\Gamma) = \sum_{i=1}^{s} N_i(\Gamma)\, \lambda_{III}^i \tag{6.9}$$

where $\lambda_I^i, \lambda_{II}^i, \lambda_{III}^i$ are the stress singularities at the *i*th crack tip node in a single enriched element. Please note that $N_i(\Gamma)$ is the element shape function along the element edge coinciding with the crack front. The number of shape function *s* depends on the dimension order of an element. For example, for a 20-noded quadratic hexahedron element that has a crack front located on the edge defined by the $\eta = -1, \rho = -1$, with $-1 \le \xi \le 1$,

$$\begin{aligned} \lambda_I(\Gamma) = \lambda_I(\xi) = &\frac{1}{2}(-\xi + \xi^2)\lambda_I^1 + (1 - \xi^2)\lambda_I^2 \\ &+ \frac{1}{2}(\xi + \xi^2)\lambda_I^3 \end{aligned} \tag{6.10}$$

In the equation above, $\lambda_I^1, \lambda_I^2, \lambda_I^3$ are the first strength of singularity at the nodes located at $\xi = -1, \xi = 0, \xi = 1$, respectively. If the projective location of some integration point on this edge is defined as $\xi = \xi_p$, $\lambda_I(\xi_p)$ would be the resulting singularity. $\lambda_{II}(\Gamma)$ and $\lambda_{III}(\Gamma)$ are defined in a similar manner.

7 User-Defined Element with Enriched Features

The application of enriched finite element has been described in previous chapters. The facture parameters are computed as extra degrees of freedom without post-calculation needed. Its accuracy and efficiency would much simplify the analysis for various types of cracks. However, it's required to create the geometry and the mesh in the external finite element software, and import these information to the specialized program code. This process would involve some manual work that is not convenient for inexperienced users.

On the other hand, the fracture mechanics analysis tools that are currently available in the standard version of ANSYS have limited capability for advanced fracture mechanics calculations. For example, 3-D fracture analysis using ANSYS requires creation of a specialized toroidal crack tip mesh to obtain accurate fracture mechanics solutions. Even for models with a properly specified crack tip mesh, accurate fracture calculations for cracks located in homogeneous medium or on bimaterial interfaces cannot be easily evaluated due to the complex nature of the crack tip singular stress state. As a result, the evaluation of complicated 3-D cracked geometries in engineering applications is a daunting task, even for the most experienced FEM modeler.

In an effort to simplify the FEM modeling for this class of critical problems, the enriched features have been implemented into the framework of commercially available ANSYS finite element software. With the addition of the FRAC3D type of enriched crack tip element into ANSYS, more users can now benefit from these enriched elements without having to transfer model information between two different finite element codes. It's hoped that most users familiar with ANSYS, will find the new user-defined enriched crack tip element an easy to use enhancement of the standard ANSYS code.

7.1 Implementation in ANSYS

Implementation in ANSYS of the enriched crack tip functionality, currently available in the FRAC3D code, required generation of the appropriate element stiffness matrices for a hybrid

user-defined element containing additional degrees of freedom beyond the regular nodal displacements. In addition, since the enriched crack tip element must integrate analytic terms associated with the asymptotic crack tip stress field, a higher-order numerical integration must be used for these elements (current default is $8 \times 8 \times 8$ for the enriched hexahedron). Since the stress intensity factors are treated as additional unknowns, great care must be taken to ensure that during the solution phase in ANSYS, the "stiffness" and "load" terms associated with these quantities are properly stored in the "global" matrices and load vectors.

Based on the user programmable features in ANSYS, a 20-noded hexahedral enriched user-defined element has been developed for use with ANSYS. The essential algorithm of computing stress intensity factors is embedded through the interface routine "*UserElem.F*". Considering simplicity and convenience for future development work, the programming logic has been uncoupled as much as possible between ANSYS and FRAC3D. Modifications in the enriched user-defined element are only transmitted through the element shape functions, the Jacobian matrix and the derivative of shape functions ([*B*] matrix) at the local element level. The assembly of global stiffness matrix and/or any bookkeeping necessary for the solution of the augmented system of equations is handled entirely by ANSYS. From the viewpoint of coding, only three former FRAC3D subroutines are invoked in "*UserElem.F*". These subroutines in turn serve as the interface to transfer all the other required functions from previous FRAC3D coding. The related global parameters are shared through common blocks (Figure 66).

The global coordinates and the connectivity are required to calculate the asymptotic terms for each user-defined enriched crack tip element. An optimized method collects the connectivity information automatically before calling the solver, saving this information in the internal memory. For each user-defined element, subroutine "*UserElem.F*" obtains the appropriate nodal connectivity by reading memory, and then automatically determining the orientation of this element with respect to the crack front and crack surfaces. After creating the cracked finite element model, ANSYS commands are issued to obtain the nodal and elemental information, as well as the loads and boundary conditions. The crack tip nodes need to be designated by the user from the ANSYS graphic interface. The stress intensity factors for three fracture

modes, K_I, K_{II}, K_{III}, are treated as three extra DOFs in the enriched user defined element. Accordingly, 120 DOFs are required for a three-dimensional 20-node enriched element, rather than the standard 60 DOFs for a regular hexahedron element in ANSYS (SOLID186). The corresponding [*B*] matrix has a dimension of 6x120, and the dimension of the enriched element's local stiffness matrix should be 120x120.

USE maxel_nod_mat_dof USE common_strc1 USE common_lnod USE maxpsr_crk USE common_crack1 USE common_crack2 USE common_crack3 USE common_intcrk USE common_eltyp USE common_crkset USE common_ansys_para	Some required common blocks are added in "*UserElem.F*"
c********** c** Call frac3d to pre-compute the asymptotic terms c********** c IF(ansysflag .ne. 999) THEN CALL frac3d(elId) c ansysflag=999 c ELSEIF(ansysflag .eq. 999) THEN c CALL pcg(0, numintpoin, elId) c END IF	"*frac3d*" is called to get the element connectivity information and pre-compute the asymptotic terms.

c If the current element is an enriched one, call shapen_20
IF(nitem .eq. 1)THEN
CALL shapen_20_120(elId, nUsrDof, nIntPnts, intPnt, wtIP, xl(1),
& yl(1), zl(1), BMat(1,1), detJac, shIso(1),
& workarr(1), FLnodes(1), ALcn(1))
ELSE
c write(*,*) "**********BREAK POINT 4**********"
c If the current element is not an enriched one, call shape_20
CALL shape_20_n(nUsrDof, nIntPnts, intPnt, wtIP, xl(1), yl(1),
& zl(1), BMat(1,1), detJac, shIso(1), workarr(1), FLnodes(1))
	"*shapen_20_120*" and "*shape_20*_n" are called to transmit the connectivity information to FRAC3D and obtain necessary functions and matrices from FRAC3D

Figure 66: Coding Details in the User-Defined Subroutines that Implement FRAC3D Enriched Element Functionality.

The format of [*B*] matrix for an ANSYS user-defined element is given below,

$$[B]_{6\times 120} = [[B_1] \quad [E_1] \quad [B_2] \quad [E_2] \quad \cdots \quad [B_{19}] \quad [E_{19}] \quad [B_{20}] \quad [E_{20}]] \tag{7.1}$$

where

$$[B_j]_{6\times 3} = \begin{bmatrix} \frac{\partial N_j}{\partial x} & 0 & 0 \\ 0 & \frac{\partial N_j}{\partial y} & 0 \\ 0 & 0 & \frac{\partial N_j}{\partial z} \\ \frac{\partial N_j}{\partial y} & \frac{\partial N_j}{\partial x} & 0 \\ \frac{\partial N_j}{\partial z} & 0 & \frac{\partial N_j}{\partial x} \\ 0 & \frac{\partial N_j}{\partial z} & \frac{\partial N_j}{\partial y} \end{bmatrix} \tag{7.2}$$

for the regular displacement DOFs, and $[E_j]_{6\times3}$ includes the asymptotic terms related to the extra DOFs.

It should be noted, that the matrix terms are arranged node by node for the user-defined enriched element. This scheme is different from the arrangement in FRAC3D's original format:

$$[B]_{6\times69} = [[B_1] \quad [B_2] \quad [B_3] \quad \cdots \quad [E_{19}] \quad [B_{20}] \quad [E_1] \quad [E_2] \quad [E_3]] \tag{7.3}$$

In the original FRAC3D enriched element formulation, only those nodes attached to the crack front have the required three extra DOFs K_I, K_{II}, K_{III}. In addition, the matrix entries for regular displacement DOFs and the entries associated with asymptotic displacements from the crack tip singularity are located separately. Thus, the [*B*] matrix required for the ANSYS implementation of the enriched crack tip element, has to be converted to the appropriate ANSYS specific format before assembly of the stiffness matrix.

Another significant issue is the correspondence of the local nodal numbering orders in the regular ANSYS element formulation and FRAC3D's original numbering order. The FRAC3D algorithm automatically rotates the coordinate system of the crack tip element in such a way as to make the crack front coincide with the element's local ξ axis. This is done in the enriched element formulation by properly incorporating the asymptotic crack tip field with any possible orientation of the crack front. For a hexahedron element there are 24 possible crack tip orientations with respect to the element edge overlapping the crack front. As a rule in the formulation, for any case the element's local coordinates are accordingly rotated so that the edge designated by nodes 5-13-6 always coincide with the crack front (Figure 67).

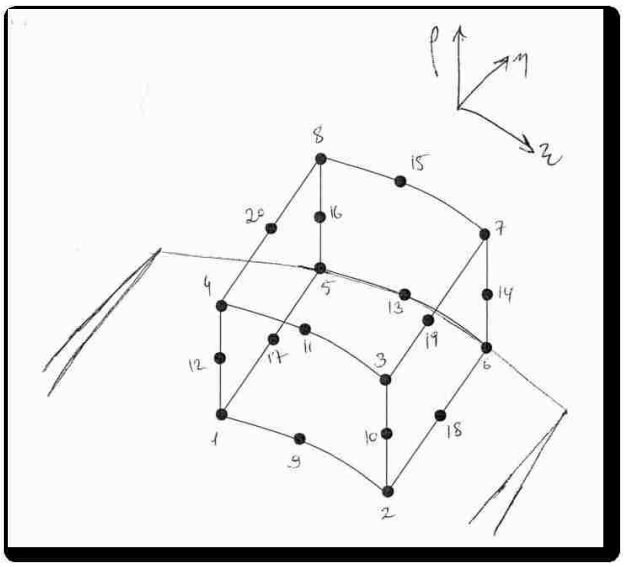

Figure 67: Primary Orientation of Enriched Element Coordinate System with respect to the Crack Front.

This reorientation scheme can potentially result in a mismatch of local nodal coordinates, or numbering order, between the element definition in ANSYS and the enriched element in FRAC3D. An internal nodal reordering process is required for the enriched crack tip elements before and after the calculation of the Jacobian matrix and asymptotic terms. In the implementation of ANSYS user-defined element, two reciprocal reordering processes [A] and [B] have been introduced. The correspondence relationship is generated automatically for each enriched crack tip element by mapping the local numbering order from FRAC3D to ANSYS.

After computing the asymptotic terms (displacements and strains) associated to the extra DOFs from the original FRAC3D subroutines, every term should be put in its correct position in the [B] matrix for the corresponding ANSYS user-defined element. This process is achieved using the correspondence of the local nodal numbering orders and the different dimensions of elemental DOFs (Figure 68).

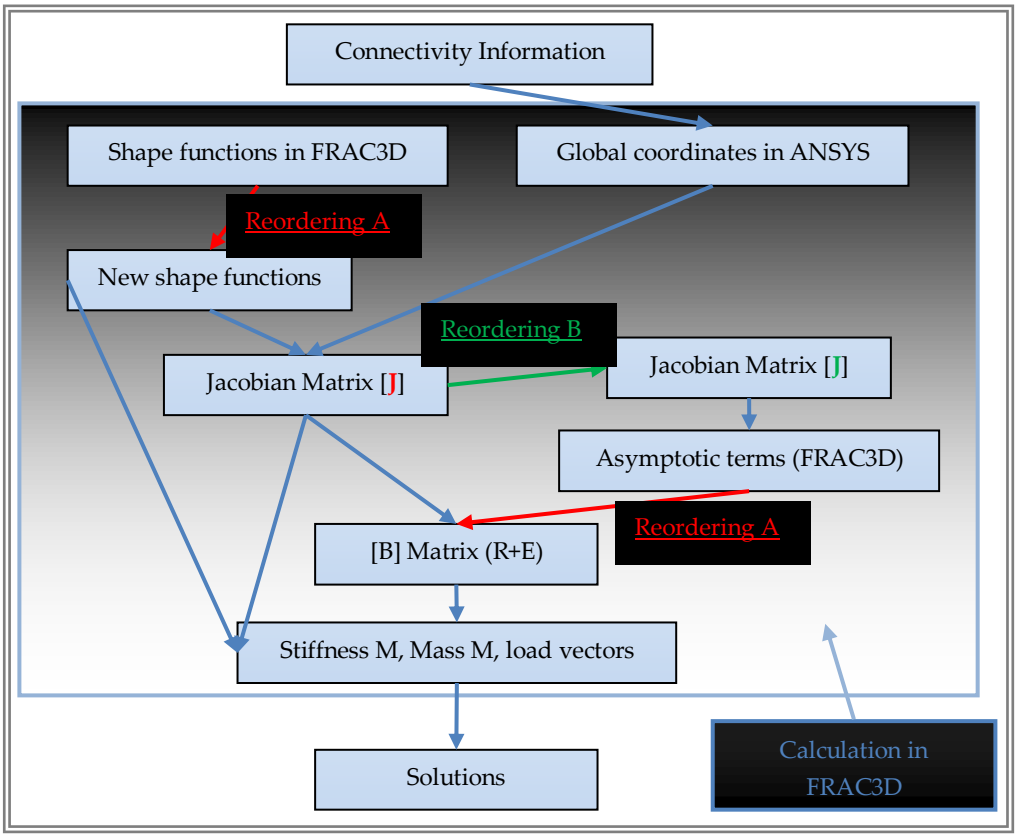

Figure 68: Schematic Showing the Nodal Renumbering Mapping Process for the Enriched Crack Tip Elements.

7.2 Compiling and Linking

User programmable features (UPFs) are ANSYS capabilities that can be used to write one's own specialized routines. Using UPFs, it is possible to tailor the ANSYS program to fit certain specialized computational needs. For example, UPFs make it possible to define a new material behavior, create a special element, or implement a modified failure criterion within the ANSYS software architecture. User modifications can range from relatively minor additions to ANSYS computational capabilities, to comprehensive optimization algorithms that call the entire ANSYS finite element program as a subroutine [63, 64].

There are some basic points that one needs to know before implementing a new user defined element within the ANSYS FEM software environment.

1) **Permission to access the appropriate ANSYS files**

An authorized ANSYS license is needed to read, modify and re-compile user-defined subroutine files.

2) **Configuration of compilers for Fortran and C++**

Both Fortran and C++ compilers need to be installed to compile and link the user-defined subroutines required for creation of a custom executable version of ANSYS.

3) **The ANSYS program**

The modeling methods in ANSYS using GUI and the script file of commands (APDL) need to be familiar with.

4) **UPF subroutines**

Before modifying and customizing ANSYS, one needs to understand clearly the logic and flow of the UDE subroutine, which provides the interface for passing all data needed between a user-defined element and database or files, to the ANSYS code above the element level. There are many examples in the "*custom*" or "*customize*" directory for each of the supported user subroutines. The relevant details are provided in the ANSYS programming manual [63, 64].

5) **Fortran**

User Programmable Features typically involve writing subroutines in Fortran. In ANSYS, Fortran 90 is the supported language, so some proficiency in Fortran90 programming is required for writing a new user-defined element.

6) **Algorithms for new elements**

Before implementing a new element, one needs to clearly understand the features of the new element; making sure that it's indeed feasible to implement the particular element within the ANSYS framework. In addition, one needs to verify the accuracy of individual computational subroutines independent of ANSYS. In this particular project, the methodology used to implement the enriched crack tip element required a number of "workarounds" that permitted implementation of the enriched element strategy within the constraints of the ANSYS main code, including its assembly and solution algorithms.

The general steps to implement the user-defined element are given as follows. The details can be found in the user guide [65].

- ✓ Setting up an appropriate development environment.
- ✓ Finding useful subroutines and related files in the "*custom*" or "*customize*" directory and put them into your working directory
- ✓ Modifying the subroutines accordingly.
- ✓ With the supported compiler listed, compiling subroutines to create the object file.
- ✓ With the supported linker, linking the compiled object file and supplied libraries to create a custom ANSYS executable.

7.3 Fracture Analysis Using User-Defined Element

After compiling and linking the user-defined subroutines, the customized executable integrating the desired enriched feature is generated in ANSYS though the user programmable interface. Right now, a new type of three-dimensional crack tip element, enriched 20-noded hexahedron, is available for use like other regular elements in ANSYS. One may utilize the user-defined element, designated as the "USER300" element, in the similar manner such as activating it in the libarary, defining its properties, and meshing the solid solid. In the first test, the "USER300" element was used as a "regular" element in a particular finite element model. Identical solution was obtained compared with that using the ANSYS "SOLID95" element. This useful cross-check verified that the user-defined element was properly implemented into the ANSYS executable code. For finite element models with designated cracks, the "USER300" element uses the enriched formulation automatically to perform the necessary fracture analysis, outputting values of the stress intensity factors, strain energy release rates, and other relevant fracture parameters along the crack front.

The analyzing has been much simplified compared with the original process. The following are necessary steps in ANSYS to use the user-defined crack-tip element

- ✓ Activating the user-defined crack tip element

- ✓ Specifying the characteristics and extra DOFs for the user-defined element
- ✓ Identifying the crack front and enriched crack-tip elements
- ✓ Assigning appropriate parameters for fracture analyses
- ✓ Checking the results

7.4 General Commands

To use the user-defined enriched crack tip element in the ANSYS program, the user should issue a series of internal commands either in the GUI command box or in the APDL script file. All the relevant commands are listed in (Table 16).

The user may also want to refer to the ANSYS programming manual [63, 64] for more details. The practical application of these commands for designating and invoking the enriched elements is discussed in the examples.

Commands	Description
/DFLAB,4,K1 */DFLAB,5,K2* */DFLAB,6,K3*	Changes DOF labels for user defined elements. This command defines three new DOFs *K1,K2,K3*, and must be issued at the beginning of the command flow.
ET,,USER300*	Defines a new element (*ET, Type No., Element Name*). "USER300" is the label for the user defined element.
KEYOPT,,1,1*	Sets element key option (*KEYOPT, Type No., No. of KPT, value*). This command is to select the element type defined in "*UserElem.F*"
USRELEM,20,3,BRICK,,3072, 3072,0,512,3,0	Specifies the characteristics (*USRELEM, No. of nodes, No. of dimensions, element shape,,,, material definition(std), max No. of integration points, stress state(3D solid), symmetric*)
USRDOF,DEFINE,UX,UY,UZ,K1,K2,K3	Specifies the degrees of freedom (*USRDOF, action type, the list of DOFs*)
EMODIF,ALL,TYPE, *EMODIF,ALL,MAT,**	Modifies the type or the material properties of the previously defined element. This command is to change the regular element to the user-defined element

F3D	This is a new macro command generated by the project developer. It is used to start graphic interactive dialogs to get useful parameters. It should be issued after meshing the model.

Table 15: Specific Commands for the User-Defined Element

7.5 An Example of Interfacial Crack

The interfacial cracking behavior can be efficiently modeled using user-defined enriched crack-tip finite elements. For example, Figure 69 schematically depicts two types of initial interface corner cracks between silicon and epoxy. Figure 70 shows example finite element meshes that can be used to compute the initial values of K_I, K_{II}, K_{III}, for corner cracks at the beginning of a fatigue simulation.

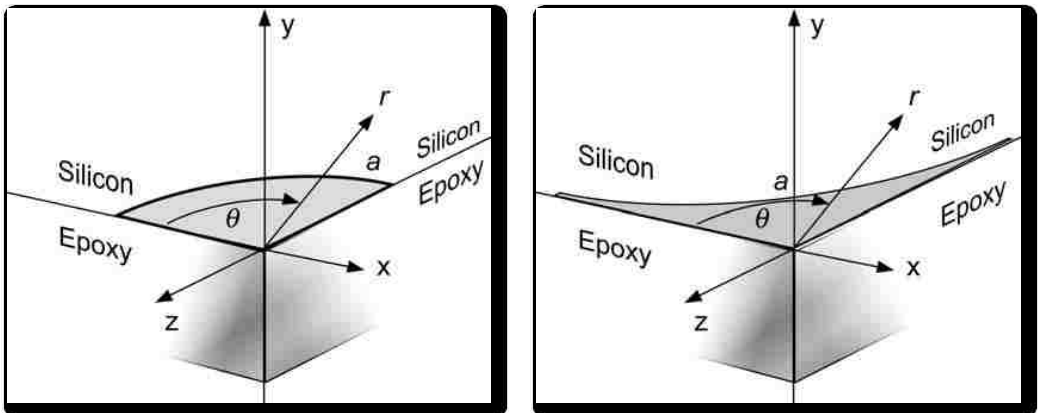

(a) (b)

Figure 69: Local Coordinates (r, θ) for a) Quarter-Circular Interface Corner Crack and b) Cusp-Shaped Interface Corner Crack between Silicon and Epoxy.

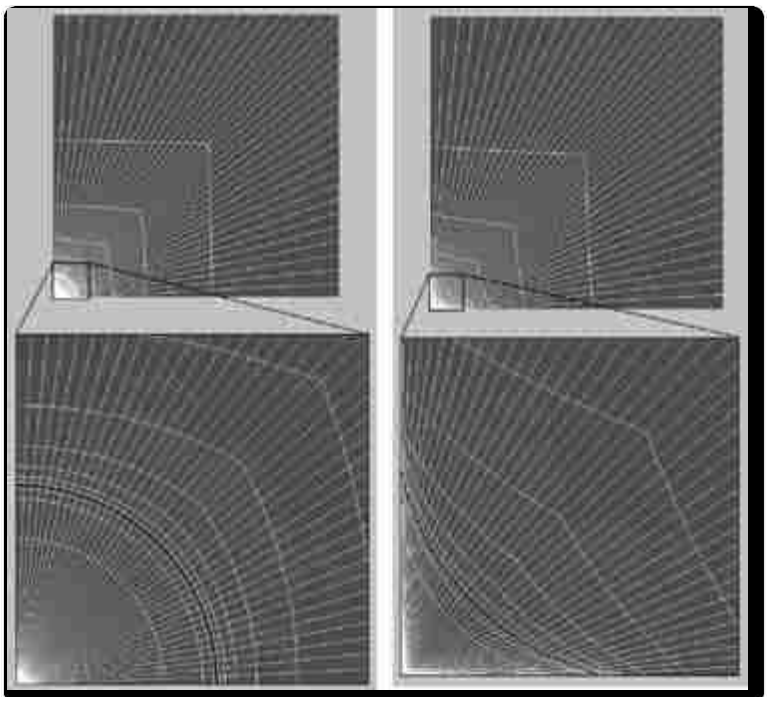

(a) (b)

Figure 70: 3-D Finite Element Model used in Simulations and Initial Mesh for Corner Crack Front (a) Quarter-Circular Crack and b) Cusp-Shaped Crack).

The specific properties for this model are given as below:

Thickness of the Model (2H)	H = 10 mm
Length of the Model (L)	L = 50 mm
Width of the Model (W)	W = 50 mm
Radius of the 1/4-Circular Crack (a)	a = 5 mm
Young's modules (*E*)	$E_1 = 2900\ \text{MPa}$ $E_2 = 128280\ \text{MPa}$
Poisson Ratio (ν)	$\nu_1 = 0.34$ $\nu_2 = 0.279$
Coefficient of Thermal Expansion (CTE)	$CTE_1 = 5.2E-5\ \ (C^o)^{-1}$ $CTE_2 = 2.6E-6\ \ (C^o)^{-1}$
Reference Temperature	$200\,C^o$

Current Temperature	$100\,C^{o}$

Table 16: Properties for the Quarter-Circular Interface Crack Model

The solid model and the 3-D mesh can be observed in the following pictures (Figure 71 & 72).

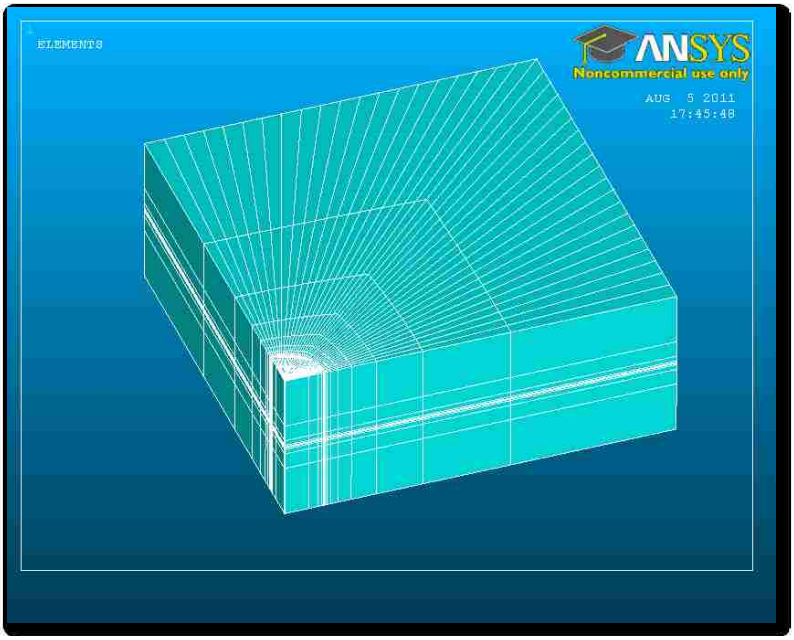

(a)

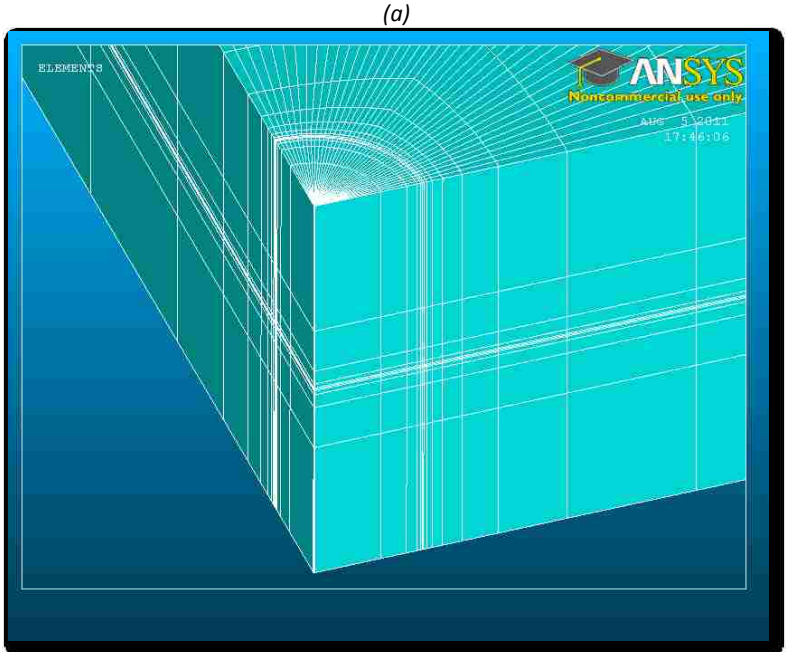

(b)

Figure 71: a) Mesh of the Quarter-Circular Crack Model; b) Zoomed mesh around the crack front area.

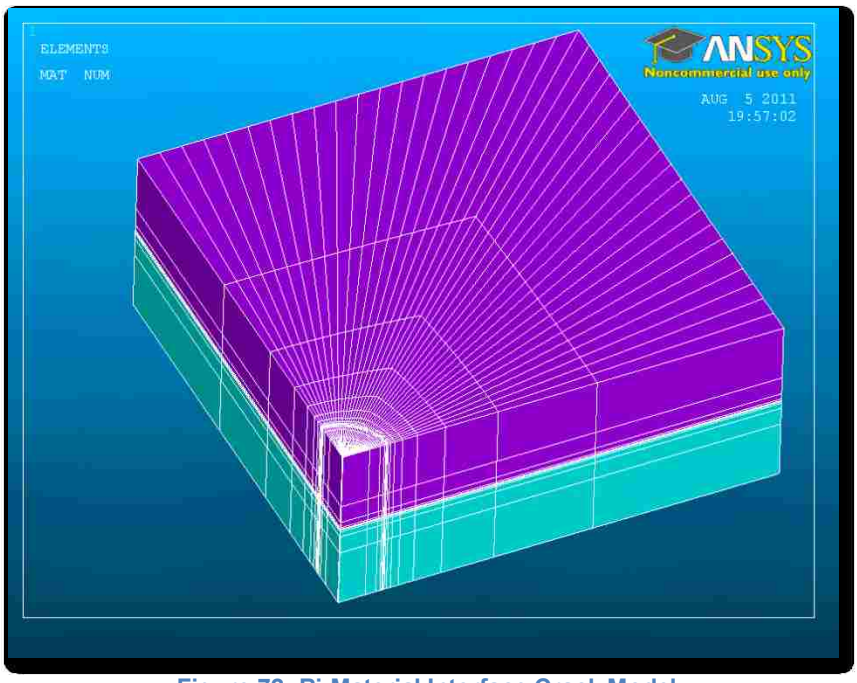

Figure 72: Bi-Material Interface Crack Model.

Then a critical step in using the enriched crack tip element is to properly identify all the nodes on the crack front arc. These nodes are selected, extracted and saved for the purpose of finding the enriched crack-tip elements. All these elements are recognized automatically by the program and the corresponding type is altered to “USER300”. Basically, all those elements attached to any crack-tip node should be identified as enriched crack-tip elements, which are shown in purple in the figure below (Figure 73).

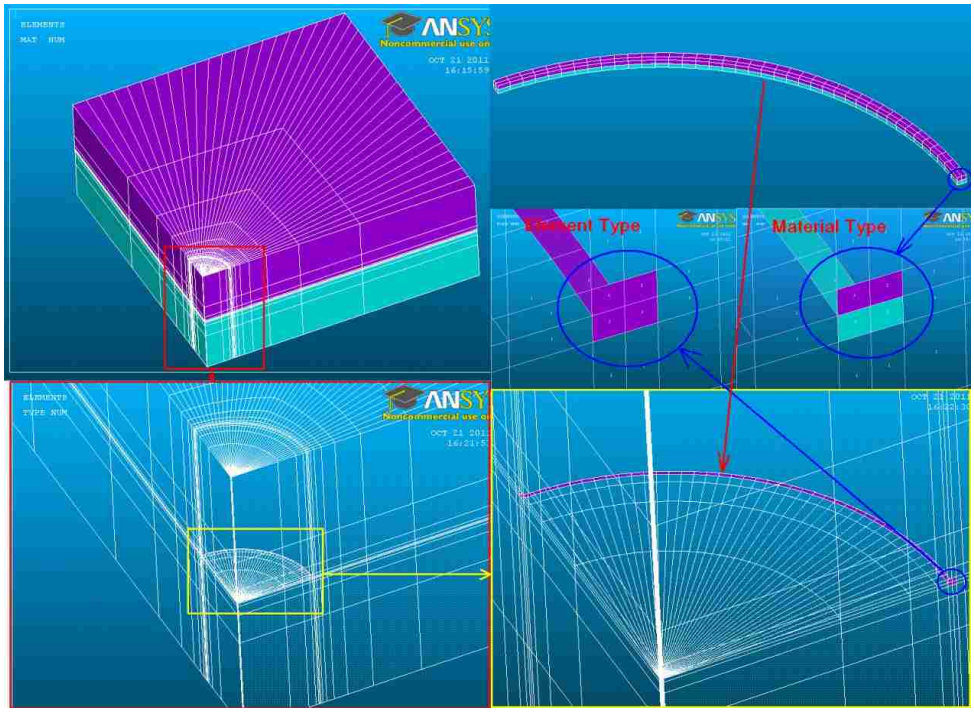

Figure 73: Quarter-Circular Crack Model Including User Defined Element

Then the finite element analysis is carried out using ANSYS' intrinsic solver. The final results can be checked out as the regular degrees of freedom. The results for this example coincide very well with the outputs by FRAC3D.

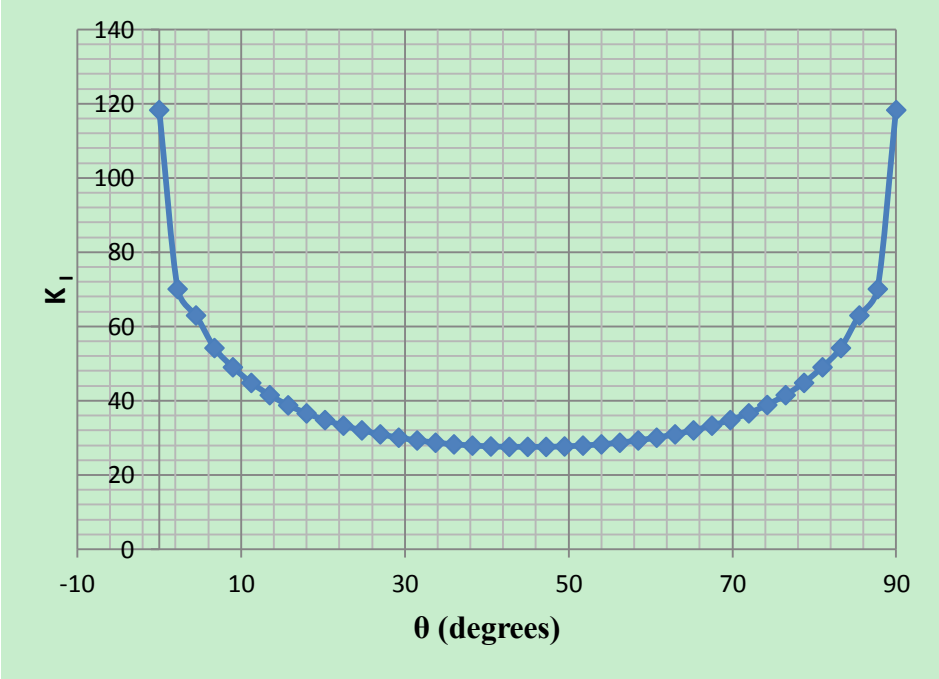

Figure 74: Distribution of K_I for Quarter-Circular Crack Model Including User Defined Element

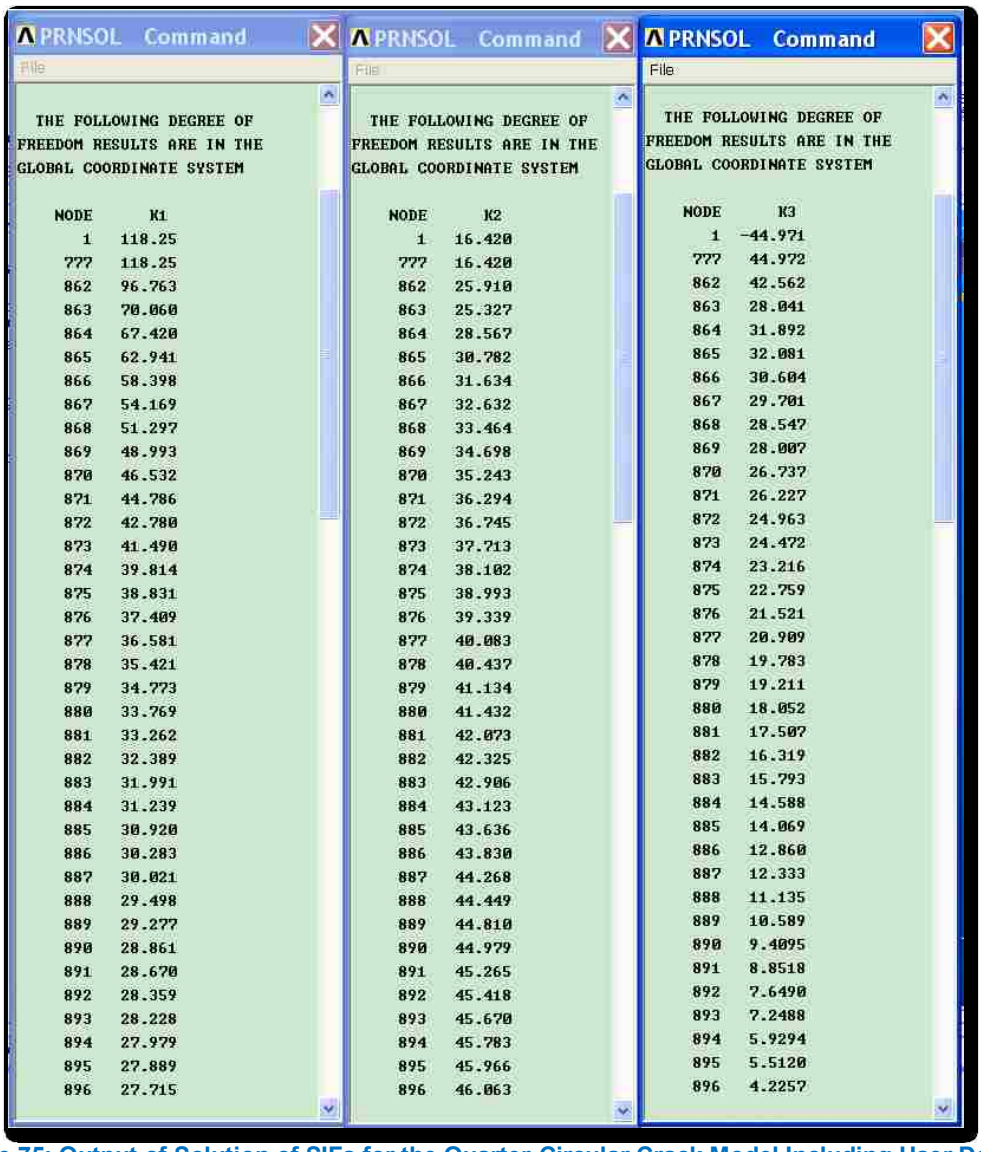

Figure 75: Output of Solution of SIFs for the Quarter-Circular Crack Model Including User Defined Element

8 Conclusion and Future work

8.1 Conclusion

In this study, the asymptotic solution was generated for an isotropic semi-finite crack impinging on the bonded interface with an arbitrary incidence angle. This general type of crack is more meaningful for investigating the strength of the singularity in the close-tip area, since the attacking angle of a crack with respect to the interface is uncertain, rather than the particular cases such as the perpendicular crack problem or the interfacial crack problem. While the nonlinear, inelastic or plastic behavior may dominate the crack-tip field, the asymptotic field in the context of linear elastic fracture mechanics is still valid if the small-scale scale yielding condition is satisfied. The formulation of the asymptotic field with split singularities was applied and extended to deal with the situation with complex dominant roots. The formulation in matrix form was implemented easily into the enriched finite element, which much simplifies the computational analysis of elastic crack problems. Basically, this study was mainly focused on the crack subject to in-plane loads since the mixed-mode nature is very complicated if the crack-tip area is bi-material. However, the explicit formulation for Mode-III crack is also given, and it can be superposed with the in-plane mode in a straight-forward way under some idealization considerations.

The entire derivation process was introduced in steps. For an isotropic crack impinging on the bonded interface with an arbitrary incidence angle, the mathematic model was generated using the Williams' series expansion method. Both the in-plane mode (Mode-I/II) and the anti-plane (Mode-III) were investigated using a two-dimensional geometry, which was divided into three zones due to the asymmetry nature. A 12x12 solution system in matrix form for in-plane case (6x6 for anti-plane) was established through applying corresponding boundary conditions. For computation convenience, this matrix was reduced to the product of two 4x4 matrices, of which one represents the mathematical essential and gives the characteristic equation, and another creates the relationship between material zones. The characteristic equation was generated, and numerically solved using a revised self-adaptive Newton-Raphson iteration method. Double roots

arises in the dominant region (0, 1), and their contribution for the final result cannot be ignored. Along with varying crack incidence angles, the transition phenomenon was observed between two real dominant roots and a pair of complex conjugated roots.

The same procedure was also carried out for the anti-plane problem. In contrast with the in-plane case, only a single root exists for any crack incidence angle.

The essential contribution in this study is the development of the asymptotic stress and displacement. Due to the asymmetry nature in material and geometry, the conventional analytical methods are difficult to use. In author's method, a linear system was established through the characteristic matrix and the relationship matrix. With the help of fundamental linear algebraic operations, the asymptotic field was derived by superposing the sub-solutions with respect to split singularities, and expressed in terms of the stress intensity factors. Different strategies of derivation for different type of singularities were discussed in details. As another contribution in this study, the split phenomenon of complex singularities was discovered and explained to coincide with the definition of complex stress intensity factors. A rotation factor was introduced as the angular function was normalized ahead the crack tip.

Next, the asymptotic terms obtained using the new derivation scheme were programmed into an academic fracture analysis software package, FRAC2D/FRAC3D, which was developed using enriched finite elements. Some examples of 2-D isotropic plane cracks were examined respectively. The normalized numerical results showed good agreement with existing theoretical solutions. The overall asymptotic stress field was built in the circumference with a characteristic radial distance, which theoretically should be selected based on the size of process zone. In this study, because the dissimilarity of materials and the obscure definition of the mixed-mode stress intensity factors, a geometric size was used for computing the stress distribution in circumferential direction. Due to the invalid strain energy release rate for interface related cracks, a modified hoop stress criterion was taken into account to predict the crack propagation direction. On the other end, a 3D crack example with varying stress singularities was given, and the distribution of stress intensity factors was depicted.

Finally, the development work of the user defined element was introduced. The features of the enriched finite element were transplanted into a commercial FEA code to benefit more users in different research field.

8.2 Future work

Basically, the research work in this study is generating an analytical solution of the overall asymptotic field for cracks terminating at the bi-material interface with arbitrary angles. It has provided an effective mathematic approach of creating the mathematic model, formulating the singular field, and computing the facture parameters. However, the object of this study is to reveal the physical nature of the crack-tip area, and establish an appropriate criterion in mechanics for predicting the crack's propagation. Thus, the following work in the future should concentrate on the discovery the corresponding physical meaning of the mathematical solution, and the application of this computational method into practical problems. According to this purpose, some suggested work can be summarized as follows:

1) This study is just for the cracks within the isotropic media. The same process can be applied for other anisotropic materials. Different constitutive laws are required, but the establishment of linear solutions system should be the same. An interesting object is to check if there is also a transition phenomenon, real to complex, for the strength of singularities as the crack's impinging angle rotates with respect to the interface.
2) It's definitely desired to find the reason and the physical meaning of the transition behavior of the strength singularities. The coupling of the crack-tip fields needs to be further explained in the field of mechanics. This would be helpful and meaningful for deep understanding the oscillatory behavior of the singular field.
3) In this study, the asymptotic solution with split singularities was extended to the complex root situation. A new rotation factor was introduced to redistribute the contribution from the complex stress intensity factor to the asymptotic field. However, this original formulation needs to further verified either by comparing with simplified cases, or through

experimental tests. This work would experience a long-term period, since we lack of relevant referenced standard and volunteered solution.

4) For a crack terminating at the interface with an oblique angle, 3-D models are more practical and should be further investigated in the future. One concern is the variation of the stress field with varying λ along the crack front. As a complicated situation, the different magnitude of the strength of singularities at different location on the crack front makes it difficult to study the stress field only using the fracture parameters. The overall stress field surrounding each crack tip needs to be established. Then, the compatibility condition through the crack front should be considered. In addition, the boundary effect from the free surface would also deserve an investigation for such type of interface-related crack, since the material mismatch may lead to a complicated mixed mode situation.

5) In this study, the fracture parameters lose their actual representation for the singular field due to the mixed mode singularities. Thus, the stress-based criterion was used to predict the crack's propagation. However, it would be more meaningful to find a single-parameter criterion in mechanics for estimating the crack's behavior. This might be an important issue which deserves an in-depth study.

References

[1] A. A.Griffith, "*The phenomena of rupture and flow in solids"*, Philosophical Transactions of the Royal Society of London, A 221: 163–198, 1921

[2] F.Erdogan, "*Fracture Mechanics"*, International Journal of Solids and Structures, 37, PP.171-183, 2000

[3] G. Irwin, "*Analysis of stresses and strains near the end of a crack traversing a plate"*, Journal of Applied Mechnics, 24, 361-364, 1957.

[4] B. Budiansky, J.W.Hutchinson, A. G. Evans, "*Matrix Fracture in Fiber-Reinforced Ceramics"*, Journal of Mechanics & Physical Solids, Vol. 34, No. 2, pp. 167-189, 1986

[5] Z.C.Xia, R.R.Carr, J.W.Hutchinson, "*Transverse Cracking in Fiber-Reinforced Brittle Matrix"*, Cross-PLY Laminates, Acta Metallurgica et Materialia, Volume 41, Issue 8, August 1993, Pages 2365–2376

[6] B. K. Ahn, W. A. Curtin, T. A. Parthasarathyy & R. E. Dutton, "*Criteria For Crack Deflection/Penetration Criteria For Fiber-Reinforced Ceramic Matrix"*, Composites Science and Technology 58 (1998) 1775-1784

[7] Herman F. Nied, "*Mechanics of Interface Fracture With Applications in Electronic Packaging"*, IEEE TRANSACTIONS ON DEVICE AND MATERIALS RELIABILITY, VOL. 3, NO. 4, DECEMBER 2003 129

[8] M. L. Williams, "*The stresses around a fault or crack in dissimilar media*", Bulletin of the Seismological Society of America, Vol. 49, No. 2, pp. 199-204, April 1959.

[9] F. Erdogan, "*Stress distribution in bonded dissimilar material with cracks*", Journal of Applied Mechanics, 32, 403-410, 1965.

[10] A. H. England, "*A Crack Between Dissimilar Media*", J. Appl. Mech. 32(2), 400-402 (Jun 01, 1965) (3 pages)

[11] Malyshev, B.M., and Salganik, R. L., "*The Strength of Adhesive Joints Using the Theory of Fradture*", International Journal of Fracture Mechanics, Vol.1, 1965, pp. 114-128.

[12] J. R. Rice, G. C. Sih, "*Plane Problems of Cracks in Dissimilar Media*", Journal of Applied Mechanics, Volume 32, pp. 418-423, 1965

[13] N. I. Muskhelishvili, "*Some basic Problems of the mathematical theory of elasticity*", Fourth Edition, 1972.

[14] M. Comninou, "*The interface crack*", Journal of Applied Mechanics, 44, 631-636, 1977

[15] M. Comninou, J. Dundurs, "*Effect of friction on the interface crack loaded in shear*", Journal of Elasticity. 10(1980) 203-212

[16] J. R. Rice, "*Elastic fracture mechanics concepts for interfacial cracks*", Journal of Applied Mechanics, 55, 98-103, 1988.

[17] C.T.Sun, W. Qian, "*The use of finite extension strain engery release rates in fracture of interfacial cracks*", International Journal of Solids and Strutures. 34(1997) 2595-2609

[18] J. W. Hutchinson, Z. Suo, "*Mixed-mode cracking in layered materials*", Advances in Applied Mechanics, 29, 63-19, 1992.

[19] A. R. Zak, M. L. Williams, "*Crack point stress singularities at a bi-material interface*", Journal of Applied Mechanics, 30, 142-143, 1963.

[20] T. S. Cook, F. Erdogan, "*Stress in bonded materials with a crack perpendicular to the interface*", International Journal of Engineering Science, 10, 677-697, 1972.

[21] K. Y. Lin, J. W. Mar, "*Finite element analysis of stress intensity factors for cracks at a bi-material interface*", International Journal of Fracture, 12, 521-531, 1976.

[22] A. C. Kaya, "*Application of integral equations with strong singularities in fracture mechanics*", PhD dissertation, Lehigh University, 1984

[23] Y. Sugimura, P.G.Lim, C.F.Shih, S.Surash, "*Fracture normal to a bi-material interface: effects of plasticity on crack-tip shielding and amplification*", Acta Metallurgica et Materialia, Vol. 43, No.3, pp. 1157-1169, 1995

[24] Tzuchiang Wang,"*A crack perpendicular to and terminating at a bi-material interface*", Acta Mechanica Sinica, Vol.14, No.1, Feb, 1998

[25] S.H.Chen, T.C.Wang, Sharon Kao-Walter, "*A crack perpendicular to the biomaterial interface in finite solid*", International Journal of Solids and Structures, Vol. 40, 2003, pp. 2731-2755.

[26] J.H.Chang, D.J. Wu, "*Calculation of mixed-mode stress intensity factors for a crack normal to bi-material interface using contour integrals*", Engineering Fracture Mechanics, Vol. 70, 2003, pp. 1675-1695.

[27] G. A. Papadopoulos, "*Stress analysis at a bi-material Interface Crack tip*", The Open Mechanical Engineering Journal, 2, 60-68, 2008

[28] Tilbrook M. T., Rozenburg K., Steffler E. D., Rutgers L, Hoffman M., "*Crack propagation paths in layered, graded composites*", Composites: Part B 37, (2006), pp. 490-498.

[29] Kaya C., Butler E.G., Lewis M.H., "*Co-extrusion of Al2O3/ZrO2 bi-phase high temperature ceramics with fine scale aligned microstructures*", Journal of the European Ceramic Society 23, (2003), pp. 935-942.

[30] D. B. Bogy, "*On the plane elastic problem of a loaded crack terminating a material interface*", International Journal of Fracture, 38, 911–918, 1971.

[31] N.E. Ashaugh, "*Stress solution for a crack at an arbitrary angle to an interface*", International Journal of Fracture, 11 (1975), pp. 205–219

[32] D. N. Fenner, "*Stress singularities in composite materials with an arbitrarily oriented crack meeting an interface*", International Journal of Fracture, Vol. 12, No. 5, October 1976.

[33] J. T. Chen, W. C. Wang, "*Theoretical and experimental analysis of an arbitrarily terminated at the bi-material interface inclined semi-infinite crack*", Journal of Strain Analysis, Volume 30, No. 2, 1995.

[34] Liviu Marsavina, Tomasz Sadowski, "*Asymptotic stress field at the tip of an inclined crack terminating to an interface*", Budownictwo i Architektura 2 (2008) 111-124

[35] Zhen Zhang, Zhigang Suo, "*Split singularities and the competition between crack penetration and debond at a bi-material interface*", International Journal of Solids and Structure,44, 4559-4573, 2007

[36] Swedlow,J.,L., Williams,M.L. and Yang,W.H. (1965). "*Elasto-plastic Stresses and strains in cracked plate*", Proc.1st.Int.Conf. Fracture.,, (pp. Vol 1, 259-282). Sendai, Japan.

[37] Henshell,R.D and Shaw,K.G. (1975). "*Crack tip finite elements are unnecessary*", International Journal for Numerical Methods in Engineering. Vol. 9, pp. 495-507, 1975

[38] Barsoum, R. "*Furthur application of quadratic isoparametric elements to linear fracture mechanics of plate bending and general shells*". International Journal for Numerical Methods in Engineering, Vol. 11, pp. 167-169, 1976.

[39] P. Tong, T. H. H. Pian, S. Lasry, "*A hybrid-element approach to crack problems in plane elasticity*", International Journal for Numerical Methods in Engineering, 7, 3, 297-308, 1973.

[40] Belytschko T, Black T., "*Elastic crack growth in finite elements with minimal remeshing*". Int J Numer Meth Engng 1999;45:601–20.

[41] Moes N, Dolbow J, Belytschko T., "*A finite element method for crack growth without remeshing*", Int J Numer Meth Engng 1999;46:131–50.

[42] Moes N, Belytschko T., "*Extended finite element method for cohesive crack growth*", Engng Fract Mech 2002;69:813–33

[43] Sukumar N, Srolovitz DJ, Baker TJ, Prevost JH., "*Brittle fracture in polycrystalline microstructures with the extended finite element method*", Int J Numer Meth Engng 2003;56:2015–37.

[44] J. Liang, R. Huang, J.H. Prevost, Z. Suo, "*Evolving crack patterns in thin films with the extended finite element method*", International Journal of Solids and Structures 40 (2003) 2343–2354

[45] Huang, R., Prevost J.H., Huang, Z.Y., Suo, Z., 2003a, "*Channel-cracking of thin films with the extended finite element method*", Engineering Fracture Mechanics 70 (18), 2513–2526.

[46] S. E. Benzley, "*Representation of singularities with isoparametric finite elements*", International Journal for Numerical Methods in Engineering, 8:537-545, 1974.

[47] E. P. Chen, "*Finite element analysis of bi-material interface crack*", Theoretical and Applied Fracture Mechanics, 3, 257-262, 1985.

[48] A. O. Ayhan, H. F. Nied, "*Stress intensity factors for three-dimensional surface cracks using enriched finite elements*", International Journal for Numerical Methods in Engineering, 54:899-921, 2002.

[49] A. O. Ayhan, A. C. Kaya, H. F. Nied, "*Analysis of three-dimensional interface cracks using enriched finite elements*", International Journal of Fracture, 142,:255-276, 2006.

[50] M. L. Williams, "*Stress singularities resulting from various boundary conditions in angular corners of plates in extension*", Journal of Applied Mechanics, 19, 526-528, 1952.

[51] M. L. Williams, "*On the stress distribution at the base of a stationary crack*", Journal of Applied Mechanics,1957

[52] C.T.Sun,Z.H.Jin, "*Fracture Mechnics*", Academic Press, 2012, ISBN: 978-0-12-385001-0

[53] F. Erdogan, "*Fracture of Nonhomogeneous Solids*", The mechanics of fracture, ASME Winter Annual Meetin, New York, NY. December, 1976

[54] F. Erdogan and G. C. Sih, "*On the crack extension in plates under plane loading and teransverse shear*", Journal of Basic Engineering, ASME 85 (1963) 519-527

[55] G.C.Sih, "*Strain energy density factor applied to mixed mode crack problem*", International Journal of Fracture Mechanics. 10(1974) 305-321

[56] R.J. Nuismer, "*An energy release rate criterion for mixed mode fracture*", International Journal of Fracture, 11 (1975), 245-250

[57] A. Cotterell, J.R.Rice, "*Slightly curved or kinked cracks*", International Journal of Fracture, 16(1980), 155-169

[58] M. Y. He, J. W. Hutchinson, "*Crack deflection at an interface between dissimilar elastic materials*", International Journal of Solids and Structures, vol. 25, No.9, 1053-1067, 1989

[59] S.W.Kwon, C.T.Sun, "*Characteristics of three-dimensional stress fields in plates with a through the thickness crack*", International Journal of Fracture. 104(2000) 291-315

[60] Benthem JP, "*State of stress at the vertex of a quarter-infinite crack in a half-space*", International Journal of Solids and Structures 1977; 13:479–492.

[61] Bazant ZP, Estenssoro LF, "*Surface singularity and crack propagation*", International Journal of Solids and Structures 1979; 15:405–426.

[62] J.P.Benthem, "*State of stress at the vertex of a quarter-infinite crack in a half-space*", International Journal of Solids and Structures, 13(1977) 479-492

[63] "*Programmer's manual for ANSYS 11.0*", Release 11.0, January 2007

[64] "*Programmer's manual for Mechanical APDL*", Release 12.0, April 2009

[65] "*User Guide – User-Defined Enriched Crack-Tip Elements for ANSYS*", Yi Chen, Xiao Liu, Murat Saribay, Herman Nied, Lehigh University, SRC Deliverable Report,Sep,2011

Vita

Xiao Liu was born on May 30, 1982 in Zhenping, Henan, China. In 1985, he moved to Zhengzhou, with his parents, Qiwen Liu and Guiying Li to continue his education.

At Zhengzhou No.1 Senior High School, Xiao Liu has won prizes in state and nationwide academic competitions. In 1998, Xiao Liu represented his school at China Mathematics Olympiad and won the first prize. At the age of 18, he was matriculated into Nankai University, Tianjin, China without the normal mandatory examination, a privilege that is granted to only whom the university considers the exceptionally gifted. In 2004, he received a Bachelor's Degree of Science in major of Computer Science and Technology from Nankai University.

In September 2004, Xiao began his graduate study in Department of Computer at Beihang University (Beijing University of Aeronautics & Astronautics), majoring in Software Engineering.

In August 2007, Xiao came to the United States to pursue his doctoral degree in Department of Mechanical Engineering and Mechanics at Lehigh University. Xiao received a Fellowship award in Spring 2008, and worked as a Research Assistant since Fall 2008. In Summer 2010, he received a Master's Degree of Science in Mechanical Engineering. Then Xiao worked as a Teaching Assistant since Fall 2010. He is a P.C. Rossin Doctoral Fellow in the engineering school at Lehigh. His current research mainly focuses on Fracture Mechanics and Finite Element Analysis.